

**Technische Universität
Ilmenau**



Biannual Report 2005/2006



**Institute of Micro- and
Nanotechnologies**

**Center for Micro- and
Nanotechnologies**



Editorial Board:

Editor:

Principal of the TU Ilmenau,
Prof. Dr. rer. nat. habil. Peter Scharff

Editorial office:

Dr. Herwig Döllefeld, ZMN

Layout/press:

Klapproth and Koch, Weimar

Funding:

μ -Comp e. V.





**Institute of
Micro- and Nanotechnologies**

**Center for
Micro- and Nanotechnologies**

Technische Universität Ilmenau



Preface

Richard P. Feynman stated: „Many of the (biological) cells are very tiny, but they are active, they manufacture substances, they walk around, they wiggle, and they do all kind of marvellous things – all on a very small scale. Also, they store information. Consider the possibility that we too can make a thing very small, which does what we want – and that we can manufacture an object that manoeuvres at that level“.

Nanotechnology has now become an umbrella term used to encompass the study, manipulation and application of matter based on its properties at the atomic scale. For more than a century, chemists have been learning to control the arrangement of small numbers of atoms inside molecules, bringing an ability to create more effective drugs, high-performance plastics and other purpose designed materials. Major technological advances have also permitted a progressive downsizing of products over the past few decades - notably in the area of electronics - reducing materials consumption, saving energy and cutting costs, while also greatly expanding functionality. Transition from micro- to the nano-domain nevertheless remains a giant step. Despite major advances in recent years, much remains to be learned about the aggregation of atoms and molecules at the lowest level.

The reason for the widespread interest in this field is that materials can exhibit very different behaviour at the nanoscale to that observed in the mass. At nanometre length scales, quantum effects prevail, so properties are determined by quantum mechanics rather than the classical mechanics that govern matter at the macro- and even micro-scale. Fundamental characteristics such as electrical conductivity, colour, strength and melting point are all subject to change, often bringing dramatic improvements in performance. Because of their very small size, nanoparticles also have a relatively huge surface area, making them ideal for use as absorbers, sensors and catalysts. Of course, these phenomena have always existed, despite the fact they were only recently recognised as such by man. Glass and ceramics are two long-established materials that depend upon nanoscale properties, while photography is a more recent process that unknowingly employed such effects. With deliberate and concerted efforts to tailor the structure of materials at the nanoscale, it will become possible to engineer novel materials that have entirely new properties never before identified in nature. However, this demands multidisciplinary knowledge acquisition through the convergence of nanoscience, biotechnology, information technology and cognitive (NBIC) sciences. Heavy investment,

wide-ranging and crosssectoral research collaboration to provide the required critical mass, as well as new approaches to education, are essential if Europe is to achieve a competitive position in world markets for the resultant materials and products.

Today, the nanotechnology revolution is still at a very early stage. Most applications to date can be described as “bulk nanotechnology” i.e. the commercial-scale production of ultra-thin films and nano-sized particles, such as metal oxides and clays. This alone is already bringing many significant advances. Examples include: zinc oxide, used to provide UV protection in sun creams. When reduced to nanosize, the particles become transparent and are thus more cosmetically appealing than the traditional white product; particles for improving lacquers and paints to provide better protection of surfaces against scratching, soiling or algae coverage; self-cleaning or self-sterilising surfaces with important applications in the food industry and healthcare. These are made by growing hydrophobic or lipophobic chains on a surface to make it water- or fat-repellent; medical devices and implants, with surfaces modified through nanotechnology nanoparticles also have the potential to accumulate in tumour cells, making them more accessible for treatment; high density data storage media making use of the major magnetoresistive properties of nanoscale granular magnetic materials.

Goals for the future are to develop fabrication processes that will permit the organisation of nanoparticles into reproducible supra-molecular arrangements, and ultimately into larger structures that have practical uses. Feynman’s imagined creation of molecular machines that are able to move and to perform given tasks represents a level of complexity that is far beyond current capabilities. Although considered by many to be a pipe dream, the nanotechnologists holy grail is to unlock the secrets of self-assembly. This is a phenomenon that is widespread in the natural world, from the growth of crystals to the formation of complex functional biological cells. Yet the mechanisms of these processes are thus far little understood, and mimicking even the simplest biological systems remains a formidable challenge.

The Center for Micro- and Nanotechnologies (ZMN) provides an outstanding infrastructure well above of state of the art to enable important contribution to the scientific fields mentioned above. Advances in engineering achieved at ZMN have made it possible to fabricate structures at the molecular level

using techniques derived from the microelectronics industry (top-down process), or to grow them using new molecular fabrication techniques (bottom-up process). It is possible to create microscopic and nanostructures with the desired dynamical response for use as sensors and switches and devices the size of biological cells. One can imagine electronic devices the size of molecules processed at the ZMN that interact directly with biological systems. Such developments are expected to revolutionize many areas of society, economic development, and our personal lives.

Micro- and nanoscale research as well as nanobiotechnology, engages a broad range of expertise from different disciplines and relates to a number of facets of the Technische Universität Ilmenau. Ilmenau's strength in Micro- and Nanosciences stems from pioneering efforts initiated in 1991 with the establishment on campus of the submicron facility. The University's emphasis in engineering and more recently in micro- as well as nanoscale science has grown and is highlighted by the *Center for Micro- and Nanotechnologies* as well as by the *Institute of Micro- and Nanotechnologies* established in 2005. Ongoing research activities of the Institute which consist of 27 departments are focused on micro-mechanical systems, microoptics, picofluidics, nanoelectronics, nanoactuation as well as nanopositioning systems. These scientific

achievements are strengthened by two new departments named *Micromechanical Systems and Micro- and Nanoelectronic Systems* as well as two junior researcher groups bridging the nano- to the micro- and macro-world, e.g. by providing the needed periphery of nano-devices and micro-systems.

Our success was enabled by outstanding efforts and support of the Federal Ministries of Research Education, as well as of Economics and Technology, the German Science Foundation, the European Commission, as well as a high variety of different industrial partners. I would like to take the opportunity to thank all my colleagues, the scientific staff, the technicians and our students for all their dedicated work and team spirit. I look forward to be part of a special team, which is able to convert the challenges of today's basic micro- and nanosciences into the all day life applications of tomorrow.



Prof. Dr. rer. nat. Oliver Ambacher
Director ZMN

Contents

Central Facility ZMN	6
Research Departments of IMN	7
MacroNano®	
Center for Innovation Competence	7
Departments of IMN	11
The Application Center Ilmenau	44
Infrastructure and Equipment	46
Finances	53
Scientific Activities	
Materials Science	56
Analytics	72
Technology	84
Design	138
Devices	152
Systems	172
Communications Science	196
Selected Publications and invited Conference Contributions	200
Theses	210
Invited Talks and Colloquia	215
Scientific Projects	216

Administration of ZMN**Prof. Dr. rer. nat. Oliver Ambacher**

– director – phone: -3402

Heiko Thust

– deputy director, former – phone: -2605

Herwig Döllefeld

– managing director – phone: -3400

Kirsti Schneider

– head of financial management – phone: -3497

Sabine Jahn

– financial management – phone: -3433

Gabriele Barthel

– financial management, former – phone: -3497

Katrin Dünkel

– financial management, former – phone: -3497

Renate Röhner

– accounting and office – phone: -3411

Simone Gutsche

– accounting and office – phone: -3401

Torsten Sändig

– head of technical engineering – phone: -3415

Olaf Marufke

– network administration – phone: -3416

Michael Fischer

– technical engineering, former – phone: -3413

Henry Romanus

– scientific coworker – phone: - 3404

Andreas Schober

– scientific coworker, former – phone: -3486

Michael Gebinoga

– scientific coworker, former – phone: -3486

Alexander Konkin

– technical coworker – phone: -3437

Birgitt Hartmann

– technical coworker – phone: -3426

Karin Friedel

– technical coworker – phone: -3426

Manuela Breiter

– technical coworker – phone: -3407



Prof. Dr. rer. nat. Oliver Ambacher

Contact:

Renate Röhner, phone: +49-(0)3677-69-3401

email: renate.roehner@tu-ilmenau.de

<http://www.tu-ilmenau.de/zmn>



MacroNano®

Center for Innovation Competence

MacroNano® is one out of six Centres for Innovation Competence within the BMBF funding initiative "Entrepreneurial Regions" for Germany's New Länder. The program ultimately aims at the strategic development of internationally competitive competence within the region into clusters of technological and entrepreneurial innovation for eastern Germany.

The funding volume of MacroNano® amounts to 4.5 Mio € until mid-2010. The staff already consists of a total of 12 scientists, 4 lab assistants and one administrator. Further support is provided by the Thuringian Ministry of Culture and the Project Executing Organisation Jülich.

More information about the BMBF programme "Entrepreneurial Regions" can be found at:
www.unternehmen-region.de/en/index.php



OBJECTIVES OF MacroNano®

- Development of novel principles for the handling of biological material and for the detection of cellular activities that support profiling of new pharmaceutical compounds
- Development of ceramic based carriers and packages for fluidic microsystems and highly integrated microwave applications

MacroNano's mission is to transfer innovative research results into market-ready technologies in order to support economic growth and development within the Thuringian Technology Region Ilmenau-Erfurt-Jena.

MacroNano® cooperates with a variety of partners in industry and academics. If you are interested in collaboration or technical support, please do not hesitate to contact us.

Functionalised Peripherals

MacroNano® – JUNIOR RESEARCH GROUP

The research of this project concentrates on multifunctional system-in-package (SiP) technologies for microwave applications up to 80 GHz with the aim to amplify the potential of microelectronic systems.

The focus points of this project are the following work packages:

- Passive structures for working frequencies up to 80 GHz
- Concentrated passive elements for frequencies up to 8 GHz
- Cooling concepts for power dissipation up to 10W/modul
- Device mounting of complex microwave modules

The research activity is based on LTCC and comprises the following subjects:

- optimisation of the design phase (costs, time) through standardisation of microwave functions (impedance controlled transitions, passiv integrated components)
- development of microwave-compatible cost-effective module concepts for power dissipation up to 10W/module
- improvement of the structure resolution for high integration densities
- development of reliable bonding technologies to connect large ceramic modules on materials with different thermo-mechanical properties (2nd level interconnect)
- increasing the applicable latitude of microwave components and circuit boards by use of new structures (design) and functional materials.

The results will be adaptable on the market and therefor transferred to potential industrial partners, specially to SME's in Germany.

Possible applications are:

- ultra broadband radar
- mobile communication
- Gbit-WLAN
- satellite communication
- high bit-rate telecommunication (40 Gbits/s)
- avionics
- automobile electronics
- medical technology
- biosensorics
- mm-wave sensors.

Faculty and Staff:

Dr.-Ing. Jens Müller

– head of research group – phone: -3381

Matthias Mach

– scientific coworker – phone: -3385

Rubén Perrone

– scientific coworker – phone: -3376

Sven Rentsch

– scientific coworker – phone: -3372

Torsten Thelemann

– scientific coworker – phone: -3440

Michael Fischer

– scientific coworker – phone: -3413

Ina Koch

– technical coworker – phone: -3455

Christine Lohmann

– technical coworker – phone: -3452



Dr.-Ing. Jens Müller

Contact:

Cordula Giewald, phone: +49-(0)3677-69-3380

email: cordula.giewald@tu-ilmenau.de

<http://www.macronano.de>

Microfluidics and Biosensors

MacroNano® - JUNIOR RESEARCH GROUP

The focus of the research group is the development of a novel highly integrated complex system for the high-content-screening, i.e. the determination of several physico-chemical parameters in a biological assay. This includes the design of new microfluidic devices and the development of novel biosensor structures which allow to transduce functional activities into electric or optic signals with high specificity and high signal-to-noise ratio. The work ranges from biophysical research, nano- and nanobiotechnological approaches to the assembly of whole systems.

The research activities can be divided into different work packages:

- Development of various parallel systems for the cultivation of cells, 3D tissues analysing the interactions between cells and tissues integrating fluidic, dosing systems together with electronic sensor arrays and optical sensor methods into a multifunctional system
- Development of generalised assays for pharmaceutical applications utilizing integrated microfluidic and biosensoric systems (cell-free and cell based assay systems like Protease-, HDAC-

assays or cell lines as HepG2, stem cell lines as the P19, Fibroblast and primary 3D tissue systems)

- System biological studies, e.g. cell differentiation and coculture
- Development of assays for activity tests of membrane proteins in cells
- Generation of stably transfected mammal cell lines which overexpress certain membrane proteins. This material constitutes the basis for assay development which helps to investigate problems in biological research and it will be used for bio-functionalisation of the sensor structures being developed.
- Evaluation and development of High-Electron-Mobility-Transistor Structures based on group-III-nitrides for biosensor applications in conjunction with cells or membrane proteins.

Proof-of-Concept-Studies will be developed to prove the feasibility of technical solutions which form the basis for application in device (or: instrument) technologies.

The results will be adaptable on the market and therefor transfered to potential industrial partners, specially to medium-sized and larger pharmacological research companies.

Faculty and Staff:**Dr. rer. nat. PD Andreas Schober**

– head of research group – phone: -3387

Dr. phil. nat. Thomas Friedrich

– head of research group, former

Michael Gebinoga

– scientific coworker – phone: -3382

Caroline Augspurger

– scientific coworker – phone: -3386

Irina Cimalla

– scientific coworker – phone: -3422

Michael Fischer

– scientific coworker – phone: -3413

Christoph Kremin

– scientific coworker, former – phone: -3426

Frank Weise

– scientific coworker – phone: -3423

Maren-Jödis Klett

– technical coworker – phone: -3421

Katharina Lilienthal

– technical coworker – phone: -3422



Dr. rer. nat. PD Andreas Schober

Contact:

Cordula Giewald, phone: +49-(0)3677-69-3380

email: cordula.giewald@tu-ilmenau.de

<http://www.macronano.de>

Departments of IMN

Department of Automotive Engineering

Founded in 1992 Professor Klaus Augsburg became the head of department in 1999 and from that time the growth concerning staff and business volume has been very high. In 2003 the department has moved to the Newtonbau, the new laboratory facility of the Faculty of Mechanical Engineering.

Daily business of the department can be divided in 2 parts: education and research & development (R&D). The first one is mainly represented by the new course of study "automotive engineering" which was introduced in October 2005. R&D is mostly linked to collaborations with external partners like well known OEM's (BMW, DaimlerChrysler, BOSCH,...).

The department is mainly specialised in the field and problems of brake technology. Generally the R&D is focussed on applied research in automotive technology, development of complex mechatronic systems, construction and preparation of stationary and mobile test facilities and investigations concerning human machine interface (HMI). In those special R&D areas the Department of Automotive Engineering is the first department in the newly-formed German states which is certified according to ISO 9001:2000.



Faculty and Staff:

Prof. Dr.-Ing. Klaus Augsburg

– head of department – phone: -3842

Robert Fetter

– scientific coworker – phone: -4687

Sebastian Gramstadt

– scientific coworker – phone: -3859

Stefan Heimann

– scientific coworker – phone: -3859

Maik Hoppert

– scientific coworker – phone: -3867

Rüdiger Horn

– scientific coworker – phone: -3360

Marat Karibayev

– scientific coworker – phone: -3863

Karl-Heinz Müsseler

– scientific coworker – phone: -3863

Jan Sandler

– scientific coworker – phone: -3852

Bernard Thomas

– scientific coworker – phone: -3860

Heinz-Dieter Vehmann

– scientific coworker – phone: -3851

Falk Amling

– technical coworker – phone: -3917

Victor Beez

– technical coworker – phone: -3917

Michael Posselt

– technical coworker – phone: -3920



Prof. Dr.-Ing. Klaus Augsburg

Contact:

Madlen Schmelcher/Kathleen Leipold,
phone: +49-(0)3677-69-3843
email: kathleen.leipold@tu-ilmenau.de
<http://www.tu-ilmenau.de/kft>

Department of Biomechatronics

The department of Biomechatronics was founded as the first chair of biomechatronics in Germany. Biomechatronics focusses on the development and improvement of mechatronic devices by transferring principles of biological and medical systems into technical systems. On one hand specific mechatronic products and methods have to be adapted to applications for biological systems and human beings focussing on their abilities and demands. On the other hand mechatronic design is "biologically inspired". This process is based on principles of bionically oriented methods of engineering. In conclusion – biomechatronic is not an opposite strategy to existing high technology, it complements und expands the methodological repertoire of engineering sciences.

Main research topics are the analysis and design of technical locomotion systems, in which the size spectrum of biological paragons from small to large organisms is considered. Great interest is directed towards the human being as a motion system, as well as an object of human medicine. Its locomotion including the use of the trunk, the gripping, and manipulation is studied with focus on prevention, diagnostics, and therapy, as well as an example of biological inspiration for adaptive mechanisms in the field of robotics. Robotic strategies, especially of swarm leading are used for e.g. touristic assistance systems with a focus on human-machine-interfaces. At the moment one main activity is the coordination between the requirements of motoric and sensoric systems.



Competences for research and teaching in cooperation with other departments at the TU Ilmenau and external specialists:

- Biologically inspired construction, and its systematics
- Bionics of micro systems
- Bionics of processes
- (Bio-) Medical Engineering
- Mechatronics for ergonomics
- Environmental sensorics
- Robotics

Faculty and Staff:

Prof. Dipl.-Ing. Dr. med. Hartmut Witte
– head of department – phone: -2456

Cornelius Schilling
– scientific coworker – phone: -1830

Emanuel Andrada
– scientific coworker – phone: -1803

Kathrin Carl
– scientific coworker – phone: -4688

Robert Fetter
– scientific coworker – phone: -4687

Ulrike Fröber
– scientific coworker – phone: -4691

Irina Gavrilova
– scientific coworker – phone: -4690

Stefan Lutherdt
– scientific coworker – phone: -2457

Jörg Mämpel
– scientific coworker – phone: -4698

Alexander Müller
– scientific coworker – phone: -4688

Wolfgang Kempf
– technical coworker – phone: -1242

Danja Voges
– technical coworker – phone: -1712



Prof. Dipl.-Ing. Dr. med. Hartmut Witte

Contact:

Kerstin Schmidt, phone: +49-(0)3677-69-2460
email: kerstin.schmidt@tu-ilmenau.de
<http://www.tu-ilmenau.de/biomechatronik>

Department of Chemistry

Carbon nanotubes are still in the focus of scientists interested in their unique physical properties, but over the last years our interest begun to focus on their chemical properties. The carbon nanotube chemistry leads to the synthesis of defined functionalised carbon nanotubes and enhances the opportunities for future technological applications ranging from nanoelectronics to composite materials with improved functional characteristics.

The department of Chemistry is involved in the development of new carbon compounds and materials from the preparation of the carbon nanotubes; their purification from catalyst residues, carbon nanoparticles, and fullerenes; their separation according to length, diameter, and chirality into semiconducting and metallic nanotubes; and finally to the understanding and control of their formation and chemistry. To be successful in these challenging fields we have a strong collaboration with other groups of the university, as well as industrial partners. We could demonstrate on different samples the functionalization of carbon nanotubes at their ends and walls. Due to the relative curvatures, the caps are much more reactive than the walls of the nanotubes, and are readily lost during chemical processing. A unique possibility for a functionalization of nanotubes is to encapsulate fullerenes inside. For the first time we could describe the insertion of fullerenes (C_{60}) into MWCNTs.

Our future research program is contributed to the design, synthesis and identification of novel carbon-based nanostructures and their application.



Faculty and Staff:

Prof. Dr. rer. nat. Peter Scharff

– head of department – phone: -3602

Uwe Ritter

– scientific coworker – phone: -3603

Joseph Braunsburger

– scientific coworker – phone: -3604

Loredana Carta-Abelmann

– scientific coworker – phone: -3604

Torsten Kaufmann

– scientific coworker – phone: -3603

Lars Weber

– scientific coworker – phone: -3273

Toni Fröhlich

– diploma student

Sebastian Osswald

– diploma student

Andreas Pönicke

– diploma student

Sabine Heusing

– technical coworker- phone: -3248

Susann Klötzer

– technical coworker – phone: -3248

Katrin Risch

– technical coworker – phone: -3248

Doreen Schneider

– technical coworker – phone: -3248

Carmen Siegmund

– technical coworker – phone: -3248



Prof. Dr. rer. nat. Peter Scharff

Contact:

Dagmar Böhme, phone: +49-(0)3677-69-3607

email: dagmar.boehme@tu-ilmenau.de

<http://www.tu-ilmenau.de/fakmn/Chemie.chemie.0.html>

Department of Design and Technology of Electronic Components

One main topic is the inclusion of technological parameters into existing CAD tools. This shall provide more exact simulation results and better designs with consideration of different technologies of realization. Most important for this investigation is the Low Temperature Cofired Ceramics (LTCC) technology.

A second topic is the development of new technologies for environmentally friendly electronic modules that are easy to recycle.

Especially new methods for the realization of microvias are under investigation with emphasis of thermal properties and manufacturing technology.

The laboratories of this group establish an interesting connection with the Microperipheric group (also

in the ZMN) which provides technological equipment for production of Printed Circuit Boards (PCB) and LTCC modules. Furthermore, modern analytic facilities at the ZMN allow testing by ultrasonic and X-ray inspection systems.

Faculty and Staff:

Prof. Dr.-Ing. Gert Winkler

– head of department – phone: -2606

Gernot Bischoff

– scientific coworker – phone: -1116

Ashraf Mokayyes

– scientific coworker – phone: -1118

Thorsten Mülln

– scientific coworker – phone: -1118

Aneta Sutor

– scientific coworker – phone: -1119



Prof. Dr.-Ing. Gert Winkler

Contact:

Regina Simon, phone: +49-(0)3677-69-2604

email: regina.simon@tu-ilmenau.de

<http://www-kte.tu-ilmenau.de>

Department of Electrical Energy and Control Engineering - Electrothermal Energy Conversion

In teaching as well as in research, the Electrothermal Energy Conversion Group represents methods and processes covering the use of electrical energy for direct treatment of materials, e.g. melts, semi-finished parts and work pieces. The group combines electrical power engineering and materials science to system knowledge for the technological use of the related electro-physical processes.

We have close scientific connections to other divisions: the Power Electronic Group, Thermodynamics Group, Fluid Dynamics Group, Materials Science Group, Automatic Controls Group and the Theoretical Electrical Engineering Group.

Further development of the division is supported by new materials, components, appliance systems and control techniques on one hand, and on the other, it is essentially required by material, micro, environment and recycling technology.

The equipment and processes utilized in the division's teaching and research are highly energy intensive and specific, thus the theoretical, numerical and experimental considerations are very important.

Junior Research Group:

"Electromagnetic Processing of Materials" (EPM)

This group intends to investigate the electromagnetic influences on materials caused by strong magnetic fields. Hence the group's business is to install and design the technical equipment, to develop materials due to its laboratory purpose and to measure its properties.



For the experimental investigations a cryogen-free DC-magnet (CFM) forms the centre of the intended research project. It is able to create magnetic flux densities up to 5 Tesla. The CFM was equipped with a specially designed high temperature furnace (HTO) allowing peak temperatures of 1500°C and a gas supply for working with defined pressures of Argon, CO/CO₂, O₂, N₂ and air.

At present, studies are accomplished concerning the crystallisation of Bariumhexaferrite (BaFe₁₂O₁₉), which is known to crystallise out of amorphous flakes of the glass system BaO-B₂O₃-Fe₂O₃ in the magnetic field.

Another objective covers the research on BaFe₁₂O₁₉ crystals directly out of the melt.

The combination of the CFM and HTO devices besides further equipment provide a wide range use in material development (glass and metal melts, glass-ceramics, influences of alloy microstructures) and in magneto hydrodynamics. There is scope of collaboration with companies. Please contact Dr. Bernd Hamann.

Faculty and Staff:

Prof.Dr.-Ing. Dietmar Schulze

– head of department – phone: -2852

Bernd Hamann

– scientific coworker – phone: -2877

Cornelia Kraffert

– scientific coworker – phone: -1505

Yvonne Ludwig

– scientific coworker – phone: -1510

Uwe Schadewald

– scientific coworker – phone: -3181



Prof.Dr.-Ing. Dietmar Schulze

Contact:

Gaby Böhme, phone: +49-(0)3677-69-2841

email: gaby.boehme@tu-illmenau.de

http://www4.tu-illmenau.de/mfd/nachwuchsgruppe/index_.htm

Department for Electrochemistry and Metal Finishing**Main research:**

- Galvanofarming of micorstructures
- Microsystems of Gold an other noble metals for swiss watchers (Partner Precision Engineering)
- Fe-Ni-alloys for microsystems by high current density deposition – LIGA-4H (Partner Forschungszentrum Karlsruhe)
- Dispersion deposition with ceramics nanoparticles in metallic alloys
- Fored electrolyte movement in microstructures of high aspekt ratios by using externe magnetic fields

Faculty and Staff:**Prof. Dr.-Ing. habil. Christine Jakob**

- head of department – phone: -3106

Thomas Mache

- scientific coworker – phone: -3112

Peter Kutzschbach

- scientific coworker – phone: -3111

Udo Schmidt

- scientific coworker – phone: -3113



Prof. Dr.-Ing. habil. Christine Jakob

Contact:

Maren Lange, phone: +49-(0)3677-69-3102
email: maren.lange@tu-ilmenau.de
<http://www.werkstoff.tu-ilmenau.de>

Department of Electronic Measurement

Communications, RF engineering, signal processing, and electronic measurement engineering are very distinct disciplines. While their respective methods and applications appear to be quite different, they share common problems in measurement data acquisition, sensor interface design, signal processing, parameter identification, data analysis and information extraction. The Electronic Measurement Research Laboratory is currently conducting several research projects that lie in the crossroad of these disciplines. The main goal is to apply advanced digital signal processing and RF circuit design methods for solving leading edge measurement problems in mobile radio and RF sensing.

Research activities:

- Measurement and Modelling of Wave Propagation in Mobile Radio
- Signal Analysis and System Identification
- Space-Time Signal Processing in Mobile Radio
- Ultra-wideband Radar and RF Sensing

Faculty and Staff:

Prof. Dr.-Ing. Reiner S. Thomä

– head of department – phone: -2622

Jürgen Sachs

– scientific coworker – phone: -2623

Vadim Algeier

– scientific coworker – phone: -1123



Frank Bonitz

– scientific coworker – phone: -1103

Michael Eidner

– scientific coworker – phone: -2623

Marcus Großmann

– scientific coworker – phone: -1157

Ralf Herrmann

– scientific coworker – phone: -1160

Aihua Hong

– scientific coworker – phone: -1157

Martin Kmec

– scientific coworker – phone: -1160

Wim Kotterman

– scientific coworker – phone: -3722

Markus Landmann

– scientific coworker – phone: -1123

Milan Narandzic

– scientific coworker – phone: -3722

Christian Schneider

– scientific coworker – phone: -1157

Gerd Sommerkorn

– scientific coworker – phone: -1115

Frantisek Tkac

– scientific coworker – phone: -2623

Sebastian Wöckel

– scientific coworker – phone: -1160

Rudolf Zetik

– scientific coworker – phone: -1160

Karl Borkowski

– technical coworker – phone: -1114



Prof. Dr.-Ing. Reiner S. Thomä

Contact:

Gitta Weber, phone: +49-(0)3677-69-2621

email: gitta.weber@tu-ilmenau.de

<http://www-emt.tu-ilmenau.de/WWW/Index.php?lang=DE>

Department of Experimental Physics I

The research activities of the department of Experimental Physics I are mainly focussed on optical, electronic and structural properties of semiconductors, semiconductor micro- and nanostructures and polymer optoelectronic devices, and on solar-energy components.

The department consists of three research groups dealing with:

- inorganic semiconductor and devices
 - hexagonal and cubic group-III-nitride semiconductors (In,Ga,Al)N and their heterostructures for development of light emitting devices and sensor structures,
 - strained InGaAs/GaAs and InGaAsP/GaA quantum well structures for high-power laser applications,
 - modulation-doped AlGaAs/GaAs heterostructures, InAs/GaAs and InAs/Si quantum dot multi-layers,
 - chalcopyrite semiconductors $\text{Cu}(\text{In,Ga})\text{S}_2$ for the development of thin film solar cells
- organic semiconductors and optoelectronic devices
 - structure-property relation of thin films made by conjugated polymers such as P3AT, PPV and novel polymers
 - related composites with nano-carbons like fullerenes or carbon nanotubes, preparation and investigation of polymer bulk-heterojunction solar cells
- development and characterization of solar-energy components
 - thermal collectors and novel absorber layers
 - support of local PV companies by optical investigations
 - benchmark tests of photovoltaic power plants



Prof. Dr. rer. nat. Gerhard Gobsch



The experimental investigations are mainly realized by several methods of optical spectroscopy (spectroscopic ellipsometry, modulation spectroscopy, photoluminescence and PL excitation spectroscopy), by electrical characterization (I-V, C-V, photocurrent, magneto-transport) and by X-ray analysis (XRD, small-angle scattering). The solar-energy components are analyzed by using an out-door test facility. Further on, the technological equipment provided by the 'Center of Micro- and Nanotechnologies' of the TU Ilmenau (lithography, ion beam etching, metal deposition etc.) is widely used.

Faculty and Staff:

Prof. Dr. rer. nat. Gerhard Gobsch

– head of department – phone: -3701

Rüdiger Goldhahn

– scientific coworker – phone: -3650

Carsten Buchheim

– scientific coworker – phone: -3168

Tobias Erb

– scientific coworker – phone: -3210

Harald Hoppe

– scientific coworker – phone: -3711

Pascal Schley

– scientific coworker – phone: -3210

Sviatoslav Shokhovets

– scientific coworker – phone: -3652

Andreas Winzer

– scientific coworker – phone: -3213

Thomas Klein – diploma student - phone: -3168

Henrik Lösch – diploma student - phone: -3168

Burhan Muhsin – diploma student – phone: -3214

Christian Napierala – diploma student – phone: -3168

Joachim Renz – diploma student – phone: -3652

Christian Würth – diploma student – phone: -3208

Helmut Barth – technical coworker – phone: -3214

Barbara Krause – technical coworker – phone: -3213

Dirk Schulze – technical coworker – phone: -3702

Norbert Stein – technical coworker – phone: -3208

Heidi Sülzner – technical coworker – phone: -3710

Contact:

Petra Sieck, phone: +49 (0) 3677-69-3700

email: petra.sieck@tu-ilmenau.de

<http://www.tu-ilmenau.de/exphys1>

Department of Experimental Physics II

In the department "Experimental Physics II/Environmental Physics" laboratory experiments are conducted to gain understanding of the physical and chemical processes that take place during the interaction of aerosols and nanoparticles with the atmosphere and to learn about their impact on the environment and the climate. The focus is laid on optical and Raman spectroscopy as well as mass spectrometry. Increasingly, technologically important inorganic nanoparticle materials prepared

with the nanoparticle beam apparatus LUCAS are investigated in close collaboration with other departments of the IMN and co-operation partners from other universities. Here, especially the catalytic and magnetic properties are of interest.

Faculty and Staff:

Prof. Dr. rer. nat. Thomas Leisner

– head of department – phone: -3672

Alexander Reinholdt

– scientific coworker – phone: -3781



Prof. Dr. rer. nat. Thomas Leisner

Contact:

Silke Syptroth, phone: +49-(0)3677-69-3670

email: silke.syptroth@tu-ilmenau.de

<http://www.tu-ilmenau.de/fakmn/experimentalphysik-I.975.0.html>

Department of Glass and Ceramic Technology

Research topics:

- Micro structuring of glasses for micro systems technology
 - * development of glasses
 - * micro structuring
 - * application
- Glass-crystallization-technology to make nano or micro crystalline oxidic powders
- Magnetic powder-composites
- Glass fiber/glass matrix-composites
- Recycling of waste glasses/cullet by remelting and pressforming or by foaming
 - Stirring of glass melts by externally generated Lorentz forces

Faculty and Staff:

Prof. Dr.-Ing. Dr. rer. oec. Dagmar Hülsenberg

– head of department – phone: -2802

Susanne Mrotzek

– scientific coworker – phone: -3246

Stefan Belau

– scientific coworker – phone: -3181

Ulrike Brokmann

– scientific coworker – phone: -3184

Bernd Halbedel

– scientific coworker – phone: -2784

Annett Hesse

– scientific coworker – phone: -3183

Uwe Krieger

– scientific coworker – phone: -1561

Petra Mahr

– scientific coworker – phone: -1664

Uwe Hoppe

– technical coworker – phone: -3158

Michael Jakob

– technical coworker – phone: -3123

Stefan Neudert

– technical coworker – phone: -3193

Frank Oßmann

– technical coworker – phone: -3154

Dagmar Raab

– scientific coworker – phone: -3163

Uwe Schadewald

– scientific coworker – phone: -3186

Karin Sönnichsen

– technical coworker – phone: -3247



Prof. Dr.-Ing. Dr. rer. oec. Dagmar Hülsenberg

Contact:

Irina Hoffmann, phone: +49-(0)3677-69-2801

email: [glas-keramik\(at\)tu-ilmenau.de](mailto:glas-keramik(at)tu-ilmenau.de)

<http://www.tu-ilmenau.de/site/gkt/Startseite.907.0.html>

Department of Materials for Electronics

The department of Materials for Electronics is concerned with the development of new materials for nanopositioning, as well as the development of new metallisation materials for wide bandgap semiconductor contacts. Furthermore, this department focusses on the analysis of liquid metals and the development of new adaptive materials which have low or negative thermal coefficients. These materials are produced by sputtering of thin films or by electrochemical or electrophoresis methods. Samples of different materials, such as deposited layers and post annealed layers, are also provided from other groups of the university, as well as from industrial partners.

The main focus of this work is analysis with different methods:

- X-ray diffraction in different measurement setups
- X-ray fluorescence spectroscopy, X-ray imaging
- analytical scanning electron microscopy (ESEM, EDX, EBSD)
- analytical transmission electron microscopy (EDX, PEELS, diffraction, high resolution)
- atomic force microscopy

- different electrical methods
- thermo wave inspection system
- classical mechanical testing of materials

Faculty and Staff:

Prof. Dr. rer. nat. Christian Knedlik

– head of department – phone: -3611

Lothar Spieß

– scientific coworker – phone: -3403

Volkmar Breternitz

– scientific coworker – phone: -3134

Maik Gubisch

– scientific coworker – phone: -3404

Thomas Kups

– scientific coworker – phone: -3109

Henry Romanus

– scientific coworker, former – phone: -3404

Friedhelm Scharmann

– scientific coworker – phone: -3135

Sören Selve

– diploma student – phone: -3404

Elvira Remdt

– technical coworker, former – phone: -3446

Jens Schawohl

– technical coworker – phone: -3403



Prof. Dr. rer. nat. Christian Knedlik

Contact:

Brigitte Weiß, phone: +49-(0)3677-69-3610

email: wet@tu-ilmenau.de

<http://www.werkstoff.tu-ilmenau.de>

Department of Media Design / Media Psychology

The *Institute of Media and Communication Science* provides Bachelor studies in "Applied Media Science" (B.A.) and Master studies in "Media and Communication Research" (M.A./M.Sc.). The studies combine a social science oriented media and communication perspective with expertise from media technology and media economy (so called "three-pillar-model of media education in Ilmenau").

The *Division of Media Design and Media Psychology* is one of seven divisions within the Institute of Media and Communication Science. It focuses on two main research questions: How should media products be designed to meet the users' needs and interests? What psychological effects do different media have?

Current research emphasis of the Division of Media Design and Media Psychology:

- Communication about Nanotechnology
- Psychophysiological Media Research
- Human-Robot-Interaction
- Social and Psychological Dimensions of Online and Mobile Communication
- Learning and Teaching with New Media
- Gender Studies
- Social Research Methods and Evaluation Research

Faculty and Staff:

Prof. Dr. phil. Nicola Döring

– head of department – phone: -4703

Andreas Ingerl

– scientific coworker – phone: -4739



Prof. Dr. phil. Nicola Döring

Contact:

Alexandra Büttner, phone: +49-(0)3677-69-4703
email: alexandra.buettner@tu-ilmenau.de
www.tu-ilmenau.de/mkmp

Department of Metallic Materials and Composite Materials

With the appointment of Prof. Dr.-Ing. habil. H. Kern as head of the department of Metallic Materials and Composite Materials Technology, the teaching and research activities related to materials at the Technische Universität Ilmenau gained new momentum. The integration of the department into the Faculty of Mechanical Engineering reflects the significance of materials science engineering. The research areas in the department cover metallic, non-metallic, inorganic, and composite materials. The focus of the research is the improvement of available conventional materials, the development of new materials and the creation of innovative material approaches.

Research Activities:

- Tribological behaviour of materials and surface topography
- Characteristics of ceramic suspensions (rheology)
- Ceramic shaping
- Electrophoretic Deposition
- Materials testing
- Metallography, microscopy and image processing techniques
- Special materials for mechanical engineering
- Composite Materials
- Metal-ceramic and ceramic matrix composites
- Glass matrix composites
- Interfacial characterisation and interface design of composites

Faculty and Staff:

Prof. Dr.-Ing. Heinrich Kern

– head of department – phone: -2450

Kerstin Pfeiffer

– technical coworker – phone: -1831



Prof. Dr.-Ing. Heinrich Kern

Contact:

Irina Hoffmann, phone: +49-(0)3677-69-2801

email: irina.hoffmann@tu-ilmenau.de

<http://www.tu-ilmenau.de/mwv>

Department of Micro- and Nanoelectronic Systems

The department of Micro- and nanoelectronic Systems deals with scientific questions concerning micro- and nanoelectronic systems.

It is expected that in the near future the technological breakthrough in the area of micro- and nanoelectronic systems will play a key role in our society.

Micro- and nanoelectronic systems become possible when combining functional micro- and nanotechniques in a miniaturized setup. It is conceivable that by joining individual nanoelectronic components by connection techniques, system architectures and signal processing concepts, the development of complex products is made possible. The goal of our division is to push the advancement of micro- and nanoelectronic systems by combining different single nanotechniques utilizing system technologies.



Faculty and Staff:

Prof. Dr.-Ing. Ivo W. Rangelow

– head of department – phone: -3718

Stefan Klett

– scientific coworker – phone: -3129

Andreas Frank

– scientific coworker – phone: -1590

Elshad Guliyev

– scientific coworker – phone: -3129

Tzvetan Ivanov

– scientific coworker – phone: -3124

Burkhard E. Volland

– scientific coworker – phone: -3124

Jens-Peter Zöllner

– scientific coworker – phone: -3127



Prof. Dr.-Ing. Ivo W. Rangelow

Contact:

Silvia Herda, phone: +49-(0)3677-69-3717

email: silvia.herda@tu-ilmenau.de

http://www.tu-ilmenau.de/site/fke_mns/index.php?id=762

Department of Micromechanical Systems

In January 2006, the Department of Microsystems Technology was renamed in "Micromechanical Systems" while Prof. Wurmus retired end of 2005 after 14 years of successful work and Prof. Martin Hoffmann took over responsibility for the department.

The department will continue in working in silicon-based micro-electro-mechanical systems (MEMS). On one hand, new basic technologies and their application - such as the use of "black silicon" needles for micro-positioning - are investigated. On the other hand, the focus is put on the system integration of MEMS based on wafer-level technologies and planar processes for mechanical functionalities. MEMS have already entered our daily life at many places: all modern cars include a large number of MEMS-sensors; computers and printers wouldn't work or wouldn't even show the performance without microsystems; mobile communication systems include more and more functionalities that make use of MEMS. For the next decade a strong and continuous increase of applications and turn-over is expected along with a spread of applications. But not all challenges are already solved.

MEMS are characterized by a complex system integration of mechanics with driving electronics as known from mechatronics, but usually they combine

all these functional blocks in wafer-level-processed components. This results in very compact subsystems with low single-die assembly effort.

System integration is still one of the major road blocks for microsystems in new fields of application: The package becomes often part of the system function (e.g. in many sensors and actuators) and a microsystem is not of interest for the user if not a common interface (electrical and mechanical) is available. Most commercially available microsystems aim for mass markets and are supplied by large companies. Small and medium sized companies (SME's) cannot participate in this market due to the high initial costs for MEMS fabrication processes. Our aim is the research for new concepts that allow the cost-efficient development and production of micro-sub-systems even in small and medium quantities. One concept is based on an "only one step more" strategy combining commercially available standard processes with a single on-top process that adds new functionalities. Currently, piezoelectric aluminium nitride is investigated for this application.

A core competence of the department is "actuation for MEMS". Four different principles can be offered in design, fabrication and test: electrostatic, electromagnetic, piezoelectric and thermo-mechanical actuation. Also microfluidics is an important part of the research. Together with partners also RF-MEMS and optical MEMS are investigated.

Faculty and Staff:**Prof. Dr.-Ing. Martin Hoffmann**

– head of department – phone: -2487

Prof. Dr.-Ing. Helmut Wurmus

– head of department, former – phone: -2487

Arne Albrecht

– scientific coworker – phone: -3426

Siegmar Hecht

– scientific coworker – phone: -2479

Heike Bartsch de Torres

– scientific coworker – phone: -3424

Jörg Burgold

– scientific coworker, former

Tamas Fischl

– scientific coworker – phone: -1295

Balazs Horvath

– scientific coworker, former

Matthias Kallenbach

– scientific coworker – phone: -3424

Jozsef Krol

– scientific coworker – phone: -1295

Mike Stubenrauch

– scientific coworker – phone: -3422

Frank Weise

– scientific coworker – phone: -3423

Christoph Kremin

– diploma student – phone: -3422

Katarina Lilienthal

– diploma student, former – phone: -3424

Ole Nagel

– diploma student, former

Sebastian Stöbenau

– diploma student, former

Lothar Dressler

– technical coworker – phone: -3421

Karin Friedel

– technical coworker – phone: -3421

Gabriele Harnisch

– technical coworker – phone: -3422

Birgitt Hartmann

– technical coworker – phone: -3426

Christine Lohmann

– technical coworker, former – phone: -3425



Prof. Dr.-Ing. Martin Hoffmann

Contact:

Annette Volk, phone: +49-(0)3677-69-2485

email: annette.volk@tu-ilmenau.de

<http://www.tu-ilmenau.de/site/mms/>

Mikromechanische_Sys.1040.0.html

Department of Microperipherics

The department of Microperipherics covers the field of assembling and connecting technologies, especially thick film and LTCC-hybrid technology.

Focal points are the calculation and modelling of lumped passive elements and transmission line devices and the enhancement and optimisation of technological processes. More layers with smaller structures will lead to a higher degree of integration. Methods for fine line structuring and approaches to control the shrinking behaviour of ceramic materials are under development.

The laboratories are located at the "Center for Micro- and Nanotechnologies" (ZMN). The whole equipment for design, screen printing, tape punching, lamination, firing and assembling of PCBs, hybrid circuits and LTCC-modules is available.

Manufacturing of complex microelectronic systems requires hybrid technologies of components, which cannot be integrated into the semiconductor chip by monolithic methods. (MCM's, packages, MEMS).

The LTCC-(Low Temperature Cofired Ceramics-) technology offers new solutions by a variety of materials (tapes, inks) and a nearly unlimited number of layers.

In addition LTCC offers possibilities to handle high power dissipation, 3D constructions, microwave applications and better EMC-behaviour. Furthermore new solutions for sensor and mechatronic applications are thinkable.

Main topics of research:

- Integration of new materials (e.g. ferrite, high k and low loss dielectrics, high temperature



conductivity materials and PZT). Characterization of material parameters up to higher limits than provided by suppliers (in view of working temperature, frequencies, environmental pollution conditions, stress or others).

- Optimisation of technologies and process parameters for special applications.
- Developing of LTCC technology for integration of sensors, microoptical, microacoustic and microfluidic elements to very complex microsystems
- Developing of more exact simulation tools for such new complex modules.

Faculty and Staff:

Prof. Dr.-Ing. Heiko Thust

– head of department – phone: -2605

Karl-Heinz Drüe

– scientific coworker – phone: -3429

Waleed Ehrhardt

– scientific coworker – phone: -1117

Michael Hintz

– scientific coworker – phone: -3430

Elisa Morillas

– scientific coworker – phone: -3429

Ruben Perrone

– scientific coworker, former – phone: -1360

Torsten Theleman

– scientific coworker – phone: -1118

Uwe Genatis

– technical coworker – phone: -3427

Ina Koch

– technical coworker, former – phone: -3455

Regina Lenk

– technical coworker – phone: -3440

Martina Sieler

– technical coworker – phone: -3428



Prof. Dr.-Ing. Heiko Thust

Contact:

Regina Simon, phone: +49-(0)3677-69-2604

email: regina.simon@tu-ilmenau.de

<http://www-kte.tu-ilmenau.de>

Department of Nanotechnology

The work scope of Nanotechnology includes the development, characterization and optimization of high quality hetero- and nanostructures processed from conjugated polymeres, silicon carbide, metal oxides or group-III nitrides in order to realize modern semiconducting devices for nano-electronic and sensor applications. The outstanding potentialities of the group of Nanotechnology are based on the expertise in the fabrication of organic devices and systems as well as on the epitaxy of wide band gap semiconductors. Further more the scientific progress is based on the long lasting knowledge in micro- and nanotechnology for processing electronic as well as optical devices.

The development and realization of novel devices is supported by a modern and state of the art analytical infrastructure for structural, electronic, as well as optical characterization of semiconducting materials and nanostructures.

The Center of Micro- and Nanotechnologies of the Technische Universität Ilmenau is placed into operation, which sets the stage for all technologies needed to process soft material and solid state nano-devices, like solar cells, light detectors or sensors for picofluidic as well as biomedical applications.

Scientific Topics

Intention of the scientific work is the growth, characterization and optimization of high quality hetero- and nanostructures based on organic materials, group III-nitrides as well as metal

oxides and carbides. The goal is the design, development and realization of novel device concepts for nano-electronic and -sensor devices, which is strongly motivated by the fabrication of smart materials and their application in the analysis of nanostructures and nano-quantities.

The following scientific topics are currently under investigation:

- Processing of nanostructures based on wide band gap semiconductors (SiC, GaN), which are grown by molecular beam epitaxy or chemical vapor deposition.
- Realization of sensors for nano- and picofluidic applications by using pyroelectric heterostructures.
- Development of AlGaIn/Si-based micro- and nanoresonators for applications as electrical filters as well as for sensing of biological and biomedical substances.
- Processing of wave guides made from pyroelectric AlGaIn/GaN lateral polarity heterostructures for optical parametric oscillators with applications in single molecule spectroscopy.
- Design and processing of emitters, sensors and single photon detectors for visible and ultraviolet light based on AlGaIn/GaN/Si hetero- and quantum dot structures for applications in the extraction and control of drinking water as well as in the optimization of combustion processes.
- Fabrication of efficient organic solar cells with active regions composed of conjugated polymers and carbon fullerenes.
- Optimization of nano-wires and nano-resonators for applications as gas- as well as liquid- sensors.

Faculty and Staff:**Prof. Dr. rer. nat. Oliver Ambacher**

– head of department – phone: -3402

Jörg Pezoldt

– scientific coworker – phone: -3412

Majdeddin Ali

– scientific coworker – phone: -1172

Maher Al-Ibrahim

– scientific coworker – phone: -3410

Carsten Buchheim

– scientific coworker – phone: -3168/3210

Dorin Cengher

– scientific coworker – phone: -3352

Genady Cherkashinin

– scientific coworker, former

Irina Cimalla

– scientific coworker, former

Volker Cimalla

– scientific coworker – phone: -3408

Gernot Ecke

– scientific coworker – phone: -3407

Christian Förster

– scientific coworker, former

Sindy Hauguth

– scientific coworker – phone: -1172

Gabriel Kittler

– scientific coworker – phone: -1172

Vadim Lebedev

– scientific coworker – phone: -3410

Ulrich Liebold

– scientific coworker – phone: -2856

Benedikt Lübbers

– scientific coworker – phone: -1172

Florentina Niebelschütz

– scientific coworker – phone: -3352

Merten Niebelschütz

– scientific coworker – phone: -3408

Francisco Miguel Morales Sanchez

– guest scientist, former

Armin Spitznas

– scientific coworker, former

Thomas Stauden

– scientific coworker – phone: -3409

Katja Tonisch

– scientific coworker – phone: -3352

Chunyu Wang

– scientific coworker – phone: -3409

Daniel Gäbler

– diploma student, former

Christian Haupt

– diploma student – phone: -3352

Stephan Maroldt

– diploma student – phone: -3412

Christoph Mauder

– diploma student – phone: -3723

Carsten Rackel

– diploma student – phone: -3723

Ilona Marquardt

– technical coworker – phone: -3407

Silvia Probst

– technical coworker, former

Dietmar Schäfer

– technical coworker – phone: -3230

Willy Schliecke

– technical coworker – phone: -3418

Jutta Uziel

– technical coworker – phone: -3230



Prof. Dr. rer. nat. Oliver Ambacher

Contact:

Simone Gutsche, phone: +49-(0)3677-69-3401

email: simone.gutsche@tu-ilmenau.de

<http://www.tu-ilmenau.de/nano>

Department of Optical Engineering

“Microoptics”, “modelling of optical imaging systems”, and “analysis, as well as synthesis of optical imaging systems” are the main topics of research, as well as teaching in the Department of Optical Engineering. Especially, the research projects related to the use of microoptical components for the optimization and integration of optical systems are closely linked to the IMN. Specific research projects in this context are dealing with:

- microoptics for optical tweezers;
- applied spectral imaging;
- holographic lithography and digital holography;
- integrated optical-fluidic microsystems for biotechnology

Funding for these projects is provided through the German (DFG) and European Science foundation (ESF), the European Community (6th FP, Interreg III C programme), the German ministry for Education and Research (BMBF) as well as the state of Thuringia.



Faculty and Staff:

Prof. Dr. rer. nat. Stefan Sinzinger

– head of department – phone: -2490

Martin Amberg

– scientific coworker – phone: -1806

Meike Hoffmann

– scientific coworker – phone: -1411

Beate Mitschunas

– scientific coworker – phone: -1805

Wolfgang Richter

– scientific coworker – phone: -2488

Sebastian Stoebenau

– scientific coworker – phone: -1806

Marcel Teschke

– scientific coworker – phone: -2489

Olga Kreis

– technical coworker – phone: -3423

Thomas Meinecke

– technical coworker – phone: -4322

Ralf Weber

– technical coworker – phone: -1949



Prof. Dr. rer. nat. Stefan Sinzinger

Contact:

Martina Klein, phone: +49-(0)3677-69-2491

email: martina.klein@tu-ilmenau.de

<http://www.tu-ilmenau.de/optik>

Junior Research Group "PADeMIS"

Aim of this research group is the development of an actively moving device for the minimally invasive surgery (MIS). The device is going to move peristaltically similarly to the motion of an earthworm. It will enter the natural canals inside the human body (e.g. spinal canal) and crawl to the operation field. The device is being hollow and carrying a hollow tube being its back linking to the outside. The surgeon is able to insert endoscopic tools towards the top of the device and location of surgery.

The development of the device requires research in the following topics: The properties of the surrounding tissue define the environment of PADeMIS, so studies of the anatomical and material conditions are made. Due to the highly sensitive environment PADeMIS will be produced from silicone rubber. Material tests are performed to investigate the long time dependency of this material and to examine the constitutive law, which is used in finite element simulations of the deformations of the worm segments leading to locomotion. Also a silicone prototyping facility is being constructed to produce the device. Additionally, a control system is being set up.

Faculty and Staff:**Dr. rer. nat. Petra Meier**

– head of junior research group – phone: -1804
(now dept. of Micromechanical Systems)

Michael Lang

– scientific coworker – phone: -1814
(now dept. of Micromechanical Systems)

Clemens Wystup

– scientific coworker – phone: -2446
(now dept. of Micromechanical Systems)

Natalie Vasev

– scientific coworker, former

Siegfried Oberthür

– scientific coworker – phone: -1814
(now dept. of Technical Mechanics/
Design of Mechatronic Actuators)

Richard Löw

– diploma student, former



Dr. rer. nat. Petra Meier

Department for Physical Chemistry and Micro-reaction Technology

The research work of the Department for Physical Chemistry and Microreaction Technology is focussed on the development of methods for the miniaturization of chemical and biological processes by use of microfluidics and microreactors. One important motivation for this work is the improvement of environmental compatibility of laboratory processes by minimization of the consumption of chemicals and other resources in research, development and education.

One part of the research work is addressed to the generation and modification of micro and nanoparticles by use of microreactors. So, the formation of metal nanoparticles by reduction of metal compounds under micro fluidic conditions and the generation of polymer nanoparticles in a micro flow-through emulsion polymerization are under investigation. A second part of research work deals with microfluidics for biomolecular and cell applications. These part includes research on micro flow-through PCR for DNA characterization, the generation and manipulation of micro fluid segments and the application of this technique for biological screening experiments. A third part of research



activities is focussed on miniaturized analytical techniques, particular on the development of micro spot arrays for the characterization of liquid analytes.

The foundation of the department was initiated by the German Environmental Foundation (DBU) in 2001. The work of the group is strongly supported by the DBU up to now. In addition, special projects are supported by the German Ministry of Education and Science (BMBF) and by the state of Thuringia. This support, the fruitful cooperation with several partners from industry and research are gratefully acknowledged, partially the cooperation with the IPHT Jena.

Faculty and Staff:

Prof. Dr. rer. nat. Michael Köhler

– head of department – phone: -3629

Alexander Gross

– scientific coworker – phone: -3152

Andreas Brösing

– scientific coworker – phone: -3643

Mike Günther

– scientific coworker – phone: -3152



Prof. Dr. rer. nat. Michael Köhler

Contact:

Petra Sieck, phone: +49-(0)3677-69-3700

email: petra.sieck@tu-ilmenau.de

<http://www.tu-ilmenau.de/fakmn/>

Physikalische-Chemie.mrt.0.html

Department of Power Electronics and Control

The department Power Electronics and Control is dealing with power converter topologies for active power filters and power converter systems and its applications. The use of simulation tools shows possibilities for loss reduction in power semiconductors, parallel and series cascading and give the possibility to predefine the thermal conditions. Microcontrollers and digital signal processors in combination with programmable logic act as control unit for electrical drives, distributed energy sources and other power electronic systems. The department examines EMI-effects and its mechanism.

Research Fields

Topology / Design

- topologies for using regenerative energy sources
- development of switching algorithms for power electronic converters
- active power filters for harmonic currents and reactive power compensation

Digital Control

- control of synchronous, asynchronous, switched reluctance and linear motors
- applications of digital signal processors and microcontrollers in machine-tools and automotive systems
- power grid connection of regenerative energy sources (wind and solar energy)



Applications of power semiconductors / switching technology

- measurements on power semiconductor devices
- characterization of applications
- research of EMI-effects and its mechanism

Digital simulation

- of the system behavior of mains configurations with regenerative energy sources
- of the system behavior of electrical drive systems
- thermal effects in power semiconductors

Faculty and Staff:

Prof. Dr.-Ing. Jürgen Petzoldt

– head of department – phone: -2851

Gotthard Berger

– scientific coworker – phone: -3857

Jürgen Büttner

– scientific coworker – phone: -2850

Pedro Catania

– scientific coworker – phone: -1542

Thomas Ellinger

– scientific coworker – phone: -1553

Uwe Franke

– scientific coworker – phone: -1554

Heiner Jacobs

– scientific coworker – phone: -1539

Hector Perassi

– scientific coworker – phone: -1531

Uwe Rädcl

– scientific coworker – phone: -1535



Prof. Dr.-Ing. Jürgen Petzoldt

Contact:

Karin Just, phone: +49-(0)3677-69-2849

email: karin.just@tu-ilmenau.de

<http://www4.tu-ilmenau.de/EI/EWA/LSE>

Department of Process Measurement

The Institute of Process Measurement and Sensor Technology consists of the departments of "Process Measurement" and "Mechanical Engineering Measurement and Production Measurement".

Extensive research collaboration with industrial partners as well as with BMBF, the DFG and the Thuringian Ministry of Culture and Education provides the basis for a well-founded and practically oriented education for students.

The emphasis of the Institute's fundamental and industrial research is in the areas of optoelectronic sensor technology, laser interferometric measurement and sensor technology, nanomeasurement and nanopositioning technology, temperature metrology, force and mass metrology and calibration technology.

The research focal points are on the one hand the universal interference optical sensor principle, whose increasing importance is brought about by advances in optoelectronics, laser technology, microelectronics, positioning systems and industrial technologies, and on the other hand the investigation of the static and dynamic behaviour of sensors and of measurement acquisition and processing systems installed in automated production lines.

Faculty and Staff:

Prof. Dr.-Ing. Gerd Jäger

– head of department – phone: -2824

Eberhard Manske

– scientific coworker – phone: -1250

Rostyslav Mastylo

– scientific coworker – phone: -1836



Prof. Dr.-Ing. Gerd Jäger

Contact:

Cordula Höring, phone: +49-(0)3677-69-2822

email: cordula.hoering@tu-ilmenau.de

<http://wcms1.rz.tu-ilmenau.de/fakmb/index.php?id=836>

Department of Production Engineering

The Institute of Production Engineering has been given a new direction since the arrival of its current director, Univ. Prof. Dr.-Ing. habil. Johannes Wilden, four years ago.

A completely new laboratory building was set up, including all new equipment and state-of-the-art machinery. Today, approximately 20 engineers and technicians as well as a large number of students form a highly competent team for co-operative projects in coating, cutting, joining as well as chipping technologies.

The current focus of research is on the analysis and understanding of scale effects in materials. As miniaturisation moves from micro- to nano- dimensions, material properties and effects clearly must be considered to fully understand the phenomena observed and improve process conditions and reliability. For instance, with high

precision milling, the cutting depth is of the same order of magnitude as the grain size of the material treated. While conventional theories fail to properly describe such a process, suitable consideration of scale effects allows to derive and develop new production systems.

In the field of coating and joining processes scale effects allow reducing working temperature, so that sensitive materials can be joined with a very low heat input.

The institute's scientists convey their experts' knowledge to workgroups of national and international experts' associations (DVS, VDI, Dechema, DIN, IIS, etc.).

Faculty and Staff:

Prof. Dr.-Ing. Johannes Wilden

– head of department – phone: -2981



Prof. Dr.-Ing. Johannes Wilden

Contact:

Bianca Attula, phone: +49-(0)3677-69-2980
email: bianca.attula@tu-ilmenau.de
<http://www.tu-ilmenau.de/fertigungstechnik>

Department of RF and Microwave Techniques

The department for RF and microwave techniques covers research activities concerned with the propagation, interactions and technical applications of electromagnetic waves, and circuits, signals and systems based on them, at frequencies between 100 kHz and 100 GHz. The department is member of the Institute for Information Technology and of the Institute for Micro- and Nanotechnologies. Correspondingly, the research projects of the RF and Microwave Department are focused on interdisciplinary concepts to use new functionality and new materials in high-frequency related applications.

Main research topics

- Ceramic microwave circuits for satellite communication systems (LTCC based reconfigurable 20 GHz switch matrix, co-operation with young-researchers group MacroNano)

- Miniaturised diversity antenna arrays with passive decoupling networks
- Piezoelectric integrated NanoElectroMechanic sensor-circuits (co-operation with Department for Nanotechnology)
- High-frequency SiGe-modulator for class-S amplifiers (High-efficiency power amplifier for mobile communications, co-operation with Department for Nanotechnology)
- Microwave applications of high-temperature superconductors

Faculty and Staff:

Prof. Dr. rer. nat. Matthias Hein

– head of department – phone: -2832

Kurt Blau

– scientific coworker – phone: -1587

Ralf Stephan

– scientific coworker – phone: -1585



Prof. Dr. rer. nat. Matthias Hein

Contact:

Germaine Hippel, phone +49-(0)3677-69-2831
 email: hmt@tu-ilmenau.de
www.tu-ilmenau.de/hmt

Department of Solid-State Electronics

The research projects of the department of Solid-State Electronics are focussed on the development and investigation of advanced semiconductor devices. The department consists of four research groups dealing with:

- Polymer devices (organic field-effect transistors, new organic materials for electron devices),
- RF and nanodevices (nanometer MOSFETs, SiGe HBTs, wide bandgap devices),
- Power electronics (IGBTs, reliability issues, control circuits),
- Sensors.

The work of the four groups includes the investigation of basic operation principles, device simulation, device design and optimisation, fabrication, and characterisation. Polymer and wide bandgap devices are fabricated in-house, while other devices, such as SiGe HBTs, are fabricated in the facilities of partners in the semiconductor industry. The research projects of the department are

supported by the European Community, German federal agencies (BMBF, DFG), the Federal State of Thuringia, and by industry (e.g. Semicron, Atmel).

Faculty and Staff:

Dr.-Ing. Susanne Scheinert

– provisional head of department – phone: -3222

Frank Schwierz

– scientific coworker – phone: -3120

Jörg Gessner

– scientific coworker – phone: -3219

Andrei Herasimovich

– scientific coworker – phone: -3406

Ingo Hörselmann

– scientific coworker – phone: -3406

Mario Kittler

– scientific coworker – phone: -1550

Gundis Bauer

– technical coworker – phone: -3406

Silvia Klaube

– technical coworker – phone: -3222



Dr.-Ing. Susanne Scheinert

Contact:

Silvia Herda, phone: +49-(0)3677-69-3717

email: silvia.herda@tu-ilmenau.de

http://www.tu-ilmenau.de/site/fke_fke/index.php?id=757

Department of Technical and Economic History

The department for the History of Technology and Economy was founded at the beginning of the 1990s. At this time, many associations of industrial managers, engineers and businessmen required the integration of non-technical and interdisciplinary subjects into the university's engineering and economic studies. By establishing our department, the TU Ilmenau realized these wishes and demands.

One part of teaching in the department for the History of Technology and Economy conveys the nowadays historical views. These historical analyses make it possible for experts and non-experts to understand the more complex technical systems as well as the connection of the technical systems with the development of the human society.

In case of the TU Ilmenau, such a treatment of the history of technology is only possible through a wide understanding of technology (technology as sociotechnological system) and a very integrative research and teaching relevant to the present day.

Tasks in teaching and research consequently are the investigation into origin and development of modern fields of technology and industry and the innovation processes within.

Focus on research is the study of media presentation of technological, scientific and economic facts. Points of interest are the study of communication in crises, risks and catastrophes

as well as technological, economic and scientific communication to non-experts in mass media. The acceptance and reflection of technology are two aspects which have influence on all studies. For these topics some content analysis studies were carried out.

Other research projects focus on special communication in engineering, technology and industry and its difficulties between experts and users. Also processes of knowledge transfer are content of research work, especially in case of communication about high technology. Research interests also are knowledge transfers through manuals and operating instructions, above all for consumer devices in the field of communication (e. g. TV, home cinema equipment, DVD recorder, cell phone) and questions of usability.

Another research takes place in the field of using content management systems (CMS) for creating websites for small museums: here the questions is, how CMS can be explained to users, which are in most cases laymen, that they are able to use the systems without any problems.

Research work is also done in the field of media history and technical history. Since 1994, the Deutsche Forschungsgemeinschaft (DFG) supported two projects of the chair, a comparative study of the radio set industry in western and eastern Germany between 1945 and the second half of the 1950s and a study about the development of the telecommunication technology areas of the Deutsche Post between 1946 and the 1980s.

Faculty and Staff:

Prof. Dr.-Ing. et Dr. phil. Alfred Kirpal
– head of the department – phone: -4694

Andreas Vogel
– scientific coworker – phone: -4675

Marcel Norbey
– scientific coworker – phone: -4675

Verena Mühr
– scientific coworker – phone: 0711-1723170

Klaus Waschke
– scientific coworker – phone: -4635

Andreas Ilsmann
– Ph.D. student – phone: -4675



Prof. Dr.-Ing. et Dr. phil. Alfred Kirpal

Contact:
Angelika Sylvester, phone: +49-(0)3677-69-4676
email: angelika.sylvester@tu-ilmenau.de
<http://www.tu-ilmenau.de/twg>

Department of Technical Physics I

Surface phenomena play a more and more important role in the age of miniaturization and nanotechnology. The Department of Technical Physics is involved in research and teaching in numerous areas of surface science such as functional biointerfaces, surface functionalization, semiconducting surfaces and tribology using advanced surface analytical techniques.

The main focus of this research is to investigate the possibilities of controlling the fundamental elements of condensed matter on an atomic scale: atoms and molecules on solid surfaces. The concept of "customized" materials plays an important role in the optimization of the performance of electronic, optoelectronic, and mechanic devices.

The ability to produce structures atom by atom or molecule by molecule would allow the creation of a large array of specialized materials and functional structures; this is the long-term goal of nanotechnology. It is already possible to manipulate single atoms, for example, by using the tip of a scanning tunnelling microscope to influence the position of adsorbed atoms or to investigate chemical reactions of single molecules. The full potential of surface sensitive techniques offers promising possibilities for future research. In this context, our group investigates organic-inorganic interfaces, the mechanical contact between macroscopic and microscopic solid surfaces (including biological systems), as well as the growth and characterization of carbon layers, specifically C₆₀-molecules and carbon nanotubes.

Another focus of our group's research is the growth and characterization of compound

semiconductors such as silicon carbide and the group III-nitrides. These materials are promising for the use as high temperature and high frequency electronic devices, as well as for sensor applications. Furthermore, electrical contacts (such as those based on metal carbides) and epitaxially grown insulating layers have a strong influence on device performance.

Recently we started investigations on the electronic, vibronic and geometric structure of room temperature ionic liquids as well as their tribological properties. Ionic liquids are an interesting class of materials which have a very low vapour pressure but are still in the liquid phase at around room temperature. Their special properties make them good candidates for many applications.

Furthermore a growing field of our research is the pyrolysis of carbon containing biopolymers. The investigation of fundamental processes during the pyrolysis of lignin and cellulose containing compounds is one of the main topics here, with the aim to develop a new material for bipolar plates in fuel cells.

Research in tribology covers three major areas: Tribology of nanopositioning (friction, wear and lubrication of bearings and couplings used in nanopositioning); Microtribology (adhesion, friction and lubrication of the Micro-Electro-Mechanical Systems); and Tribochemistry (interaction of lubricants and lubricant additives with contacting surfaces).

Additionally, several analytical measurements are performed by our group within collaborative studies with a variety of researchers inside and outside the TU Ilmenau as well as for companies.

Topics

- Processing of ultrathin layers
- Surface and interface properties on an atomic scale
- Structural, electronic and vibronic properties of carbon related materials, InP, oxides, and group III-nitrides
- Doping profiles in semiconductors
- Interaction of hydrogen with silicon surfaces
- Room temperature ionic liquids
- Properties of new materials for the use in fuel cells
- Tribology of nanopositioning
- Microtribology
- Tribochemistry
- Technical properties of fluorescent lamps

Faculty and Staff:**Prof. Dr. rer. nat. Jürgen A. Schäfer**

– head of department – phone: -3609

Stefan Krischok

– scientific coworker – phone: -3405

Imad Ahmed

– scientific coworker – phone: -3215

Maxim Eremtchenko

– scientific coworker – phone: -3712

Wolfram Hild

– scientific coworker, former

Marcel Himmerlich

– scientific coworker – phone: -3417

 Gudrun Hungenbach

– scientific coworker – phone: -3782

Mikhail Kosinskiy

– scientific coworker – phone: -3679

Yonghe Liu

– scientific coworker – phone: - 5074

Pierre Lorenz

– scientific coworker – phone: -3417

Anita Neumann

– scientific coworker – phone: -3175

Rolf Ötting

– scientific coworker – phone: -3215

Jens Uhlig

– scientific coworker – phone: -3712

Vasil Yanev

– scientific coworker, former

Annette Löffert

– technical coworker – phone: -3417



Prof. Dr. rer. nat. Jürgen A. Schäfer

Contact:

Jana Spindler, phone: +49-(0)3677-69-3608

email: jana.spindler@tu-ilmenau.de

http://www.tu-ilmenau.de/fakmn/Technische_Physik_I.974.0.html

Department Theoretical Physics I

Major research interests of the department of Theoretical Physics I include semiconductor nanostructures, theoretical material physics (electronic structure calculations, mainly density functional theory), as well as quantum chemistry and many-particle physics. These are pursued by combining analytical and numerical approaches.

- Quantum mechanics and statistics of disordered systems
- Many-particle theory: highly correlated electronic systems, heavy-fermion materials
- Optical properties of low-dimensional systems
- Time-dependent nanophysics: ultra-fast kinetics
- Energy relaxation processes and optical coherence
- Transport in nanostructures, non-equilibrium Green's functions
- Growth mechanisms and structure of semiconductor hetero interfaces
- Quantum chemistry calculations, density functional theory
- Electronic structure of solids, band structure calculations
- Elementary excitations in amorphous systems
- Molecules on surfaces
- Conjugated polymers
- Excitons in molecular systems

Semiconductor nanostructures

Optical properties of semiconductor-based nanostructures are determined to a large degree by growth related disorder. Optical experiments at low temperature with excitation energy close to the fundamental band gap at low excitation density show light emission primarily out of localized exciton states. Ultra-fast experiments using femtosecond lasers and experiments with high spatial and high spectral resolution (*Near-field Optical Scanning Microscopy*) provide complementary information on the localized quantum states.

In the last decade, a detailed theoretical understanding of the localized quantum states as a basis for a description of the ultra-fast excitation kinetics and the related energy relaxation processes was obtained. A comprehensive overview by the group leader was published as contribution *Excitons in semiconductor nanostructures* to the Solid State Physics series (Vol. 57, edited by H. Ehrenreich and F. Spaepen, Academic Press, San Diego, 2002).

The importance of optical coherence was stressed in a review together with R. Zimmermann and V. Savona in *Quantum Coherence, Correlation and Decoherence in Semiconductor Nanostructures* (edited by T. Takagahara, Elsevier Science, Oxford, 2003).

Recent work in the group addresses the spin-dependent exchange splitting of exciton states and a more detailed description of the electromagnetic field in near-field experiments.

Theoretical material physics

It is well known that the rich physics of transition metals, lanthanides and actinides with partially occupied d- and f-shells results from the interplay/competition of kinetic energy (hybridization) – which tends to delocalized electrons and to quench orbital moments – and intra-atomic electron correlations as described by Hund's coupling – which tends to maximize the local moments. It was recently suggested that this competition leads to so-called partial localization. Different electrons within the same shell behave differently: Some orbitals are fully occupied, thereby increasing the local moments. Other electrons "hop" from one atom to the next and, thus, reduce the total kinetic energy. These hopping processes involve only few orbitals, selected such that large atomic moments exist before and after the hopping. It is interesting to see which of the widely used approximation methods for many-particle systems (Hartree-Fock, Gutzwiller-Ansatz,..) can reproduce the phenomenon of partial localization.

Quantum chemistry of conjugated polymers

Conjugated polymers and copolymers, as well as their blends with fullerene derivatives are an intriguing class of materials. They find application in a broad variety of devices, such as light-emitting diodes, photovoltaic cells, field effect-transistors, and sensors. Charge and excitation transport in these materials - and finally the device performance - are crucially influenced by the morphology on the nanometer scale. The latter results from self-organized processes, which in turn reflect in part the underlying chemical structure. Thus for a directed design of appropriate molecules, a theoretical modeling of the polymer conformations based on quantum chemical calculations is very much called for.

In cooperation with the Fachgebiet Experimentalphysik I, the Cavendish Laboratory (Cambridge, UK), and the Department of Chemical Physics at Lund's University (Sweden), we investigate the conformation of several polythiophenes, which are promising conjugated polymers for solar cells. We applied quantum-chemical methods, e.g. td-DFT and CASPT2, to determine the conformation-dependent interaction between the monomeric units. Following a multi-scaling approach, we used these results as input parameters for Monte-Carlo simulation of these polymers within a bead model. Additionally, we developed the so-called line-dipole approximation in order to simulate the excitation transport on and between polymer chains efficiently. This enabled us to compare our calculations with results from femtosecond-resolved optical spectroscopy.

Many-particle physics

Systems of strongly interacting electrons on lattices with geometric frustration have received considerable interest in recent years. The arguably most spectacular prediction in this field is the existence of quasi-particles, i.e. low-energy excitations, with exotic properties such as half-integer charges. This poses several questions of fundamental interest. Unfortunately, quantum Monte Carlo techniques can not be used due to

the fermionic sign problem. Thus, the method of choice are numerically exact diagonalization and related approaches (calculation of spectral function via the Lanczos method, solution of the time-dependent Schrödinger equation etc.).

Considered as matrices, the corresponding Hamiltonian operators are sparsely occupied, but their dimensions grows exponentially with system size. However, several important issues can only be resolved if the system size is sufficiently large so that two quasi-particles can be considered as spatially separated. Thus, numerical calculations are very demanding, requiring resources such as the *Massively Parallel Compute Cluster* MaPaCC at the UniRZ. The many-particle physics activities are pursued mostly in collaboration with the Max-Planck-Institute for Physics of Complex Systems.

Faculty and Staff:

Prof. Dr. rer. nat. Erich Runge

– head of department – phone: -3707

Wichard Beenken

– scientific coworker – phone: -3258

Rolf Ötting

– scientific coworker – phone: -3215

Stephan Schwieger

– scientific coworker – phone: -3258



Prof. Dr. rer. nat. Erich Runge

Contact:

Dagmar Böhme, phone: +49-(0)3677-69-3607

email: dagmar.boehme@tu-ilmenau.de

<http://www.tu-ilmenau.de/theophys1>

The Application Center Ilmenau



The Application Center Ilmenau (APZ) is located right next door to the Center for Micro- and Nanotechnologies (ZMN). As part of the Regional Innovation System, it offers ideal conditions for technology oriented innovative companies and start-ups. It provides all the basic technology and equipment – including special gear, laboratories and clean room. With the help of fittings and equipment, the center supports the efficient implementation process, starting from research results and the product idea right up to pilot series production.



The APZ building

The Application Center assists its lessees in rising up a new business within an optimal infrastructure: Offices, laboratories and a clean room stand for a premium high-tech surrounding. The APZ even provides phone and office services as well as IT and network services – so the APZ users can focus entirely on their own projects.

The two centers (ZMN and APZ) are at close quarters on the campus of the Technische Universität Ilmenau (TU), but they are still discrete. The ZMN is specialized on doing scientific activities, whereas the APZ is concentrated on their commercial implementation. This generates some positive effects: Due to the proximity of both devices, the transfer of know-how is guaranteed as well as the utilization of research findings in the commercial sector. Moreover, ZMN and APZ complete each other, as the technology fields occupied by both devices are complementary.

The following technology domains are covered by APZ:

- wafer technologies
- microstructuring and nanostructuring
- circuit and hybrid technology
- imaging
- instrumentation sensors
- medical technology
- power electronics
- electronics packaging

At the beginning of 2006, the APZ put wafer reclaim technology into operation. By means of this innovative equipment, it is possible to prepare wafers by various corrosion, polishing and cleaning treatments and to make them available for fabrication again. The technology is designed for wafers of 300 mm height. Nanolay AG, a start-up offering wafer re-claim technology, is settled in the APZ and employs more than 15 staffers due to the favorable order situation.

The ZMN and the APZ conduct various joint activities: They attend and consult those concerned about each center's core service – i.e. about fundamental research or the renting of spatial or device-related resources. The ZMN is proficient in research activities and the APZ offers the leasing of rooms, equipment and devices.

Another main focus of the cooperation between ZMN and APZ are integrated public relations. In co-published brochures and leaflets the conjoint offers are to be found.

Mutually, the APZ and ZMN are exhibiting at trade fairs like Hannover Messe. In 2007, both centers will be part of a shared booth of the Microtechnology Network (IVAM). The booth will be situated in the area of microtechnology in hall 15. Together with the department of Micromechanical Systems (MMS) of Technische Universität Ilmenau the APZ presents its offers and cooperation options.

Cooperation is highly emphasized by both APZ and the ZMN. The ZMN as an interdisciplinary institution, but also a couple of institutes at the Technische Universität Ilmenau are worthwhile partners for the APZ. Several achievements prove that:

Due to the close cooperation between the Institute of Process Measurement and Sensor Technology at TU Ilmenau, SIOS Messtechnik GmbH and Sartorius AG, a highly precise measurement instrument could be developed: A comparator balance that is the most exact balance of the world. As it measures with a precision of 100 nanograms, it serves for the comparison measurement between very precise weights, e.g. between national prototypes for 1kg and the original kilogram in Paris. Upon

completion, the comparator balance was placed at the disposal of the International Office for Weights and Measures in Sèvres near Paris. The balance is being constantly enhanced by the SIOS GmbH at APZ premises. The utilization of the infrastructure of APZ constitutes a successful example for the development of high technology. Design and equipment of the rooms represent ideal conditions for the improvement of the highly complex measurement systems.



The Tetekera GmbH, situated in APZ since four years, is another striking example for the vivid relationship between TU and APZ – and for the unceremonious alternation between research and application. Tetekera provides three-dimensional laser shaping (ablation) of various materials. The Tetekera owner and executive secretary Torsten Thelemann also occupies a part time position as a scientific coworker in a junior researcher group from TU Ilmenau.



In future the link-up between APZ and TU will be even extended. Since July 2006, two junior researcher groups from TU Ilmenau use laboratories and offices at the APZ premises. The project is called "MacroNano" and is financed by an innovation program initiative of the Federal Ministry of Education and Research. Many departments like mechanical and electrical engineering, computer science and natural sciences work together. Resulting from the scientific activities in "MacroNano", further start-ups are estimated.



*Administration of the APZ (left to right):
Tino Wagner, Johannes Przybylski, Karsta Rödiger,
Dr. Bertram Harendt (Managing Director)*

Contact:

Betreibergesellschaft für Applikations- und
Technologiezentren Thüringen mbH (BATT)
Gustav-Kirchhoff-Str. 5, 98693 Ilmenau
phone: +49-(0)3677-20 10-0
email: info@apz-ilmenau.de
<http://www.apz-ilmenau.de>

Infrastructure and Equipment

The science center, which holds an overall laboratory space of more than 1000 m², hosts a clean room facility of about 700 m² with various clean room classes. While about 400 m² are classified as clean room class 10,000, the remaining space of 300 m² is classified as class 1,000 or even as low as class 100 in the lithography area.

Outside the clean room there are facilities for different technologies, such as the printing of circuit boards, a laser lab for the trimming and cutting of specimens addressing the packaging applications of devices. Furthermore, the central application lab offers security standard S1 for handling of genetically modified organisms which addresses the construction of large and sophisticated complete systems for biological, medical, and pharmaceutical research. Additional analytical devices on the nanoscopic scale which require a very low level of vibration are located in the basement of the building.

Technological labs and equipments inside the clean room:

Polymer electronics lab

Evaporation system (Edwards Auto 306)
 Glove box used for preparation of polymer films (Braun)
 Mask aligner (JUB 2104 Elektromat)
 Spin coater (Convac)



Glove box

Thin film measurement lab

Optical surface profiler (UBM, UBC 16)
 Measurement system for degradation of conductive layers (Karl Süss)

Div. microscopes (Leitz, Zeiss)
 Ellipsometer (SD 2300 - Plasmos)
 Stress measurement system (TENCOR)
 Tactile surface profiler (Ambios Technology)
 Film thickness measurement system (Mister)



Ellipsometer

Optical lithography lab

Anodic bonding tool EV501 (EVG)
 Automatic spin coater CEE 4000 (Brewer Science)
 Double side mask aligner AL6-2 (EVG)
 Semiautomatic spin coater CEE CB100 (Brewer Science)
 Spray developer Delta 20 (BLE)
 Mask cleaning system (Hamatech)
 E-beam lithography system RAITH 150 (Raith)



Optical lithography lab



Spin coater



Electron beam lithography



Double side mask aligner

Wet chemical processes lab

Quick dump rinser
 Rinser-dryer (Semitool)
 RCA cleaning process
 Wet benches for several wet chemical etching processes (Kufner)(metals, metal oxides, silicon, SiO₂, Si₃N₄)



Wetbench

PVD/RIE lab

(physical vapor deposition / reactive ion etching)
 Simple evaporation system for metallic layers (Edwards Auto 306)
 Cluster system with ISE, sputtering chamber for metals, e-beam evaporation system (Ardenne LES 250)



Sputtering system Ardenne (Ardenne LES 250)

Cool sputtering system for preparation of SEM samples (Emitec)

ECR dry etching process for silicon carbide
(Balzers PLS 500)

ICP dry etching process for silicon (STS - ASE)



High rate anisotropic silicon etching (ICP-ASE)

Leybold sputtering system (LAB 500)

PECVD system for SiO_2 and Si_3N_4 (STS 310 PC)

Plasma stripper for resists removal (TEPLA 200)

Scanning microscope (Hitachi SD 2700)

RIE dry etching process for SiO_2 and Si_3N_4 (STS 320 PC)

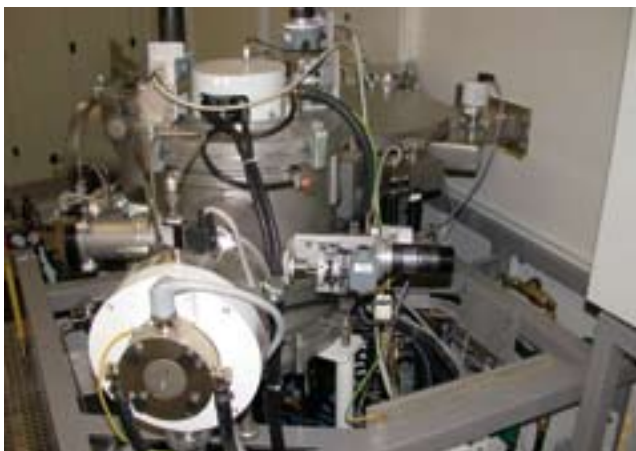
RTP system (Jipelec)

Sputtering system for tungsten carbide und silicide
(Ardenne LA 440)

Sputtering system for ZnO-films (Nordiko 2000)

ICP chlorine based dry etching process for GaN
(STS-ICP)

RIE chlorine based dry etching process for Al
(Alcatel RDE300)



Unviarsal thin film deposition tool (Ardenne LA 440)

High temperature processing lab

Atmospheric oxidation system for silicon substrates
(wet oxide)

4-stock LPCVD system for Si_3N_4 , TEOS, poly-Si, doped
poly-Si (Tempress Systems)

2-reactor MOCVD system for GaN, AlGaN, AlN and
metal oxides like ZnO (Aixtron)



MOCVD system

Mounting technologies lab III

(mounting and connection technologies)

Cyberscan

Hole punch for LTCC tapes (PTC)

Isostatic press

Screen exposure system

Screen printer (EKRA)

Screen washing system

Annealing systems (ATV)

Via filling system (PTC)



CyberScan

MBE/Surface analytics lab

(Molecular beam epitaxy)

MBE system for SiC, GaN, InN, AlN (Balzers UMS 500)

Surface analytic module with several technologies (OMICRON) (STM, AFM, XPS, UPS, AES, RHEED, PEEM, EELS, MBE)



MBE system, detail



Surface analytic module

Electrical characterisation lab

Measurement system for gas sensors

Hall measurement system (Agilent)

Wafer probe station with HP-tools for electrical characterisation (Agilent)

Waferprober



Wafer prober

Solid state analytics lab

Auger electron spectroscopy (AES) (VG scientific 350)

IR ellipsometer (Sentec)



Auger electron spectroscopy

Backend technology lab

(lab for electronics and testing)

Dicing saw DAD-2H/6T (Disco)



Dicing saw

Chemical mechanical polishing system PM5 (Logitec)

Wet bench for sample preparation



Chemical mechanical polishing

Fluidics and bionics lab

Surface tension measurement system (Krüss)

Tribometer (Tetra)

Viscometer

Dosing systems for liquids

Advantix system to manipulate liquid volumes ranging from picoliters to microliters

Mass spectrometer for liquid samples



Surface tension measurement system

Technological labs outside the clean room:

Mounting technologies lab I

(mounting and connection technologies)

Heating press (Schmidt)

NdYAG laser (LPKF)

SMD mounting system

Annealing system (ATV)

Trimming laser system (Aurel)



NdYAG-Laser

Mounting technologies lab II

(mounting and connection technologies)

Die bonding system (Delvotec)

Wire bonding system (Delvotec)

Fine placer for SMD components

SMD soldering station

Ultrasonic measurement system (Sonoscan)

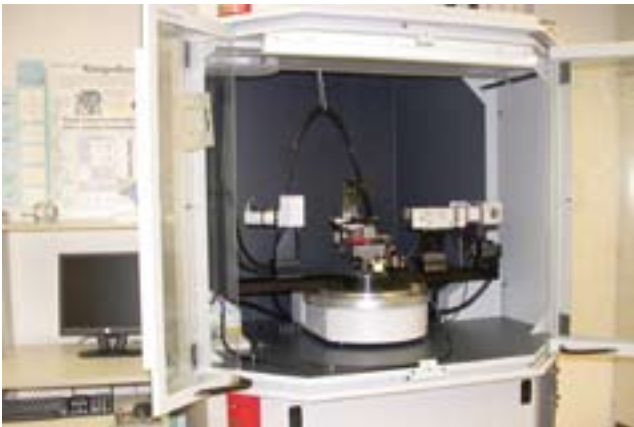
Wedge bonding system (Delvotec)



Ultrasonic measurement system

X-ray analytics lab

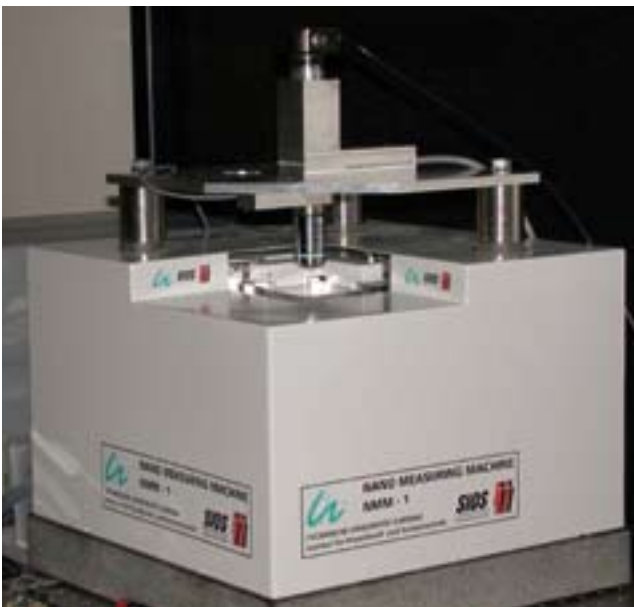
- X-ray diffractometers (Siemens)
- X-ray analytics (Feinfocus)
- HRX-ray diffractometer (Bruker AXS D8)



High resolution X-ray diffractometer

Nanomeasurement technology lab

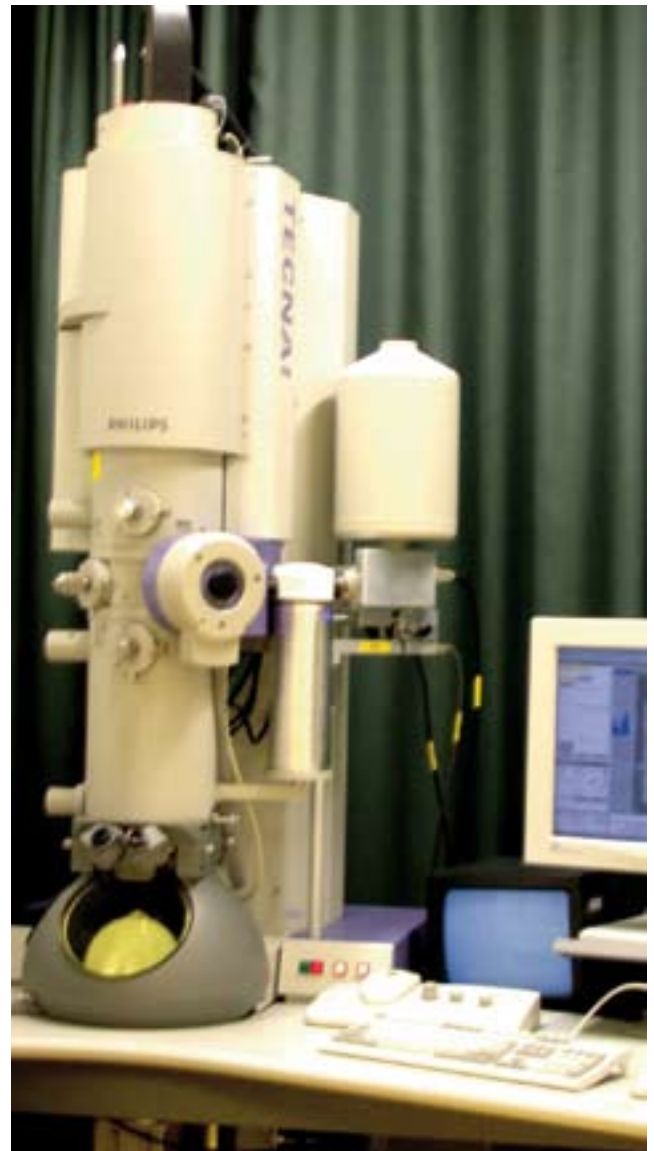
- Nanopositioning and nanomeasurement machine (SIOS)
- Vibration free lab benches
- Interferometer for surface analysis



Nanopositioning and measurement machine

Electron microscopy lab

- (transmission and scanning electron microscopy)
- Atomic force microscope (NT-MDT)
- Transmission electron microscope (Philips TECNAI)
- Scanning electron microscope (Philips TECNAI)



Transmission electron microscope



Scanning electron microscope

AFM/FIB lab

FIB 200 (FEI)
AFM Topometrics
AFM Park



Focussed ion beam

Biological lab I (S1)

Glove box for experiments with biological or chemical samples (Ganuk)
Laminar flow box with UV-Sterilisation (Ganuk)
Incubator (Heraeus)
Centrifuge (Eppendorf)
Concentrator 5301 (Eppendorf)
Thermocycler (Biometra)
div. Microscopes (Nikon)
Refrigerators/Freezers (Axofreeze)
Pure water system (ELGA)



Biological Lab I

Biological lab II (S1)

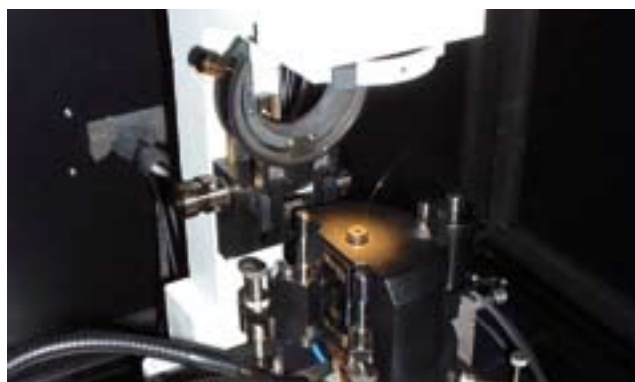
Centrifuge (Eppendorf)
Heraeus Medifuge (Heraeus)
PCR-System
div. Microscopes (Nikon)



Biological Lab II

Optical characterisation lab

Solver SNOM (NT-MDT)
UV-VIS Spectrometer (Varian Cary 5000)
Photothermal deflection spectroscopy (PDS)



Scanning nearfield optical microscope

Laser ablation lab

Laser ablation system LUCAS



Laser universal cluster ablation/evaporation source, detail

Finances

In 2005 basic funding for the ZMN was provided by the Technische Universität Ilmenau. This covers the costs for the basic operation of the building and the equipment contained within. The income for ZMN operation amounted to 21,000 €. This funding came from the following agencies: 7,000 € from the central funding of the university, 7,000 € from the different faculties and the final 7,000 € by the chairs

active in the center. In addition unique 50,000 € were provided for completion of the technology practical course for teaching students in micro- and nanotechnologies. Another 29,700 € were applied for maintenance and repair of the sophisticated scientific infrastructure. The specific expenditures are listed in detail in figure 1.

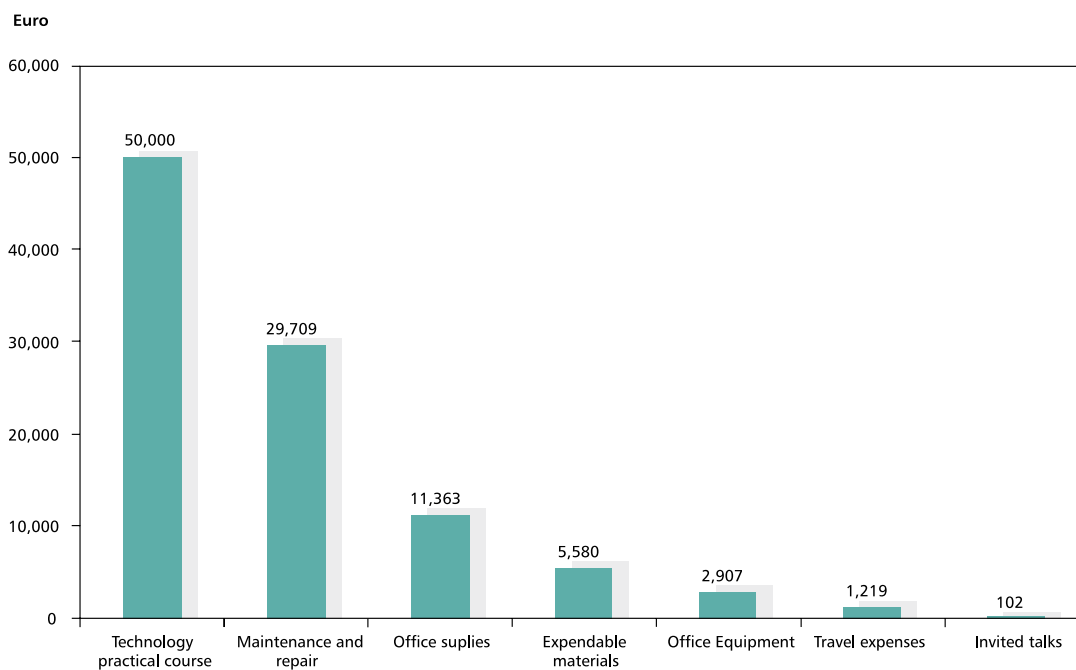


Fig. 1: Corporate finance of the ZMN in the year 2005

Research costs are solely provided by a third means, i.e. external funding such as e.g. federal or state government, as well as industry. They amount to

4.1 Mio € in 2005. Figure 2 gives an overview of the different sources of funding for the year of 2005.

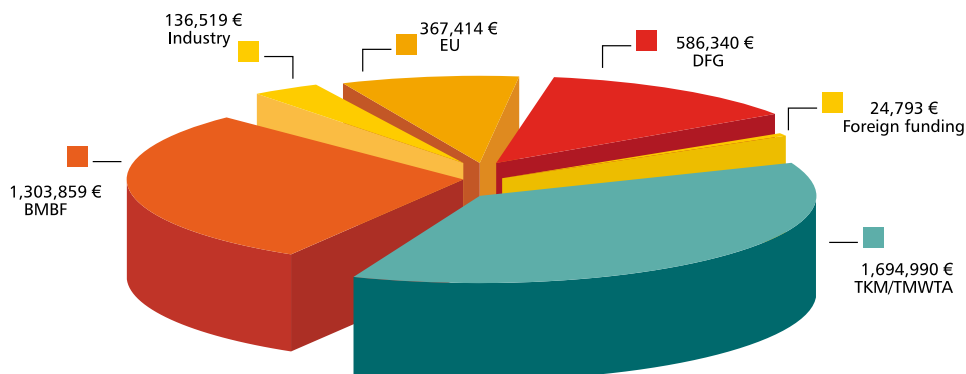


Fig. 2: Research projects in the year 2005

The development of the overall financial volume of the research projects in the time period of 2002 – 2005 is plotted in figure 3. The overall research costs in the time period from 2002 to 2005 amount to 10.2 Mio €, which are provided by different funds. Figure 4 gives an overview of funding agencies and the sizes of their shares.

BMBF	Federal Ministry of Education and Research
DFG	German Science Foundation
EFRE	European Fond for Regional Development
EU	European Union
FhG	Fraunhofer-Gesellschaft
TKM/TMWTA	Thuringian Ministries

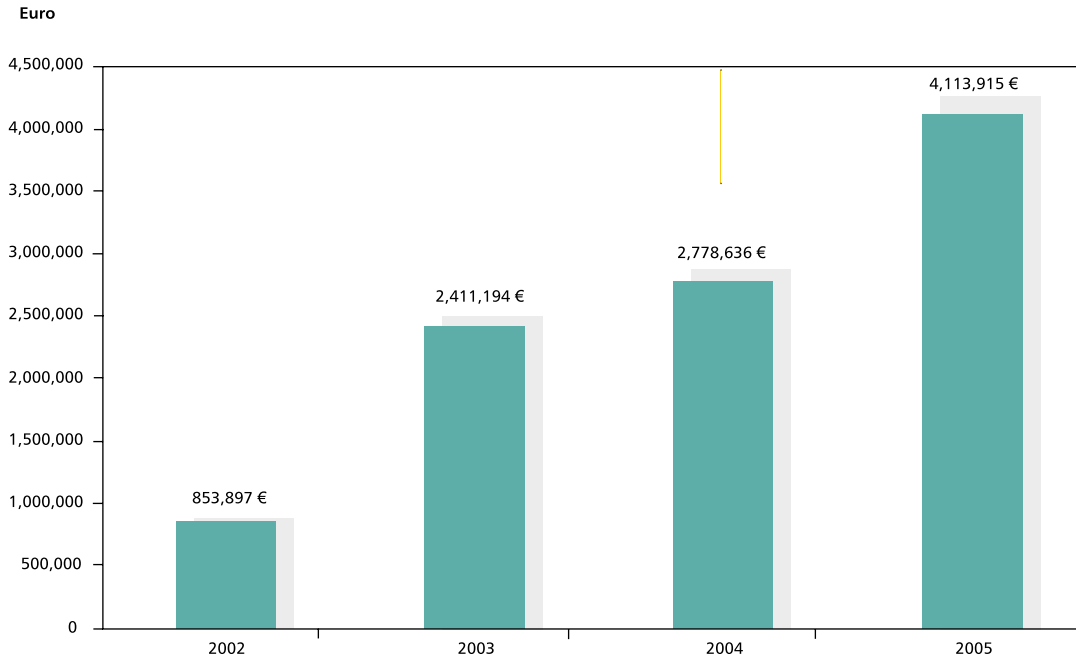


Fig. 3: Development of research projects in the time period of 2002-2005

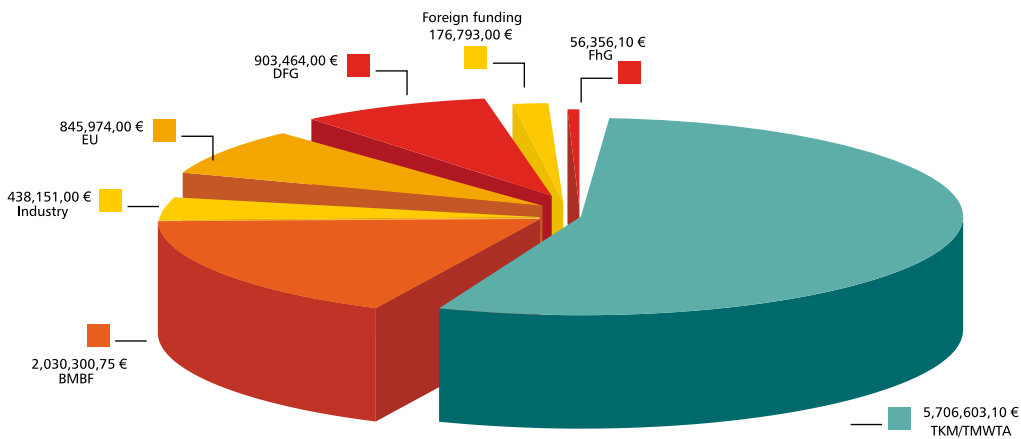


Fig. 4: Funding of the research projects in the time period of 2002-2005

In 2006 85,000 € are provided for the central facility ZMN by the Technische Universität Ilmenau including 67,150 € for maintenance and repair of the

scientific infrastructure. Figure 5 provides an overview for the currently targeted amounts spent on other different issues.

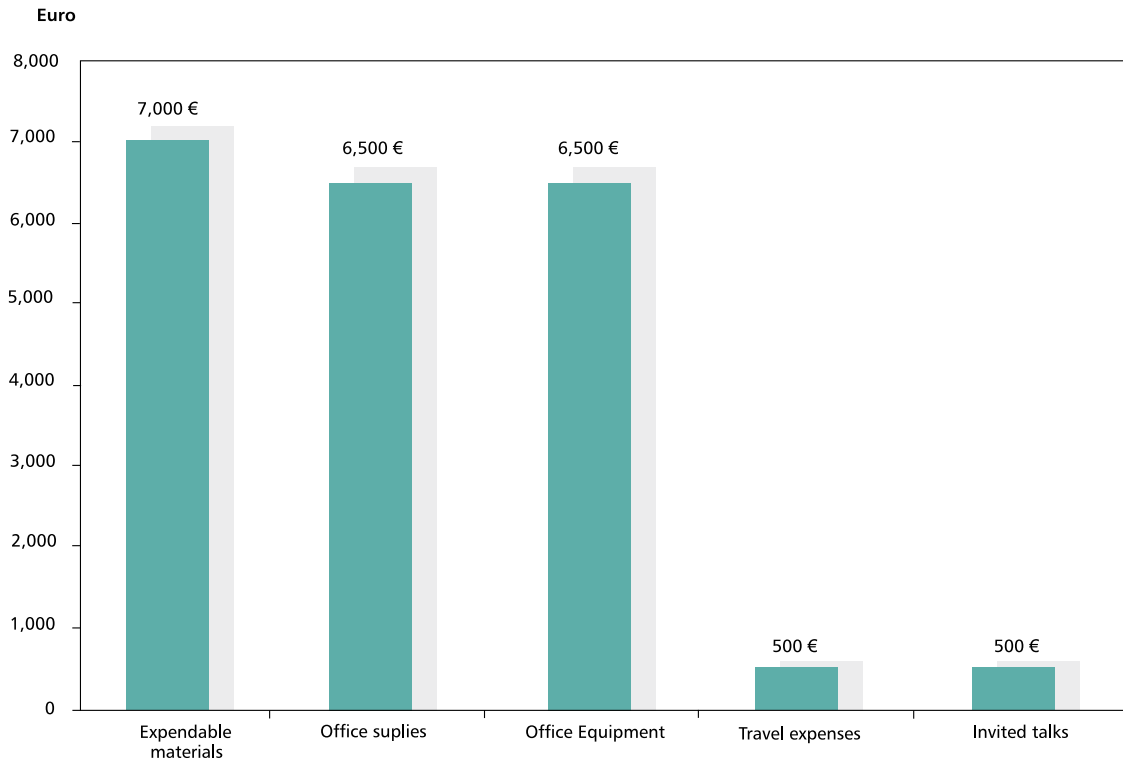


Fig. 5: Predicted expenses of the ZMN in the year 2006

In the future the development of the funding for research projects again looks very promising. In 2006 until October funding of 3.9 Mio € already was achieved.

Synthesis of New Soluble C₆₀ and C₇₀ Derivatives for Use in Organic Solar Cells

U. Ritter*, P. Scharff, T. Weber, and L. Carta-Abelmann

Department of Chemistry

For the construction of donor-acceptor polymeric solar cells the donor polymer has to be combined with soluble fullerenes mostly in blends. Besides of the well known side-chain substituted fullerenes, like PCBM ((1-(3-methoxycarbonyl)propyl-1-phenyl)[6,6]C₆₁), we present new soluble fullerenes on the basis of C₆₀ and C₇₀ together with dimers and oligomers of these fullerenes. The use of C₆₀ and C₇₀-derivatives in cooperation with optically excited conjugated polymers and the observation of a highly increased photoconductivity of such systems is the basis for the well known polymeric solar cells up to now. Efficient charge transfer from donor to acceptor components, effective charge transport and charge injection into the electrodes are important parameters for design and optimization of fullerene based acceptor

materials. Since the semiconducting polymers are mainly processed from solution, the search for new fullerene derivatives has to be concentrated on the solubility of these compounds and their electron acceptor behavior.

For this reason we developed a range of fullerene derivatives with decreased symmetry compared to C₆₀ (Fig. 1).

Our main purpose is to increase the anisotropic properties of the polymeric matrix. Electrochemical data were measured and give us valuable information for the relative position of LUMO levels of these materials (Fig. 2). To find suitable donor-acceptor pairs the knowledge of these values is of great importance.

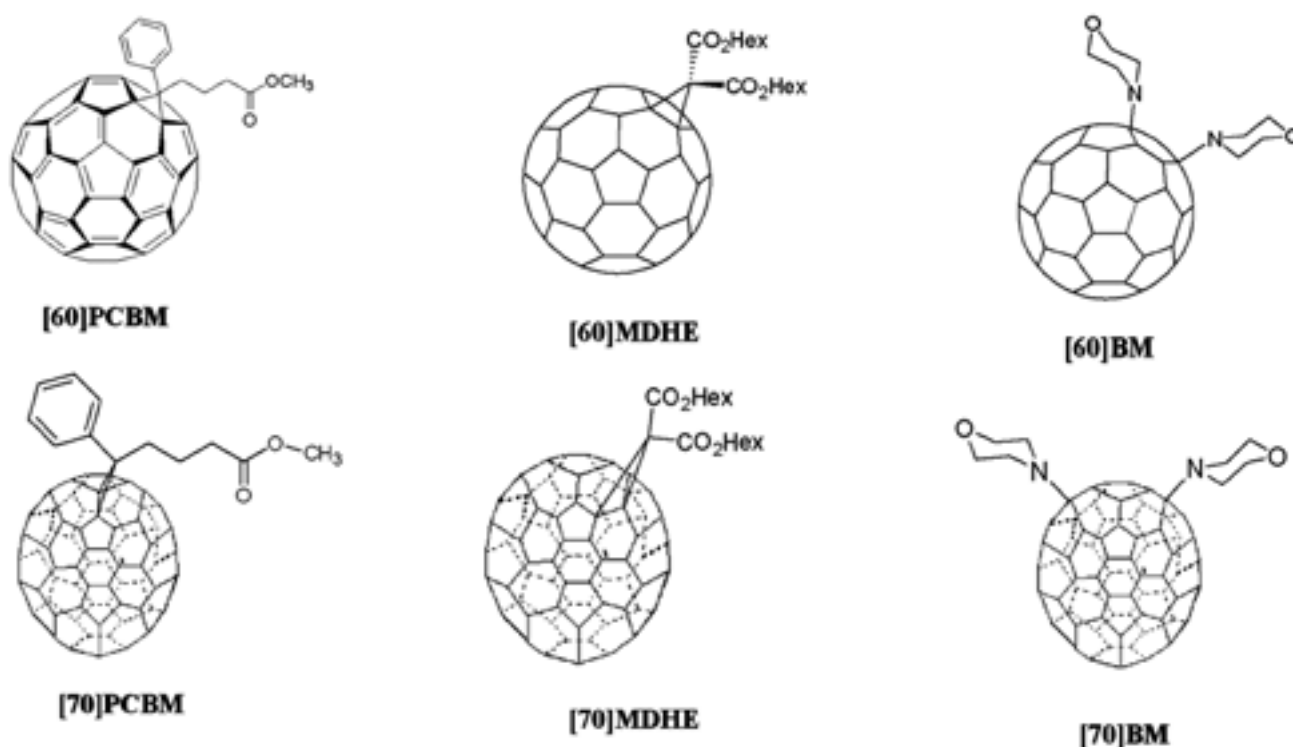


Fig. 1: Examples of synthesized fullerene derivatives on the basis of C₆₀ and C₇₀.

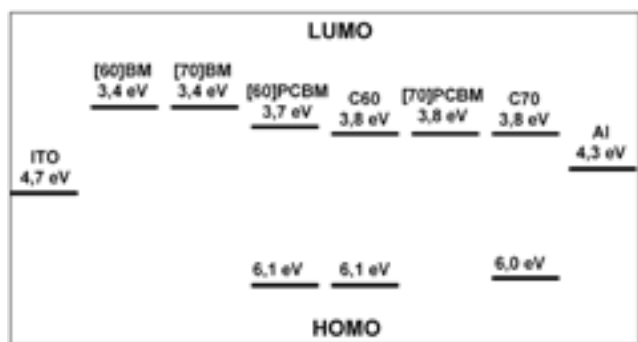


Fig. 2: Calculation of the LUMO levels from CV measurements in solution.

Besides of the bis-morpholino-derivatives ([60]BM and [70]BM) the LUMO level is not influenced by the side chain substitution. Otherwise the solubility in organic solvents of the derivatives is increased and due to the decreased symmetry in the C_{70} derivatives, we expect an anisotropic effect of these materials in the polymer blends. The synthesis of the $[C_{70}]PCMB$ is shown in figure 3.

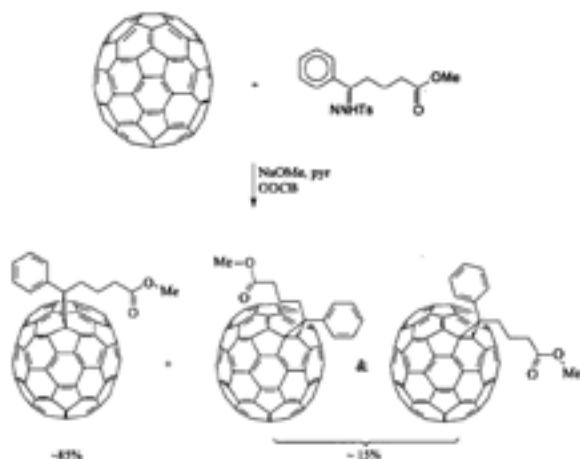


Fig. 3: Synthesis of [70]PCBM.

A further increase of the anisotropic properties is expected by combining more fullerene molecules in oligomeric and polymeric materials based on fullerenes (Fig. 4.2)

Since their discovery fullerene-polymers have attracted much interest, due to their peculiar properties.

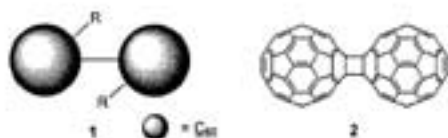


Fig. 4: Two different types of C_{60} -dimers.

By polymerization of fullerenes, a large increase in conductivity is observed.

We synthesized fullerene dimers (C_{120} ; Fig. 4.2) through conversion of C_{60} with the interhalogen compound iodine-monobromine at 80°C and normal pressure. The isolation of the product was performed by preparative HPLC and the characterization by Raman measurements. Under the same conditions a further reaction of the purified dimers with IBr leads to the formation of short C_{60} -polymer-chains (Fig. 5).

Conjugated C_{60} or C_{70} -chain-polymers with up to 12 connected monomer packages can also be produced by activation in an UV reactor under argon atmosphere.

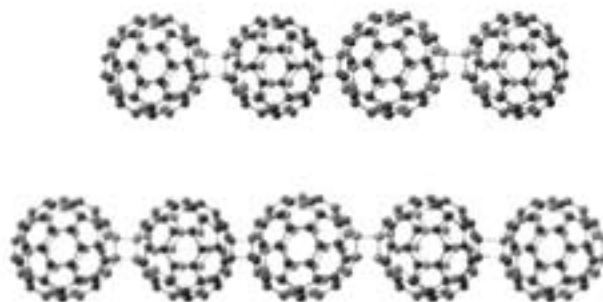


Fig. 5: Examples of C_{60} -oligomers.

Therefore a C_{60} or C_{70} solution of toluene was filled into the reactor and irradiated for 60 minutes. Afterwards the materials were characterized by Raman scattering and ^{13}C -NMR spectroscopy.

As a conclusion it can be said that it is possible to produce one dimensional polymer chains using two different methods. First, the synthesis of one-dimensional C_{60} -chains can be done by photo polymerization using an UV-reactor under argon atmosphere. Second, we showed that it is possible to polymerize C_{60} by another preparation route, using normal pressure and only moderately elevated temperatures by converting the monomer unit several times with the interhalogen compound IBr and treating the brominated product with polar organic solvents. Preliminary results indicate that further chemical modification reactions leads to substituted C_{120} molecules (Fig. 3.1) which are highly soluble in organic solvents and therefore have a great potential for the use as electron acceptors in polymeric solar cells.

Influence of Mixing Ratio and Annealing on Structural and Optical Properties of Thin P3HT/PCBM Films

T. Erb^{1,*}, U. Zhokhavets¹, H. Hoppe¹, G. Gobsch¹, M. Al-Ibrahim², and Oliver Ambacher²

¹ Department of Experimental Physics I

² Department of Nanotechnology

Introduction

Conjugated polymers are widely used in organic devices like solar cells, organic light-emitting diodes (OLEDs) and organic field-effect transistors (OFETs). At present, bulk heterojunction polymer solar cells based on organic materials are being intensively investigated in order to increase their efficiency [1-4]. In thin film bulk heterojunction solar cells, the absorption of sun light and the transport of the generated charge carriers depend on structural and optical properties of the conjugated polymer-fullerene blend. It was shown, that the optical absorption of thin P3HT/PCBM (poly[3-hexylthiophene 2,5 diyl]/[6,6]-phenyl C61 butyric acid methyl ester) films and the efficiency of P3HT/PCBM solar cells can be improved by annealing of the layer [5-10].

Here we investigate the correlation between mixing ratio and annealing considering structural and optical properties of thin P3HT/PCBM blend films.

The crystallinity of thin P3HT/PCBM-films was studied using X-ray diffraction (XRD) in grazing incidence geometry. The size and orientation of polymer crystallites in untreated and annealed films for different mixing ratios were determined. The XRD results were compared with absorption coefficients, which were determined by spectral ellipsometry on the same films. We demonstrate a clear correlation between the P3HT crystallinity and the optical properties of the blend films.

Experimental

Thin P3HT/PCBM-films were prepared by spin-coating from 1.0 wt. % chloroform solution on silicon substrates. The P3HT/PCBM compositions were 1:1, 1:2 and 1:3 by weight. The investigated samples had a film thickness of about (57±3) nm. The samples were annealed on a hot plate at 125°C for 5 minutes.

XRD measurements were performed using a Philips X'Pert-Pro diffractometer. The thin films were studied in grazing-incidence diffraction (GID) geometry to increase the effective X-ray path length for scattering in the P3HT/PCBM layer and to minimize the contribution from the substrate. The angle between film surface and incident beam was fixed at 0.3°. As radiation source a monochromatic CuK α beam with a wavelength of $\lambda=0.154$ nm was applied. The detector scans at the angle 2θ in a plane defined by the incident beam and the surface normal [11,12]. Ellipsometric data were obtained by means of

a Woollam VASE variable angle spectroscopic ellipsometer with rotating analyzer (RAE) in the spectral range $\hbar\omega=1.5-4.0$ eV in steps of 0.02 eV. The spectral resolution was 3 nm (0.01 eV at $\hbar\omega=2.0$ eV). The measurements were performed at several angles of incidence between 60°-75° at room temperature in air. For the analysis of the ellipsometric spectra the Woollam WVASE software was used. The anisotropic dielectric function (DF) of the films and the film thickness were obtained from the Multiple Sample Analysis as described in [13-15]. In our work we analyzed simultaneously three samples prepared from the same solution, but using slightly different spin frequencies, which results in a slightly different film thickness. The average film thickness was (57±3) nm for all P3HT/PCBM mixing ratios. The anisotropic DF of the films was obtained by a point-by-point fit of the ellipsometric data using an anisotropic layer optical model. The surface roughness was neglected in the analysis. The film thickness was not affected by the annealing. Finally, from the DF the absorption coefficients were calculated.

Results and discussion

XRD diffractograms of three P3HT/PCBM-films having a mixing ratio of 1:1, 1:2 and 1:3 are shown in Fig. 1. The untreated samples show basically no crystallinity. The annealed samples show one single peak at $2\theta=5.4^\circ$ and in two cases a weak second order peak at $2\theta=10.8^\circ$. The corresponding lattice constant d can be calculated using Bragg's law [16] $2d \sin(\theta) = n\lambda$ (eq. 1) where $\lambda=0.154$ nm is the wavelength of incident beam, 2θ is the angle between incident and scattered X-ray wave vectors and n is the interference order. Applying equation (1) results in a lattice constant of $d=(1.63\pm 0.02)$ nm. In comparison with the literature [11,12,17], it can be concluded, that the detected peak originates from the polymer crystallites with (100) orientation (backbone parallel and side chains perpendicular to the substrate, as shown in the inset in figure 1). In all cases no crystallites with (010) or (001) orientation were detected.

A lower limit for the mean size of the polymer crystallites L can be estimated using the Scherrer relation $L \sim \frac{0,9\lambda}{\Delta_{2\theta} \cos(\theta)}$ (eq. 2), where $\Delta_{2\theta}$ is the full

width half maximum of the peak [16]. We obtain an L of about 10 nm for all annealed samples.

The height of the peak at $2\theta=5.4^\circ$ is proportional to the number of P3HT nanodomains per unit volume and consequently to the crystallinity of the investigated samples.

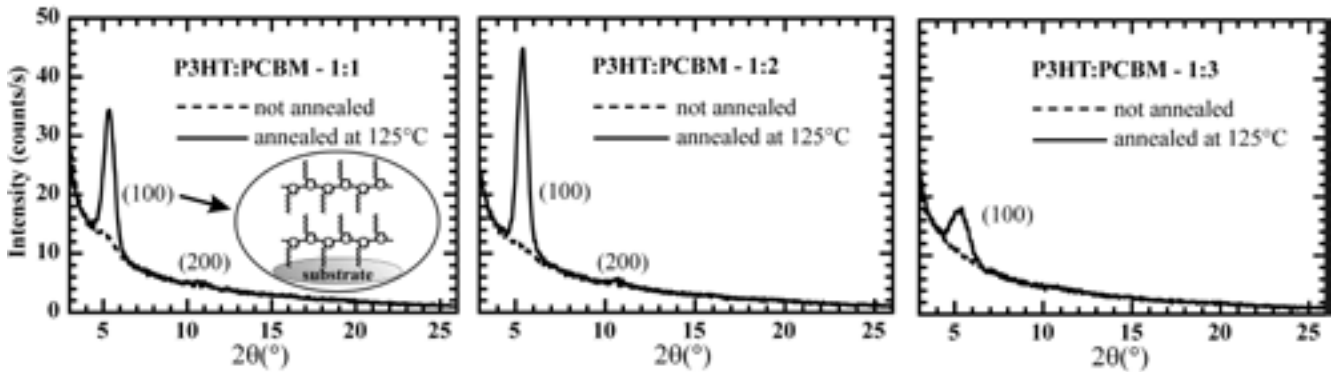


Fig. 1: Diffractograms (GID-geometry) of three P3HT/PCBM composite films (mixing ratio 1:1, 1:2, 1:3) deposited on Si-substrates, before and after annealing.

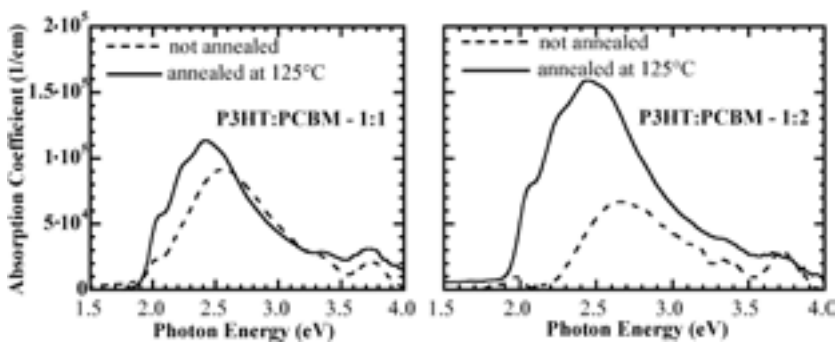


Fig. 2: Absorption coefficients of two P3HT/PCBM composite films (mixing ratio 1:1, 1:2) deposited on Si-substrates, before and after annealing. The absorption coefficients reflect only the portion of P3HT, as we have subtracted the part originating from the fullerene PCBM.

We conclude, that annealing of the P3HT/PCBM-film results in the formation of crystalline P3HT domains. The mixing ratio 1:2 results in the highest crystallinity of all investigated blends (Fig. 1). Therefore we believe, that this P3HT/PCBM mixing ratio is the best for the formation of P3HT-crystallites upon annealing. In this case, no PCBM crystallites could be found using XRD [18].

In first approximation the absorption coefficients of the P3HT/PCBM composite $\alpha^{\text{BLEND}}(\hbar\omega)$ can be assumed as a superposition of the absorption coefficients of the constituents $\alpha^{\text{BLEND}}(\hbar\omega) = f \cdot \alpha^{\text{PCBM}}(\hbar\omega) + (1-f) \cdot \alpha^{\text{P3HT}}(\hbar\omega)$ (eq. 3) where $\alpha^{\text{PCBM}}(\hbar\omega)$ and $\alpha^{\text{P3HT}}(\hbar\omega)$ are absorption coefficients of PCBM and P3HT, respectively. The fullerene volume fraction $f=0.594$ (mixing ratio 1:2) and $f=0.423$ (mixing ratio 1:1) was derived from the P3HT and PCBM densities of 1.1 g/cm^3 and 1.5 g/cm^3 , respectively. Applying equation (3), we calculate the absorption coefficient of P3HT $\alpha^{\text{P3HT}}(\hbar\omega)$.

The optical absorption coefficients of P3HT in the blend films having mixing ratios 1:1 and 1:2 are shown in Fig. 2. The absorption coefficients reflect only the portion of P3HT, as we have subtracted the part originating from the fullerene PCBM. The P3HT absorption coefficients of the annealed samples are larger than those of untreated samples over the whole spectral range. Especially in the energy region below 2.5 eV a significant increase

of optical absorption and the growth of an absorption shoulder at 2.05 eV is observed upon annealing. Due to crystallization of P3HT, the interaction between the P3HT molecules becomes stronger which leads to a coplanarization of the thiophene rings [19]. We believe this to be the origin of increased optical absorption in visible region.

This work has been supported by the TKM (NANORG1, 20101276).

- [1] C. J. Brabec, N. S. Sariciftci, J. C. Hummelen: *Adv. Funct. Mater.* 11 (2001) 15.
- [2] H. Hoppe and N. S. Sariciftci: *Organic Photovoltaics*, edited by S.-S. Sun and N. S. Sariciftci, (Taylor & Franzis, 2005), p. 217.
- [3] K. M. Coakley, M. D. McGehee: *Chem. Mater.* 16 (2004) 4533.
- [4] H. Spanggaard, F. C. Krebs: *Sol. Energy Mater. Sol. Cells* 83 (2004) 125.
- [5] F. Padinger, R. S. Rittberger, N. S. Sariciftci: *Adv. Funct. Mater.* 13 (2003) 85.
- [6] D. Chirvase, J. Parisi, J.C. Hummelen, V. Dyakonov: *Nanotechnology* 15 (2004) 1317.
- [7] M. Al-Ibrahim, O. Ambacher, S. Sensfuss, G. Gobsch: *Appl. Phys. Lett.* 86 (2005) 201120.
- [8] H. Hoppe, N. Arnold, D. Meissner, N. S. Sariciftci: *Thin Solid Films* 451-452 (2004) 589.
- [9] Y. Kim, S. A. Choulis, J. Nelson, D.D.C. Bradley, S. Cook, J.R. Durrant: *Appl. Phys. Lett.* 86 (2005) 063502.
- [10] X. Yang, J. Loos, S.C. Veenstra, W. J. H. Verhees, M. M. Wienk, J.M. Kroon, M.A.J. Michels, R.A.J. Janssen: *Nano Lett.* 5 (2005) 579.
- [11] T. Erb, S. Raleva, U. Zhokhavets, G. Gobsch, B. Stühn, M. Spode, O. Ambacher: *Thin Solid Films* 450 (2004) 97.
- [12] K. E. Aasmundtveit, E. J. Samuelsen, M. Guldstein, C. Steinsland, O. Flornes, C. Fagermo, T. M. Seeberg, L. A. A. Petterson, O. Inganäs, R. Feidenhans'l, S. Ferrer: *Macromolecules* 33 (2000) 3120.
- [13] U. Zhokhavets, R. Goldhahn, G. Gobsch, W. Schlieffe, *Synth. Met.* 138 (2003) 491.
- [14] L.A.A. Petterson, F. Carlsson, O. Inganäs, H. Arwin: *Thin Solid Films* 313-314 (1998) 356.
- [15] M. Tammer, A.P. Monkman, *Adv. Mater.* 14 (2002) 210.
- [16] B. D. Cullity: *Elements of X-Ray Diffraction* (Addison-Wesley Publishing Company Inc., 1956)
- [17] T.J. Prosa, M. J. Winokur, *Macromolecules* 25 (1992) 4364.
- [18] T. Erb, U. Zhokhavets, G. Gobsch, B. Stühn, P. Schilinsky, C. Waldauf, C. J. Brabec: *Adv. Funct. Mater.* 15 (2005) 1193.
- [19] W. J. D. Beenken, H. Lischka: *J. Chem. Phys.* 123 (2005) 144311.
- [20] U. Zhokhavets, T. Erb, G. Gobsch, M. Al-Ibrahim, O. Ambacher: *Chem. Phys. Lett.* 418 (2006) 347.

THz Emission from InN Surfaces

B. Pradarutti¹, G. Matthäus², C. Brückner¹, S. Riehemann¹, G. Notni¹, S. Nolte², V. Cimalla^{3,*}, V. Lebedev³, O. Ambacher³, and A. Tünnermann^{1,2}

¹ Fraunhofer IOF, Jena

² Institut of Applied Physics, Jena

³ Department of Nanotechnology

Introduction

Ultrafast terahertz (THz) pulses are of increasing importance for time-resolved spectroscopy in condensed matter, chemical spectroscopy, imaging in medicine and material science up to applications in security systems. Coherent THz emission can be obtained from semiconductor surfaces after excitation by ultrafast laser pulses. Here, narrow bandgap semiconductors have attracted much attention due to the high absorption and the electron mobility. Up to date, InAs was found to have the highest emission efficiency [1]. Recently THz emission has been demonstrated on InN surfaces as well [2]. A direct comparison to InAs has shown a similar or even higher emission from InN [3]. In this work we provide a study of the dependence of THz emission on the InN properties and propose an extension of common models by taking into account the peculiarities of the InN band structure.

Experimental Setup

Two slightly different experimental setups have been used to investigate InN as THz surface emitter at 1060 nm and 800 nm (Fig. 1).

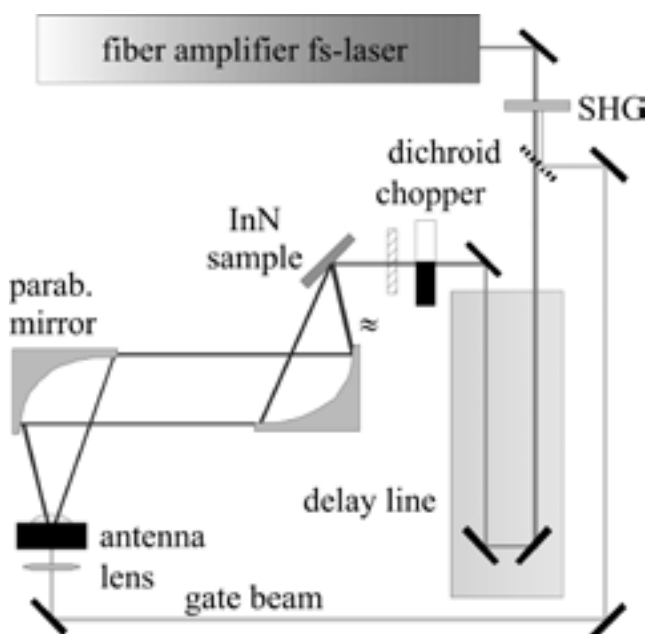


Fig. 1: Experimental setup for THz emission.

At a wavelength of 1060 nm ultrashort laser pulses with 2 W average power, a repetition rate of 76 MHz and a pulse length of about 100 fs are emitted by a fiber laser amplifier [4]. A small part (<1%) is frequency doubled by a phase matched 300 μm thick KTP crystal. The beam is split into a pump beam at 1060 nm (1.17 eV) and a gate beam at 530 nm (2.34 eV) by a dichroid. The gate beam is focus-sed on the back of a low temperature grown (LT) - GaAs dipole antenna. The photons excite electrons over the band gap (1.43 eV). The pump beam is guided through a delay line and collimated at an angle of 45° to the surface of the surface emitter with a spot size of about 2 mm, where THz radiation is emitted. The THz emitter is placed in the focal point of an off axis parabolic mirror leading to a parallel THz beam. A second off axis parabolic mirror focuses the THz beam on a silicon lens attached on the dipole antenna. The THz pulse accelerates the free electrons in the LT-GaAs antenna excited by the gate beam and a current proportional to the electric field of the THz signal is measured. Because the laser pulses are one magnitude of order shorter than the THz pulse, only a small part the THz pulse is measured. By moving the delay line the phase between the THz pulse and the fs-pulse is changed and the electric field of the THz pulse can be sampled.

At 800 nm a Ti:Sa laser with a pulse length of 130 fs and a output power of 1.3 W is used. Due to the photon energy of 1.54 eV at 800 nm no frequency doubling is necessary for detection with LT-GaAs antennas and the dichroid is replaced by a beam splitter.

Sample Preparation

The InN layers were grown by plasma-induced molecular beam epitaxy (MBE) on various epitaxial templates (Tab. 2). The thin SiC layers are formed ex situ by carbonization of the silicon surface [5]. The AlN and GaN template epilayers were grown in situ on sapphire [6] and on SiC/Si(111) [7] in a two-dimensional Frank-van der Merwe mode at substrate temperatures of $\sim 900^\circ\text{C}$ and $\sim 710^\circ\text{C}$ for AlN and GaN, respectively. Finally, the templates were overgrown in situ by InN at a substrate temperature of $\sim 380^\circ\text{C}$. All InN epilayers were grown under stoichiometric (1:1) conditions to prevent surface

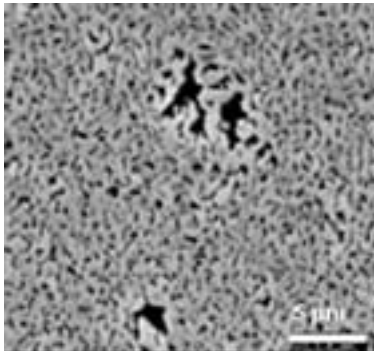
metal accumulation. The thickness of the InN layer has been varied from $0.35\ \mu\text{m}$ to $2.2\ \mu\text{m}$. Depending on the template, the layer thickness and the growth conditions, very different layer properties can be achieved. Figure 2 shows the morphology of two different InN layers with rough (a) and smooth (b) surface.

Additionally a p-doped InAs layer has been measured as reference.

Results and Discussion

Two examples for the THz emission from a rough and a smooth InN layer are shown in figure 3 in comparison to the reference sample InAs. Similar results have been obtained with 1060 nm excitation. The measured THz intensity demonstrates generally an increased emission if the layer quality is improved, i.e, the electron concentration and mobility are decreased and increased, respectively. The highest intensity, higher even than from the reference InAs sample, was observed for InN with an atomically smooth surface indicating the importance of the surface. (Fig. 3).

a)



b)

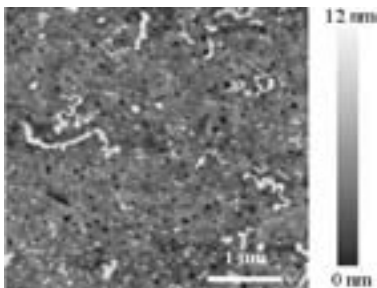
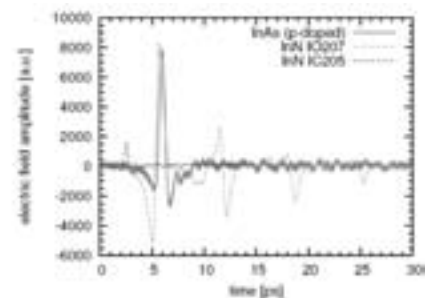


Fig. 2: (a) Scanning electron microscopy image of a co-lumnar InN layer (IC199) and (b) atomic force microscopy image of a smooth InN layer (IO207).

Typically, the discussion about the origin of the surface emission is based on ultrafast charge transport phenomena in an intrinsic surface field or due to the photo-Dember effect. However, these models cannot sufficiently explain the high THz emission from InN.

The direction of the extraordinary surface field in InN rules out its dominant role in THz emission from InN. Rather, the small light penetration depth in low-bandgap semiconductors causes absorption of the excitation pulse near the surface, thus, the THz emitting dipoles are created near the surface as well. Consequently, for effective InN based THz emitters the surface-near region of the film should be as defect-free as possible. Finally, our proposed model points out the dominant influences of (i) the low band gap, (ii) the high electron mobility, and (iii) the reduced probability of intervalley scattering, which makes InN the most promising candidate for THz emission.

(a)



(b)

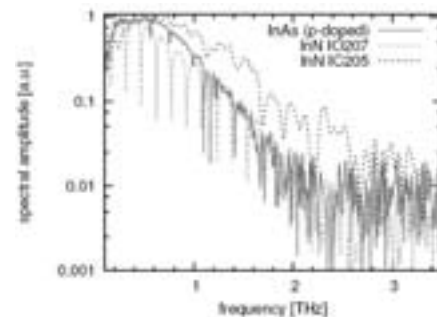


Fig. 3: (a) THz pulses of InN IO207 (smooth) and IC205 (rough) in comparison to p-doped InAs excited with 800 nm fs-pulses; (b) spectral amplitude obtained by FFT from the time domain signal.

This work was supported by FhG internal program (MAVO 813907), by the Thuringian ministry of culture and the European Union (B509-04011, EFRE: B 678-03001, 6th framework: GaNano NMP4-CT2003-505614).

- [1] C. Weiss, R. Wallenstein, and R. Beigang, *Appl. Phys. Lett.* 77 (2000) 4160.
- [2] R. Ascazubi, I. Wilke, K. Denniston, H. Lu, and W.J. Schaff, *Appl. Phys. Lett.* 84 (2004) 4810.
- [3] B. Pradarutti, G. Matthäus, C. Brückner, S. Riehemann, G. Notni, S. Nolte, V. Cimalla, V. Lebedev, O. Ambacher, and A. Tünnermann, *Proc. SPIE* 6194 (2006) 619401.
- [4] G. Matthäus, T. Schreiber, J. Limpert, S. Nolte, G. Torosyan, R. Beigang, S. Riehemann, G. Notni, and A. Tünnermann, *Optics Express* (submitted).
- [5] V. Cimalla, J.K. Karagodina, J. Pezoldt, and G. Eichhorn, *Mater. Sci. Eng.* B29 (1994) 170-175.
- [6] V. Lebedev, F. M. Morales, H. Romanus, S. Krischok, G. Ecke, V. Cimalla, M. Himmerlich, T. Stauden, D. Cengher, and O. Ambacher, *J. Appl. Phys.* 98 (2005) 093508.
- [7] V. Lebedev, V. Cimalla, U. Kaiser, Ch. Foerster, J. Pezoldt, J. Biskupek, and O. Ambacher, *J. Appl. Phys.* 97, (2005) 114306.

Origin of N-Type Doping in InN

V. Cimalla^{1,*}, V. Lebedev¹, F. M. Morales¹, R. Goldhahn², and O. Ambacher¹

¹ Department of Nanotechnology

² Department of Experimental Physics I

Introduction

Indium Nitride is a low band-gap material, which received an increasing attention over the last years due to its very prospective properties. In particular, the high electron mobility [1] should predestine the material for high frequency devices. A major drawback, however, is the high electron concentration in InN layers, which up to date prevents the development of any kind of electronic device. Despite of the remarkable progress in the growth of InN by different techniques (plasma-induced molecular-beam epitaxy, MBE and metalorganic chemical vapour deposition) all layers appear to be degenerated with electron concentrations higher than 10^{17} cm^{-3} and the exact mechanisms of its origin are still under debate. Several n-type doping mechanisms were identified for InN (see Tab. 1); however, no single mechanism can explain the observed dependence of the electron concentration on the layer thickness for a series of InN films grown at similar growth conditions [2]. The possible contributions to the apparent electron

concentration can be classified by three models (i) a localized electron accumulation with specific sheet carrier concentration $N_{s,0}$, (ii) a homogeneous background volume concentration n_b , and (iii) an inhomogeneous carrier distribution n_{inhom} over the InN film. Consequently, the net electron density in dependence on the InN film thickness th will be:

$$n = \frac{1}{th} N_{s,0} + n_b + \frac{1}{th} \int_0^{th} n_{inhom} dz \quad (1)$$

The aim of this work is to evaluate the influence of the different doping mechanism in dependence of the layer thickness for MBE-grown InN films and to demonstrate the importance of threading dislocations (TD).

Experimental

The InN layers were grown [9] in a BALZERS MBE system using conventional effusion cells for In, Ga, and Al and a rf nitrogen plasma source. All InN epi-layers were grown on AlN buffer layers on sapphire at a substrate temperature of $\sim 380^\circ\text{C}$ under stoichiometric (1:1) conditions to prevent surface metal accumulation. The thickness of the InN layer has been varied from 0.17 to 2.2 μm . The electron concentration was determined by Hall measurements in van der Pauw geometry. Microstructural analysis was performed by transmission electron microscopy (TEM) with an accelerating voltage of 200 kV. The TD density was estimated by a digital imaging processing of cross sectional TEM micrographs and confirmed by the analysis of a series of plan view TEM micrographs taken at samples with different InN film thickness [9]. The resulting TD density in dependence on the distance to the interface to the AlN buffer layer is shown in figure 1.

Results and Discussion

The apparent carrier concentration is decreasing with increasing film thickness similar to the most extensive studied series of InN films available in the literature, which was taken as reference [2, 3], which implies the same underlying doping mechanism. Moreover, for thicker layers the determined TD density shows a good agreement with previous TEM studies [10],

Sample	Location	Origin	$N_{s,0}[\text{cm}^{-2}]$	$n[\text{cm}^{-3}]$	Technique	Ref.
InN	surface		1.57×10^{13}		C-V	3
InN/AlN	surf/interf		4.3×10^{13}		Hall, extrapolated	3
InN/GaN	surf/interf		2.5×10^{13}		Hall, extrapolated	3
InN	bulk			1×10^{17}	variable field Hall	4
InN/AlN	surface	intrinsic	2.5×10^{13}		HREELS	5
InN/GaN	surface	intrinsic	2.4×10^{13}		HREELS	5
InN/AlN	interface	defects	1.9×10^{13}		extrapolated	5
InN/GaN	interface	defects	$< 0.5 \times 10^{13}$		extrapolated	5
InN/GaN, AlN	surface	oxygen	2.2×10^{13}		depth profiling	6
InN/GaN,	bulk			4.5×10^{17}	depth profiling	6
InN/GaN	interface	defects	0.5×10^{13}		depth profiling	6
InN/AlN	interface	polarization	0.5×10^{13}		calculated	7
InN/GaN	interface	polarization			calculated	7
InN	bulk	hydrogen				8
InN	bulk	dislocations			TEM	9

Tab. 1: Summary of the published n-type doping mechanism in InN.

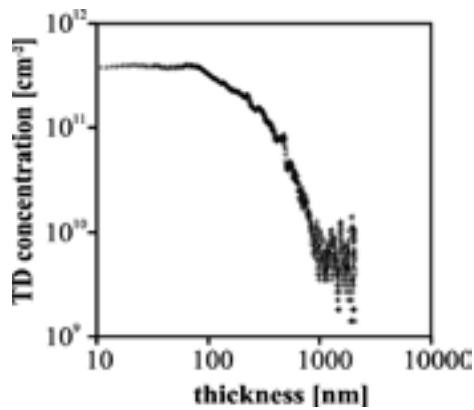


Fig. 1: Density of threading dislocations in a 2.2 μm thick InN in dependence on the distance to the AlN-InN inter-face.

where a TD density of $2.2 \times 10^{10} \text{ cm}^{-3}$ was estimated for 760 nm InN layers grown on a GaN/AlN buffer. Lu et al. [3] observed a strong reduction of the electron concentration with increasing film thickness and concluded a high accumulation at the surface of the InN layers. This surface accumulation was discussed as an intrinsic property of InN due to the extraordinary low conduction band minimum at the Γ -point [5], which allows donortype surface states to be located inside the conduction band. As a consequence, on clean InN surfaces a surface Fermi level of about 0.9 eV above the conduction band minimum was estimated. Recently we found a very similar behaviour on air-exposed InN surfaces by *in situ* measurements of the resistance of an InN film during sputter depth profiling [6], and a very good agreement between oxygen and electron concentration close to the surface by Auger electron spectroscopy (AES).

However, figure 2 clearly demonstrates that the data cannot be fitted with a linear law $n = N_{s,0}/th$ as expected for a dominant influence of the surface accumulation ("surface"). Also, homogeneous background doping estimated by variable field Hall [4] cannot explain the slope in figure 2 ("surface+background"). On the other side, the density of dislocations in heteroepitaxial layers is typically monotonically decreasing with the layer thickness.

For quantification it is assumed that each dislocation creates donors with a specific distance in the growth direction. Using the concentration profile of figure 1, its influence is shown in figure 2 for the TD's only ("TD") and for the sum of all the discussed effects ("sum"). A very good agreement with the measured data is achieved if the distance in growth direction is about 1.14 nm, i.e. if in a TD only every second InN unit cell bears an effective donor or only 50% of the dislocations are active.

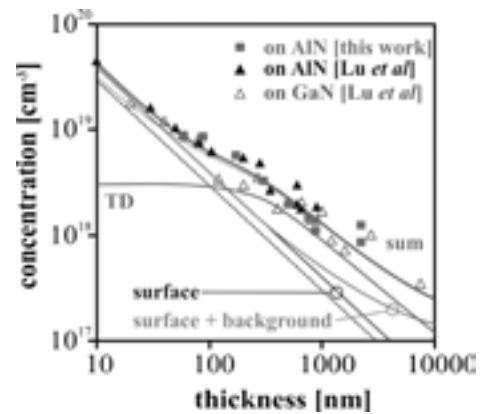


Fig. 2: Average electron carrier concentration in dependence on the InN film thickness, "surface" means the influence of a localized sheet carrier density of $4.3 \times 10^{13} \text{ cm}^{-2}$ at the surface, "background" the influence of a fixed bulk concentration of $1 \times 10^{17} \text{ cm}^{-3}$, "TD" the contribution of threading dislocations, and "sum" the addition of all effects. Dashed lines represent InN on GaN/AlN buffer. For comparison, the data of Lu and Schaff [2, 3] are shown as filled and open triangles for InN on AlN and GaN/AlN buffers, respectively.

In conclusion, for state-of-the-art MBE grown InN three major mechanisms determine the apparent electron concentration on different thickness scales. First, the accumulation of electrons at the surface and the interface clearly dominates the electronic properties of InN for thin layers with $th < 300 \text{ nm}$. For non-degenerate InN an electron concentration below 10^{17} cm^{-3} would be necessary and already the accumulation layers would prevent to achieve this for InN films up to $\sim 5 \mu\text{m}$. Second, layers in the micron range are strongly affected by threading dislocations. Finally, the background concentration of InN is already well controlled and would influence the apparent carrier concentration only for films with $th > 10 \mu\text{m}$. As a consequence, for an application of InN films for electronic devices both, the reduction in density of threading dislocations and the suppression of the electron accumulation at the interfaces is of crucial importance.

This work was supported by the Thuringian ministry of culture (TKM) and the European Union (B509-04011, EFRE program: B 678-03001, 6th framework program: GaNano NMP4-CT2003-505614).

- [1] V. M. Polyakov and F. Schwierz, Appl. Phys. Lett. 88, 032101 (2006).
- [2] H. Lu, W.J. Schaff, L.F. Eastman, J. Wu, W. Walukiewicz, D.C. Look, and R.J. Molnar, MRS Symp. Proc. 743, L4.10 (2003).
- [3] H. Lu, W.J. Schaff, L.F. Eastman, and C.E. Stutz, Appl. Phys. Lett. 82, 1736 (2003).
- [4] C.H. Swartz, et al., J. Cryst. Growth 269, 29 (2004).
- [5] T.D. Veal, L.F.J. Piper, I. Mahboob, H. Lu, W.J. Schaff, and C.F. McConville, phys. stat. sol. (c) 2, 2246 (2005).
- [6] V. Cimalla, G. Ecke, M. Niebelschütz, O. Ambacher, R. Goldhahn, H. Lu, and W.J. Schaff, phys. stat. sol. (c) 2, 2254 (2005).
- [7] V. Cimalla, Ch. Förster, G. Kittler, I. Cimalla, R. Kosiba, G. Ecke, O. Ambacher, R. Goldhahn, S. Shokhovets, A. Georgakilas, H. Lu, and W.J. Schaff, phys. stat. sol. (c) 0, 2818 (2003).
- [8] E.A. Davis, S.F.J. Cox, R.L. Lichti, and C.G. van der Walle, Appl. Phys. Lett. 82, 592 (2003).
- [9] V. Lebedev, V. Cimalla, T. Baumann, P. Morales, and O. Ambacher, J. Appl. Phys., submitted.
- [10] C.J. Lu, L.A. Bendersky, H. Lu, and W.J. Schaff, Appl. Phys. Lett. 83, 2817 (2003).

Transition energies and bowing parameters for In-rich InGaN and InAlN alloys

R. Goldhahn^{1,*}, P. Schley¹, A.T. Winzer², C. Buchheim^{1,2}, H. Lu³, and W.J. Schaff³

¹ Department of Experimental Physics I

² Department of Nanotechnology

³ Department of Cornell University Ithaca, NY, USA

Growth and characterization of In-rich InGaN alloys have attracted much interest recently. It arises from the band gap correction for InN from the long time accepted value of 1.9 eV down to only about 0.7 eV. Due to the reduced band gap a renewed evaluation of many material parameters of InN and their compositional dependence for (In,Ga)N and (In,Al)N alloys is mandatory. For this aim, determination of the dielectric function (DF) by spectroscopic ellipsometry (SE) has become one of the most powerful methods for studying absorption related properties of In-compounds both around the band gap as well as in the range of the high-energy critical points (CP) of the band structure [1-3]. For example, the experimentally determined shape of the DF and the optical anisotropy of InN [1] has been theoretically reproduced recently [4]. Here, we report ordinary DF's up to 9.5 eV for In-rich InGaN and InAlN alloys and their analysis, i.e. transition energies for the CP's and their compositional dependences (bowing parameter). The latter data were determined by fitting the third derivatives of the DF.

The DF's of three $\text{In}_x\text{Ga}_{1-x}\text{N}$ films ($x=0.67$, $x=0.69$, $x=0.77$) with ~ 300 nm thickness and three $\text{In}_x\text{Al}_{1-x}\text{N}$ films ($x=0.91$, $x=0.83$, $x=0.71$) with ~ 400 nm thickness were determined. Samples were grown on (0001) sapphire by plasma-induced molecular beam epitaxy (MBE) using either GaN or AlN buffer layer. Further growth details as well as results of the structural, electrical and optical characterization have been published elsewhere [2,5].

Figure 1 shows the imaginary part of the DF's for the InGaN (a) and InAlN (b) alloys and in comparison to the data of InN over the whole investigated range from 0.74 eV up to 9.5 eV. Due to the c-axis orientation normal to the surface, these data correspond to the ordinary dielectric tensor component [3]. The data above 4 eV were obtained from the BESSY ellipsometer at the 3m-NIM-monochromator, the excellent matching to the data recorded with a commercial ellipsometer (J.A. Woollam Co., Inc.) in the energy range from 0.74 up to 4.5 eV should be noted. Beside the gap structure in the low-energy range, the shape of the ordinary tensor component is strongly influenced by contributions arising from at least five critical points of the band structure in the energy range above 4.5 eV.

All of them are clearly resolved for the alloys despite a larger broadening compared to InN. It confirms the good crystalline quality of the InGaN and InAlN films. As expected for an alloy system, they undergo a continuous shift to higher energies with increasing Ga(Al)-content.

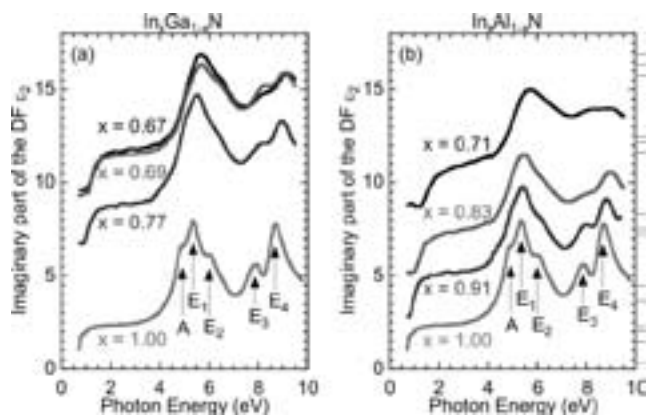


Fig. 1: Imaginary parts of the DF of $\text{In}_x\text{Ga}_{1-x}\text{N}$ (a) and $\text{In}_x\text{Al}_{1-x}\text{N}$ (b) alloys obtained from fitting ellipsometric data Ψ and Δ . The alloy data are vertically shifted for sake of clarity according to the Indium content.

Following accurate approach was used for a determination of the transition energies of the critical points in high resolution. One calculate the third derivative of the point-by-point obtained DF (after surface roughness correction) multiplied by the square of the photon energy E . The resulting spectra can be fitted [6] via

$$\frac{d^3}{dE^3} (E^2\epsilon) = \sum_{j=1}^5 e^{i\phi_j} \cdot \frac{C_j}{(E + i\Gamma_j - E_j)^{n/2}}$$

where ϕ_j , C_j , Γ_j , and E_j denote the phase angle, the magnitude, the broadening energy, and the transition energy of the j -th CP, respectively. With $n=6$ corresponding to a two-dimensional critical point, we obtain excellent agreement to the experimental data which is exemplarily demonstrated for $\text{In}_{0.77}\text{Ga}_{0.23}\text{N}$ and $\text{In}_{0.91}\text{Al}_{0.09}\text{N}$ in Fig. 2(a) and (b), respectively.

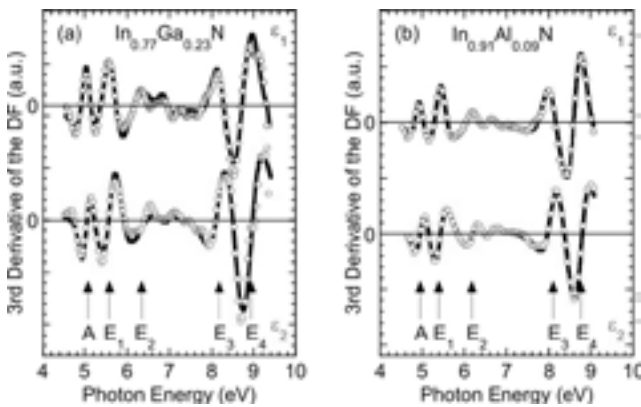


Fig. 2: Fit of the third derivative of the DF for the $In_{0.77}Ga_{0.23}N$ (a) and the $In_{0.91}Al_{0.09}N$ (b) sample. The circles represent the experimental data, and solid lines are the best fit. The transition energies of the critical points are marked by arrows.

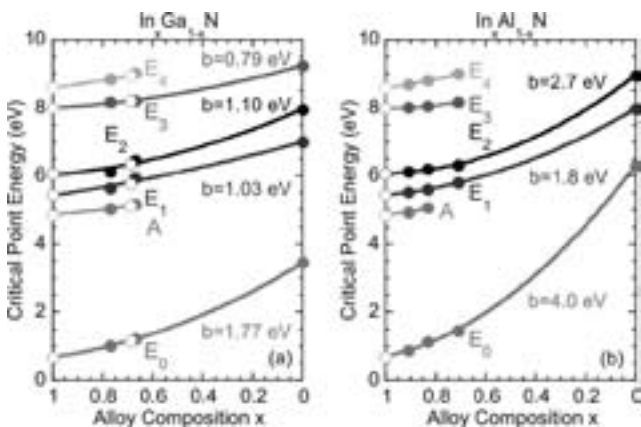


Figure 3(a) displays all fitted critical point energies for $InGa$ alloys. They amount for InN : 4.86 eV (E_A), 5.37 eV (E_1), 6.14 eV (E_2), 7.99 eV (E_3), and 8.59 eV (E_4). With the values for GaN of 7.00 eV (E_1), 7.96 eV (E_2), 9.25 eV (E_3) bowing parameters of $b=1.03$ eV (E_1), 1.10 eV (E_2), and 0.79 eV (E_3) are obtained. For the determination of the band gap values, carrier induced band gap renormalization and Burstein-Moss shift was taken into account [2]. Taking the values for InN of $E_0=0.68$

eV [2] and for GaN of $E_0=3.45$ eV the fit yields $b=1.77$ eV for the fundamental band gap bowing, which is in good agreement with the previously published value of 1.43 eV [7]. Figure 3(b) evinces the results for $InAlN$ alloys. With the values for AlN of 6.30 eV (E_0), 7.97 eV (E_1) and 8.95 eV (E_2) bowing parameters of $b=4.0$ eV (E_0), 1.8 eV (E_1) and 2.7 eV (E_2) are obtained. No estimations can be made for the other critical points due to the lack of corresponding data for AlN .

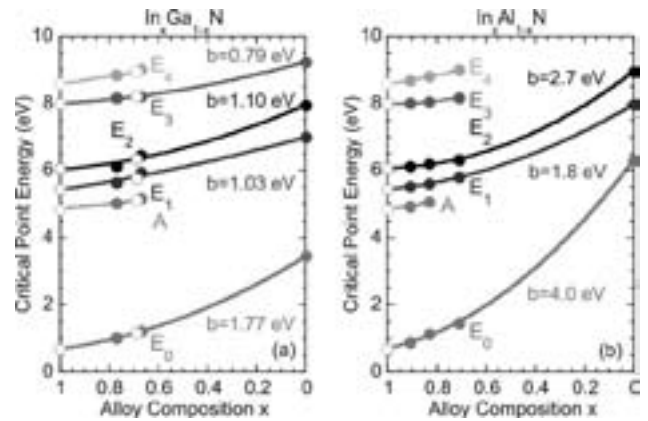


Fig. 3: Resulting critical point energies of $InGa$ (a) and $InAlN$ (b) alloys as a function of composition. The open and full circles refer to the samples grown on GaN buffer and on AlN buffer, respectively. The solid lines represent the fit results.

In summary, we have determined the DF's of $InGa$ and $InAlN$ alloys in the energy range from 0.74 eV up to 9.5 eV. Applying a third derivative based DF line shape fitting procedure yields the transition energies in the range of the critical points of the band structure with highest resolution. From the transition energies the bowing parameters for the compositional dependence of four and three critical points for $InGa$ and $InAlN$ alloys, respectively, are derived.

The work at BESSY was supported by the BMBF grants 05KS4KTb/3 and 05ES3XBA/5. R.G. and the Ilmenau group acknowledge support by the DFG (GO 1378/2,3) and by Thüringer Ministerium für Wirtschaft, Technologie und Arbeit (B509-04011), respectively. The Cornell group is supported by ONR(N000149910936).

[1] R. Goldhahn, A.T. Winzer, V. Cimalla, O. Ambacher, C. Cobet, W. Richter, N. Esser, J. Furthmüller, F. Bechstedt, H. Lu, and W.J. Schaff, *Superl.&Microstruc.* **36**, 591 (2004).
 [2] R. Goldhahn, P. Schley, A.T. Winzer, G. Gobsch, V. Cimalla, O. Ambacher, M. Rakel, C. Cobet, N. Esser, H. Lu, and W.J. Schaff, *phys. stat. sol. (a)* **203**, 42 (2006).
 [3] R. Goldhahn, P. Schley, A.T. Winzer, M. Rakel, C. Cobet, N. Esser, H. Lu, and W.J. Schaff, *J. Cryst. Growth* **288**, 273 (2006).
 [4] J. Furthmüller, P.H. Hahn, F. Fuchs, and F. Bechstedt, *Phys. Rev B* **72**, 205106 (2005).
 [5] P. Schley, R. Goldhahn, A.T. Winzer, G. Gobsch, V. Cimalla, O. Ambacher, M. Rakel, C. Cobet, N. Esser, H. Lu, and W.J. Schaff, *phys. stat. sol. (b)* (in press).
 [6] D.E. Aspnes, *Phys. Rev. Lett.* **28**, 168 (1972); D.E. Aspnes and J.E. Rowe, *Phys. Rev. B* **5**, 4022 (1972).
 [7] J. Wu, W. Walukiewicz, K.M. Yu, J.W. Ager III, E.E. Haller, H. Lu, and W.J. Schaff, *Appl. Phys. Lett.* **80**, 4741 (2002).

Modelling of SiC Antidot Ordering

A. A. Schmidt¹, Yu. V. Trushin¹, K. L. Safonov², V. S. Kharlamov¹, D. V. Kulikov¹, and J. Pezoldt^{3,*}

¹ A. F. Ioffe Physical-Technical Institute, St. Petersburg, Russia

² St. Petersburg State Polytechnical University, St. Petersburg, Russia

³ Department of Nanotechnology

Introduction

Semiconductor industry nowadays requires new materials improving the performance of silicon-based devices. The growth of silicon carbide on silicon allows to combine the potential of SiC as a material for high-temperature, high-frequency and high-power applications with the well-developed silicon technology. Recently a number of molecular beam epitaxial growth techniques for the epitaxy of SiC on Si have been reported. Although molecular beam epitaxy allows the effective formation of new nano-sized structures, further development of this method is hampered by the lack of physical understanding of various processes which take place during the silicon carbon interaction during carbonization, i.e.: deposition of carbon atoms, diffusion of both Si and C and nucleation of two-dimensional and three-dimensional SiC clusters. A purely theoretical investigation of the problem is not possible – not only because of the complexity of the processes, but also due to the fact that most of them have considerable differences in time and spatial scales. For a deeper understanding of the transformation process of silicon into silicon carbide under molecular beam epitaxy conditions a computer simulation should be applied. Since the above-mentioned basic processes have notably different time and spatial scales, it is not possible to describe all of them in the framework of a single model. This is why a complex of different simulation methods is required. Three numerical methods were used, namely: Molecular Dynamics (MD), kinetic Monte Carlo (KMC), and the Rate Equations (RE).

MD method was used for the estimation of the kinetic parameters of atoms at the surface, which are input parameters for other simulation methods. KMC allowed the atom scale simulation of cluster formation, which is the initial stage of the SiC growth. The RE method gave an opportunity to study the growth through longer time periods. In such a way all stages of the nanostructure formation could be investigated.

Molecular dynamics

MD simulation technique is a numerical solution of a system of coupled equations of motion for atoms. The interaction forces are derived from the interatomic potential. In the present work a manybody Tersoff potential for the Si-C system was

used. This potential was constructed to reproduce material properties such as lattice distance, cohesive energy, bond length, elastic constants, etc. Velocity Verlet method with a variable time step was used for integration of the Newton's equations of motion, linked cells algorithm combined with Verlet spheres for fast neighbour search and effective force field calculation algorithm for Tersoff-like potential.

We used model crystal cells (boxes) containing up to 2.5×10^4 atoms. To study surface effects periodic boundary conditions in two lateral (x- and y-) directions were applied. In z-direction two surfaces were kept free. To set up the desired equilibrium temperature T in the simulation cell a thermalization procedure (and a quick quenching method to reach $T=0\text{K}$) was implemented.

Kinetic Monte Carlo

KMC method was implemented to study the transition from nucleation of two-dimensional clusters to three-dimensional growth, depending on the experimental conditions and the growth stage. Fixed lattice approximation was used, i.e. silicon and carbon atoms were allowed to occupy fixed sites of the diamond lattice and jump to nearby empty sites (only short-range jumps to the first, second and third coordination spheres were taken into account). The hop probability for each atom depends on its environment. Alongside with the diffusion, the deposition events take place according to the carbon atom flux. The influence of elastic stress was taken into account by the model suggested in [1].

For further details see [2].

Monte Carlo simulations allowed us to investigate basic processes leading to the transition from 2D nucleation to 3D cluster growth and to validate the energy barriers values obtained in MD and the physical model used in the RE simulations.

Rate equation

To study cluster evolution on a long time scale (up to tens of minutes) RE method was implemented. At first it was tested in case of two-dimensional cluster nucleation at low temperatures. Good agreement both with experimental data and theoretical predictions was obtained [5]. The influence of strain on cluster growth was included in the model as well: elastic stress energy near the cluster is determined by its shape and size and correspondingly lowers the

*phone: +49-(0)3677-69-3412, e-mail: joerg.pezoldt@tu-ilmnau.de

energy barrier for C and Si particles to jump up to the top layers. In accordance with available experimental AFM data [6], SiC clusters were assumed to have conical shape, and so they were treated by base radius and height distribution functions. Further details of the physical RE model where [10-12]. According to the suggested model the time evolution of the particles concentrations and clusters size distribution function was simulated.

Modelling results

As far as the developed Monte Carlo model proved itself to be efficient to study three-dimensional growth of SiC on Si, it was used to study effects of the substrate morphology on the process of clusters nucleation and self-ordering. There are experimental evidences that on metal surfaces in the presence of terraces clusters tend to nucleate at the terraces edges [3]. If the mean terrace width is about the mean distance between clusters, they will nucleate *only* at the edges, so self-organizing in chains. Recently the same process was observed in the SiC/Si system [4].

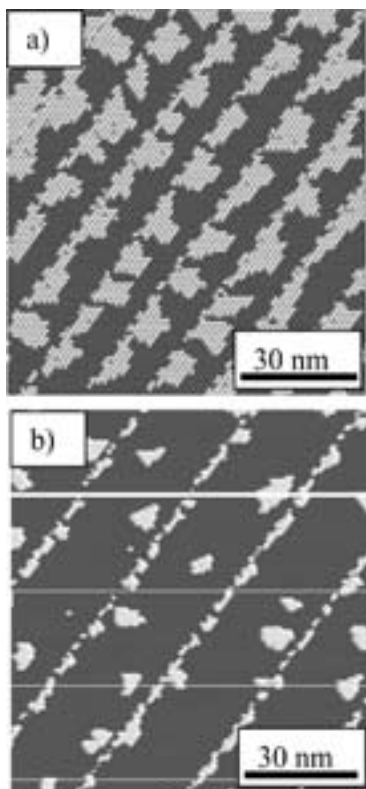


Fig. 1: Nucleation of clusters in the presence of terraces on the substrate:
 (a) terrace width corresponds to the mean distance between clusters and they can only nucleate at the terraces edges and self-order in chains;
 (b) terrace width is greater then the mean distance between clusters they nucleate randomly, no self-ordering is observed.

The effect of terraces was studied by KMC method using the energy barriers for diffusion at the free Si-(100) and Si-(111) surfaces determined by MD.

To study the influence of the elastic strain caused by the lattice mismatch between Si and SiC on the surface diffusion of adatoms, simulation of small SiC clusters formed on Si substrates was performed. The strain decreases from the substrate layers just below the cluster into the depth and from the cluster center towards the periphery. The diffusion of Si and C atoms in the vicinity of the cluster is strongly affected by the strain fields.

The KMC simulation of the nucleation ordering consists in two steps. First at a given carbon flux F and substrate temperature T the mean distance between clusters was estimated. Then two simulations were performed: growth on a substrate with terrace width w about two times greater than l , and growth on a substrate with .

The results of the simulation for a flux $F=5.5 \times 10^{13} \text{ cm}^{-2}\text{sec}^{-1}$ and substrate temperature $T=660^\circ\text{C}$ are shown in figure 1. The mean distance between clusters was determined to be 12 nm (lattice constants). In case of $w=13.5 \text{ nm}$ clusters nucleate only at the edges and there is self-ordering (see Fig. 1a), while in case of $w=32.5 \text{ nm}$ no evidence of self-ordering is found (see Fig. 1b).

Conclusion

A simulation program complex, capable to study MBE growth of SiC on Si at diverse time and spatial scales was developed. The results obtained by the implementation of this complex are in good agreement with experimental data and allow to predict parameters of the grown structures and so contribute to the improvement of MBE growth technology. Moreover, with the help of this complex it is also possible to study other heterostructure materials with lattice mismatch (i.e. SiGe/Si, InGaN/GaN etc.)

The work was supported by Russian Foundation for Basic Research grant 05-02-16679, Federal program for support of scientific schools 2160.2003.2 and scientific program of SPb Scientific Centre RAS. A.A.S. is also grateful to "Dynasty" non-profit foundation.

- [1] E. Schoell and S. Bose: Solid-State. Electronics, 42 (1998) 1587.
- [2] A.A. Schmidt, V.S. Kharlamov, K.L. Safonov, Yu.V. Trushin, E.E. Zhurkin, V. Cimalla, O. Ambacher and J. Pezoldt: Comp. Mater. Sci., 33 (2005) 375.
- [3] K.L. Safonov, D.V. Kulikov, Yu.V. Trushin and J. Pezoldt, Proc. of SPIE, 4627 (2002) 165.
- [4] K.L. Safonov, Yu.V. Trushin and J. Pezoldt: In: Modern Problems of Nuclear Physics and Physics and Chemistry of condensed Matter, Eds. A.L. Suvorov, F.S. Dzheparov, M.A. Kozodaev, S.V. Stepanov, Akademprint, 2004, pp. 173-175.
- [5] H. Brune, M. Giovannini, K. Bromann and K. Kern: Nature, 394 (1998) 451.
- [6] V. Cimalla, A.A. Schmidt, Th. Stauden, K. Zekentes, O. Ambacher, J. Pezoldt, J. Vac. Sci. Technol. B, 22 (2004) L20.

Electrical Properties of Low Temperature Cofired Ceramics with Integrated Bulk Metals

M. Hintz^{1,*}, H. Thust¹, K. H. Drüe¹, H. Bartsch de Torres², and M. Kallenbach²

¹ Department of Microperipherals

² Department of Micromechanical Systems

Introduction

Low Temperature Cofired Ceramics (LTCC) technology is a well established technique to realise multilayer circuits. It allows the integration of passive components like conductors, resistors, capacitors and inductors into the circuit carrier.

Typically, screen printing is used to apply the passive structures on unfired ceramic foils. Certainly the requirements on the features of multilayer circuits are becoming more demanding. For the needs of the future, further miniaturisation and better electrical behaviour are necessary.

Zero-shrinkage techniques for LTCC, especially the technology of Pressure Assisted Sintering (PAS), prevent the substrate from shrinking in x/y-direction during sintering and allow the use of new materials for buried structures.

Motivation

Today screen printing technology is the most used technique to realise cofired structures. Advantages of this technique are small costs and simple processibility. Unfavourable is the electrical and geometrical behaviour of printed structures.

Screen printed conductors base on paste materials. The paste contains metal particles and sometimes an additional amount of glass. This limits the conductivity after sintering (Fig. 1).

Material	Sheet resistance [mOhm/□] / thickness	Specific conductivity[m/(Ohm*mm ²)]
Silver paste DuPont L737	3.7 at 8 μm	33.8
Silver paste DuPont 6453 [1]	2.2 at 10 μm	45.5
Silver bulk metal		61.3
Gold paste DuPont 5717 [1]	5.0 at 6 μm	33.3
Gold paste Heraeus C5007 [2]	6 at 8 μm	20.8
Gold bulk metal		45.5

Fig. 1: Conductivity of pastes and bulk metals.

Furthermore, the resolution and accuracy of edges is restricted. The aim of these investigations was to improve the properties of integrated structures in LTCC multilayers.

The cofired integration of bulk metallic materials could help to overcome the limits of pastes in the following fields:

- electrical and thermal conductivity
- resolution and geometrical behaviour (edge quality)

Technology

Metallic pastes shrink during sintering. Normally the shrinkage of conductors and ceramic should be comparable, to prevent cracks and warping.

Bulk metallic conductors show no shrinkage during firing. That is why a zero shrinkage process is necessary for the cofired integration of such structures.

Combined with 0-shrinkage technologies it is possible to use the higher conductivity and accuracy of such structures.

Pressure assisted sintering (PAS) is such a kind of process. Release tapes on the outsides of the LTCC laminate, combined with an uniaxial pressure during sintering eliminate the lateral shrinkage.

However a difficulty of integration of bulk metals is to apply the metallic structures on the sensitive unfired ceramic foils. Different technologies were determined to solve this problem.

The utilization of a temporary carrier is suitable for the structuring of bulk metallic lines by electroplating.

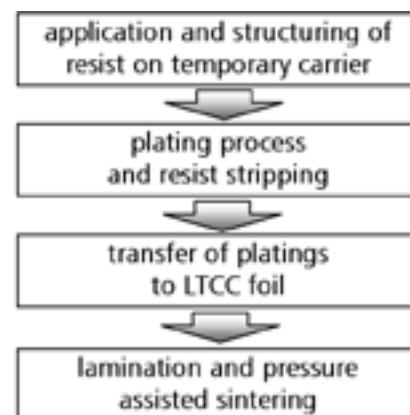


Fig. 2: Integration of electroplated structures in LTCC.

With this process (Fig. 2), higher resolutions and aspect ratios are possible (Fig. 3). A gold plating process was used on a temporary metallic carrier. After the process the structures were transferred to the LTCC foil.

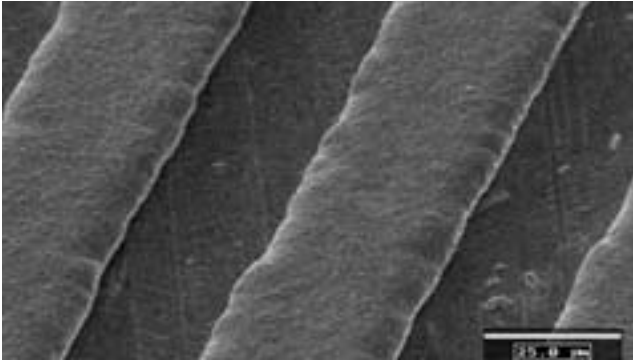


Fig. 3: Electroplated gold lines (30μm) on temporary carrier.

Electrical Behaviour

Inductor coils as typical passive elements were chosen to determine the electrical properties of buried bulk metals. Different LTCC multilayer test structures with integrated coils were manufactured and measured using an L-C-R-meter.

The bulk metallic structures were produced by electroplating of gold. Prints of gold paste were used to make comparisons. The connection of the buried elements with the substrate surface was realized by paste filled vias. PAS was used to sinter all substrates. The fired thickness was 0.9 mm.

The sheet resistivity of the bulk metallic lines was obviously lower than those of paste prints. Higher sheet resistivity leads to higher resistance of the inductors. The resistance of coils in dependence of the line width is shown in figure 4.

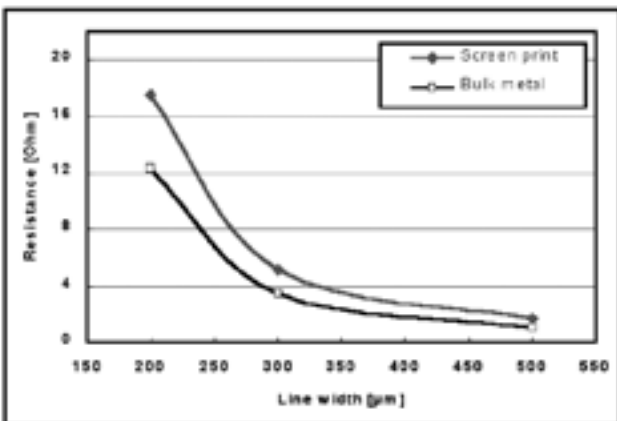


Fig. 4: Resistance of different inductors (10 mm x10 mm)

Reasons are higher specific conductivity of the material and better accuracy of the edges. Especially the resistance of small printed lines is influenced by deformation in the area of edges.

Smaller lines allow a higher number of windings and a higher inductivity at the same area. Often the increasing resistance limits the miniaturization of inductors. In this case bulk metals could be an alternative.

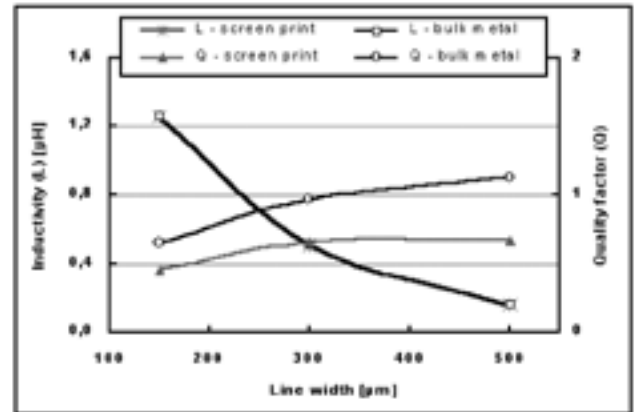


Fig. 5: Inductivity (L) and quality factor (Q; f = 1MHz) of different inductors (area 10 mm x 10 mm).

The conductivity and the quality factor of the inductors were improved (Fig. 5). As expected, the inductivity was scarcely influenced by the conductor type.

Conclusions

The introduced new technology for buried conductors in LTCC can improve the electrical behaviour of circuits for low as well as high frequency applications. The combination of bulk materials with typical paste systems is possible.

Higher conductivity and possible thickness of bulk metallic lines are advantageous, especially for integrated high power circuits. Buried inductors have shown the potential for resistance reduction. Prospectively lower losses and higher thermal conductivity in combination with a higher possible line resolution allow further miniaturization of ceramic multilayers.

This work has been supported by the BMBF (project: "MIKROFUN").

[1] DuPont, "Green Tape® material system", Produkt Information Sheet DuPont United Kingdom Ltd., 1996 - 2006.
 [2] Heraeus, "Low Temperature Cofireable Heratape", Development Product Information Sheet, W.C. Heraeus GmbH, Hanau, 2005.

Temperature dependence of interlayer coupling

S. Schwieger^{1,*}, E. Runge¹, J. Kienert², W. Nolting², J. Lindner³, and K. Baberschke³

¹ Department of Theoretical Physics I

² Institut of Physics, Humboldt University, Berlin

³ Department of Physics, Freie Universität Berlin

Following the discovery of the Giant Magnetoresistance effect, metallic ultrathin multilayer systems have received considerable attention. The interest is driven by the possible technological use of special film designs based on sequences of magnetic and nonmagnetic ultrathin layers. The useful magnetic properties of these systems result from the interlayer exchange coupling (IEC): Two magnetic layers (as e.g. Fe, Co or Ni) which are separated by a nonmagnetic spacer layer (as e.g. Cu) are coupled ferro- or anti-ferromagnetically depending on the spacer layer thickness. The coupling is caused by electrons in the spacer layer which are reflected at the spacer/magnet interfaces with spindependent intensities.

The IEC can be used to build small and sensitive magnetic field sensors (which can be used, e.g., in reading heads) due to following two properties: First the coupling energy of the IEC (μeV or smaller) is comparable to magnetic field energies. Therefore the configuration of an anti-ferromagnetically coupled film can be switched from antiparallel to parallel by the external magnetic field. Secondly the transversal resistance is much larger for antiferromagnetic films than for ferromagnetic ones. This allows for an easy detection of these magnetic configurations. A sketch of a prototype IEC-system is shown in Fig. 1.

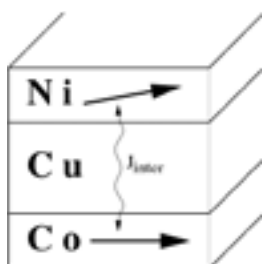


Fig.1 Sketch of a typical IEC film-system. The magnetization of the ferromagnetic layers (here Co and Ni) are coupled through the non-magnetic spacer (here Cu)

In the past, much work focused on the oscillating dependence of the IEC on the spacer thickness [1], but also on interface quality or spacer doping. Our activities concern the temperature dependence of the IEC and combine experiment and theory in order to clarify the source of the well-known reduction of the coupling energy with increasing temperature. There are three sources of the temperature dependence of IEC:

(i) the softening of the spacer Fermi surface [2], (ii) the reduction of the spin asymmetry of the reflection coefficients at the spacer/magnet interfaces, and (iii) thermally excited spin waves in the magnetic layers[3]. We propose a theory which can separate the T -dependence due to the spacer effects (i) and (ii) on the one hand and due to the magnetic layer effect (iii) on the other. The theory is applied to ferromagnetic resonance (FMR) experiments [4] on the prototype IEC system $\text{Ni}_7/\text{Cu}_9/\text{Co}_2/\text{Cu}(001)$ (subscripts: number of monolayers) performed at different temperatures. The IEC is described by a fit parameter termed J_i . This parameter is not the free coupling energy, but defined in a way that a possible temperature dependence of J_i is solely due to the spacer effects. However, when the calculations are performed with artificially switched off spin-waves, the temperature dependence of the fit parameter J_i is caused by spacer and magnonic effects. Thus comparing fits with switched on and switched off spin-waves allows for a separation of the magnonic effect (iii).

The Hamiltonian we use to describe the film system reads:

$$\begin{aligned}
 H = & - \sum_{\langle ij \rangle \alpha} J_{\alpha} \mathbf{S}_{i\alpha} \mathbf{S}_{j\alpha} - \sum_{i\alpha} g_{J\alpha} \mu_B \mathbf{B}_0 \mathbf{S}_{i\alpha} - \\
 & - \sum_{\langle ij \rangle \alpha \beta} J_I \mathbf{S}_{i\alpha} \mathbf{S}_{j\beta} - \sum_{i\alpha} K_{2\alpha} S_{i\alpha z}^2 + \\
 & + \sum_{lm} g_{0lm} \left(\frac{1}{r_{lm}^3} \mathbf{S}_l \mathbf{S}_m - \frac{3}{r_{lm}^5} (\mathbf{S}_l \mathbf{r}_{lm}) (\mathbf{S}_m \mathbf{r}_{lm}) \right)
 \end{aligned}$$

Greek indices α, β refer to layers, while the indices i, j denote sites within a layer. Further l, m are multiindices with $l, m = (i\alpha), (j\beta)$. The first term describes nearest-neighbor Heisenberg coupling J_{α} between spins within the same magnetic layer. The magnetic layers are described by atomic monolayers. Higher thicknesses are absorbed into J_{α} which are used to realize the Curie temperatures of the single magnetic layers. The second term contains an external magnetic field \mathbf{B}_0 in arbitrary direction with the Lande factors $g_{J\alpha}$ and the Bohr magneton μ_B . The spacer layer is not considered explicitly. The interlayer exchange coupling mediated by the spacer is described by the (nearest neighbor) parameter J_I (third term). The

fourth and fifth term represent second order lattice anisotropy and dipolar interaction, the latter leading to shape anisotropy. $K_{2\alpha}$ and g_{0lm} are microscopic anisotropy parameters, S_{icz} is the z-component of $S_{i\alpha}$ which is perpendicular to the film plane and r_{lm} is the distance between the lattice sites l and m .

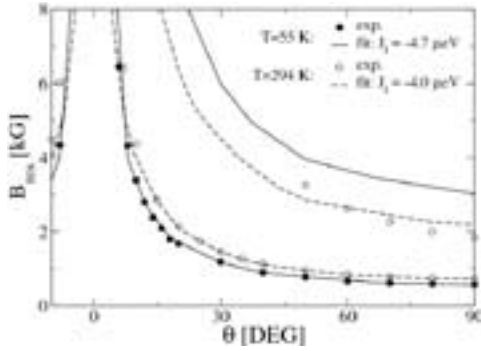


Fig.2: Resonance field B_{res} for $Ni_7/Cu_9/Co_2/Cu(001)$. The angle θ is measured with respect to the film normal. Parameters: Cobalt: $S=2.5$, $g_j=2.1$, $K_2=-20.25 \mu_B kG$, $g_0=1.95 \mu_B kG$, $J=4.1 meV$. Nickel: $S=1$, $gJ=2.1$, $K_2=3.0 \mu_B kG$, $g_0=4.5 \mu_B kG$, $J=30 meV$.

We summarize shortly our method to solve the Hamiltonian for the singlemagnon Green function (GF) $\langle\langle S_{i\alpha}^+; S_{j\beta}^- \rangle\rangle$ and refer the reader to Refs.[5] for de-tails. In order to treat the anisotropy terms properly we rotate the coordinate system self-consistently such that the new z axis is parallel to the direction of the magnetization. Higher order GFs stemming from the Heisenberg exchange and the dipole anisotropy are decoupled using the Tyablikov (RPA) method and the $K_{2\alpha}$ terms are treated in the Anderson-Callen approximation. By this approach the effects of thermally excited spinwaves are taken into account. For the desired comparison of fits with and without these spin waves, the latter can be switched off artificially. Formally, this is equivalent to a calculation at $T=0$.

The crucial quantity to connect experiment and theory is the (external) resonance field $B_{res}(T, \theta)$ at which a probing microwave (frequency ν_{hf}) excites uniform ($\mathbf{q}=0$)-spin-wave modes in the system. With our method it is possible to compute the spin wave frequencies $\nu_{sw}(\mathbf{q}, \mathbf{B}_0, T)$ and read off the resonance field given the (experimental) parameter ν_{hf} . The comparison of measured and calculated resonance fields is used to fit the parameter J_j . In the case of

switched off magnons, we will also use the term $J_j^{(0)}$ in the following.

Fig. 2 shows the resonance field as a function of the direction of the external magnetic field. There are two branches at a given T corresponding to acoustic (lower branch) and optical (upper branch) modes, respectively. The anisotropy parameters stem from fits of the single uncoupled films. Thus the fit parameter J_j is the only one for the *coupled* system. We carried out the fitting at a fixed angle $\theta=90^\circ$ for a variety of temperatures with switched on and switched off spin-waves. It turns out that J_j decreases with T in both cases indicating more contributions to the IEC temperature dependence than just magnon excitations

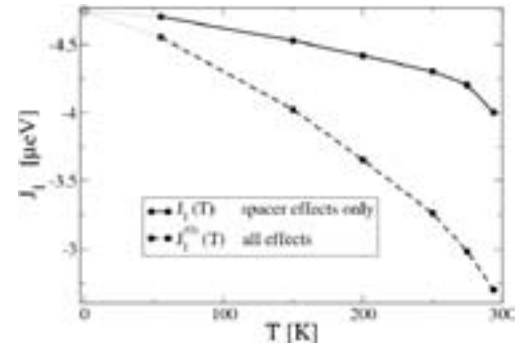


Fig.3.: Temperature dependence of interlayer exchange coupling in $Ni_7/Cu_9/Co_2/Cu(001)$. Symbols result from fitting the experimental resonance field at $\theta=90^\circ$ at the given temperatures. Circles: temperature-dependent calculation. Squares: calculation at $T=0$. Lines are guides to the eye.

(3). However the decrease of J_j is much stronger in the case of switched of magnons (Fig. 3). From Fig. 3, we can read off that the magnon contribution to the T -dependence of IEC prevails significantly. However given a ratio of about 1:3 of spacer vs. magnon effects the former cannot be neglected.

In summary, we fitted FMR experiments on the interlayer exchange coupling system $Ni_7/Cu_9/Co_2/Cu(001)$ using a microscopic theory based on an extended Heisenberg Hamiltonian in order to study the temperature dependence of IEC. The main result is that the magnonic part dominates the spacer part by a factor of about 3.

[1] J. Unguris, R. J. Celotta, and D. T. Pierce, Phys. Rev. Lett. 79 (1996), p. 2734.
 [2] P. Bruno, Phys. Rev. B. 52 (1995), p. 411.
 [3] N. S. Almeida, D. L. Mills, and M. Teitelman, Phys. Rev. Lett. 75 (1994), p. 733.
 [4] J. Lindner and K. Baberschke, J. Phys.: Condens. Matter 15 (2003), p. R193;
 J. Phys.: Condens. Matter 15 (2003), S465.
 [5] S. Schwieger, J. Kienert, and W. Nolting, Phys. Rev. B 71 (2005), p. 024428;
 Phys. Rev. B 71 (2005), p. 174441.

Surface properties of room temperature ionic liquids

S. Krischok^{1,*}, M. Himmerlich¹, P. Lorenz¹, M. Eremtchenko¹, Y. Liu¹, S.-I.-U. Ahmed¹, R. Ötting¹, W.J.D. Beenken², E. Runge², V. Kempter³, and J.A. Schaefer¹

¹ Department of Technical Physics

² Department of Theoretical Physics

³ Institute of Physics and Physical Technologies, Technical University Clausthal

Room temperature ionic liquids (RT-ILs) have attracted much attention for their unique properties. They show, e.g. a wide temperature range of liquid phase, a very low vapor pressure at RT, a high chemical stability, potential as "green" solvents, and high heat capacities. These properties make them good candidates for the use in many fields [1,2], such as thermal storage, electrochemical applications, homogeneous catalysis and dye-sensitized solar cells. In order to be able to refine the performance of RT-ILs, detailed knowledge of the geometric, electronic and vibronic structure of RT-ILs appears indispensable.

We combined experimental surface sensitive techniques with abinitiodensityfunctionaltheory(DFT)calculations for the cation-anion complex of 1-Ethyl-3-methylimidazolium bis(trifluoromethylsulfonyl)imide ([EMIM][Tf₂N]) as a model system [3,4]. This particular RT-IL is in addition a member of a class of ILs that can apparently be distilled at moderate temperatures and reduced pressure, although the distillation rates are low [5,6].

Thin films of [EMIM][Tf₂N] have been deposited on a polycrystalline Au substrate and introduced into an ultra-high vacuum chamber. By combining the extremely surface sensitive technique MIES (metastable induced electron spectroscopy) with UPS and XPS (ultra-violet and X-ray photoelectron spectroscopy) a wide range of depth resolution is covered. The absence of any substrate (Au) related spectral features in XPS (in Fig. 1 corresponding spectra for the C(1s) and N(1s) peak are shown) proves that a closed [EMIM][Tf₂N] film of more than 10 nm thickness was successfully prepared. As expected, F, N, O, S, and C are detected. No evidence of impurities by other elements could be found.

A calculation of the chemical composition leads to a F:O:N:C:S ratio of about 6:3.9:3.3:10.8:2.2 (close to the expected ratio of 6:4:3:8:2).

As expected N(1s) and the C(1s) peaks are split into several components due to chemical shifts (see Fig.1). Two well-separated N(1s) components with a relative peak area of 1:1.9 were observed. The larger peak at higher binding energy is assigned to N located at the [EMIM]⁺ cation ring. Due to the presence of C in various chemical environments, the structure of C(1s) is, as expected, more complicated. The peak at 293.7 eV is associated with the CF₃ groups of the [Tf₂N]⁻ anion due to the high electronegativity of fluorine.

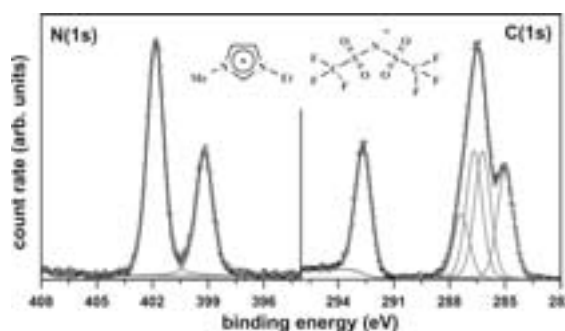


Fig. 1: XPS Spectra for [EMIM][Tf₂N] (left: N(1s) spectrum, right: C(1s) spectrum).

From the molecular structure (see inset in Fig.1) of the [EMIM][Tf₂N] we expect that the low-binding energy part of the C(1s) peak consists of four components caused by (i) the two neighbouring C-atoms of the [EMIM] aromatic ring, (ii) the two C-atoms of the [EMIM] alkyl groups directly bonded to the nitrogen of the aromatic ring, (iii) the C-atom between the two N-atoms of the [EMIM] aromatic ring, and (iv) the [EMIM]-CH₃ ethyl end-group. Indeed, a good agreement of the fit with the measured data is observed.

Fig. 2 presents the valence band spectra collected at 300 K with MIES, UPS, and XPS together with DFT using B3-LYP functional and 6-311G(3d, 2pd) basis set.

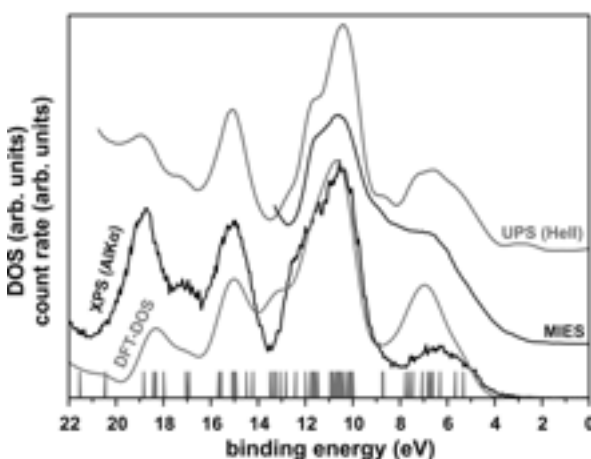


Fig. 2: Valence band spectra collected at 300 K using MIES, UPS, and XPS in comparison to DFT calculations.

For the $[\text{EMIM}][\text{Tf}_2\text{N}]$ complex the calculated DOS was convoluted using Gaussians with a variance of 0.8 eV. The result is shown together with the experimental data in Fig. 2. The calculated spectra are shifted by 1.35 eV towards lower binding energy and normalized to match the most prominent peak in the XPS spectrum at 10-12 eV. This shift most probably accounts for the interaction to other ions in the liquid environment of the complex, which could not be considered in the DFT calculations.

A remarkable good agreement between experimental and theoretical data is found. The HOMO energy, which represents the valence band edge, is found to be 5.5 eV below the vacuum level. The corresponding Kohn-Sham MO is shown in Fig. 3 A. Most MOs of states in the upper valence band (5.5 eV to 7.8 eV) are located on the $[\text{Tf}_2\text{N}]^-$ anion. Among the states located on the $[\text{EMIM}]^+$ cation, the closest to the valence band edge are the HOMO-10 and the HOMO-12. These states correspond to the HOMO and HOMO-1 of the isolated $[\text{EMIM}]^+$ cation (Fig. 3 B and C).

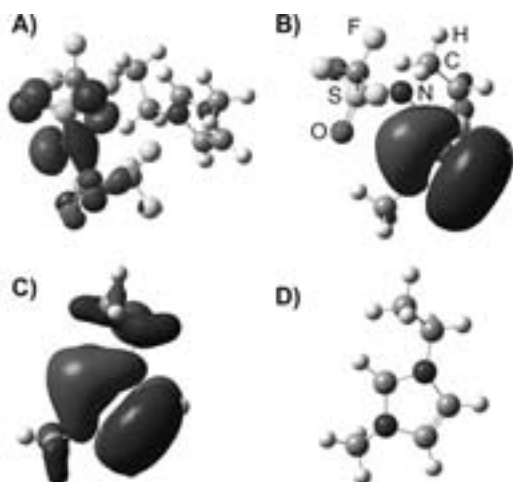


Fig. 3: Visualization of selected MOs: A) the HOMO and B) the highest $[\text{EMIM}]^+$ MO (=HOMO-10) in the $[\text{EMIM}][\text{Tf}_2\text{N}]$ complex, respectively; C) the HOMO of the isolated $[\text{EMIM}]^+$ cation; D) the molecular structure of the $[\text{EMIM}]^+$ cation.

The most pronounced spectral feature of the XPS spectrum is located between 9.5 eV and 12.5 eV binding energy. The corresponding MOs in this region are delocalized over the $[\text{EMIM}]^+$ cation and the nonbonding AOs of the fluorines in the anion. The band around 15 eV consists of states which are MOs located almost exclusively on the $[\text{Tf}_2\text{N}]^-$ anion. Upon cooling, all recorded spectra show little dependence on the sample temperature between 300 K and 230 K.

However, upon cooling the IL layer further, the spectra change drastically. Photoelectron spectroscopy

measurements with comparatively high photon flux give evidence for a charging of the surface, which is a result of a decreased conductivity. Additionally, in MIES and UPS (HeI) a strong decrease of the emission intensity between 10 eV and 12 eV is observed at ~ 154 K, and may also be related to the glass transition process taking place at these temperatures.

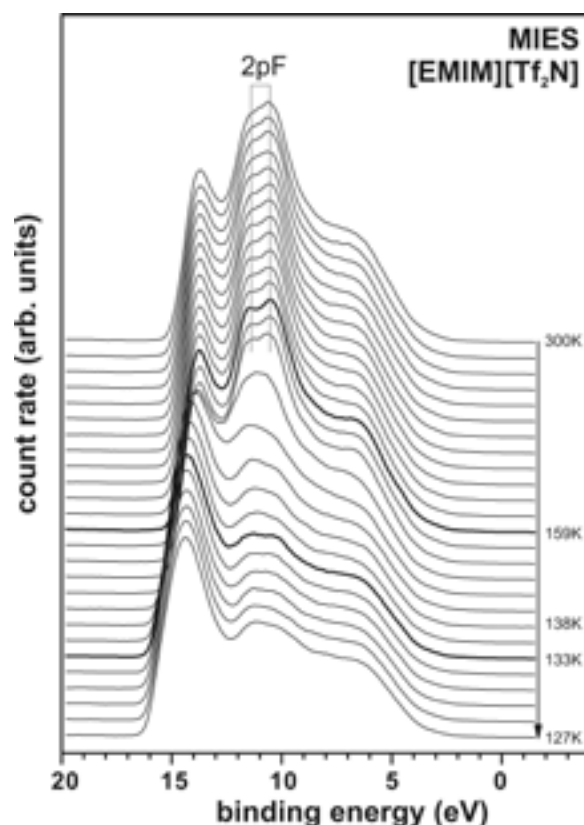


Fig. 4: Temperature dependence of the MIES spectra upon cooling down to 127K.

We conclude, that the observed changes in the spectra are related to changes in the molecular orientation in the $[\text{EMIM}][\text{Tf}_2\text{N}]$ film. A more detailed analysis of the spectral changes based on the DFT calculations, which enable the assignment of spectral features to certain molecular orbitals, is subject of current research.

Currently, we (1) supplement the present studies by HREELS results, and (2) extend them to RT-ILs which possess either a different cation or anion.

We thank F. Endres (TU Clausthal) for providing the RT-IL.

- [1] P. Wasserscheid, W. Keim; *Angew. Chemie* 112 (2000) 3926.
- [2] K. Binnemanns; *Chem. Rev.* 105 (2005) 4148.
- [3] O. Höfft, S. Bahr, M. Himmerlich, S. Krischok, J.A. Schaefer and V. Kempter, *Langmuir* 22 (2006) 7120.
- [4] S. Krischok, R. Ötting, W.J.D. Beenken, M. Himmerlich, P. Lorenz, O. Höfft, S. Bahr, V. Kempter, J.A. Schaefer, *Zeitschrift für Phys. Chem.* (2006) in press.
- [5] L. Rebelo et al. *J. Phys. Chem.* 109 (2005) 6040.
- [6] M.J. Earle et al. *Nature* 439 (2006) 831.

Analysis of Nanostructures by Means of Auger Electron Spectroscopy

G. Ecke^{1,*}, V. Cimalla¹, K. Tonisch¹, V. Lebedev¹, H. Romanus², F. Weise³, and O. Ambacher¹

¹ Department of Nanotechnology

³ Department of Micromechanical Systems

² Center for Micro- and Nanotechnologies

Introduction

There are a lot of analytical methods using focused electron, ion or photon beams as well as mechanical tips as a probe for the excitation of a sample. Electrons, ions, neutrals or photons coming back from the sample as well as interaction forces between tip and sample surfaces can be measured. Each of these analytical methods is denoted by its special characteristics, possibilities, excellences, disadvantages and fields of application. These huge family of analysis methods can be classified into several groups: methods for chemical composition measurements and methods for the investigation of the structural, morphological and optical / electronic characteristics of the sample. Key characteristics of those methods are sensitivity, detection limit, elemental range, quantification and, as one of the most important features, the spatial and the depth resolution.

In modern nanotechnology analysis methods are needed, which are able to investigate extremely small volumes, that means surface sensitive techniques with a high spatial and depth resolution. Concerning the capability of high lateral and depth resolution Auger electron spectroscopy (AES) is one of the outstanding analytical methods for nanotechnology. In modern Auger spectrometers, equipped with a field electron gun, probe diameters below 10 nm are reached. Electron beams can be focused very well, whereas the focusing of ion beams and x-ray or visible light beams is much more complicated or impossible on the nanoscale. The depth resolution of Auger electron spectroscopy depends on the energy of the Auger electrons. But within the usual range from 50 eV to 2000 eV the attenuation length is approximately 0.5 nm to 4 nm. As a consequence that most of the Auger signal comes from a thin sample surface layer with a thickness of some atomic layers. Whereas large area AES has a detection limit of 0.1 at% it impairs for laterally highly resolved measurements. With a detection limit of approximately 1%, a spatial resolution of 10 nm and a depth resolution of 1 nm 50 atoms of one kind can be detected. No other method is able to reach the same detection limit, except analytical cross-sectional transmission electron microscopy (XTEM) with very high preparation efforts and other constrictions.

The following examples have been carried out by an Auger Microlab 350 THERMO, equipped with a small spot electron gun with a field electron tip, a conventional noble gas sputtering ion gun and a high resolution hemispherical energy analyzer.

Example 1: Si segregating on epitaxial AlN

After the epitaxial growth of AlN layers on Si substrates by plasma induced molecular beam epitaxy (PIMBE) segregation structures on the surface of the AlN layer could be detected [1]. It was assumed that silicon passes the AlN layer along grain boundaries from the substrate and segregates on the surface. Figure 1a shows the secondary electron image of the sample surface with one of the segregation structures. AES spectra on and besides the segregation structure, sputtering cleaned by Ar ion bombardment, revealed that the prominent structure is consisting of Si whereas the layer surface is AlN. Figures 1 b and c show the scanning Auger maps of Si and Al of a 200 nm wide feature of a segregation structure, respectively.

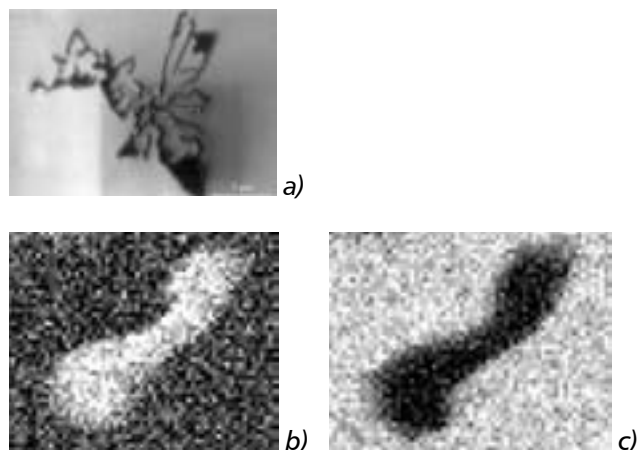
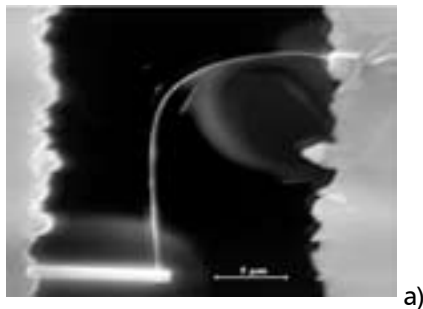


Fig. 1: a) Secondary electron microscopy (SEM) image of a Si segregation structure on AlN, b) Si and c) Al Auger maps.

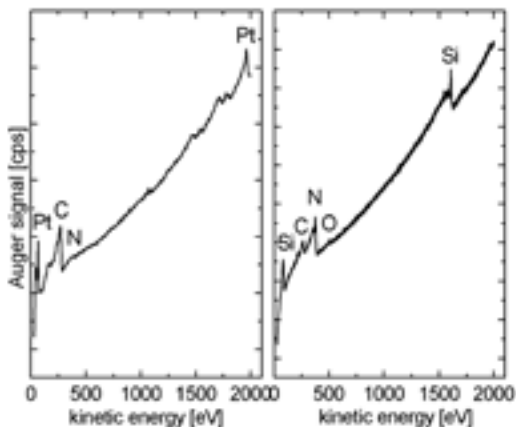
Example 2: Pt contacted Si nanowires

On the SiO₂ surface of a Si/SiO₂ substrate Ti/Au metallisation pads have been created by means of sputtering. Afterwards, Si nanowires have been grown

by low pressure chemical vapor deposition (LPCVD) on glass and transferred onto the SiO_2 surface. These Si nanowires were connected to the metallisation pads on one side. Focused ion beam technique (FIB) was applied to deposit Pt locally to connect the second end of the Si nanowires to a second metallisation pad, in order to enable the I-U characteristic measurement of these nanowires. AES measurements were applied in order to measure the elemental composition of the nanowires and the composition of the FIB deposited Pt connects.



a)



b)

c)

Fig. 2: a) SEM image of Si nanowire, b) Auger spectrum of the wire and c) Auger spectrum on the metal connect.

The AES results show, that the nanowire is consisting of Si which contains a high amount of nitrogen or SiN even after ion beam sputtering and that the metal connect which is made intentionally of Pt by FIB consists of Pt with a high C content.

Example 3: AlN nano - flowers

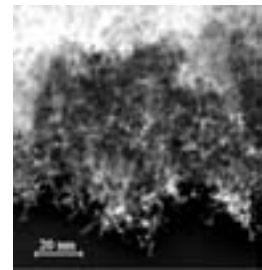
Under special conditions for the AlN growth on sapphire by metal organic chemical vapor deposition (MOCVD)

special structures are developing, so called 'nanoflowers' [2]. They consist of nanowires with diameters of about 20 nm. Figure 3 a shows the SEM image of a typical nanoflower on sapphire substrate.

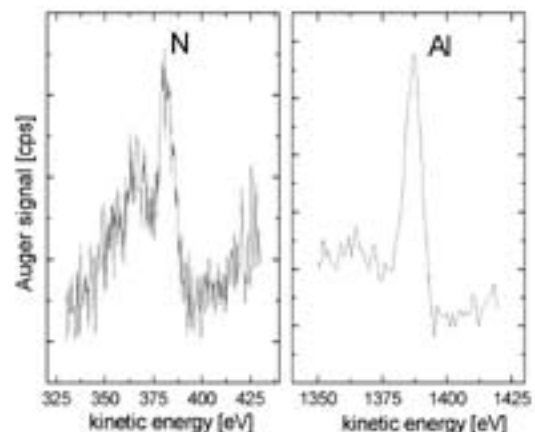
In figure 3 b one can see the nanowires which are the basis of these flowers. Auger measurements showed, that the nanowires consist of AlN, (Figs. 3 c and d), but the surface of these wires is highly covered by C and O (not shown) which are adsorbates from the technological process or from the contamination by air between the process and the Auger measurement.



a)



b)



c)

d)

Fig. 3: a) SEM image and b) detail view of the AlN nanoflower and c) N KLL and d) Al KLL Auger peaks of the nanowires.

Conclusions

Three examples of Auger measurements on nanostructures are presented to document the capability of Auger electron spectroscopy as a surface sensitive technique with a brilliant spatial resolution. These properties enable this method to be one of the most promising surface analysis methods in nanotechnology research and development.

- [1] Lebedev, F.M. Morales, H. Romanus, G. Ecke, V. Cimalla, M. Himmerlich, S. Krischok, J.A. Schäfer, O. Ambacher, *phys. stat. sol. (c)* 3 (2006) 1420-1424.
 [2] V. Cimalla, Ch. Förster, D. Cengher, K. Tonisch, O. Ambacher, *phys. stat. sol. (b)* 243 (2006) 1476-1480.

Correlation between surface and electrical properties of indium tin oxynitride thin films

M. Himmerlich^{1,*}, S. Krischok¹, M. Koufaki³, M. Sifakis³, Ch. Mauder², G. Ecke², V. Cimalla², E. Aperathitis³, and J.A. Schaefer¹

¹ Department of Technical Physics

² Department of Nanotechnology

³ Microelectronics Research Group, IESL, Foundation for Research & Technology – HELLAS, Heraklion, Greece

Indium-tin-oxide (ITO) is almost the only widely used transparent conductive oxide. For optoelectronic devices it serves as optical as well as contact material. Even though ITO is a wide bandgap material, it is a n-type degenerate semiconductor (where oxygen vacancies and tin contribute to conductivity). Due to the lack of p-type oxides with similar properties, (wide band-gap and at the same time high conductivity) ITO has been used on many III-V based optoelectronic devices, e.g. for ohmic contacts on p-GaN layers [1,2]. RF-sputtered indium-tin-oxynitride (ITON) thin films have slightly worse electrical characteristics compared to ITO films deposited in the same way, but they exhibit improved optical properties [3]. In this work, we investigate the role of the incorporated nitrogen in the ITON structure by employing photoelectron spectroscopy together with a characterization of the electrical properties of ITON layers as contacts on p-type GaN.

ITON and ITO thin films with a thickness of ~200 nm were deposited by RF-sputtering from an indium-tin-oxide target in N₂ and Ar plasma, respectively. The typical surface morphology of the resulting polycrystalline ITON films is shown in Fig. 1.

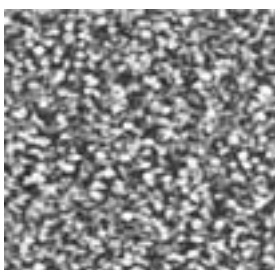


Fig. 1: AFM image showing the surface morphology of polycrystalline ITON thin films prepared by RF-sputtering (size 2x2 μm², z-scale ~50 nm, rms ~6 nm).

The material properties were investigated after post-deposition treatments involving rapid thermal annealing (RTA) in nitrogen atmosphere (flow 450 sccm) at temperatures of up to 800°C. The surface chemical composition, including the presence and role of nitrogen in the ITON films, was examined by X-ray photoelectron spectroscopy (XPS). Quadrupole mass spectroscopy (QMS) was used to detect species

desorbed from the sample surface during annealing. The electrical properties of the prepared contacts on p-GaN were determined by Hall measurements using the four-probe Van-der-Pauw method.

The major difference in the properties of the ITON films compared to those of ITO is that, ITON films deposited in pure nitrogen plasma exhibit the largest shift of the absorption edge to shorter wavelengths after annealing. Typically, the carrier concentration and conductivity of as-prepared ITON films is lower than that of ITO [4]. Annealing at 600°C leads to a strong increase in carrier concentration (see Fig. 2) but the conductivity and mobility of ITON is inferior to that of ITO.

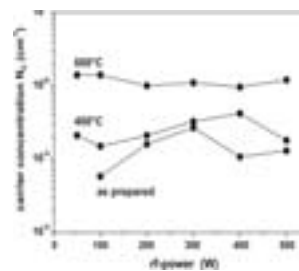


Fig. 2: Dependence of the carrier concentration on annealing temperature of ITON thin films.

The results of the XPS measurements of the In3d_{5/2} core level are shown in Fig. 3. ITON samples exhibit a narrow symmetric peak at a binding energy (BE) of 444.7 eV, whereas an additional shoulder at ~0.9 eV higher BE in all core level spectra is observed for ITO. This behavior originates from the existence of oxygen vacancies in the bixbyite structure or, in other words, oxygen deficiency [5]. Therefore, the differences seen in the XPS peak shapes between the as-deposited ITON and ITO samples explain the observed lower carrier concentration of as-deposited ITON films. Upon annealing, the ITON films become more conductive and after annealing at 800°C their resistivity is almost identical to that of the ITO films (5x10⁻⁴ Ωcm). After RTA at 800°C no differences in the carrier concentration of the films is observed, but the mobility of the ITON films is almost half of the ITO films (30 cm²/Vs for ITON and 64 cm²/Vs for ITO films). The decrease in ITON resistivity with annealing is accompanied by changes in the XPS spectra of the In3d, Sn3d and O1s peaks.

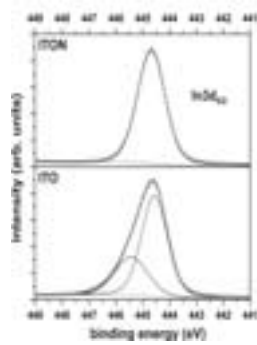


Fig. 3: $In3d_{5/2}$ core level spectra of as-prepared ITON and ITO thin films deposited by RF-sputtering.

The influence of nitrogen present in the ITON structure on the above described observations was further examined by monitoring the N1s peak. The results for films annealed at different temperatures are presented in Fig. 4. Without any annealing, three different nitrogen states are found on the surface. The state at 396.7 eV is attributed to nitrogen bound to metal atoms, while the one at 398.3 eV is found to originate from oxynitride bonds (oxygen and metal atoms are located in the surrounding of the nitrogen atoms). The structure at 404.0 eV can have two origins: a) NO_2 bonds or b) unbound nitrogen. Besides a small reduction of the total nitrogen concentration, no changes in the nitrogen states were observed after annealing at 400°C, but after annealing at 600°C the state at 404.0 eV disappeared along with almost the entire oxynitride component.

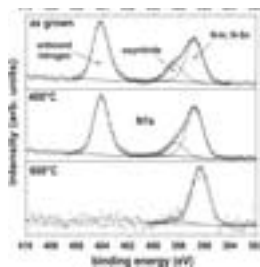


Fig. 4: N1s core level spectra of ITON thin films after deposition and annealing up to 600°C.

QMS measurements revealed that at $T > 550^\circ\text{C}$ a strong desorption of nitrogen takes place, while no release of NO, NO_2 or N_2O is found. Therefore, according to investigations on the nitridation of III-V semiconductor surfaces [6], we assign the structure at 404.0 eV to incorporated unbound nitrogen.

It is anticipated that after annealing ITON films at 400°C the contribution to the observed decrease in resistivity is not originating from the non-stoichiometric phase, but mainly from the incorporated nitrogen and oxynitride states. Annealing at 600°C results in the removal of incorporated nitrogen, as well as in the creation

of oxygen vacancies. In addition, the effect of Sn segregation towards the surface is found. These effects result in a further decrease of the ITON film resistivity. It should be mentioned that the mobility of the ITON films exhibit the biggest increase after annealing in the range from 400°C to 600°C ($4 \text{ cm}^2/\text{Vs}$ to $25 \text{ cm}^2/\text{Vs}$); which could be attributed to the removal of the incorporated nitrogen and oxynitride states, which might act as scattering centers for the carriers.

The contact behavior of ITON and ITO films on p-type GaN layers was examined by monitoring the current-voltage characteristics as a function of the annealing temperature. For ITO films, no ohmic behavior could be found upon annealing up to 800°C. However, the ITON films formed ohmic contacts to p-GaN after annealing at 600°C. Further heating at higher temperatures deteriorated this behavior creating a non-ohmic contact (see Fig. 5).

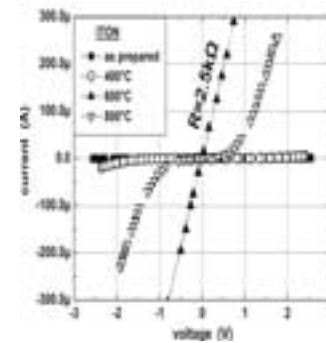


Fig. 5: Current-voltage characteristics of ITON thin films as contacts on p-GaN layers for annealing temperatures up to 800°C.

It is important to note that the temperature of 600°C, where the ITON films exhibit ohmic behavior, is apparently related to the temperature ($\sim 550^\circ\text{C}$) where the film showed the fastest release of incorporated nitrogen. However, the mechanism which resulted in ohmic behavior for the ITON film on p-type GaN at 600°C is not completely understood at this time. It might be associated with the diffusion of atoms through the ITON-GaN interface, thus creating an interfacial layer which alters the electronic properties of ITON at the interface.

In summary, for ITON films a correlation was found to exist between the chemical bonding derived from the analysis of XPS spectra and the electrical behavior. Above 600°C, the release of nitrogen is accompanied by the formation of oxygen vacancies and Sn surface segregation resulting in improved electrical characteristics.

This work was supported by the research program IKYDA 03 and partially by the EU project "GaNano" as well as the TMWTA.

- [1] T. Margalith et al., Appl. Phys. Lett. 74 (1999) 3930.
- [2] S.-H. Su et al., J. Electrochem. Soc. 153 (2006) G87.
- [3] E. Aperathitis et al., Thin Solid Films 450 (2004) 101.
- [4] E. Aperathitis et al., J. Appl. Phys. 94 (2003) 1258.
- [5] R.X. Wang et al., Semicond. Sci. Technol. 19 (2004) 695.

AFM Measurements for Positioning Markers

M. Niebelschütz^{1,*}, H. Romanus², F. Will¹, V. Cimalla¹, and O. Ambacher¹

¹ Department of Nanotechnology

² Center for Micro- and Nanotechnologies

Motivation

The characterisation of complex materials and structures has recently caused further improvements of analytic methods, especially for surface and interfaces which are very important for process control. The possibility of non-destructive electrical, magnetic and structural analysis is beneficial for fast technology inspection. In this case a method to analyse large areas, in a range of mm, with a high resolution of a few nm is required. It is beneficial to integrate all these analytic methods in a single set up. This integration is realised by the nanopositioning and –measuring machine (NPMM). The combination of a NPMM with an Atomic Force Microscope (AFM) enables to join the high resolution of an AFM and the large operation area of a NPMM. Functionalised AFM probes additionally offer the option to analyse different properties at the same position. Therefore a NPMM should also be able to replace automatically probes and nanotools in dependence on the defined task. In figure 1 an example of a NPMM with an AFM and an automatic tip changer is shown. This requires the determination of the AFM probe position after every change of the probe. For the adjustment of the various probes a defined structure with different characteristics is needed.

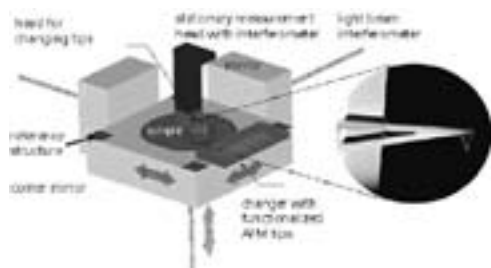


Fig. 1: Concept of a NPMM with integrated Atomic Force Microscope and an automatic tip changer.

For the preparation of these structures we embark on two different ways. On the one hand we have directly written different structures on quartz glass, silicon or SiC by means of Focused Ion Beam (FIB) which serve as topographic marks. On the other hand for the analysis modus (EFM, MFM) we have processed a cross section of a multilayer with sharp contrast in physical properties of relevance, e.g. AlN/Ni multilayer structure on sapphire or silicon.

Position markers for topography

The preparation of alignment marks by the FIB (FIB200 ODP, FEI Company) was first taken into account [1]. The FIB defines hierarchic structures on a substrate with self-organized random nano objects to locate a single nano structure as reference, which is used for fine adjustment of the AFM probes. These patterns were realized either by deposition of platinum or by cutting trenches with Ga-ions. For the approximate adjustment Pt markers with sizes of $750 \times 520 \mu\text{m}^2$ and $375 \times 260 \mu\text{m}^2$ were defined. The following smaller hierarchic marking field consists of a square with a side length of $150 \mu\text{m}$ and $74.6 \mu\text{m}$. Inside of this field rectangular trenches which are arranged in V form with an opening angle of 30° were written. These alignment marks cover a width from $1.5 \mu\text{m}$ down to 90 nm and a depth or height of about 20 nm to 200 nm (Fig. 2). The V-markers are patterned by a Ga-Ion beam to achieve sharp edges. This V-pattern enables the localization of self-organized SiC nanostructures, which are prepared by carbonization of a silicon substrate using molecular beam epitaxy [2].



Fig. 2: SEM image of the V-pattern to locate the SiC nanostructures in by AFM.

The characterization of the artificial and the self-organized structures was accomplished by an AFM NT-MDT Solver Pro in non contact mode. In figure 3 such a non contact image of the V-pattern and the self-organized SiC nanostructures are shown. Two parallel lines with a distance as large as possible were selected from the AFM images. On both of these lines the position of the structure edges was determined. The knowledge of these points contains sufficient information to calibrate the NPMM with an accuracy of about 200 nm after a probe change. The angle of

the V-pattern serves as additional control parameter. The achieved accuracy is sufficient to approach a single SiC nanostructure for the precise adjustment. Such a SiC nanostructure can also be used to define the probe geometry. To calibrate the probe every time at the same structure, one SiC structure is marked by the FIB (Fig. 3).

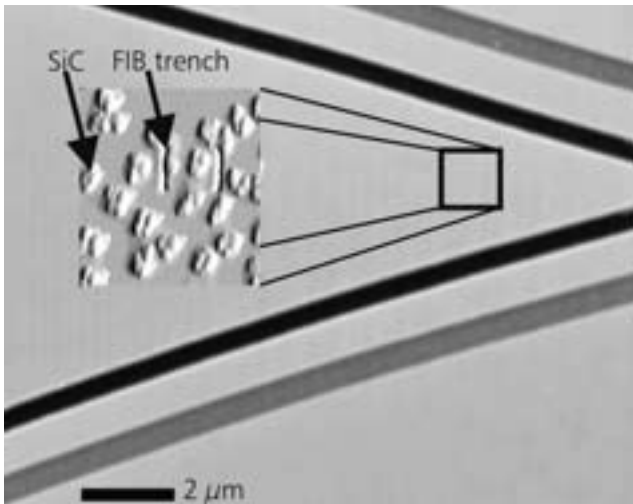


Fig. 3: Non contact AFM image of the V-pattern and the self-organized SiC nanostructures marked by FIB.

In addition, the influence of probe geometry and symmetry, scan direction, spring constant of cantilevers and resolution has to be examined in more detail, i.e. more precise defined probe geometry will enhance accuracy.

Position markers for special mode

The other technique to create reference structures for the NPMM was the preparation of a cross section of an AlN/Ni multilayer. This multilayer offers not only a calibration mode for topography but also a calibration mode for special AFM modes like electrostatic force microscopy (EFM), magnetic force microscopy (MFM) or spreading resistance. The multi-layer is deposited on sapphire or silicon substrate by sputtering of AlN and e-beam evaporation of Ni. Figure 4a and figure 4b show a Scanning Auger Microscopy image of such a multilayer (four AlN and four Ni layers) and a Transmission Electron Microscopy image (two AlN and two Ni layers), respectively. These analytic methods are used to find out the layer thicknesses of the different materials. In figure 5 an EFM image of a 3xAlN/Ni multilayer is shown which is prepared as cross section in the same way like the TEM-samples. The resolution of the EFM for

these two materials is in the range of 100 nm which is comparable with measurements of other groups [3]. The resolution of the EFM or MFM depends on the interface of AlN and Ni. By optimization of this interface it should be possible to push the spatial resolution of the EFM and MFM below 100 nm.

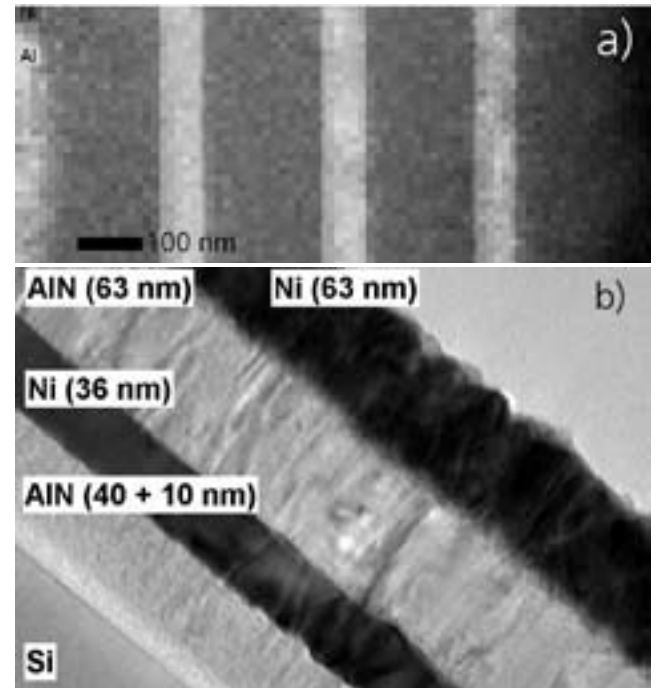


Fig. 4: a) Scanning Auger Microscopy of 4xAlN/Ni multi-layer b) Transmission Electron Microscopy image of 2xAlN/Ni multilayer.

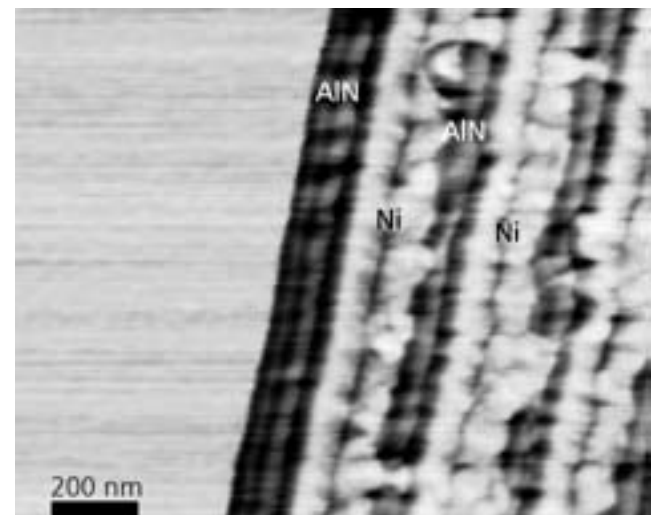


Fig. 5: EFM image of a 3xAlN/Ni multilayer cross section on sapphire.

This work is supported by "Deutsche Forschungs Gemeinschaft: SFB 622 Nanopositionier- und Messmaschine" project A8 "Multifunctional Nanoanalysis".

- [1] U. Sennhauser, P. Jacob, P. Gasser, *Praktische Metallographie* 41 (4) (2004) 199-209.
- [2] V. Cimalla and K. Zekentes, *Mater. Sci. Forum* 389-393 (2002) 747-750.
- [3] K. M. Jones et al., *Appl. Phys. Lett.* 78, (2001) 2497.

Advanced Electrical and Stability Characterization of Untrimmed and Variously Trimmed Thick-Film and LTCC Resistors

W. Ehrhardt^{1,*}, H. Thust¹, A. Dziejczak², and A. Kolek³

¹ Department of Microperipherals

² Faculty of Microsystem Electronics and Photonics, Wrocław University of Technology, Poland

³ Department of Electronics Fundamentals, Rzeszów University of Technology, Poland

Abstract

The increase of packaging density of electronic modules demands miniaturisation of passive components. But the as-fired thick-film resistors have a resistance tolerance within $\pm 20\%$. Moreover this tolerance is increased for smaller components. Therefore they have to be trimmed and novel trimming methods are necessary for microresistors, especially when they are embedded in LTCC substrates. Most often the quality of trimmed resistors is characterised only by a resistance drift caused by various long- and/or short-term exposures. This paper compares electrical (normalised temperature dependence of resistance, low frequency noise) and stability properties (relative resistance drift, changes of current noise index) of untrimmed, voltage pulse trimmed and laser trimmed unglazed thickfilm resistors after step increased long-term thermal ageing at 160°C, 210°C, and 250°C. Moreover the effect of longterm exposure (1000 h, 125°C) and thermal shocks (1000 shocks between -55°C and 125°C) is analysed for untrimmed and voltage pulse trimmed buried LTCC resistors.

Description

Currently, laser trimming is the dominant trimming method of thick-film and LTCC resistors. However, because of the continuous trend in electronics industry for smaller, lighter, faster and cheaper products, a significant dimension reduction of thick-film and LTCC resistors as well as the fabrication of buried components is noted at present. On one hand, laser trimming is insufficient for the smallest thick-film and LTCC resistors, on the other hand, the tolerance of as-fired resistors is within $\pm 20\%$ and increases with reduction of dimensions. Since approximately ten years, an intensive search for alternative trimming methods has been performed. The most advanced research is connected with trimming by energy of high voltage pulses.

In general, the susceptibility to high voltage pulses and electrostatic discharges is very important and has been investigated for thick-film resistors for almost 30 years [1,2].

Such investigations can be performed with the aid of single or series of "long" pulses (rectangular shape surges with 1 to 20 ms duration) or by the series of "short" rectangular voltage pulses (with duration from several hundred nanoseconds up to several hundred microseconds). Tobita and Takasago and then a group from the Technische Universität Ilmenau [3-6] and a group from the Wrocław University of Technology [7,8] tried to trim thickfilm or LTCC resistors by the pulse voltage method. Very recently the Ilmenau group has built and tested a high voltage capacitor discharging generator allowing controllable resistance changes of low and high ohmic thick-film resistors [9,10].

Results

In this paper we presented a wide spectrum of electrical (normalised temperature dependence of resistance, low frequency noise) and stability (relative resistance drift, changes of current noise index after ageing) properties of untrimmed, laser trimmed as well as high voltage trimmed thick film resistors. Moreover they were correlated with additional resistor high temperature ageing after the trimming process. According to our knowledge, this is the first detailed comparison of various trimming methods. During these investigations the following was found:

- There is distinct difference in longterm thermal stability of the investigated components. The drift of untrimmed and laser trimmed resistors is similar, but structures trimmed by series of voltage pulses after extreme temperature stress have a stability worse by about one order of magnitude. The drift is larger for pulse trimmed resistors having a larger resistance difference before and after trimming.
- In this article we reported comparison of resistance drift induced by long-term thermal ageing at three different temperatures 160°C, 210°C, and 250°C. The samples were kept at every temperature for about 200 hours. The relative resistance changes of high voltage discharge trimmed resistors are shown in figure 1.

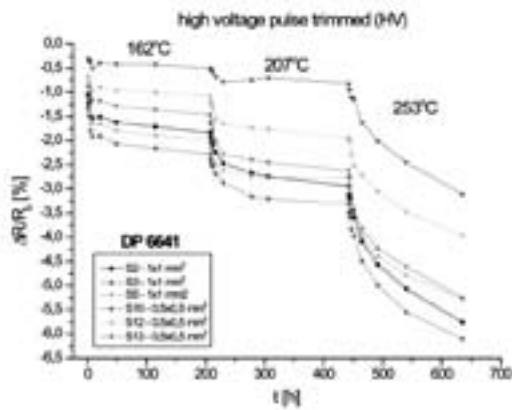


Fig. 1:

- The temperature dependences of resistance in a wide temperature range are similar for untrimmed and laser trimmed components. However the minimum of resistance in HV-trimmed resistors is shifted to higher temperatures. Moreover, an unexpected change of the $R(T)$ curve shape appears near 100°C.
- The noise with a typical $1/f$ shape caused by an equilibrium of resistance fluctuations is dominant in the low frequency range independently of the trimming method. The initial (before ageing) noise intensity is comparable for all resistors made of the same ink and of identical planar dimensions. However, the current noise index increases noticeably for HV-trimmed resistors after longterm thermal ageing in spite of resistance diminishing. This increase is larger in the case of strongly trimmed structures. On the other hand, the noise level of untrimmed and laser trimmed resistors does not undergo changes after the ageing process.
- Trimming of unglazed resistors by high voltage pulses induces other ageing mechanisms than those, which are predominant in untrimmed or laser trimmed resistors, which is essential for high temperature load. Such trimming method is useful in many standard applications where the temperature of resistors does not exceed 100°C.
- Further stability investigations of overglazed resistors are necessary for the extension of the application range of the high voltage trimming method.
- The HV-trimmed buried (hermetic) LTCC resistors have a better long term stability in comparison with unglazed thickfilm ones made on alumina substrate.

Table 1 shows that some of the used resistor systems are suitable for high voltage trimming. Some of them (C-10k, B-10k, C-100) have a deviation <1% after preconditions and thermal ageing, and others (A-10, A-100, A-1k) have a drift up to 6%. This observation points out that the trimming stability after thermal ageing depends on the resistor paste.

Paste	R_{sq} after 3 refirings and tolerance	trim range and direction	drift after precond. and direction	untrimmed stability after precond.
A-10	50 Ω /sq $\pm 50\%$	> 25% \uparrow	typ. 1.3% \uparrow (max: 6%)	< 0.5% \downarrow
A-100	40 Ω /sq $\pm 50\%$	> 25% \uparrow	> 5% \uparrow	< 0.5%
C-100	80 Ω /sq $\pm 20\%$	> 25% \uparrow	typ. 1% \uparrow	< 0.3% \downarrow
A-1k	130 Ω /sq $\pm 20\%$	> 25% \uparrow	typ. 0.7% \hat{a} (max: 6%)	< 0.2%
B-10k	2.3 kW/sq $\pm 25\%$	< 20% \downarrow	< 1% \downarrow	< 0.1%
C-10k	3 kW/sq $\pm 30\%$	< 10% \downarrow	< 0,8% \downarrow	< 0.05%

Tab. 1:

- Trimming of commercial SMD resistors and buried resistors in LTCC are applications of interest and currently supported by the German government research projects (BMW-KF 0207104KTD3).

[1] Y. Saitoh, Y. Katsuta, K. Suzuki; Effect of surge voltages on thick film resistors, Proc. Int. Microelectronics Symp. (ISHM-USA), 1979, p.289-294.
 [2] J.-P. Constantin, M. Moulin, J.-B. Ranger; Effect of surge voltages on thin and thick film resistors, Proc. 2nd Int. Microelectronics Conf. (ISHM-Japan), 1982, p.51-55.
 [3] J. Müller, H. Thust, B. Sjoling, S. Turvey; Trimming of buried resistors in LTCC-circuits, Proc. 33rd ISHM Nordic Conf., Helsingor (Denmark) 1996, p.166-173.
 [4] H. Thust, K.-H. Drüe, T. Thelemann, E. K. Polzer, J. Müller; Is buried better?, Advanced Packaging, vol. 7, no 3 (March/April 1998), p.40, 42, 44, 46.
 [5] H. Thust, K.-H. Drüe, T. Thelemann; Trimming arrangement of buried resistors in LTCC by high-voltage-pulses, Proc. 36th IMAPS Nordic Conf., Helsinki, 1999, p.150-157.
 [6] W. Ehrhardt, H. Thust; Trimming of thick-film resistors by energy of high voltage pulses and its influence on microstructure, Proc. 13th Eur. Microelectronics and Packaging Conf., Strasbourg, 2001, p.403-407.
 [7] A. Dziedzic; Trimming and stability of thick-film resistors with reduced dimensions, Proc. 25th IMAPS Poland Conf., Polańczyk 2001, p.163-166.
 [8] A. Dziedzic, L. J. Golonka, J. Kita, H. Thust, K.-H. Drüe, R. Bauer, L. Rebenklau, K.-J. Wolter; Electrical and stability properties and ultrasonic microscope characterisation of LTCC resistors, Microelectronics Reliability, vol.41 (2001), p.669-676.
 [9] W. Ehrhardt, H. Thust, J. Müller; Manufacturability and reliability of trimmed buried resistors in LTCC, Proc. 2003 IMAPS Conf. on Ceramic Interconnect Technology: The Next Generation, Denver (USA), April 2003, p.183-188.
 [10] W. Ehrhardt, H. Thust; Behaviour of sheet resistors by impulsive discharge, Proc. 14th European Microelectronics and Packaging Conf., Friedrichshafen (Germany), June 2003, p.148-153.

Near-field images of semiconductor nanostructures

E. Runge^{1,*} and C. Lienau²

¹ Department of Theoretical Physics I

² Max Born Institute for Nonlinear Optics and Short Pulse Spectroscopy, Berlin

Ever since the early days of near-field spectroscopy, near-field imaging and spectroscopy of low-dimensional semiconductor nanostructures, i.e., of quantum wells (QW), wires (QWR) and dots (QD), has received considerable attention. Recent progress in apertureless near-field spectroscopy and in the fabrication of aperture-based fiber probes has pushed the spatial resolution to less than 20 nm. This allows to attempt real-space imaging of *individual* quantum dots. The photoluminescence (PL) of single excitons (X) and biexcitons (XX) localized in interface thickness fluctuations (interface quantum dots, IQD) of a thin GaAs QW were imaged with a resolution of about 30 nm [1]. This is well below the apparent size of the measured X (100 nm) and XX (70 nm) PL images. Consequently, it was concluded that the extent of the biexcitonic center-of-mass wave function in these IQD is smaller than that of a single exciton.

For semiconductors, the study of individual quantum systems is particularly relevant, as - even with the most advanced growth techniques - fluctuations in size, geometry and/or composition of the nanostructures or their environment result in considerable variations of the optical spectra from one nanostructure to the next. On the theoretical side, ultrahigh spatial resolution spectroscopy of nanostructures has sparked great interest because it allows to study the non-local nature of the excitation and detection process, different polarization selection rules, the loss of evanescent wave components in the far-field, near-field coupling to optically dark states and a possible modification of their radiative decay.

In Ref. [2,3], we have looked in particular at the effect of the experimental configuration on the near-field images and shown that due to the inherent optical nonlinearity in X and XX spectroscopy as well as in the near-field imaging process, the images represent a rather complicated convolution of the true local wave function probability density and the local electric field. Thus considerable care - and possibly a detailed theoretical analysis - is needed for quantitative interpretations of near-field images in this high-spatial resolution regime.

The elementary optical excitations of semiconductor nanostructures are excitons, i.e. bound states of

quantum-confined electrons and holes. Exciton generation and luminescence are determined by the absorption rates r_α of the individual states α . These rates are given by the square of the transition amplitudes M_α of the fundamental light-matter interaction Hamiltonian. We assume that in-plane disorder is weak enough to allow excitons to move as entities. Formally, this corresponds to a factorization of the exciton wave function in a center-of-mass part ψ_α and a term describing the relative motion of electron and hole. This allows us write

$$M_{X,\alpha} = C_{X,\alpha}^{XQD} \int dR E(R - R_T) \psi_\alpha(R)$$

with the electric field E near the tip position R_T and a prefactor C that contains Kane's matrix element and other constants. These so-called optical matrix elements M_α contain all the relevant information about the quantum mechanical localization of the wave functions ψ_α .

For the interpretation and quantitative analysis, we have to distinguish between on the one hand resonant excitation of a specific quantum state α with detection of re-emitted light primarily from this state and on the other hand non-resonant excitation of (an ensemble of) quantum state(s) β at energy ϵ_β and luminescence detection from state α with different energy ϵ_α . This requires in principle to account for the complex and strongly temperature-dependent real-space transfer of an X and the accompanying relaxation in energy space.

Different images are obtained for the illumination-collection (i-c) mode and for the collection (c) mode. In the former, both excitation and detection are performed through the near-field probe, whereas in the latter conventional optical far-field excitation is used. The general expression for the near-field image, i.e., the incoherent excitonic luminescence $I_X(R_T)$ collected at frequency ω_c after illumination at frequency ω_i recorded as function of tip position R_T involves a sum over all initial states β and all final states α weighted with the rates r_β and r_α for absorption and luminescence, respectively. Fortunately, for spectrally broad far-field excitation the luminescence simplifies to

$$I_X^c(R_T, \hbar\omega_c) \sim \sum_{\alpha} \delta(\hbar\omega_c - \varepsilon_{\alpha}) |M_{\alpha}(R_T)|^2$$

In contrast, in typical resonant experiments ($\omega_c = \omega$), the $\alpha = \beta$ contributions will dominate:

$$I_X^{c-} (R_T, \hbar\omega_c) \sim \sum_{\alpha} \delta(\hbar\omega_c - \varepsilon_{\alpha}) |M_{\alpha}(R_T)|^4$$

We simulated near-field imaging of bright and dark single exciton as well as biexciton states in interface quantum dots for two different model confinement potentials: a parabolic potential (HO) and a cylindrical box (box). Both allow for an easy analytical treatment in terms of exponential functions and Bessel functions, which are characterized by the full width at half maximum I_F of the exciton density $|\psi\alpha|^2$. We model the electromagnetic field distribution by that of an perfectly conducting metallic circular aperture of the radius a_0 right above the semiconductor sample (characterized by its optical density (Bethe-Bouwkamp model [5]). Examples of calculated near-field images are shown in Figs. 1 and 2.

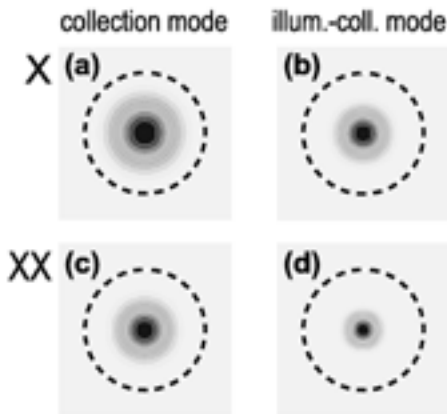


Fig. 1: Calculated near-field images of excitons (top row) and biexcitons (bottom row) of an interface quantum dot in GaAs ($n \approx 3.5$) 20 nm below the sample surface for a collection mode (left column) and illumination-collection mode (right column) geometry. The FWHM width of the exciton density is $I_F = 100$ nm, the aperture radius is $a_0 = 10$ nm. The cylindrical box potential with a radius of 107 nm is indicated by a dashed line.

Intensities are given on a gray-scale in linear 10% steps. Smaller image sizes are found for the illumination-collection mode geometry and for biexcitonic transitions due to the non-linear nature of the corresponding imaging process [3].

The intrinsically nonlinear intensity dependence of biexcitonic emission gives rise to important differences in the spatial variation of X and XX PL images in Fig. 1.

Note that for XX case not even the collection mode image in the limit of infinitely high resolution reflects the XX wave function or its density.

In the limit that the aperture diameter is considerably smaller than the extent of the X center-of-mass wave function, the collection-mode near-field images indeed match the excitonic density closely. More interesting, and probably more realistic, is the case that the aperture is larger, and of similar dimension as the exciton wave function, see lower row of Fig. 2. Now, the image of the round (*s*-like) ground state exciton is strongly deformed by the anisotropic electromagnetic field distribution. The apparent images of the excited states $\psi_{1y'}^{(box)}$, $\psi_{1x'}^{(box)}$ are localized almost exclusively outside of the potential well (dashed circle in the figure), whereas the excitons themselves are exclusively *inside* the well.

$$I_X^c(R_T, \hbar\omega_c) \sim \sum_{\alpha} \delta(\hbar\omega_c - \varepsilon_{\alpha}) |M_{\alpha}(R_T)|^2$$

Fig. 2: Calculated collection-mode near-field images of excitons in cylindrical boxes with 107 nm (upper row, $I_F = 100$ nm) and 32 nm (lower row, $I_F = 30$ nm) radius. Aperture radii are 10 nm and 80 nm, respectively. From left to right: ground state $\psi_{gs}^{(box)}$ and first excited states $\psi_{1y'}^{(box)}$, $\psi_{1x'}^{(box)}$. The incident light is linearly polarized along the vertical *y* axis. The intensities are normalized and given on a gray-scale in linear 10% steps. Normalization factors relative to the ground state panel (left) in each row are included in exponential notation. Note that all exciton densities strictly vanish outside the boxes marked by the dashed circles [3].

Perhaps the most general conclusion that can be drawn from our simulations is that direct imaging of the local X density happens only in collection mode experiments with nonresonant excitation in the high-resolution limit. For other geometries and for XX states, the images reflect not only the size and shape of the wave function and the spatial resolution of near-field probe but also in particular the inherent optical nonlinearity of the imaging process. The rather complex convolution of true local wave function probability density, local electric field and imaging nonlocality and nonlinearity calls for a careful theoretical analysis of near-field wave function experiments. Radiative couplings between near-field probe and quantum object and the effects of carrier dynamics, quantum coherences and quantum transport on the imaging process are interesting topics that yet remain to be explored from both a theoretical as well as experimental perspective.

[1] J. K. Matsuda, T. Saiki, S. Nomura, M. Mihara, Y. Aoyagi, S. Nair, and T. Taka-gahara, Phys. Rev. Lett. **91** (2003), 177401.

[2] E. Runge and C. Lienau, Phys. Rev. B **71** (2005), 035347.

[3] E. Runge and C. Lienau, Appl. Phys. B **84** (2006), 103.

[4] E. Runge, Solid State Physics, Vol. 57, edited by H. Ehrenreich and F. Spaepen, Academic Press, San Diego (2002), p. 149-305, and references therein.

[5] C. J. Bouwkamp, Philips Res. Rep. **5** (1950), 321.

Magnetic Augmented Laser Beam Cladding

J. Wilden*, J. P. Bergmann, and M. Dolles
Department for Production Engineering

Introduction and Motivation

Laser beam cladding represents a high quality coating process, which allows applying metallic materials for wear and corrosion protection. Beyond the high quality of the generated coatings, e.g., smooth surface, metallurgic bonding towards the base material, fine microstructure, minimal thermal influence, etc., the technique shows a high flexibility and allows the application of a wide range of materials. On the other hand the low efficiency of the process and the resulting high cladding costs limit its utilization in the industry to special applications. Consequently, a lot of research work had been done to increase the efficiency of the process [1-4], but all the techniques, which are focused on the energy management of the process, did not satisfy the requirements of the industry. Thus, new strategies are necessary to enlarge the application range of this process. A promising attempt is the application of an external force towards the melt pool and to adapt the geometry of them. For the cladding of large areas, a flat and broad cladding is necessary. The generation of 3D-structures, on the other side, requires slim walls with a high aspect ratio. Electromagnetic Lorentz forces (Fig. 1), caused by an electric current and a magnetic field, allow to freely form the shape of the cladding geometry.

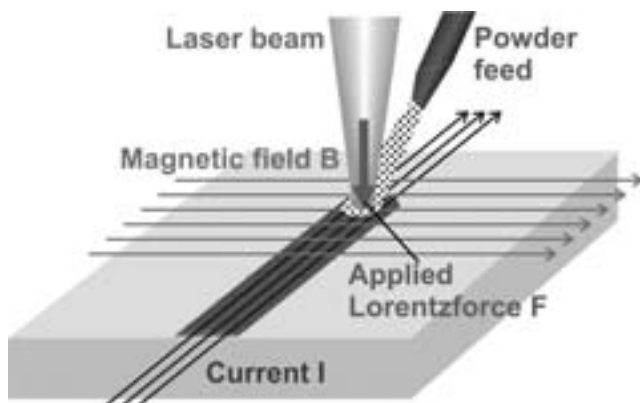


Fig. 1: Setup for the magnetic augmented laser cladding.

Process Design

The basic setup of the magnetic augmented laser beam cladding is that of a conventional coating process with a focussed laser beam. It melts the

materials and is fed by a powder or wire fed process. Additionally, a magnetic field and an electric current within the melt pool must be present. The resulting Lorentz force is perpendicular to the current and the magnetic field. Due to its orientation, the force applied to the liquid metal allows forming of the melt pool and the resulting coating geometry. For the magnetic field it is possible to use two different options. First, permanent magnetic fields and a direct electric current can be used to apply a force towards the material. The second option is to use high frequency magnetic fields and the resulting skin effect to generate an electromagnetic force.

Results

The application of permanent magnetic fields shows several different results. The magnetic field calms and reduces convection in the melt pool which is independent from the materials used. The current resulting from the motion of the liquid metal within the melt pool causes a force which acts against the flow direction of the melt. Due to the damping of the convection the treated area for laser beam remelting is reduced. For laser beam cladding the damping leads to an improved surface quality of the applied coatings and allows minimizing any finishing efforts. No variation of the coating geometry was observed. Consequently, a controlled current in the melt pool is necessary. One possibility is to exploit thermoelectric currents which result from the interaction of two materials with different thermoelectric potential under a temperature gradient. The interaction between the current and the applied magnetic field allows generating a force within the melt pool and shaping of the coating geometry. For a constant current direction, the orientation of the magnetic field allows to control the direction of the generated force, and thereby, the shape of the coating. A force directed downwards produces flat and broad coatings, whereas a rotation of the magnetic field leads to a flip of the force direction and produces slim walls with an increased aspect ratio compared to coatings without electromagnetic forces. Moreover, due to the free orientation of the magnetic field, it is also possible to apply a lateral force. However, the strength of the effect correlates with the difference between the thermoelectric potentials of the two materials. Consequently only suitable combinations, e.g., coppernickel, show significant effects, while

the more established coating systems did not show a sufficient thermoelectric potential difference. Therefore, the effect can only be used with a few materials. To use electromagnetic Lorentz forces for technical applications, the current must be generated by an external potential difference.

Due to orientation of the magnetic field and the electric current it is possible to apply a force towards the melt pool (Fig. 2).

For samples with a small cross section the technique shows promising results. Due to the temperature dependence of the electric resistivity, large samples led to a decrease of the current density within the melt pool and the strength of the effect decreases, too. While the cladding area shows a very high temperature (above the melting point) and consequently a high resistance, the conductivity of the surrounding "colder" material is higher. Thus, the current density within the melt pool is very low and a shaping of the cladding geometry can not be reached. For specimen with a small cross section, the laser heats up the whole specimen and a significant variation of the melt pool geometry occurs. For large specimen another technique must be used to apply an external electromagnetic force.

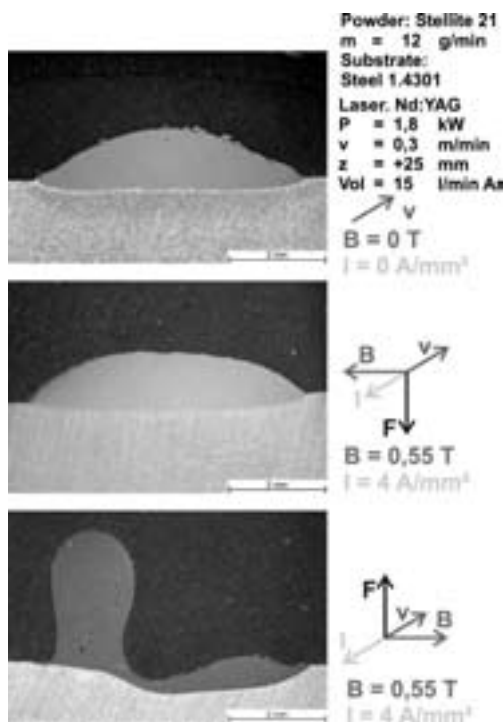


Fig. 2: Lorentz forces through external current.

Beyond inductive heating, high frequency magnetic fields generate a force towards the surface of the metallic materials (SKIN-effect). According to the shape and the position of the coil geometry it is possible to achieve a flat and broad (Fig. 3), or a slim and high coating geometry.

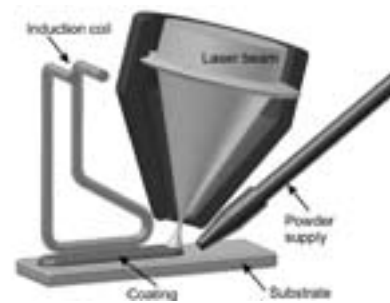


Fig. 3: Process setup for high frequency magnetic fields.

To achieve claddings with an increased aspect ratio a coil must be positioned on either side of the melt pool.

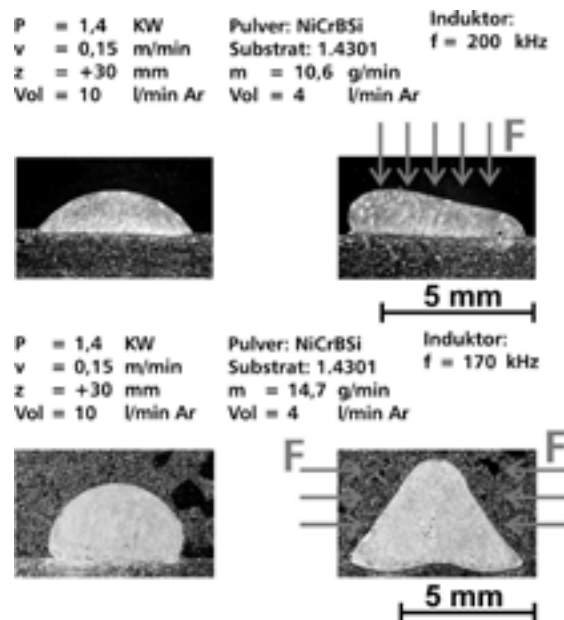


Fig. 4: Magnetic forces generated by the skin effect.

Figure 4 proves the possibility to use high frequency magnetic fields to actively shape the coating geometry. Adapted coil cross sections allow to improve the results for flat coatings. Moreover, by this technique it is possible to increase the aspect ratio of the cladding. Up to now, the stability of the melt pool limits the maximum aspect ratio. Consequently, further investigations concerning the force distribution within the melt pool and the resulting stability of the liquid metal will be the subject of future work.

The project was supported by the German Research Foundation (DFG).

[1] Partes, K.; Theiler, C.; Seefeld, T.; Vollertsen, F.: Laser cladding powered by diode lasers at high processing speed; in Proceedings of the 2nd Internat. WLT-Conference on Lasers in Manufacturing; LIM 2003; Munich; page 51-55; 2003.
 [2] Wilden, J.; Emmel, A.; Bergmann, J.P.; Dolles, M.: Optimisation of energy management through plasma-augmented-laser cladding (PALC); in Proceedings on Internat. Thermal Spray Conference; ITSC 2004; Osaka; Japan; page 5-11; 2004.
 [3] St. Nowotny et al; Hybrid Techniques and Highest Precision in Laser Cladding; LaserOpto 33.2001, Pages 57-60; 2001.
 [4] A. Wetzig, D. Lepski und B. Brenner; Induction assisted Laser Remelting of Grey Cast Iron with Different Chromium Contents; Lasers in Engineering 10.2000, Pages 19-35; 2000.
 [5] Kern, M., Berger, P.; Hügel, H.: Magnetisch gestütztes Laserstrahlschweißen. In: Proceedings of SLT 99, Stuttgarter Lasertage 1999; page 12-17.

Direct Laser Pyrolysis of Nanostructured Micro Components

J. Wilden*, J. P. Bergmann, and S. Schlichting

Department of Production Engineering

Motivation

The aim of this project is to develop components with superior material properties, which cannot be achieved by established processing technologies. Therefore, special attention has to be addressed to the material composition, to the bonding structure and the structural layout in general.

Using polymeric precursors of ceramics appears to be a promising way to produce endmaterials with tailored properties. By means of the process regime, polymerisation and pyrolysis can be controlled in a way to "design" the microstructure of the end component and thereby determine its mechanical and corrosive properties.

In order to best utilize the potential of nanostructured materials for use in microsystem engineering, further development efforts in material design and manufacturing strategies will be needed. Among the great bandwidth of available molecular substances, siliconbased organic polymers are a favourable starting materials to develop a precursor for pyrolytic conversion to ceramic. Because of their resistance against corrosion, oxidation, and wear, materials based on Si-C-N(-O) possess a high potential for applications especially in the field of micro system technology. These organic silicon substances show the ability to generate compact ceramics, by way of cross linking and substitution reactions and formation of covalent or coordinate bonding and resulting thermolysis. Besides the design of a polymeric molecular precursor with regard to required component properties, the pyrolysis process has to be investigated. To enable mass production, it is necessary to produce components with the correct free form shape as well as the intended other properties. Moreover, free form ceramic synthesis is highly suited for rapid prototyping processes. Via Laser supported processes, limitations in surface quality and hardness should be reduced. The laser process discussed in this paper establishes a new method to fabricate parts from preceramic polymers directly. Laser heating of selected regions induces the preceramic polymer to decompose and the resulting product serves to bind the ceramic grains together.

Raw Material

The free form parts are fabricated starting from the commercially available liquid precursor KiON VL20. This polysilazane is a versatile low viscosity

liquid thermosetting resin and consists of repeated monomers in which silicon and nitrogen atoms are bonded in an alternating sequence of cyclic and linear features. It cures to a solid by heating to 180°C-200°C. Besides hydrolysis of vinyl groups and vinyl-polymerization, dehydro-interlinking or reductive amination are the most important cross linking reactions in this polymerization (Fig. 1). These reactions have already been scrutinized with IR- or NMR-spectroscopy as described in the literature [1, 2, 3]. Gaseous by-products are ammonia, hydrogen and methane.

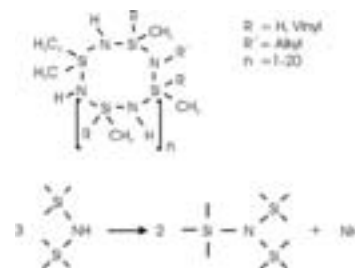


Fig. 1: Polysilazane KiON VL20 and reductive amination.

At elevated temperatures the polymer converts to an inorganic amorphous ceramic. Depending on the kind of process gas, further temperature enhancement leads to either crystalline silicon carbide or silicon nitride ceramics. The transition is caused by separation of small molecules like nitrogen, hydrogen, ammonia, methane and derivatives of them. During transformation to crystalline form under higher temperatures, only slight outgassing reactions occur. With respect to the specifications of the free form parts, polysilazane and also polycarbosilane are the most promising polymer groups, because beside the high ceramic yield of 75%-85%, these polymer families lead to the formation of stable SiCN or SiC/C ceramic matrixes with excellent mechanical properties.

Technology

The energy for the conversion from precursor to ceramic is supplied by a pulsed Nd:YAG laser (LASAG FLS 542) with a wave length of $\lambda=1064$ nm, a maximal mean power of 500 W and a pulse duration of 0.1 ms to 20 ms. The laser beam, with relatively low mean power of about 4 W and pulse durations between 0.1 ms and 2 ms, is focused on the

liquid precursor coated substrate, where absorption takes place. To compose free form parts in the liquid resin, the precursor layer is, in distinction to most literature reports [4, 5], some millimeters thick. Therefore, a minimization of the beam energy density beyond the focal spot has to be guaranteed to avoid unwanted cross linking in this area.

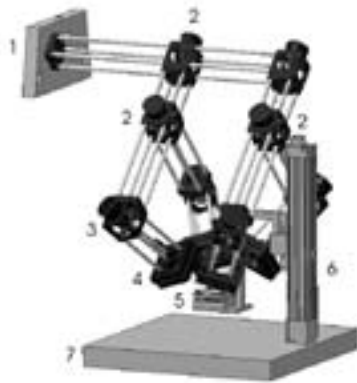


Fig. 2: Optical setup (1 connection to Nd:YAG laser, 2 beam splitter, 3 tilted mirror, 4 focal unit with lenses $f=80$ mm, 5 precursor reservoir, 6 linear axis, 7 xy-table).

In addition to focus lenses with focal distances as small as possible and an expansion of the laser beam to the maximum aperture of the optical components, separation of laser beam is a promising option to reduce the energy density outside the focus (Fig. 2). Furthermore, separation and overlapping of the several beams lead to a precisely defined focal spot, where the energy density is high enough to initiate polymerization and pyrolysis.

Experiments

For the first examinations, rectangular sample parts, with angle length 2×1 mm were produced. A CrNi-steel has been used as substrate material. The structure in figure 3 had been build up by several laser cycles ($n=3$).

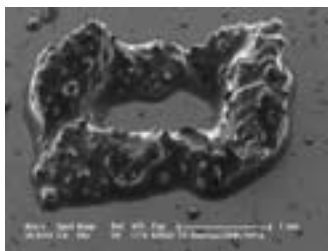


Fig. 3: Laser produced ceramic part on a CrNi-steel substrate, rectangle 2×1 mm, precursor KION VL20.

The shrinkage occurring during pyrolysis can be compensated by a point-to-point process mode.

Moreover, this way of processing will also reduce internal stress, which occurs during oven synthesis of larger parts. Due to the small activated volume, the formation of pores during the pyrolysis reaction is suppressed, as well. Pores, which develop on the surface of pyrolysed ceramics will be closed by liquid precursor and converted by the next laser cycle. Figure 4 shows the microstructure of produced ceramic in a cross section of one side of the rectangle. The white arrow points at the interface between two planes which originate from two laser cycles.

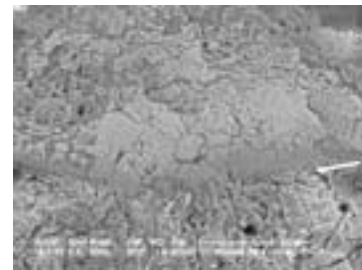


Fig. 4: SEM analysis of laser produced ceramic part.

SEM analysis was applied to characterize the micro-structure of the generated ceramic, while phase characterization was done with X-ray diffraction analysis (XRD). Figure 5 shows a differential measurement of a CrNi-steel substrate with and without a layer of ceramic material on it.

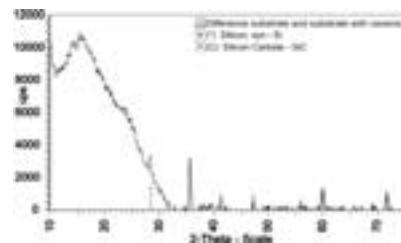


Fig. 5: XRD, substrate and substrate with ceramic.

The denoted peaks could be traced back to cubic silicon carbide (beta silicon carbide) or a silicon-carbo-nitride-like structure with reflexes at the same angles – and pure Silicon crystalline phases. The low intensity of the reflexes suggests that the ceramic was not fully converted into the crystalline form. The amorphous peak between 10 and 30 degree hints to the existence of a large glassy phase or a not pyrolysed polymer residue. Furthermore, hardness measurement showing HU_{korr} in the order of 0.1 GPa and resolving the structural integrity during longer XRD examinations also indicates that unpyrolysed material is still present in the sample.

[1] Bill, J. and Aldinger, F.; Precursor-Derived Covalent Ceramics, *Advanced Mat.*, Vol. 7, No. 9; 1995.

[2] CERASET; Inorganic Polymers, Technical Bulletin, Lanxide Performance Mat. Inc.; 1996.

[3] Kroke, Li, Konetschny, Lecomte, Fasel and Riedel; Silazane derived ceramics and related materials, *Mat. Sci. & Engineering*, R26, Nos. 4-6; 2000.

[4] Krauß, H. J., Otto, A. and Motz, G.; Examinations on laser pyrolysis of preceramic polymers, *LANE 2004*, pp. 949-960.

[5] Motz, G., Ziegler, G., Krauß, H. J., Geiger, M.: Eigenschaften und Anwendungen polymerer und keramiktartiger Schichten auf Polysilazanbasis, *Verbundwerkstoffe und Werkstoffverbunde*; pp. 749-753; 1999.

Profile simulations of Plasma Etching Processes

B. E. Volland*

Department of Micro- and Nanoelectronic Systems

Introduction

Plasma etching of silicon and silicon compounds (Si oxide, Si nitride) is a key technology in the semiconductor and MEMS fabrication. A key feature of plasma (or dry) etching of silicon is the ability to etch silicon in a desired isotropic or anisotropic profile, regardless of crystal orientation.

It is the aim and the dream of the process engineer to precisely predict the outcome of a process recipe without the need for lengthy and costly experiments. Numerical simulations of the physical laws involved in plasma etching seem to be a promising approach. In practice, it is required to incorporate approximations for the sake of simplification and hence faster calculation. Furthermore, usually not all model parameters (e.g., rate constants, cross sections) or even initial conditions are exactly or at all known. Here, assumptions must be used instead.

Our present research work is focused on profile simulations of gas chopping etching of silicon, and of reactive ion etching of 'nano-scale' features in silicon.



Fig. 1. The perfect profile simulator. The three main modules are shown along the center. Initial or boundary conditions are depicted on the left. Arrows symbolized the interaction between modules and boundary conditions. From ref [1] (c) B.E. Volland 2004

Ideal Profile simulator

An ideal plasma etching simulator is depicted in figure 1. It consists of 3 main modules, the plasma module, the transport module, and the surface module. The plasma module deals with the generation of active species, the transport module diffusion and drift of species to the surface, as well as surface-particle interactions like adsorption or reflection. The surface module considers the reactions that lead to surface modification, such as etching or deposition. The modules are strongly interconnected. Each foregoing module supplies the initial condition of the following one. Furthermore, subsequent modules influence foregoing modules through feedback channels. For instance, the consumption of reactant in the surface module diminishes the concentration of that species in the plasma bulk, and hence in the plasma module.

It is these multiple and simultaneous interactions between modules that make profile simulations a challenging task.

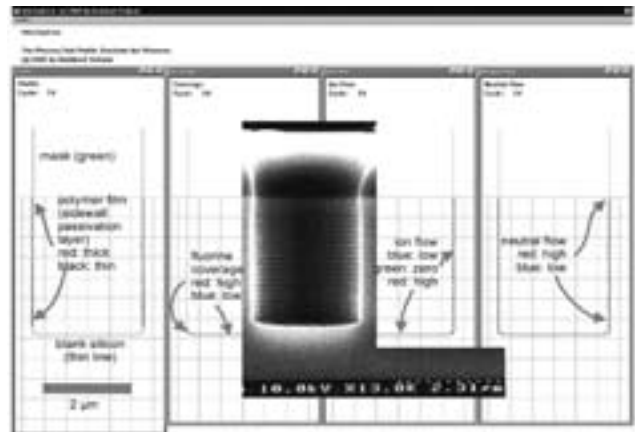


Fig. 2: Etching Profile Simulator "WinSimEtch". The left screen shows the profile and the material composition. Red is sidewall passivation polymer, black is silicon, and green is photo resist. The other screens depict the calculated degree of fluorine coverage, and the flow rates of ions or neutral fluorine radicals. [1]

Real Profile Simulator

For the realised profile simulator, the 3 main modules have been partially decoupled. Furthermore, some of the effects, boundary and initial conditions have

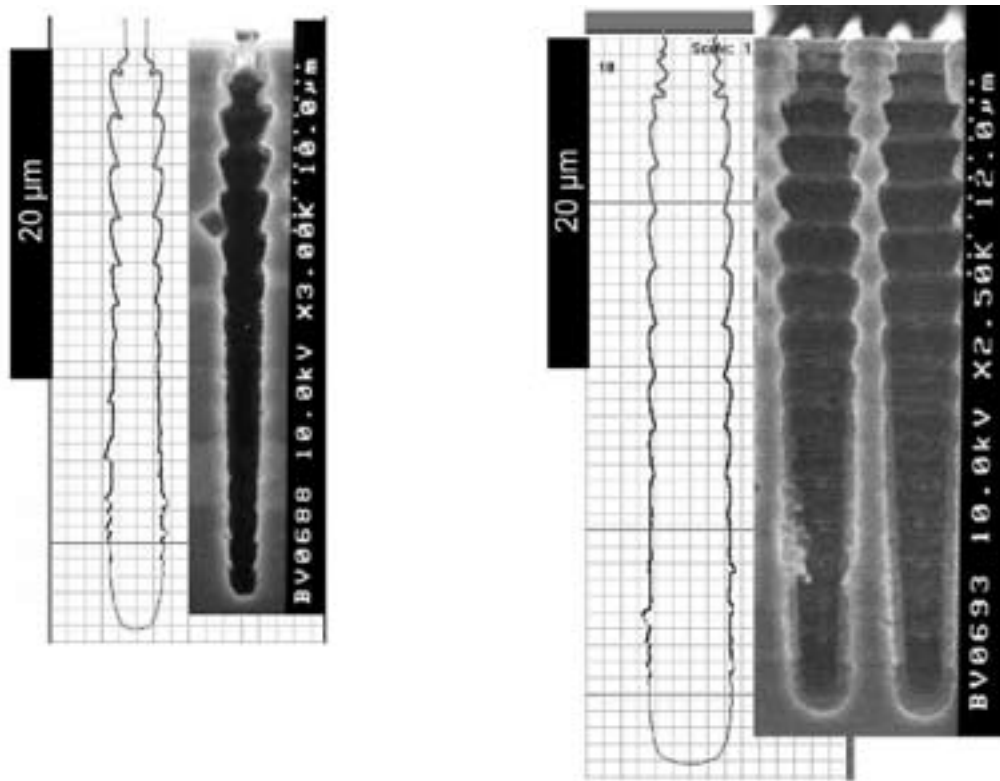


Fig. 3: Simulated and experimental profiles for a 1:1 etching/deposition timing. The simulated profiles agree well with the experimental for both narrow (left) and wider (right) mask openings.[2]

been approximated instead of modelled. Figure 2 shows the realised profile simulation program "WinSimEtch".

Experimental verification

Verification was done by comparing simulated with experimental profiles. The simulations reproduced experimental profiles for different mask openings, depths of etching, and timing ratios between deposition and etching cycles. The good agreement between experimental and simulated profiles (Fig. 3) indicates that the transport effects, as well as the surface reactions are modelled in a suitable way.

European project "nanoPlasma"

The aim of the European research project "nanoPlasma" is the development of a profile simulator including more materials to be etched and more effects taking during plasma etching, namely charging, loading, etc. This research has recently started within our research project "nanoPlasma" (funded by the European commission), assembling leading research groups in the field of process modelling, plasma diagnostics, software and hardware development, and tool manufacturers. Using process simulations, a closed-loop control system for the etching tool, allowing for in situ control and adjustment of relevant internal plasma parameters for stable and reproducible processes independent of tool conditioning and history, shall be developed.

[1] Burkhard E. Volland, "Profile simulations of gas chopping etching processes - Model development and comparison with experiments -", Dissertation Universität Kassel, URN: urn:nbn:de:hebis:34-1167, URL: <http://opus.uni-kassel.de/opus/volltexte/2004/116/> (2004) (c) 2004 B. E. Volland.

[2] Burkhard E. Volland and Ivo W. Rangelow: The influence of reactant transport on the profiles of gas chopping etching processes: a simulation approach, *Microelectron. Eng.* 67-68, pp. 338-348 (2003).

Scanning Proximity Probes for Nanoscience and Nanotechnology

T. Ivanov^{1,*}, K. Ivanova², Y. Sarov², A. Resud², S. Klett¹, B.E. Volland¹, J.-P. Zöllner¹, E. Guliyev¹, and I.W. Rangelow¹

¹ Department of Micro- and Nanoelectronic Systems

² Institute of Microstructure Technologies and Analytics, University of Kassel

The works presented are devoted to the realization of Scanning Proximity Probes (SPP) used as nanotools. It is expected that in the near future major technological breakthroughs in scanning proximal probe nanotools will allow for key scientific impact on analysis and synthesis of nanostructures. All the cantilever sensors used here are based on advanced silicon micromachining and standard CMOS processing. The sensing element or transducer is a piezoresistor embedded in the arms of the cantilever. The change of the piezoresistor resistance, which is caused by the stresses due to the cantilever bending, can be easily converted into an electrical signal suitable for measurement. Moreover, using a newly optimized piezoresistive detection scheme process comprising a Wheatstone bridge, we have designed and fabricated piezoresistive cantilevers for atomic force microscopy [1], which improve surface topography resolution by an order of magnitude to 0.1 nm. The elegance of this concept is that by using an almost identical detection principle and differently functionalized tips or cantilever surfaces, we can detect subtle sample interactions (mechanical, electrical, thermal, and chemical) with a significantly more compact system than with optical beam deflection techniques (Fig.1).

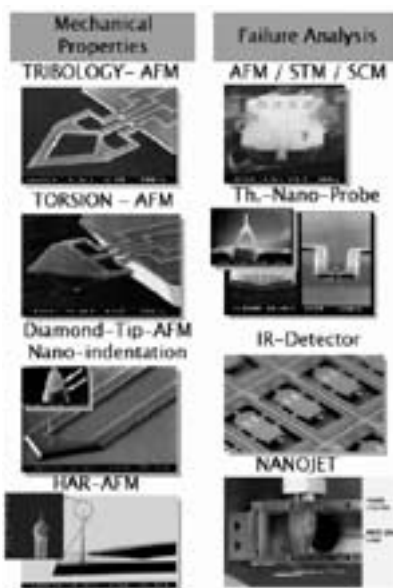


Fig. 1: Piezoresistive scanning probe used as probes for mechanical properties and failure analysis

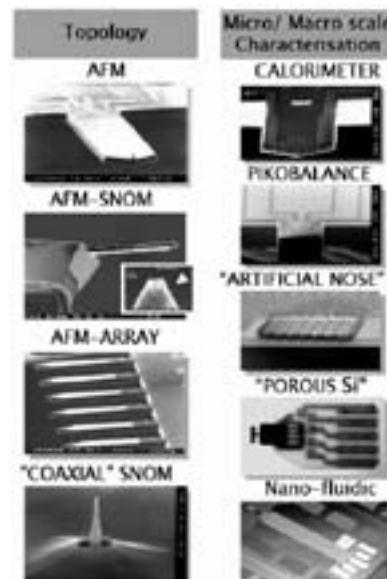


Fig. 2: Functionalized piezoresistive scanning probes for topology and micro characterisation

Furthermore, these piezoresistive cantilevers are much more suited for operation in higher resonance modes compared to optical detection schemes, which require laser beam alignment and monitoring the deflection with a laser spot at different locations along the cantilever in order to avoid the vibration nodes [2]. Consequently, to the integration of the detecting piezoresistive sensor, actuator integration into the cantilever has to be considered as fundamental for the realisation of fast, high-resolution imaging. For signal conversion from the electrical to the mechanical domain, it is necessary to add conversion elements compatible with CMOS processing, using thin film technology. The micro-actuators used in our work are based on the so-called bimetal effect. The actuator consists of a sandwich of layers, namely Al, SiO₂ and Si. The aluminium layer forms the heating microresistor and is used as the driving element. Besides their widespread use in SPPs, where the connection between the probe and sample is realized at a single point (the tip), microcantilevers have recently been used as sensors for measuring extremely small bending moments that are produced by thermally or chemically generated stresses over the whole cantilever surface. Working on such principles,

the advancement of the microcantilever beams as ultra-sensitive force sensors increase enormously. Moreover, nowadays the nano-probes themselves are mechanically, physically, chemically or biologically functionalized for specific physical, chemical or biological applications at high spatial resolutions (Fig.2). Such microcantilever based sensors are irreplaceable in many different scientific fields such as visualization and measurement of different physical quantities in the nanoscale range, as well as for such

applications as information science, microfabrication, quality control, nano-science technology and biological research.

Furthermore, scanning proximity probes (SPP) are uniquely powerful tools for molecular analyses and sensing; they are capable of addressing and manipulating surfaces at the atomic level. Therein lie the keys to unlocking the full potential of nanotechnology.

- [1] Tzv. Ivanov, T. Gotszalk, T. Sulzbach, I. Chakarov, and I.W. Rangelow "AFM cantilever with ultra thin transistor-channel piezoresistor: Quantum confinement", *Microelectronic Engineering*, 67-68C, pp. 534-541, (2003).
- [2]. R. Pedrak, Tzv. Ivanov, K. Ivanova, T. Gotszalk, N. Abedinov, I. W. Rangelow, K. Edinger, E. Tomerov, T. Schenkel and P. Hudek, "Micromachined AFM sensor with integrated piezoresistive sensor and thermal bimorph actuator for high-speed tapping-mode AFM and phase-imaging in higher eigenmodes", *J. Vac. Sci. Technology B* 21 (6), pp.3102-3107, (2003).

Tuning of Resonant MEMS Structures by Internal Strain

V. Cimalla^{1,*}, Ch. Foerster¹, F. Will¹, K. Tonisch¹, J. Pezoldt¹, K. Brueckner², R. Stephan², M. E. Hein², and O. Ambacher¹

¹ Department of Nanotechnology

² Department of RF and Microwave Techniques

Introduction

Resonant MEMS are known for their high sensitivity to the environment [1-3]. The most often used sensing principle is focusing on the detection of a small mass load. The detection of monolayers of molecules, of single virus [4] and of attogram of gold [5] are outstanding results that have been demonstrated previously. Usually a high quality factor Q is necessary for high output signals. This can be realized by storing a high amount of mechanical energy in the resonant MEMS sensor; i.e. the resonator has to be sufficiently heavy. This requires typical MEMS sizes of several $10\ \mu\text{m}$ for the width w and the thickness t , and a length of $L > 100\ \mu\text{m}$. Functionalizing the surface of such structures enables to create arrays of selective sensing elements like electric noses or tongues [6]. With a homogeneous mass load, these arrays are sensitive to monolayers of absorbed substances. However, since the change of the resonant frequency f is given by:

$$\Delta f = -\frac{1}{2} f \frac{\Delta m}{m} \quad (1)$$

the large weight m makes such devices insensitive for single particle measurements, where a very small mass load Δm has to be detected. To achieve a higher sensitivity for smaller mass loads, the dimensions of the devices can be scaled down to nanoelectromechanical systems (NEMS) [3, 7, 8]. However, the Q -factor also decreases with the resonator volume (Fig. 1 [3]).

For an operation as sensing device in air, the main mechanism defining the Q -factor is the viscous damping. An example for a NEMS resonator was published recently [8] showing the decrease of the Q -factor in vacuum and air from 5000 to 30, respectively (Fig. 1). Consequently, most of the fundamental studies on NEMS resonators as well as the demonstration of ultrasensitive mass detection were performed in ultra-high vacuum (UHV) and at low temperatures.

For the operation in air despite the high damping we developed a pulsed mode operation [11] based on the magnetomotive actuation of the resonators [12]. Moreover, we demonstrate the increasing of the Q -factor for the operation in air by specific control of the resonant frequency at a given geometry through variation of the internal strain in such resonant devices [9].

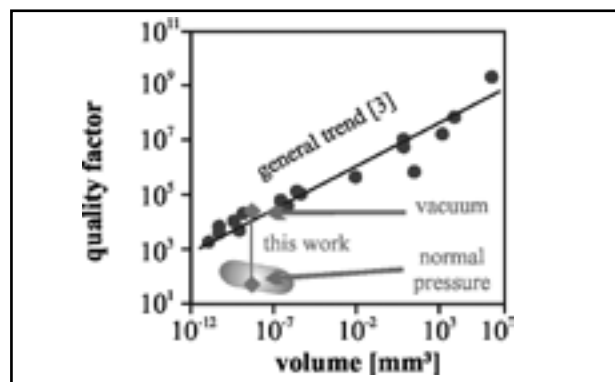


Fig. 1: Maximum quality factor of MEMS and NEMS resonators versus volume [3]. In addition, two examples for the operation of NEMS resonators are shown: The filled area represents our results at normal pressure [9]; the arrows point on the highest and the lowest Q -factor for a NEMS resonator operating in vacuum and at normal pressure, respectively, after ref. [10].

Experimental

The resonator beams were fabricated with AlN and SiC as active layers on Si [3]. 180-250 nm thick single crystalline SiC layers have been grown epitaxially on (100)Si by high-vacuum chemical vapor deposition at temperatures of about 1000°C . 50-110 nm thick polycrystalline AlN layers were deposited on carbonized (111)Si by reactive DC sputtering. 50 nm Au acts as mask for the following etching as well as conducting film for the magnetomotive actuation.

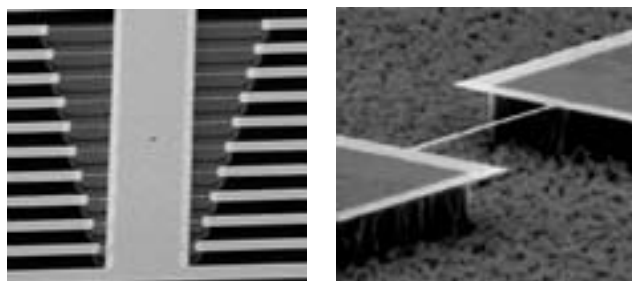


Fig. 2: Scanning electron microscopy images of realized AlN resonator arrays with constant width $w = 4\ \mu\text{m}$ and varying length L (left), and magnification of a single AlN resonator bridge (right) [9, 13].

The measurements were performed in air at a static magnetic field $B \sim 0.4$ T. The pulse mode operation was used to separate the tiny output signal from the excitation voltage in the time domain [11].

Theoretical description

The resonant behavior is characterized by two fundamental parameters [11]. The resonant frequency f of a double clamped resonator can be expressed by:

$$f \approx 1.028 \sqrt{\frac{E}{\rho}} \frac{t}{L^2} c(\epsilon) \quad (2)$$

where E and ρ are Young's modulus and mass density, respectively, and $c(\epsilon) = \left(1 + 0.3 \times (L/t)^2 \times \epsilon\right)^{1/2}$, considers the influence of internal strain ϵ . The influence of air damping on the quality factor is given by:

$$Q = \frac{2}{3} \frac{\rho \cdot t \cdot w}{\left(\frac{\eta_0}{f_{res}} + \frac{w}{2} \sqrt{\pi \cdot \rho_0} \frac{\eta_0}{f_{res}} \right)} \quad (3)$$

where η_0 and ρ_0 are the viscosity and the mass density of the environment, respectively. It can be seen that the resonant frequency is an additional parameter in equation (3), which can be tuned according to equation (2) by modification of the internal strain [9]. This internal strain usually emerges in heteroepitaxial layers as the result of differences in thermal expansion coefficient between epitaxial layers and substrate.

Results and Discussion

The measured dependence of the resonant frequency and the Q -factor on L is shown in figure 3 along with the theoretical curves following equation (2) and (3). The resonant frequency does not show the proportionality to $1/L^2$ as expected for a relaxed beam [11]. Instead, f scales with $1/L$. Consequently, in equation (2) the strain-related term $c(\epsilon)$ becomes dominant, and this internal strain is an additional fitting parameter for the frequency dependence in figure 3. The strain inside the resonator beam can be adjusted independently by the growth condition; however, it is partially released after the formation of the freestanding 3D resonator bridges [1]. A good qualitative agreement was found between the biaxial strain in epitaxial SiC layers on Si, measured by XRD and FTIR ellipsometry. In contrast, the Q -factor of the resonator beams can be reproduced only qualitatively (Fig. 3b). In all cases, the measured Q -factor was higher than expected for air damping according to equation (3). Thus, the simplified model for viscous damping assuming a chain of vibrating spheres has to be refined for a quantitative analysis. Nevertheless, the opposite dependence on the L (compared to Fig. 1) clearly demonstrates the

influence of viscous damping and strain. Moreover, for small lengths ($L < 200 \mu\text{m}$), the Q -factor is higher by a factor of 10 compared to previously obtained results for resonator beams operating in air (Fig. 1). The obtained Q -factor decreases if the internal strain and, consequently, the resonant frequency are decreasing [16]. Values up to 300 were obtained for highly strained SiC beams [9]. The lowest values of $Q \sim 25$ were measured for nearly unstrained AlN beams in agreement with the values reported for unstrained poly-Si beams of the same volume ($Q \sim 30$ [8]). In conclusion, a pulsed mode magnetomotive operation of resonant MEMS was demonstrated in air, where the viscous damping limits the Q -factor of the device. A mechanism to increase the Q -factor by tuning the resonant frequency in strained resonator structures was proposed. For highly strained epitaxial layers an increase of the quality factor by one order of magnitude from about 30 to 300 was achieved. The improvement of the so caused sensing performance of such resonators is the subject of ongoing studies.

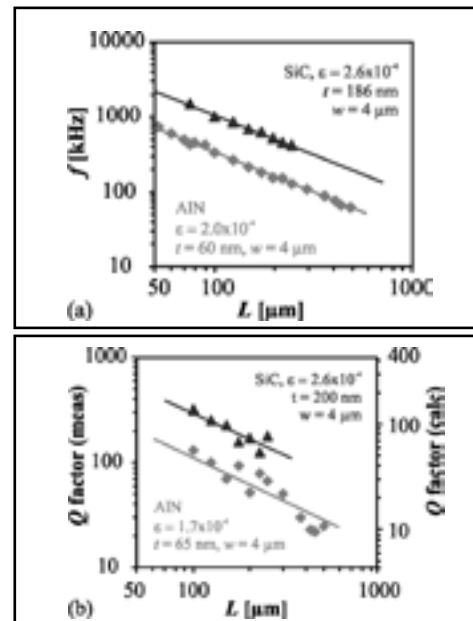


Fig. 3: (a) Resonant frequency and (b) Q -factor measured in air. The lines represent the calculation using equations (2) and (3).

This work has been funded by the German Science Foundation (DFG), Priority program 1157 (AM 105/2-1) and by the German Academic Exchange Service (DAAD).

- [1] Y. Arntz et al, Nanotechnology 14, 86 (2003)
- [2] J. Fritz et al, Science 288, 316 (2000).
- [3] K.L. Ekinci and M.L. Roukes, Rev. Sci. Instrum. 76, 061101 (2005).
- [4] B. Ilic et al, Appl. Phys. Lett. 85, 2604 (2004)
- [5] K.L. Ekinci et al, Appl. Phys. Lett. 84, 4469 (2004).
- [6] H.P. Lang, et al, Appl. Phys. A 66, S61 (1998).
- [7] H.G. Craighead, Science 290, 1532 (2000).
- [8] E. Forsen et al, Appl. Phys. Lett. 87, 043507 (2005).
- [9] V. Cimalla et al, Appl. Phys Lett. 88, 253501 (2006).
- [10] B. Ilic et al, Appl. Phys. Lett. 86, 193114 (2005).
- [11] K. Brueckner et al, Proc. 35th European Microwave Conference, Paris, October 2005.
- [12] A. Cleland et al, Appl. Phys. Lett. 79, 2070 (2001).

Sacrificial Layer Technique for the Fabrication of GaN-Based MEMS on Sapphire

K. Tonisch^{1,*}, F. Will¹, V. Cimalla¹, H. Romanus¹, M. Eickhoff², and O. Ambacher¹

¹ Department of Nanotechnology

² Walter Schottky Institute, Technical University of Munich, Garching

Introduction

Group III-Nitrides such as aluminium or gallium nitride (AlN and GaN) and their ternary alloys are favorite materials for many devices due to their exceptional electrical and chemical properties [1]. Besides high-temperature applications and high electron mobility transistors, there already exist several sensor concepts based on the pyro- and piezoelectric properties of Group III-Nitride heterostructures [2]. So far only few applications for GaN-based microelectro-mechanical systems (MEMS) have been reported. This is mainly due the fact that the best epitaxial results are achieved on sapphire and SiC, which are materials of an extraordinary chemical stability. While this stability is very favourable when it comes to biocompatibility or applications in harsh environments, it causes great difficulties when in MEMS fabrication, as the processing is most often accomplished by underetching the functional layers to realize freestanding structures.

Whereas vertical etching of sapphire by reactive ion etching (RIE) based on a BCl_3 and Ar gas mixture with a high physical (sputtering) component has been demonstrated [3], isotropic undercutting of the sapphire substrate has not been achieved yet.

One possibility to circumvent these difficulties is the use of sacrificial layers that can be etched easily. Thus, a material has to be chosen as sacrificial layer that serves simultaneously as a buffer for the epitaxial growth of the following active layer and can be etched selectively afterwards. If no suitable material is available, the chemical stability of a sacrificial layer can be intentionally altered (in comparison to the active layer) by lowering the crystal quality. It is widely known that especially wet etching proceeds much faster at crystal defects such as threading dislocations, grain boundaries or pores [4]. The epitaxial growth of GaN on various porous materials such as TiN, SiC and on porous GaN has been achieved by several groups [5, 6]. Some groups even report an improvement of the GaN layer quality compared to more common substrates and templates due to strain relaxation.

Thus, porous or nanocrystalline layers are etched much faster than a single-crystalline layer of the same material and are suitable for a following epitaxial growth step, which predestines them for the use as sacrificial layers. We present a novel approach

to fabricate GaN-based MEMS on sapphire with the help of a sacrificial layer of sputtered nanocrystalline AlN.

Experimental

The AlN films have been grown on sapphire substrates at 350°C by reactive magnetron sputtering of a high purity Al target in pure nitrogen atmosphere. They were analyzed by RHEED (Reflection High Energy Electron Diffraction), AFM (Atomic Force Microscopy) and HRXRD (High Resolution X-Ray Diffraction) prior to the growth of the epitaxial GaN layers. The GaN growth was accomplished using a commercial MOCVD AIX200RF (Aixtron).

The resonator bars of different geometries were defined by optical lithography. A multilayer of Ti/Au/Ni was structured by lift-off and served as etch mask and conductive layer for magnetodynamic actuation. The GaN bars were dry etched by an anisotropic chlorine-based RIE process. Finally, wet etching with 25% KOH removed the sacrificial AlN layer underneath the bar.

Results and Discussion

The nanocrystalline sacrificial AlN layers of 100 nm to 500 nm thickness exhibited a columnar growth with a column diameter of about 20 nm (Fig. 1). XRD analysis showed a pure c-axis orientation with a FWHM of about 4° of the rocking curve.

The GaN layers with a thickness of 550 nm reached the structural quality of those grown on sapphire substrates with a standard growth process. The AFM topography displays a smooth surface with the typical steps of a two-dimensional layer-by-layer growth (Fig. 1).

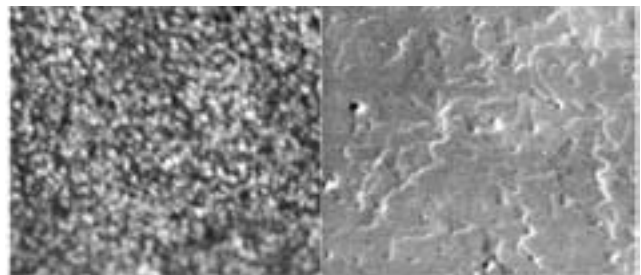


Fig. 1: AFM topography of a sputtered AlN film ($1 \mu\text{m}^2$, left), surface of the GaN layer ($5 \mu\text{m}^2$, right).

Although the AlN layer shows a profound recrystallisation, it remains defect-rich compared to the GaN layer and therefore well etchable. Both interfaces display a strong epitaxial relationship (Fig. 2). Since the AlN surface remains three-dimensional, also the AlN/GaN-interface is not even and resembles very much the interface that emerges in a typical MOCVD-growth of epitaxial GaN with a low temperature AlN-nucleation layer.

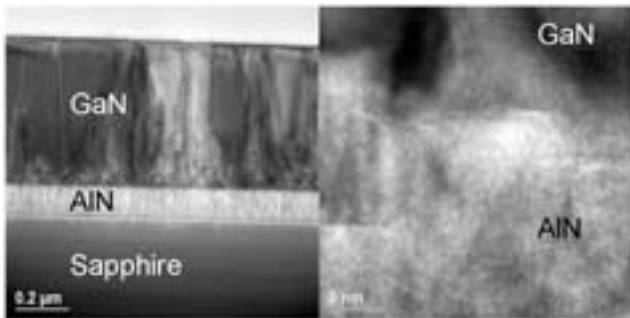


Fig. 2: TEM cross section of the multilayer epitaxial GaN/ sputtered AlN on sapphire (left, magnification: 21 000) and of the interface GaN/AlN (right, mag.: 880 000).

For the fabrication of MEMS the strain of the active layer is very important. While tensile strain of the active layer results in both, a higher resonant frequency and a higher quality factor, compressive strain reduces these characteristics and hence the signal quality drastically due to buckling effects [7]. The expected result for growing a material epitaxially on a second material with a smaller lattice constant would show compressive strain of the material on top, which is in our case the active layer. The lattice constants of GaN were gained from reciprocal space maps of the symmetric (002) and asymmetric

(20-5) reflection peak by HRXRD with $a=3.1917 \text{ \AA}$ and $c=5.183 \text{ \AA}$. The theoretical values of the lattice constants a (and c) of GaN and AlN are $a = 3.189 \text{ \AA}$ ($c=5.185 \text{ \AA}$) and $a=3.112 \text{ \AA}$ ($c=4.98 \text{ \AA}$), respectively. Unexpectedly, the derived lattice constants show only a small but tensile strain of the GaN layer, which is a perfect result for the fabrication of MEMS. Thus, sputtered nanocrystalline AlN films are suitable as sacrificial layers and enable the fabrication of single-crystalline GaN-based MEMS on sapphire.

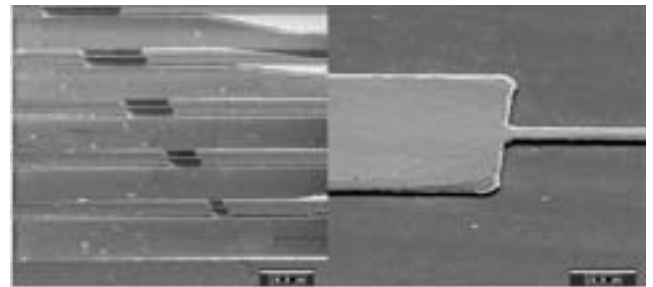


Fig. 3: Double-clamped GaN-resonators processed by sacrificial layer technique.

Further research will include the theoretical modelling and experimental characterization of the resonators in terms of their resonant frequency and quality factor under ambient conditions as well as in vacuum [8]. Since all materials used in this technology are stable in biological environments, these resonators are appropriate tools to monitor biological processes. Combining this new technology with AlGaIn/GaN heterostructures (with an inherent polarization-induced 2D electron gas as possible readout), novel and sophisticated sensor concepts will be feasible in the near future. Thereby the intended actuation will be based on the piezoelectricity of the group III-nitrides [9].

This work has been funded and supported by the Deutsche Forschungsgemeinschaft, SPP 1157: "Integrierte elektrokeramische Funktionsstrukturen", contract no. AM105/2-1 and SPP 1165: "Nanodrähte und Nanoröhren", contract no. CI 148/2-1.

- [1] O. Ambacher, J. Phys. D: Appl. Phys. 31 (1998) 2653.
- [2] M. Eickhoff, J. Schalwig, O. Weidmann, L. Görgens, R. Neuberger, M. Hermann, G. Steinhoff, B. Baur, G. Müller, O. Ambacher, and M. Stutzmann, phys. stat. sol. (c) 0 (2003) 1908.
- [3] C.H. Jeong, D.W. Kim, H.Y. Lee, H.S. Kim, Y.J. Sung, G.Y. Yeom, Surf. Coat. Techn. 171 (2003) 280.
- [4] I. Cimalla, Ch. Foerster, V. Cimalla, V. Lebedev, D. Cengher, O. Ambacher, phys. stat. sol. (c), accepted for publication.
- [5] Y. Fu, F. Yun, Y.T. Moon, Ü. Özgür, J. Q. Xie, X.F. Ni, N. Biyikli, H. Morkoc, L. Zhou, D.J. Smith, C.K. Inoki, T.S. Kuan, J. Appl. Phys. 99 (2006) 033518.
- [6] C. K. Inoki, T. S. Kuan, A. Lee, A. Sagar, E. M. Feenstra, D. D. Koleske, D. J. Diaz, P. W. Bohn, I. Adesida, J. of Elec. Mater. 32, No. 8 (2003).
- [7] T. Ikehara, R.A.F. Zwijze, K. Ikeda, J. Microm. Microeng. 11 (2001) 55.
- [8] Ch. Foerster, V. Cimalla, K. Brueckner, V. Lebedev, R. Stephan, M. Hein, O. Ambacher, phys. stat. sol. (a), 202 (2005), 671.
- [9] K. Tonisch, V. Cimalla, Ch. Foerster, H. Romanus, D. Dontsov, O. Ambacher, Sens. Act. A (2006), in press.

Bonding of MEMS devices with black silicon

M. Stubenrauch^{1,*}, C. Kremin², M. Fischer², O. Nagel¹, A. Albrecht¹

¹ Department of Micromechanical Systems

² Junior Research Group Microfluidics and Biosensors, MacroNano[®] – Center for Innovation Competence

I. Motivation

Black silicon is known as side effect of most reactive ion etch processes (RIE). Some applications for this modification of silicon on wafer surfaces have come up in recent years like optical absorber elements [1], field emitters [2] and non-wettable surfaces using the Lotus-effect [3]. A completely different approach is the use of black silicon for mechanical applications [4].

During manipulation in the laboratory two small pieces of a wafer with black silicon on the surface came in contact with each other and stuck together tightly (see Fig. 1). Doing this deliberately, we found that this sticking effect could be reproduced with high retention forces.

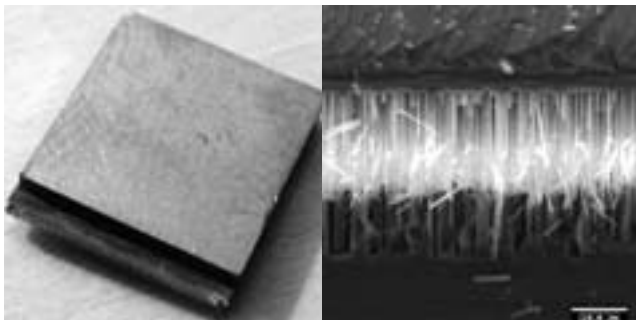


Fig. 1. Silicon chips bonded with black silicon

II. Technology

A detailed investigation of the samples showed needle-like structures with a high lateral density up to 10^6 needles per mm^2 . The needles are about 15-25 μm long, depending on the process time. With very long process times (>40 min) the etch rate shows a significant saturation effect which limits the maximum needle length to about 25 μm . The diameter of the needles at the tip varies from 300-500 nm. Due to the gas chopping during the process the side walls of the needles are typically barbed (see Fig. 2).

Therefore, we propose that the contact of two surfaces with black silicon leads to a force-assisted, form fitting bond. Adhesion between the drastically increased surface areas may also contribute to the retention force. The process for generating the black silicon on our ICP-ASE[®] facility from STS[®] was optimised to get a homogeneous distribution over 4"

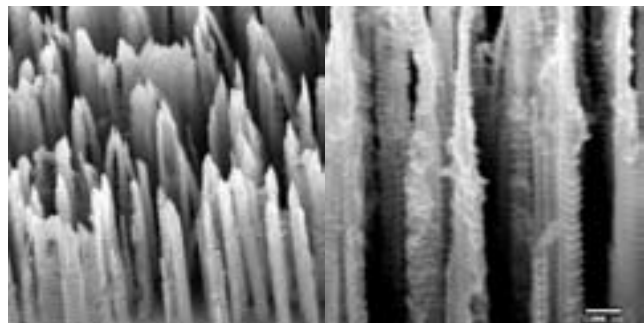


Fig. 2. Detailed view of the silicon needles.

wafer surfaces. For finding the optimal parameters, design of experiments (DOE) was applied to reduce the required effort. For applications in MEMS it is necessary to assemble pre-structured wafers. Thus, we showed the possibility to generate black silicon with determined parameters on different surfaces like the bottom of dry etched trenches, top-level surfaces of dry etched wafers, as well as side walls of wet etched V-grooves. It was possible to implement the process into most of our process chains. So far, we have not discovered any incompatibilities as long as we have a full 4" wafer without through-holes.

III. Experiments

The bond process, which works at room temperature and without any additional layer or material produces retention forces of up to 380 N/cm^2 (3.8 MPa). To qualify the resulting forces, several test runs with a bond surface of 1 cm^2 and a contact force of 5 kN have been conducted. The curve in figure 3 shows the dependency between failure rate and test force generated with a modified industrial pull tester.

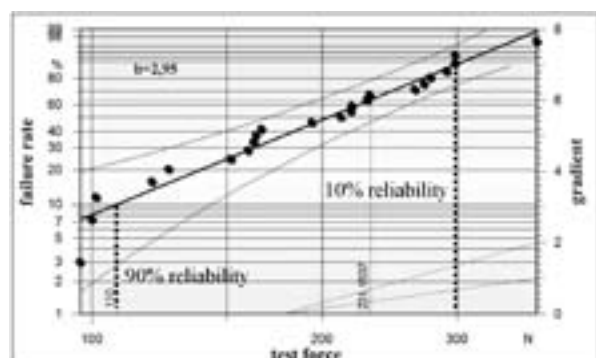


Fig. 3. Weibull analysis of the retention forces

The calculated value of the Weibullmodule is $b = 2.95$ which indicates an increasing failure rate at higher test forces. The curve demonstrates that with a reliability of 90 % a retention force of approximately 110 N (1.1 MPa) can be guaranteed. The retention force strongly depends on various parameters such as the applied contact force, the characteristics of the black silicon as well as the surface qualities of the wafers.

The simple, Velcro®-like concept of the bonding provides multiple usage. Therefore three test series with different contact forces were performed, to determine the decrease of adhesiveness by multiple usage of the bond surface. Figure 4 shows the measured curves which lead to no measurable retention after the 12th use. This is caused by the increasing rate of disintegration of needles at each bond process. A microscopic analysis of the probes confirmed the virtually complete destruction of the needles after the 12th use. Due to this effect, effective multiple usage of the same bond surface is limited to low contact forces with up to five uses, only. The detachment process can be enhanced through the use of ultrasonic waves to lower the necessary detachment force and therefore limit the rate of disintegration of needles.

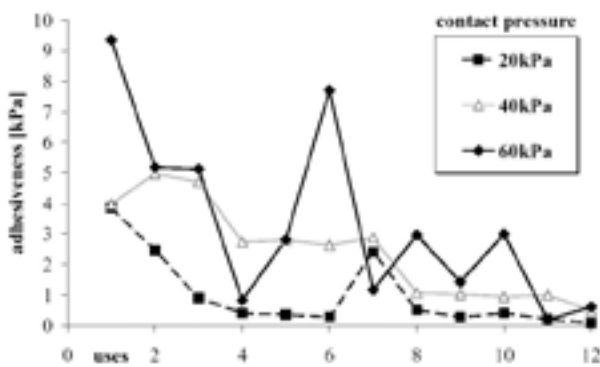


Fig. 4. Repeated use of the black silicon bonding

Another test series was conducted to examine the impact of the assembly (contact) force on the penetration depth and on the retention force. A nonlinear correlation between the two parameters was found. The penetration depth can not exceed the needle length L . Therefore, the achievable retention force is limited which results in a saturation effect for high compression forces. The necessary contact force to reach full retention force saturation lies between 200 N and 10 kN and depends strongly on the geometries of the needles and other fabrication process parameters.

III. Applications

The alignment of MEMS components with nm-precision and arbitrary positions without any

drift offers a wide range of applications for this new bonding technology like microfluidic systems and micro optical or mechanical mountings. Fig. 5 shows one of the developed microfluidic systems to test and evaluate the different properties of the bond, e.g. nonpermeability for liquids and gases, bond strength etc. The bonded areas vary between 70 and 85 mm². The system can be supplied with different feed-in-pressures through an attached fluidic connector on the top. For the shown system the leak rate achieves 2 ml/min for air with a feedin pressure of 100 kPa (1 bar). Wetting the system causes the leak rate to drop to almost zero due to capillary forces which pull the fluid into the remaining interstitials and seal off the bond interface more tightly. Another application area can be the support of gluing processes. A severe problem of these assembly techniques is the mechanical drift of the components during application or curing the adhesive. Using our process for a pre-fixation of the samples at the required position can prevent any drift. Even a leveling of small samples in μm steps can be done to get a parallel alignment within the range of the penetration depth (15-25 μm).

All these assembly or fixation processes can be done at any desired temperature.

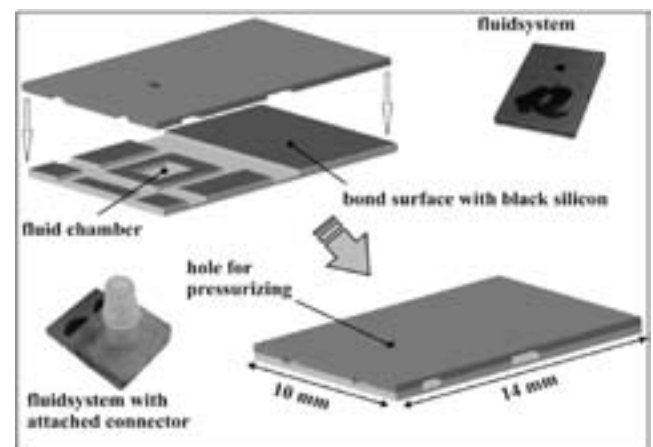


Fig. 5. Fluidic test chip bonded with black silicon

IV. Summary and outlook

It was shown that black silicon is a very useful material for mechanical applications. The bonding strength of black silicon interfaces (about 3.8 MPa) can be compared with good adhesive bonding. Reversible alignment and fixation of microparts can enable new methods for the assembly of hybrid micromechanical systems, e.g. microoptics, sensor and actuator arrays or even as carrier systems for ultra-thin wafers.

- [1] Burgers A.R., Tool C.J.J., Hylton, A.W., Weeber A.W., Verholen A.G.B.J., Gardieniers J.G.E., Boer M.J. and Elwenspoek M.C.: Silicon Solar Cells Textured By Reactive Ion Etching and Processed With Screen Printing, 2nd World Conference and Exhibition on Photovoltaic Solar Energy Conversion, Vienna, pp. 1531-34. (1998).
- [2] Kanechika M., Sugimoto N., Mitsuhashi Y.: Control of shape of silicon needles fabricated by highly selective anisotropic dry etching, Jour. of Vacuum Science & Technology B: Microelectronics and Nanometer Structures Vol. 20, I. 4, pp. 1298-1302 (2002).
- [3] Kim, J., Kim C.: Nanostructured surfaces for dramatic reduction of flow resistance in droplet-based microfluidics, IEEE Conference MEMS, Las Vegas, pp. 479-482 (2002).
- [4] Stubenrauch M, Fischer M, Kremin C, Stoebenau S, Albrecht A and Nagel O, Black silicon - new functionalities in microsystems; J. Micromech. Microeng. 16, pp. 82-87 (2006).

Monolithic Integration of Functional Liquid Crystalline Elastomers into MEMS

J. Król^{1,*}, M. Hoffmann¹, H. Wurmus¹, A. Sánchez-Ferrer², and H. Finkelmann²

¹ Department of Micromechanical Systems

² Institute of Macromolecular Chemistry, Albert-Ludwig University of Freiburg

Introduction

Fulce (FUnctional Liquid Crystalline Elastomer) is a complex elastomer material with liquid crystalline components included in a network of an elastomer backbone and crosslinkers that is developed and produced by Prof. Finkelmann and A. Sánchez in Freiburg.

Fulce's unique property is a reversible macroscopic change of its length. The temperature-induced macroscopic change can reach up to 380% of film elongation. [1] The nematic-isotropic phase transition is the switch process. Figure 1 is the characteristic temperature-shrinking curve of one sample, where $T_{red} = T/T_{ni}$ and $l_{iso} = L/L_{iso}$. The UV-induced change in length is smaller but also remarkable.

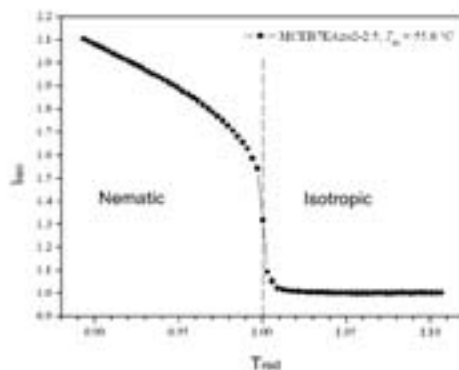


Fig. 1: Phase transition characteristics of Fulce (Courtesy of A. Sánchez).

Fulce has side-chain and main-chain material families, depending on the position of the liquid crystals in the network. The material we used in our experiments is from a side-chain-type polymer. There are two forms of Fulce used in Ilmenau: elastomer stripes with actuator properties and a prepolymer. Here, we deal with the prepolymer form of the material.

We want to use Fulce as an actuator material in micromechanical systems. The application of aligned, working films is not always suitable due to their size and handling problems.

To gain a macroscopic movement the material has to be oriented. The alignment can be done with an external magnetic field or by mechanical stress. The weak diamagnetic liquid crystals turn parallel to the field lines, or upon stress parallel to the

force. Crosslinking in this ordered state leads to the macroscopic switching property.

Technology and Design

We designed silicon demonstrator structures to integrate Fulce into microsystems.

During the iterative development process of the silicon structures first we had to estimate the actuator force of Fulce. In previous designs we estimated 75 mN (sample w*th: 5 mm*0.3 mm). In the last design we scaled down the Fulce to 0.15 mm*0.05 mm, the estimated force is then 2.5 mN which leads to a complete redesign of the silicon structures too.

For this reason we reduced the forces of the spring system from 70 mN to 2 mN, the characteristic silicon structure width from 500 μm to 50 μm and the chip size from 18 mm*55 mm (w*h) to 3.7 mm*8.4 mm. The reduction of the width increases also the achievable magnetic field strength between the flux-guiding parts of the magnetic circuit.

We also simulated and designed a new magnetic circuit with permanent magnets and flux-guiding parts to reach the required field strength in the air gap. Figure 2 shows the measured field strength in the gap at various distances. One small picture in the figure shows one simulation result of the magnetic field, the other the solid body model cut in the simulated plane. There is 2.35 Tesla field strength in the 2-mm airgap.

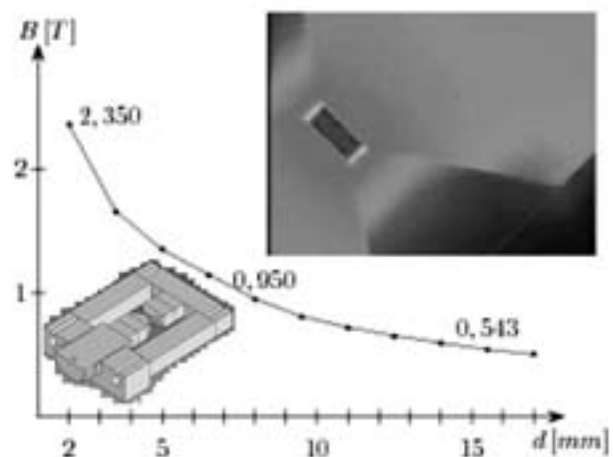


Fig. 2: Magnetic field strength in the air gap at various distances.

The most suitable demonstrator is a symmetric, parallel spring system (see Fig. 3). It has a capillary gap where one droplet of the prepolymer is positioned. The fluid forces hold the droplet in position as long as the solvent evaporates, afterwards a thin polymer film remains.

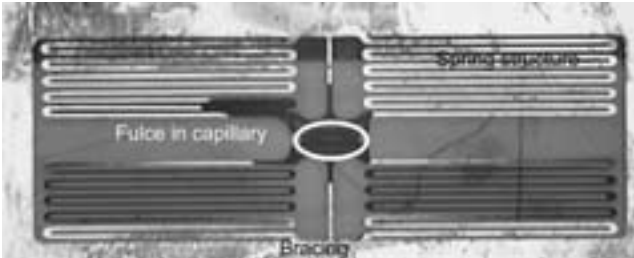


Fig. 3: Picture of a braced spring system with Fulce in the capillary.

The next step was the alignment. Due to bracing in the structure – for better shock resistance during processing – the alignment with the mechanical stress is not applicable. So we used the magnetic circuit for the external magnetic field.

After finishing the magnetic alignment, the samples were crosslinked in the magnetic field by UV-light. (Wavelength: 365 nm, intensity: 3 W/cm², time: 10 seconds).

Experiment

A silicon hotplate with integrated temperature sensor and controlling was built. It was heated up to 68 °C, which is over the nematic-isotropic temperature of this Fulce. The natural cooling process was observed by optical microscopy, and pictures were captured every second until the sample and the hotplate cooled down to room temperature.

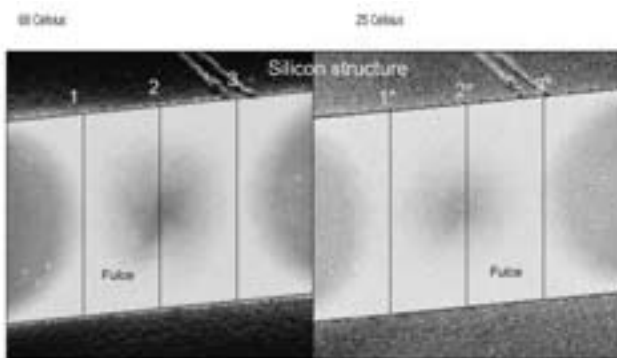


Fig. 4a: Aligned Fulce with measuring lines at 68°C and room temperature.

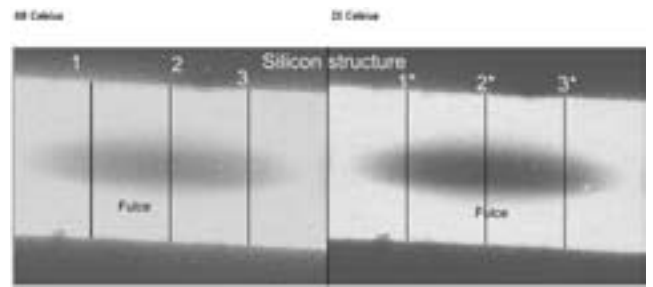


Fig. 4b: Not aligned Fulce with measuring lines at 68°C and room temperature.

The ellipse in figure 3 shows the area which was photographed in the experiment.

In the figures 4a and 4b the drawn vertical lines are the help lines for the lengths measurement, we calculated an average length of them and compared the lengths taken at 68 °C and room temperature.

We could observe the normal thermal behaviour of the compliant structure on an unaligned, crosslinked structure, on cooling the gap shrank 49.77 %.

In contrast to this phenomenon we could observe an elongation of the silicon structure with integrated, aligned and crosslinked Fulce on cooling. The elongation was 3.59 ‰. As a control we also observed the phase transition of the material in the microscope. There was a change in the visible structure, graininess of the Fulce.

Conclusion

We could integrate Fulce into a micromechanical system in the monolythic way, align and crosslink the material and detect a movement of the aligned Fulce.

This work was partially supported by the European Community's Human Potential Programme under contract HPRN-CT-2002-00169, Fulce.

[1] Wermter, Hendrik; Finkelmann, Heino: Liquid crystalline elastomers as artificial muscles. In: e-Polymers 013 (2001); http://www.e-polymers.org/papers/finkelmann_210801.pdf.

Hybrid Integration of FULCE Actuators in Microsystems

T. Fischl*, H. Wurmus, M. Stubenrauch, A. Albrecht, and M. Hoffmann

Department of Micromechanical Systems

Introduction

The development of FUnctional Liquid Crystalline Elastomers (FULCE) allows to use this new type of actuator combined with microsystem technologies. This rubber-elastic actuator material shows a shrinking of 70% under thermal load, so it provides new possibilities in micro-actuation. Our purpose is developing new applications which benefit from big deformations of FULCE materials, but require low actuator forces (max. stress 41kPa). We combine FULCE actuators with structured poly(dimethyl)siloxane (PDMS) membranes in a hybrid way, that can follow the deformation of the actuator without losses of time or movement.

We show a method to measure the deformation of the elastic actuator with an integrated sensor membrane without external measuring devices. This experiment allows to use insulating rubber-elastic membranes as electromechanical transducer by elastic sensor actuator systems.

FULCE materials are composed of two subsystems: the mesogenic groups that self-assemble to give the mesomorphic properties and the weak density of polymeric chains reticulations that leads to the rubber elasticity [1, 2]. The differing chemical and physical properties, as well as the unusual behaviour during switching provide the innovation of the material. The functional liquid crystalline elastomers usually are called "an artificial muscle". The name refers to its actuator function. The crystalline molecules (mesogenic groups) of the aligned elastomers lose its orientation by increasing temperature during switching (nematic-isotropic transition), which results in macroscopic shortening of the film ([2], see Fig. 1).

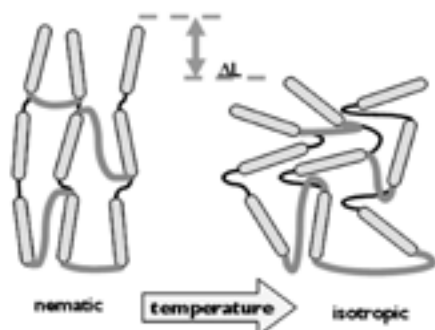


Fig. 1: Nematic-isotropic transformation of thermo-mechanical FULCE actuators.

Technology of the compliant structure

Earlier experiments have already shown that FULCE actuators work together with silicone rubber because of their similar chemical structure. The adhesive forces are sufficient to crosslink thin ($\sim 50 \mu\text{m}$) structured silicone rubber on the surface of the actuator.

The characterisation of the FULCE actuators showed that the actuator stress is too small for actuating classical microtechnical applications, such as silicon arms or membranes.

Our purpose is to develop suitable systems in which structured membranes are loaded by pulling or pressing. The defined concertinalike structure is able to agree this purpose.

The mould consists of two parts of etched silicon (see Fig 2.) and is prepared by wetetching in KOH.

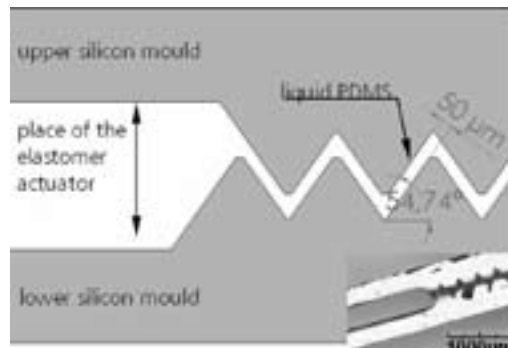


Fig. 2: Model and photo of the closed silicon tools.

A thin releasing agent is used between the silicone rubber and silicon to reduce the adhesive forces after cross-linking. The releasing agent layer is tri-chloro (perfluorooctyl)silane ($\text{CF}_3(\text{CF}_2)_5\text{CH}_2\text{CH}_2\text{SiCl}_3$) made by Aldrich.

The FULCE polymer block (fully cross-linked) is inserted into the mould and space between the moulds is filled up with not cross-linked silicone rubber: The moulds are dipped in silicone rubber (Sylgard 182, from Dow Corning), air bubbles are avoided by filling the moulds due to surface tension effects.

Technology of the sensor membrane

The deformation of the compliant structure follows exactly the movement of the actuator (Fig. 3). The large displacements (145%) of the elastic system

can be sensed with help of adsorbed nano-particles on the surface. The deformation of the structure is translated to a change of the electric resistance of the surface, so we get a proportional quantity from the deformation of the super elastic structure.

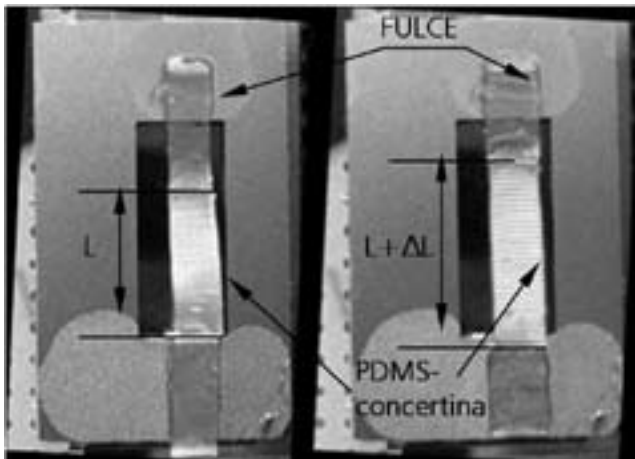


Fig. 3: Series connection of structured PDMS and FULCE actuator on a hot plate: left: at room temperature; right: at increased temperature; see stretched PDMS concertina.

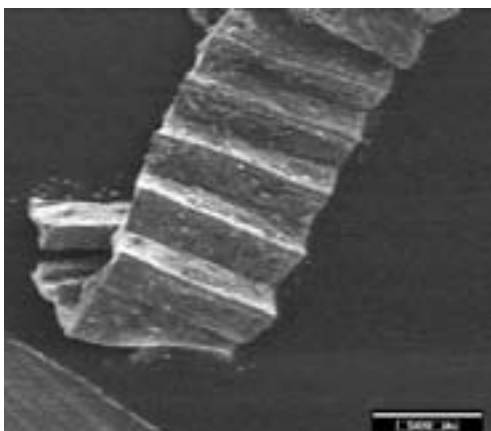


Fig. 4: SEM photo of the electrically conductive concertina structure.

The adsorption of the carbon particles was originally designed for heating of the FULCE [FULCE conference, Ljubljana 2005 by Martin Chambers]. The concertina-like structure is placed in cyclohexane. A carbon-in-solvent dispersion with 7.5 g/l C-content was used to adsorb the carbon nano-particles onto the surface. The diffusion process of the carbon particles is supported with ultrasound. We used "carbon black" with 30 nm primary particle grade from Degussa AG (Printex XE2) for this experiment (see Fig. 4).

Experiments

The electrical properties of the adsorbed carbon black particles are analysed as a function of the deformation. The deformation of the conductive super elastic membrane is measurable with a full Wheatstonebridge joint to the membrane. The resistivity of the doped super elastic structure is $\rho=2,11 \Omega\text{m}$ at a deformation of $\Delta\epsilon=0\%$. The measured structured has 9 periods between the measuring point. Its thickness is $50\mu\text{m}$, its breadth 1.4 mm. The length of the measured compliant structure is $L=2.67 \text{ mm}$.

A dependence of the response time is found by these measurements. The electric resistance is decreasing by about 1% (elongation 122.5%: $R_0=213 \text{ k}\Omega \rightarrow R_{122.5}=209 \text{ k}\Omega$). The specific curves represent a given position of the membrane. The electrical properties of the compliant structure are measured between 85%-129.96% ($\epsilon=(L_0+\Delta L)/L_0$) deformation. A surface was fitted on the measured point (see Fig. 5).

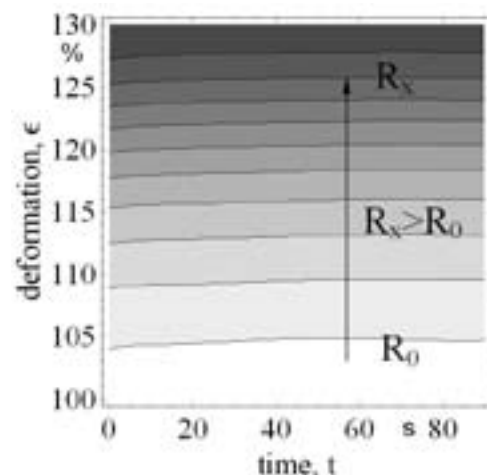


Fig. 5: Electric resistance (resistance-levels) (R) in dependence of time (t) and deformation (ϵ) by the electric conductive super elastic PDMS structure.

Outlook

For further improvements, we will combine FULCE actuators with "Black Si" for fixation in microsystems. This will also allow an easy electrical connection between the sensing concertinalike structure and the Wheatstone bridge.

Special thanks to Dr. Bernd Halbedel and Michael Jakob from the Department of Glass and Ceramic Technologies for the help with developing the carbon dispersion. T. Fischl acknowledges the financial support provided by the European Community's Human Potential Programme under contract HPRN-CT-2002-00169, FULCE.

- [1] B. Donnio, Hendrik Wermter, H. Finkelmann, A simple and Versatile Synthetic Route for the Preparation of Main-Chain, Liquid-Crystalline Elastomers, in: *Macromolecules* 33 (2000), 7724-7729.
- [2] H. Wermter, H. Finkelmann, Liquid crystalline elastomer as artificial muscles, in: *e-Polymers* 2001, no. 013.

Microembossing of LTCC Green Tapes

H. Bartsch de Torres^{1,*}, M. Kallenbach¹, A. Albrecht¹, J. Botiov¹, and M. Hintz²

¹ Department of Micromechanical Systems

² Department of Microperipherals

Introduction

Low Temperature Co-fired Ceramics, also referred to as LTCC, are interesting materials for the realisation of MEMS in the mesoscale [1], i.e. dimensions in the range of 100 μm up to millimetres. Another application is in the field of MEMS packaging, for example performed by the Mach-X system [2], a construction kit consisting in modular components, which allows flexible assembling of complex microsystems. Since vias and conductor paths are produced by low-cost techniques like screen printing, the assembly of well-priced multilayer packages is possible. By laminating of several layers to one green part, complex three-dimensional structures are achievable. The tapes are flexible in the green state and therefore easily processable by techniques like punching or laser cutting. Typical pattern width amounts here 100 μm . To produce structures in the micrometer range, microembossing becomes more and more interesting.

Embossing process

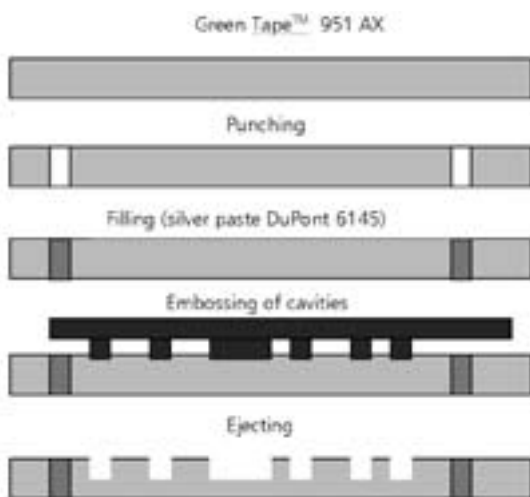


Fig. 1: Technological scheme of the embossing process.

The process is an interesting complement to the range of technologies for processing LTCC tapes. It stands out against other LTCC structuring processes like laser cutting or acetone-jet etching [3], especially due to its high structure resolution. With regard to

the application of LTCC materials for building up microfluidic systems, smoothing the surface by the embossing process and the related modification in the moistening behaviour are particularly interesting. The technique fits in optimally as a parallel procedure in the whole LTCC processing. Figure 1 depicts the process schema. Even complex structures are generated in one only step.

Structure dimensions of 50 μm can be imaged accurately. Up to 100- μm deep embossings have been achieved in green state.

Applications

1. Wiring Paths with High Ampacity

The thickness of wiring paths produced by screen printing is limited to approx. 10 μm . Therefore their sheet resistance usually is low. Its decreasing as well as the increasing of inductor's ampacity is necessary for applications in the high frequency or actuator ranges.

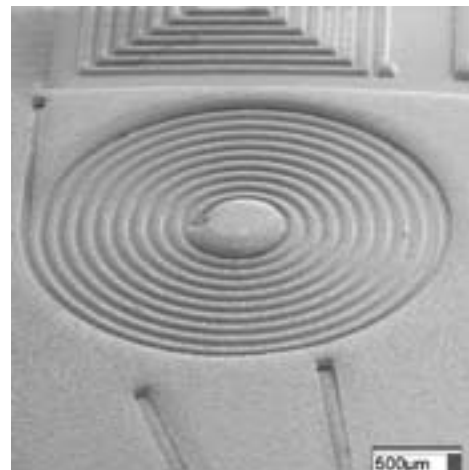


Fig. 2: Embossed coil in LTCC tape.

As a basic alternative, wiring paths were inserted in the embossed material by means of masked screen printing. This is an established process and represents the technologically easiest alternative for depositing function layers. The resolution is limited to approx. 20 μm . The SEM-picture in figure 2 shows an embossed wiring path of a coil.

A silver paste for inner layers with a high metal fraction (DuPont 6145) has been screen printed into the embossed structures. A complete, blister-free structure filling with a depth of 100 μm has

been achieved with a small pressure. By means of lamination and sintering, the layer thickness is reduced to approx. 60 μm . However, the nearly rectangular cross section is kept. Figure 3 depicts a micrograph of a sintered multilayer's cross section.

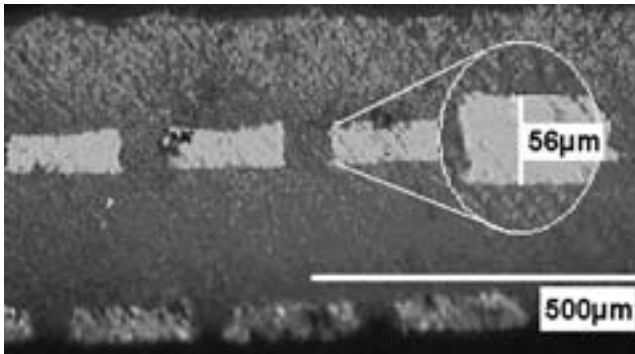


Fig. 3: Cross sections of a sintered LTCC multilayer with embossed conductor paths produced by masked screen printing.

Alternatively, the structures were filled using the Fodel® process, whereby a paste with a photosensitive binder is pressed over the substrate surface and the structures are then defined with a photolithographic process. By combining structure embossing and photostructuring, the layer thickness is no longer restricted by the thickness of the exposable layer, limited to approx. 7 μm . Wiring paths of up to 50 μm in thickness have been realized. A micrograph of a wiring path's cross-section shows figure 4. Compared to conventional screen printing, this process allows higher resolutions.

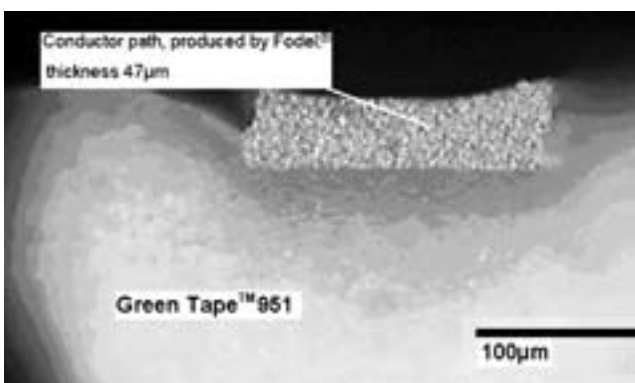


Fig. 4: Cross sections of a sintered LTCC multilayer with an embossed conductor track produced by Fodel process.

2. Fluidic structures

The roughness of embossed surfaces has been investigated to evaluate embossed structures concerning their application in microfluidic devices.

The microstructure of Du Pont's Green Tape™ 951 in the green state is depicted in Figure 5. Compared to the crude surface, the embossed surface is smoother. The smoothing can be used for applications, where adhesion and friction at the surface influence important parameters like flow resistance or transient behaviour. The table below faces the roughness parameters for an embossed and a crude surface measured on Green Tape™ 951 AX. After embossing the average surface finish R_a is around 300 nm. Crude surfaces feature an average surface finish R_a of about 400 nm.

Measured roughness parameters of Green Tape™ 951

Roughness parameters	Embossed surface	Crude surface
R_a [μm]	0.323	0.434
R_{rms} [μm]	0.418	0.537
Rz_{DIN} [μm]	1.95	2.61
R_{max} [μm]	2.38	3.11

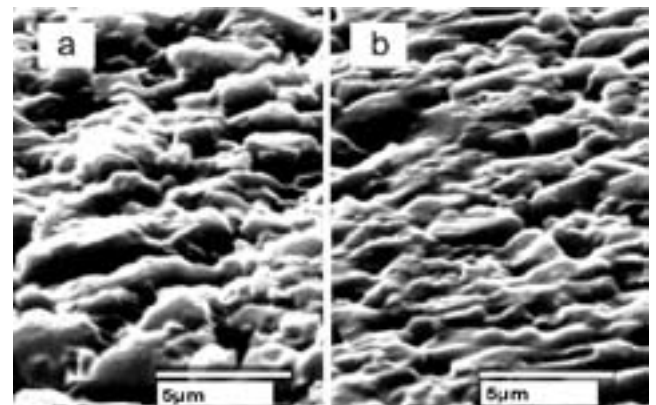


Fig. 5: SEM-picture of Green Tape™ 951 AX: a) Crude surface b) Embossed surface.

Summary

Microembossing of Low Temperature Co-fired Ceramics is an interesting complement to the conventional LTCC processing. Lateral structure's accuracy in the range of 5 μm is achievable. Complex geometries can be produced in only one parallel procedure. Using this technique, fluidic channels and wiring paths with low sheet resistance can be produced.

[1] M.R. Gongora-Rubio, P. Espinoza-Vallejos, L. Sola-Laguna, J.J. Santiago-Avilés: Overview of low temperature co-fired ceramics tape technology for meso-system technology (MsST), Sensors and Actuators A 89 (2001), 222-241.

[2] <http://www.pb.izm.fhg.de/match-x/index.html>

[3] J. Park, P. Espinoza-Vallejos, L. Sola-Laguna, and J. J. Santiago-Avilés: Etching and Exfoliation Techniques for the Fabrication of 3-D Meso-Scale Structures on LTCC Tapes*. Proceedings of International Microelectronics and Packaging Society (IMAPS) 1998, 142.

Microfluidic Structures in Ceramic Multilayers

H. Bartsch de Torres* and M. Hoffmann
Department of Micromechanical Systems

Introduction

Low Temperature Cofired Ceramics, also referred to as LTCC, are interesting materials for the realisation of MEMS in the meso-scale [1], i.e. dimensions in the range of $100\ \mu\text{m}$ up to millimetres. By laminating of several layers into one green part, complex three-dimensional structures are achievable. The typical pattern width of conventionally used techniques like punching or laser cutting amounts to approx. $100\ \mu\text{m}$. These techniques usually cut the tape's thickness completely, therefore only structures with a depth of integral multiples of the tape's thickness are achievable and the precision depends on the tolerance of the doctor blade process.

Microembossing adds to the variety of technologies for processing LTCC tapes. Structure dimensions of $50\ \mu\text{m}$ can be realised easily. In addition to previous studies focused on the aspect to produce conductor paths of high ampacity [2, 3, 4], the present work introduces an embossing technique to achieve fluidic channels with dimensions in the μm -range using conventional technologies.

Embossing process

The embossing step, as a parallel procedure, can be easily integrated in the LTCC process chain.

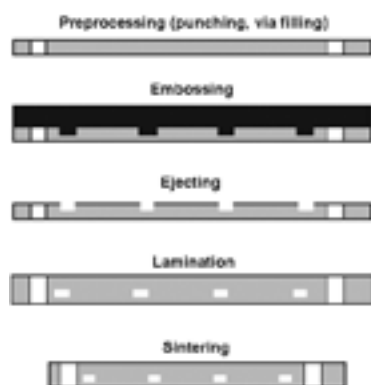


Fig. 1: Process schema.

Figure 1 depicts the process schema. Embossing can be carried out either as the first step or after preprocessing like punching and via filling. The main process parameters are temperature, dwell time and the die's pressure. The embossing has been carried out at a temperature of 57°C , using a pressure of $120\ \text{MPa}$ and a dwell time of 5 minutes.

Under these conditions, DuPont 951 GreenTape™AX has been embossed with a mould made of silicon. Profile scans of the mould and the embossed tape are shown in figure 2.

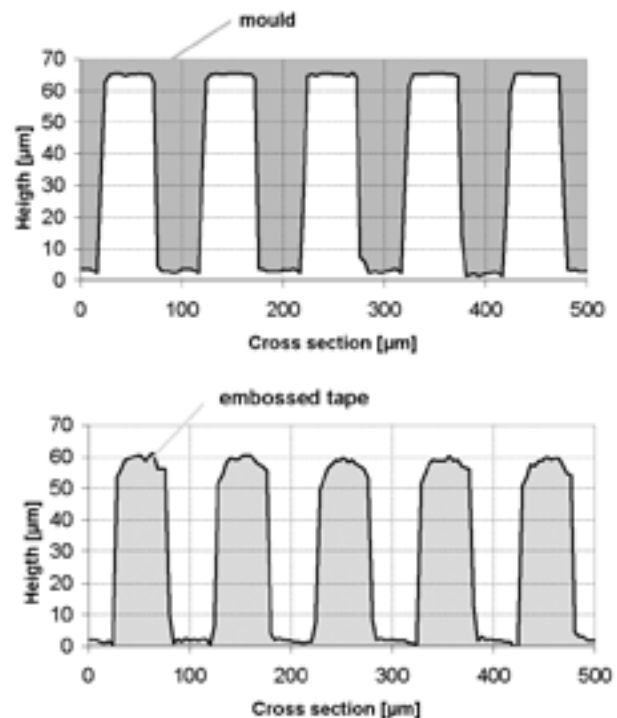


Fig. 2: Profiles of a mould (top) and embossed DuPont 951 GreenTape™ AX in the green stage (bottom).

The dimensions of the used embossing die are $50\ \mu\text{m}$ lines and spaces in lateral direction and $65\ \mu\text{m}$ in z-direction.

The lateral dimensions are imprinted accurately. In z-dimension the embossed height is reduced to about 92%. The reason of this deviation might be the elastic deformation of the tape material.

The embossed structures have been laminated with one layer of DuPont 951 GreenTape™AT, which has a thickness of $114\ \mu\text{m}$ in the green stage, at a reduced pressure. No fugitive phases or any other additives have been used. The primary structures height has been reduced of approx. $10\ \mu\text{m}$ by the lamination step. Figure 3 shows SEM-micrographs of the fluid channel's structures in the embossing die and of the embossed channels in the green stage.

Small fissures are generated by the embossing step. After sintering no cracks have been found, especially not in the edges of the hollows.

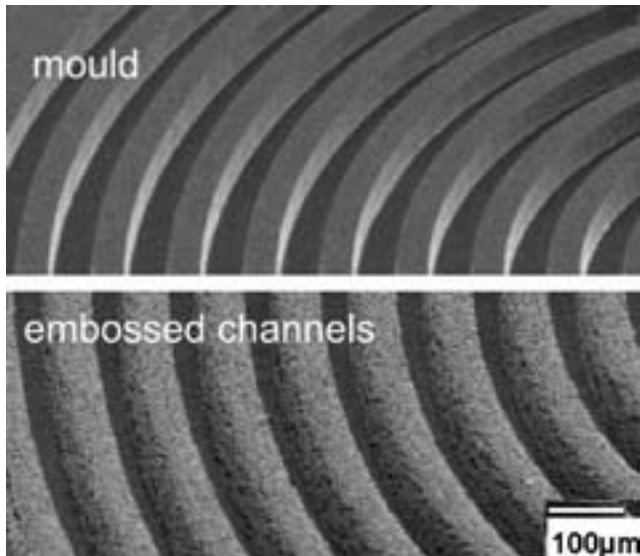


Fig. 3: SEM-micrograph of die and embossed structure.

The probe has been sawn to examine the channels geometry after sintering. Figure 4 depicts the SEM-micrographs of channel's cross sections and a longitudinal section, respectively. The channel's cross sections have rectangular geometry and dimensions of $35\ \mu\text{m} \times 35\ \mu\text{m}$.

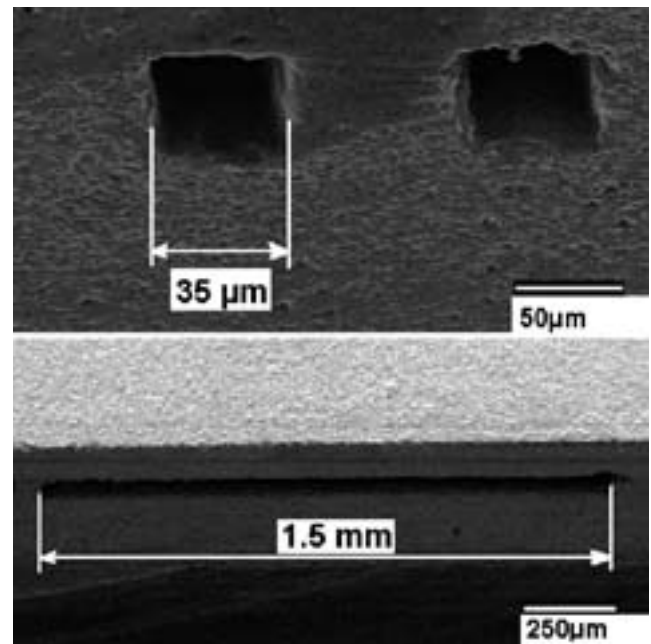


Fig. 4: SEM-micrograph of channel's cross section (top) and longitudinal section (bottom).

Conclusions

Fluidic channels with a dimension of $35\ \mu\text{m} \times 35\ \mu\text{m}$ have been produced by an embossing process into Low Temperature Cofired Ceramic Multilayers. The channels have rectangular cross sections. As a completely parallel process the procedure can be easily integrated into the LTCC process chain. Possible applications are for instance feeding channels in BIO-MEMS packagings or complex fluidic systems.

The authors would like to thank the TKM (Thüringer Kultusministerium) for the funding within the project Kerafema, No 20 11 47 01 76.

- [1] Gongora-Rubio M R, Espinoza-Vallejos P, Sola-Laguna L, Santiago-Avilés J J: Overview of low temperature co-fired ceramics tape technology for meso-system technology (MsST), *Sensors and Actuators A* 89 (2001), 222-241.
- [2] Albrecht A, Botiov J, Fischer M, Drüe K H, Hintz M, Wurmus H 2003 Alternative Way to High Current structures in LTCC 14th European Microelectronics and Packaging Conference & Exhibition Friedrichshafen, Germany, 23-25 June 2003, Proceedings.
- [3] Botiov J, Albrecht A, Wurmus H, Drüe K H, Hintz M 2005 LTCC Technologie als Grundlage für mikromechanische Funktionselemente 50. Internationales Wissenschaftliches Kolloquium, Technische Universität Ilmenau, Germany, 19.-23. September 2005, Proceedings.
- [4] Kallenbach M, Bartsch de Torres H, Albrecht A, Botiov J, Hintz M, Mikroprägen als Strukturierungsverfahren für LTC-Keramik. Mikrosystemtechnik-Kongress Freiburg, 12.-15.10., Proceedings, 2005.

Embedded Micro Connector Injection Process (EMCI)

G. Bischoff*, G. Winkler, A. Sutor, and A. Mokayyes

Department of Design and Technology of Electronic Components

Abstract

The impact of rules and regulations for the conservation of the environment is increasing. Today many electronic devices contain multilayer printed circuit boards. The materials and fabrication steps often use or contain environmentally harmful substances. To make these devices conform to requirements it is essential to eliminate or reduce such substances in the PCB (Printed Circuit Board) production process. New applications in electronics (i.e. LED-Lighting) require improved thermal management which can be achieved by new materials and technologies for PCB's. One possible solution to solve these problems is the Embedded Micro Connector Process (EMCI) which is investigated in the Cooperative Research Project under the Sixth Framework Program of the European Community (COOP-CT-2003-508172-EMCI).

Partners besides the TU Ilmenau in this project are:

- I.T.C. Intercircuit Electronic GmbH (Germany)
- Feinwerkbau Westinger und Altenburger GmbH (Germany)
- KEKON Ceramic Capacitors (Slovenia)
- EUROPRINT N.V (Belgium)
- Friedrich-Alexander Universität Erlangen-Nürnberg
- Budapest University of Technology and Economics.

Description

The major objective of this project is the realization of the brand new patent pending **Embedded Micro Connector Injection Process (EMCI-process)** technology, developed by the company ITC INTERCIRCUIT, Munich, for the benefit of the printed circuit board manufacturing industry, with a special consideration of environmental and cost cutting factors. The EMCI-process together with Printed Circuit Boards (PCBs) of 100 μm microvias, would be used to establish a robust and reliable fine-pitch technology in combination with a traditional PCB printed wire pattern process sequence. The EMCI boards would be developed in order to be compatible with fine pitch naked dice for flip-chip or wire bonding and will have an enhanced routability for dense area array packages (μBGAs -micro Ball Grid Arrays, CSPs -Chip Scale Packages), assuring compatibility with SMD technology. Micro component inclusion instead of contact pins will be studied, together with injection methods for all pin types, into and under the surface

of the PCB's, creating the possibility of a 3-D circuit board space.

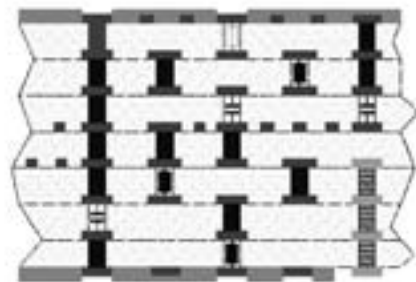


Fig. 1: Illustration of a cross section of a PCB board produced by using the EMCI-Process.

The work packages include the development of necessary machines and tools needed for the EMCI-process: the accelerator, the injector firing the pins into the board, considering aspects such as production testing and reaching the aim of reducing the chemical use during the PCB production. Another task is the fabrication of suitable EMCI processed boards for use as core multilayer boards for sequential build-up. Also during the R&D stages, a new printed circuit layout design system will be created by adapting established CAD systems, considering special EDA designs. Furthermore functional demonstrators will be built to validate the research work.

Required Physics

The base for the EMCI process can be derived from the basics of the insertion technology. The insertion technology is well known as a contacting procedure in printed circuit boards. A substantial difference between the insertion technology and the EMCI-process is to select a usable material combination for the insertion zone. While in the insertion technology drilled and plated through vias are used and therefore, a combination of metallic case and metallic pin is the standard, in the EMCI process the retaining forces will be maintained by the base material of the printed circuit board (plastic) and the inserted wire (metal alloy).

The research project starts with standard base materials, which are well known in the printed circuit board technology. These materials are the rigid base materials of the FR-4 group (epoxy resin / glass fibre

laminates). It is a plastic that „flows“. The result from this is that the EMCI process apply a very strong ‚over‘ pressing. The pin should have an oversize to the drill hole of 0.2 – 0.5 mm.

In the insertion technology copper alloys are used as contacting material. The tin bronze CuSn_6 is the standard carrier material of this technology. The relaxation properties of the pin material have an important behaviour on the reliability in the EMCI process. Figure 2 gives an overview of these properties for some typical alloys. Nature-hard alloys (CuSn_4 , CuSn_6 , CuSn_8) possess low to middle values, which are sufficient for most applications.

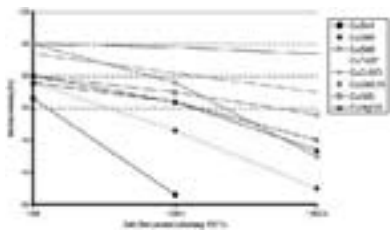


Fig. 2: Relaxation properties of typical copper alloys.

The principle of a first injector prototype construction shows figure 3. It works with a air pressure of 120 ... 180 bar and barrels for pins with diameters of 0.8, 0.9, and 1.0 mm.

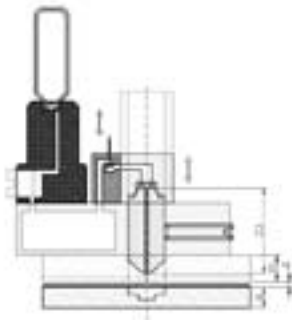


Fig. 3: Sketch of the injector construction.

First Results

A part of a test board is shown in figure 4. The test board contains drilled holes with diameters of 0.75, 0.85, and 0.95 mm, etched copper tracks and pads on the top and bottom side.

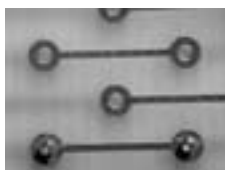


Fig. 4: Testboard with injected CuSn_6 -pins.

The cross section in figure 5 shows a typical EMCI via with low electrical resistance, high thermal conductivity and sufficient holding force.

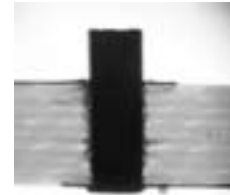


Fig. 5: Cross section of an intact interconnection.

A problem in this technology is the lift off of the annular copper ring on the bottom side (Fig. 6). At the moment this fact decreases the yield and the reliability of the EMCI process. A modification of the injector construction can be used to solve this problem.

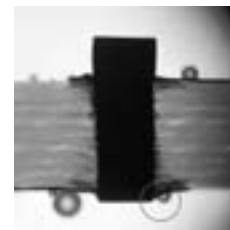


Fig. 6: Cross section of a defect interconnection.

The resistance between the annular ring of the copper pad and the injected pin is 0.01 ... 3 Ohm. After a thermal test for 24 h at 85°C, the resistance is increased by oxidation of the copper. The contacting area is not a gas-proof interconnection. More investigations are required to optimize the process parameters and to increase the yield.

- [1] Nolde, R.: Einpresstechnik; Leuze Verlag; Saulgau, 1994.
- [2] Vinaricky, E.: Elektrische Kontakte, Werkstoffe und Anwendungen; Springer Verlag; Berlin, 2002.
- [3] Krause, W.: Konstruktionselemente der Feinmechanik; Hanser Verlag; München, 2004.
- [4] Schröder, K.-H.: Werkstoffe für elektrische Kontakte und ihre Anwendungen; expert-Verlag; Renningen-Malmsheim, 1997.
- [5] Hanke, H.-J.: Baugruppentehnologie der Elektronik – Leiterplatten; Verlag Technik Berlin, 1994.
- [6] Scheel, W.: Baugruppentehnologie der Elektronik – Montage; Verlag Technik Berlin, 1999.
- [7] Herrmann, G.: Handbuch der Leiterplattentechnik Band 1 Laminat; Leuze Verlag; Saulgau, 1982.
- [8] Herrmann, G.: Handbuch der Leiterplattentechnik Band 2 Neue Verfahren; Leuze Verlag; Saulgau, 1991.
- [9] Herrmann, G.: Handbuch der Leiterplattentechnik Band 3 Leiterplattentechnik; Leuze Verlag; Saulgau, 1993.
- [10] Jillek, W.: Handbuch der Leiterplattentechnik Band 4; Leuze Verlag; Saulgau, 2003.
- [11] Kreisel, S.: Einpresstechnik; Diplomarbeit TU Ilmenau, 2004.
- [12] Hochleistungsdrähte aus Kupferlegierungen; Wieland Werke AG Ulm.

3D Interconnection Technology for LTCC RF Modules up to 60 GHz

R. Perrone^{1,*}, J. Müller¹, H. Thust², and J. Trabert³

¹ Junior Research Group Functionalised Peripherals, MacroNano® – Centre for Innovation Competence

² Department of Microperipherals

³ Department of RF and Microwave Techniques

Introduction

The aim of this work was to develop wideband line transitions among different signal layers with good RF properties for LTCC multilayer modules. This target was achieved considering technological as well as design challenges.

Regarding the design challenges the RF properties of grounded coplanar and striplines were investigated up to 67 GHz. Complementing experimental and EM simulation results effective rules to design the shielding via fence structure for both line types were deduced. Using these rules, the resonances which appear in the shielding structures of these lines and affect their RF properties [1], [2] can be avoided in a desired frequency range.

The derived design rules together with a 3D field simulation program were used to design and optimize wideband multilayer line transitions.

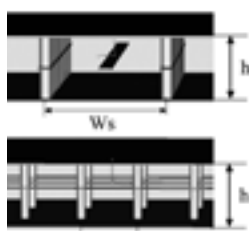
The optimized line transitions were manufactured combining two advanced LTCC technologies, namely the Fodel® patterning technique and microvias. The used microvias had a fired diameter of approximately 65 μm .

Description of the Manufactured Teststructures

• Coplanar and Striplines

Coplanar lines were manufactured in one thickness (210 μm , 1 layer DP 951 PX) and striplines in two different thicknesses (420 and 840 μm , 2 and 4 layers DP 951 PX).

a)



b)

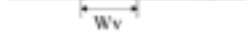


Fig. 1: Parameters of the shielding via arrangement.

Coplanar Lines		Striplines	
Ws[mm]	Wv[mm]	Ws[mm]	Wv[mm]
0.7	0.225	1.15	0.5
1	0.3	1.4	0.6
1.2	0.5	1.6	0.7
1.5	0.7	2	0.8
-	-	2.45	1
-	-	-	1.22

Tab. 1: parameters of the investigated shielding via arrangement.

To investigate the influence of the ground shielding arrangement on the RF properties of coplanar and striplines, the distances Wv and Ws were varied.

In figure 1 the distances Ws and Wv , as well as the tape thickness are shown for a stripline as an example. The used values for these parameters are depicted in table 1.

• Wideband Line Transitions

Four different coplanar to stripline transitions were manufactured. They are shown in figures 2.a) to 2.d). In line transition type a) the signal is led from the top to the first inner layer whereas in transition type b) to the second inner layer. Finally, in figures 2.c) and 2.d) the signal is led to the fourth inner layer in one and two steps (of two layers each) respectively. In the figures all layers consist of LTCC tape DP 951 PX from DuPont.

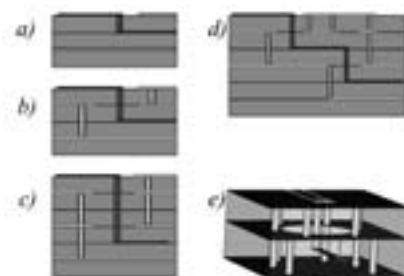


Fig. 2: Signal path is led from top layer to: a) first inner layer, b) second inner layer, c) and d) fourth inner layer. Line transition manufactured with coplanar pads on the top layer.

The transitions 2.b), 2.c) and 2.d) were manufactured with coplanar and microstrip lines on the top layer. A 3D view of a coplanar to stripline transition is shown in figure 2.e) as an example.

Technology

The vias were punched in a diameter of 75 μm on the tape DP 951 PX (unfired thickness: about 254 μm). All vias were filled from the mylar backing film side with silver paste DP 6162 in a via fill machine using punched mylar masks. The metal structures on all layers were patterned with the Fodel® paste DP 6453 according to the standard procedure.

To achieve a very good via alignment the tapes were processed with mylar backing film as described in [3]. The achieved via stacking alignment was about 30 μm .

Simulation, RF Measurement and Analysis of the Test Structures

The geometry of the manufactured structures were simulated and optimized using the 3D field simulation program CST Microwave Studio®.

The S-Parameters of the manufactured structures were measured up to 67 GHz with a PNA network analyzer from Agilent and GSG Probes from Picoprobe. The PNA was calibrated using SOLT standards.

• **Striplines**

Complementing measurement and simulation results the following equations to design the via shielding arrangement of this line type for a desired frequency range of application were derived:

$$W_s < \frac{c_0}{2 * f_{max} * \sqrt{\epsilon_r}} \quad \text{for } W_s > h$$

$$W_s < \frac{c_0}{4 * f_{max} * \sqrt{\epsilon_r}} = \frac{W_s}{2}$$

W_s and W_v are expressed in [mm], c_0 in [m/s]. ϵ_r is the permittivity of the LTCC material and f_{max} the desired cut-off frequency for the striplines.

Using these rules to arrange the shielding structures of striplines the undesired resonances in the frequency range of interest can be avoided. The accuracy of these equations is better than 10 %.

• **Coplanar lines**

Based on measurement and simulation results an equation to calculate the $f_{cut-off}$ of grounded coplanar lines in dependence of W_s , W_v , ϵ_r as well as the effective dielectric constant ϵ_{eff} (Fig. 3) was derived:

$$f_{cut-off} [GHz] = \left(-25.6 + 0.82 * W_s * \sqrt{\epsilon_{eff}} \right) * W_v * \sqrt{\epsilon_r} + \frac{300}{2 * W_s * \sqrt{\epsilon_{eff}}}$$

W_s and W_v are expressed in [mm] and $f_{cut-off}$ in [GHz]. ϵ_{eff} can be calculated using standard equations [4] or any software tool for this purpose.

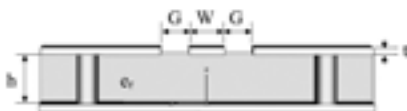


Fig. 3: coplanar line and its geometrical parameters.

This equation has an accuracy of better than 5% under the condition that $W_s > 3 * h$. For other W_s to h relationships it has to be further optimized.

The presented equations or rules for both types of lines were verified by RF measurements up to 50 GHz and partially 67 GHz and S-Parameter simulations. They apply for the material system DP 951, the investigated structures and similar ones (also for thinner substrates). The generalization to other material systems and thicker substrates is part of a future work.

• **Line transitions**

The shielding via fence of the line transitions presented in figures 2.a) to 2.e) was arranged according to the equations introduced before. The dimensions of the lines were optimized with a 3D field simulation program to match an impedance of 50 Ohm. For the simulations, an ϵ_r of 7.8 (constant over the frequency) was used.

Because of memory space limitations, the measurement and simulation results corresponding to only one line transition are shown. In figure 4 the measured and simulated $S[1,1]$ parameter for a coplanar to stripline transition (see Fig. 2.b) and 2.c)) are shown. This structure shows a reflection coefficient under -20 dB up to 53 GHz. In the frequency range from 53 to 65 GHz $S[1,1]$ is better than -16 dB.

The small differences between simulated and measured scattering parameters are probably caused by manufacturing tolerances.

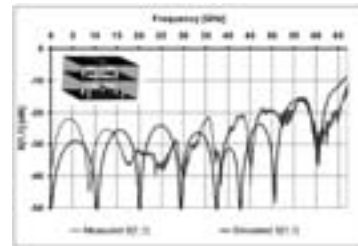


Fig. 4: Measured vs. simulated $S[1,1]$ parameter for a coplanar to stripline transition.

Although not shown, the measured and simulated $S[1,1]$ parameter of all remaining line transitions is better than -20 dB up to 50 GHz.

Conclusions

Simple equations to arrange the shielding via fence of coplanar and striplines were presented. These rules apply for the material system DP 951 from DuPont®. Several line transitions among different signal layers were manufactured. The RF measurement results demonstrate the ultra wideband capability of line transitions if fine line patterning technologies and microvias are combined with a suitable design. These transitions may allow the production of multilayer LTCC modules for RF wideband applications up to 50 GHz or 65 GHz.

This work was supported by D.A.A.D. and the BMBF Projects "Keramis" and "MacroNano®". Some of the test structures were manufactured at the Ceramic Electronics Packaging Laboratory (CEPAL), Department of Electrical Engineering, University of Arkansas. The authors would like to express their gratitude to A. Elshabini, F. Barlow and G.Wang for the technology support. The authors would also like to thank M.Hein, R.Stefan, I.Koch and D.Förster for their valuable contribution to the realization of this piece of work.

[1] H. Thust, R. Perrone, M. Hintz and D. Förster: Optimale Gestaltung von Mikrowellen Anwendungen mit Fodel® und Vollmetallfeinstrukturen, Deutsche IMAPS Konf. 2005, Oct. 10-11, 2005, München, Germany.
 [2] K.Guinn, K.Goverdhanam, Y.Lee, A.Becker, A.Lyons, "Broadband Interconnection using Dupont 943 low loss LTCC", Advanced Technology Workshop on Ceramic Technologies for Microwave, March 26-27, 2001, Denver, Colorado.
 [3] G.Wang, F.Barlow and A.Elshabini, "Interconnection of Fine Lines to Micro Vias in High Density Multilayer LTCC Substrates", Proc. of the 38th International Symposium on Microelectronics, Sept. 25-29, 2005, Philadelphia, Pennsylvania.
 [4] Brian C. Wadell, "Transmission Line Design Handbook", Boston: Artech House Inc., p.79-80, 1991.

High functional density low-temperature co-fired ceramic modules for satellite communications

J. F. Trabert^{1,*}, M. A. Hein¹, J. Müller³, R. A. Perrone², R. Stephan¹, and H. Thust²

¹ Department of RF- and Microwave Techniques

² Department of Microperipherals

³ Department of Micro Systems Engineering GmbH & Co., Berg

Up to now, compact microwave circuits are laid out like singlelayer printed circuit boards. Typically, connections between the *RF* components are placed on the top layer, and the bottom layer is used as ground. This is a serious limitation of complexity. Several multi-layer techniques have been proposed to overcome this limitation. Most of these techniques have to cope with organic materials that usually suffer from poor dielectric properties, i.e. the losses of the dielectric layers prevent applications at K-band operating frequencies. One promising solution is the LTCC (low-temperature cofired ceramic) technology, which incorporates multi-layer thick-film ceramic structures with good *RF* and microwave performance in a single module.

This paper focuses on the description of a 4×4 reconfigurable switch matrix (RSM) for satellite communication downlinks in the Ka/K-band as one example of a highly hybrid-integrated modular package. Other examples, like modules for solidstate power amplification and frequency synthesis, are developed by our project partners [2]. The functionality and small size of all of these demonstrators are representative of the needs of satellitebased communication systems. Here, the principle-of-operation of a RSM and the potential to achieve competitive performance are investigated.

Design and Technology

The aim of our research is to achieve a truly three-dimensional hybrid integration of passive and active components, including biasing networks, *DC*-blocks, power splitters et cetera, in a single LTCC multi-layer structure. At the same time, reduction of semiconductor expenses is to be achieved by minimising the complexity of the semiconductor components, e.g., by transferring matching and decoupling circuits into the ceramic tile instead of being monolithically integrated on-chip. Such benefits imply that the LTCC microwave components are manufactured by reliable technological processes with reproducibly high quality and high yield. Furthermore, it is necessary to develop suitable *RF* interconnections, like transitions between different layers (vertical connections) or different types of transmission lines, second-level interconnections between the ceramic module and the main board (here: the microwave wafer probing station), and transitions suitable for a hermetic housing [3].

A RSM provides a variety of digitally controllable signal paths for adaptation, reconfiguration, and functional multiplexing, as depicted in Figure 1. The matrix is designed for eight commercial active controlled switch circuits. For our demonstrator, we selected the most recent commercial PIN diode-based switch-ICs for frequencies from 2 up to 25 GHz in a singlepole quadruple-throw (SP4T) architecture. This multiplicity defines a particular signal distribution topology as well as the number of crossings of microwave transmission lines. Scaling to distinctive complexities $N \times M$ of the RSM (i.e., N inputs and M outputs) can be achieved by a serial or/and parallel arrangement of such switches.

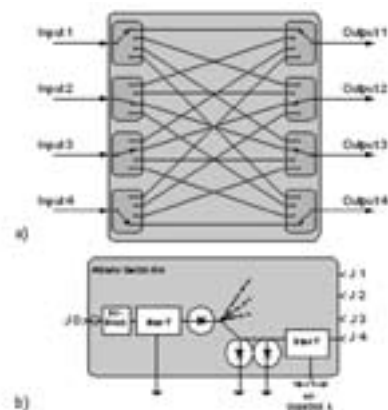


Fig. 1: Architecture of the LTCC-based 4×4 RSM. a) Singlepole multi-throw architecture consisting of eight SP4T switch ICs. b) Block diagram of the incorporated SP4T switch die.

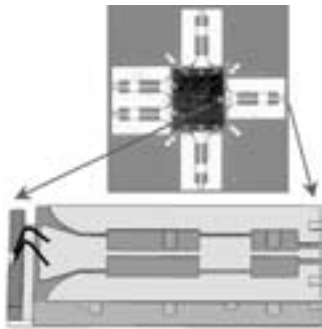
For a minimum-coupling design of a 4×4 matrix architecture, a stacked layout is required: Four separate microwave signal layers, one layer for control lines (*DC*), six intermediate ground layers for shielding, and the top-layer with the second-level microwave interconnections and *DC* supply terminal points.

The first test version of a complete RSM module was realised by a LTCC-stack of eleven layers, using Du-Pont-951-AX tape, with a size of $18 \text{ mm} \times 25 \text{ mm}$ and a total height of 2.2 mm. The inner conductor layers were manufactured with high resolution in terms of linewidth (down to $40 \mu\text{m}$) and edge precision ($\pm 2 \mu\text{m}$), to optimise impedance matching and bandwidth efficiency.

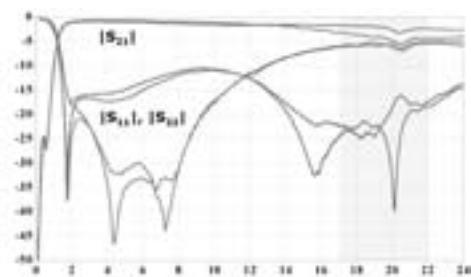
Commercial switch dies were countersunk into cavities resected from the three top layers of the LTCC module, mounted with electrically conductive epoxy, and wirebonded. The S-parameters of one complete signal path indicated fairly good performance up to 12 GHz, with a total insertion loss of about 3 dB, and a return loss ≤ -15 dB. However, above 12 GHz, the insertion loss increased to 10 dB, and the return loss approached levels around 5 dB.

The results for the prototype matrix led us to design an improved concept, which also includes more sophisticated chip interconnections. In the course of iterative optimisation steps, we have re-designed and amended distinctive passive components.

Figure 2a shows a picture of a LTCC module with a single wire-bonded switch-IC and the schematic of the recently developed low-pass filter type impedance matching networks. The S-parameters measured (diagram of figure 2b) in the LTCC environment reflect the uncompensated broadband response (grey lines) of a series circuit consisting of the passive transmission line elements and the RF-junction switched into its onstate.



a)



b)

Fig. 2: Impedance matching of a single switch-IC. a) Photograph of countersunk switch-IC (die) and schematic of developed impedance matching networks. b) Measured scattering parameters. Without compensation: grey colored lines; with compensation network: red colored. Relevant frequency range: 17 to 22 GHz.

The RF-performance of the switch matrix can be improved by the implementation of compensation

networks optimised for each switching circuit. These planar structures are on the top layer which realise good control of conductor geometry, simple accomplishment of the required impedance range and impose moderate dissipation losses. Furthermore, the use of two parallel bondwires and the conversion of the switch-IC-inherent microstrip mode to coplanar propagation-mode at the 1st-level interconnection is also beneficial for low insertion loss and enhanced bandwidth. The red lines in figure 2b depict the valuable improvements of RF-properties by the applied compensation networks. The reflections coefficients $|S_{11}|$ and $|S_{22}|$ are decreased by more than 10 dB in the relevant frequency range from 17 up to 22 GHz. But most important, the transduced RF-power, indicated as $|S_{21}|$, is nearly doubled.

First steps have been undertaken successfully towards the realisation of a compact 4×4 reconfigurable LTCC switch matrix with high functional density for satellite communications. We have designed, characterised, and improved the individual building blocks on the basis of high-resolution LTCC-technology. The S-parameters of individual components and sealed packages revealed promising microwave response in the frequency band of interest. In detail, insertion losses below 1 dB/cm and reflection losses below 20 dB, measured for an embedded stripline and a hermetic package with an embedded CPWG transmission line, prove that it is possible to exploit the potential of a truly three-dimensional spacequalifiable hybrid integration at microwave frequencies up to 25 GHz.

The required performance of the complete switch matrix imposes serious restrictions on the choice of commercially available switch ICs. The desired performance can eventually be achieved by use of band-width-limited compensation networks in combination with a precise layout of the microwave transmission lines, the transitions between different types of waveguides, and the bondwiring to the chips.

The next steps towards realistic satellite applications will be the design and characterisation of an improved reconfigurable switch matrix with high isolation between the individual signal paths.

This work has been supported by the German Federal Ministry of Education and Research (BMBF, No. 50YB0313). We gratefully acknowledge valuable contributions from K. Drüe, S. Rentsch at Ilmenau, and M. Spinnler and B. Hespeler at Tesat-Spacecom GmbH.

[1] J.F. Trabert, R. Perrone, R. Münnich, R. Stephan, M.A. Hein, H. Thust, "20 GHz LTCC Applications for Satellite Communications – Challenges for Design and Technology", 11th International Student Seminar on Microwave Applications of Novel Physical Phenomena, St. Petersburg Electrotechnical University "LETI", St. Petersburg, Russia, June 7-9, 2004.

[2] A. Jacob et al., Interim Report of project KERAMIS (No. 50YB0313), DLR, Germany, unpublished.

[3] R. Perrone et al., "Development and Evaluation of Photodefined Elements for Microwave Modules in LTCC for Space Applications," 2005 EMPC, European Microelectronics and Packaging Conference, Brugge, Belgium, June 12-15, 2005.

[4] F.J. Schmückle, A. Jentzsch, W. Heinrich, J. Butz, M. Spinnler, "LTCC as MCM Substrate: Design of Strip-Line Structures and Flip-Chip Interconnects," 2001 IEEE MTT-S Int. Microwave Symposium Dig., vol. 3, pp. 1903-1906, June 2001..

Characterization of a Photoresist for the Fabrication of Continuous-relief DOEs

S. Stoebenau*, M. Hoffmann, and S. Sinzinger
Department of Optical Engineering

Motivation

Diffractive optical elements (DOEs) offer new design flexibility for classical optics as well as for integrated microoptical systems. In these elements, light is diffracted at laterally periodic structures. Their potential lies in the fact that any phase profile can be fabricated as a DOE [1].

As the efficiency of DOEs increases with the number of phase levels, i.e. surface steps, the fabrication of elements with multilevel or continuous-relief profiles is desirable. Therefore, as an alternative to multimask processing, a greyscale illumination can be applied, as it is possible in holographic lithography through interferometric illumination. In this maskless approach, the superposition of at least two coherent wavefronts (object and reference) leads to an intensity pattern, which is used for the illumination of a photoresist layer. Thus, the continuous phase profiles can be fabricated with a single exposure.

The focus of our work lied in the investigation of the performance of the positive resist "Allresist SX AR-P 3500/6" [2] under different processing conditions. We investigated the response curves of the resist-developer-system and evaluated its suitability for holographic lithography.

Continuous Surface Profiles in Positive Photoresists

The resist under investigation is a so-called DQN positive photoresist. This type of resist basically consists of three components: a base resin, a photoactive compound (commonly called inhibitor) and solvents. The exposure of the resist to light of a specific spectrum converts the inhibitor into a carboxylic acid and thus increases locally the solubility of the film. This photochemical reaction can quantitatively be expressed using the change in the local inhibitor concentration M which is the fraction of inhibitor remaining after exposure relative to that before [3]. The development rate R (thickness of removed film per time) is only a function of M so that the determination of the $R(M)$ -curve is essential.

M depends on the exposure energy E but is not necessarily proportional. However, proportionality can be assumed if multiple reflections at the interfaces of the coated substrate and bleaching of the resist during exposure can be neglected.

That is reached by working with glass substrates and by index matching between substrate and resist. Furthermore, if the wavelength of the illumination

source is in the visible blue-violet, the absorption is very poor and the irradiance is low, requiring long exposure times to saturate the material. Thus, changes in the intensity pattern during exposure because of bleaching are negligible [4]. These requirements were fulfilled in our experiments and it was sufficient to determine the $R(E)$ -curves instead of the $R(M)$ -curves. They represent the response of the photoresist film to uniform light exposure and can be experimentally measured [5].

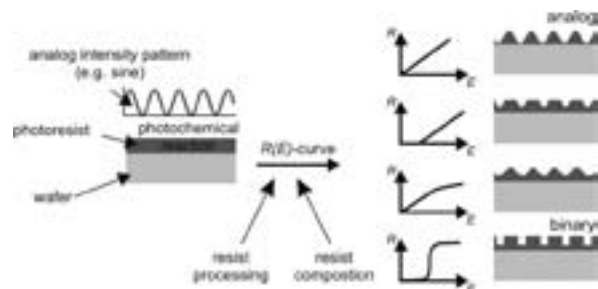


Fig. 1: Schematic description of the process of profile forming.

As it is depicted in figure 1 the resulting profile depends on the shape of the $R(E)$ -curve. It can be influenced actively by the resist processing parameters, especially during the prebake and the development steps.

For a resist suitable for the formation of analog profiles, following effects need to be excluded [3]:

- surface inhibition (a lower solubility of the resist surface compared to the bulk material resulting in underetching),
- dark development (partial destruction or conversion of the photoactive compound without any exposure resulting in dissolution of unexposed areas), and
- bleaching (decreasing absorbance of a DQN-resist layer during exposure due to the conversion of photoactive compound into carboxylic acid).

Furthermore, it is essential to work in the linear range of the $R(E)$ -curve to generate profiles with a direct correlation between exposure energy and profile depth.

Experimental Results

To evaluate the bleaching behavior we determined the so-called Dill's A and B parameter with a simple optical setup for transmission measurements proposed by

Dill et al. [5]. The absorption coefficient α of a DQN-resist depends on the inhibitor concentration M :

$$\alpha = AM(x,t) + B \quad (1)$$

We found out that for this resist B is approximately one order of magnitude greater than A so that the absorption coefficient primarily depends on B and does not change significantly over time. Thus, bleaching is negligible.

Our work then focused on the mapping of the $R(E)$ -curve under different prebake und development conditions. Therefore, we illuminated resist layers of about $4.2 \mu\text{m}$ thickness with a uniform intensity (wavelength 457.9 nm) over different time segments resulting in different exposure energies. After developing the wafers by immersion for 30 s we measured the removed resist thickness with a profilometer. The determined curves are shown in figures 2 and 3.

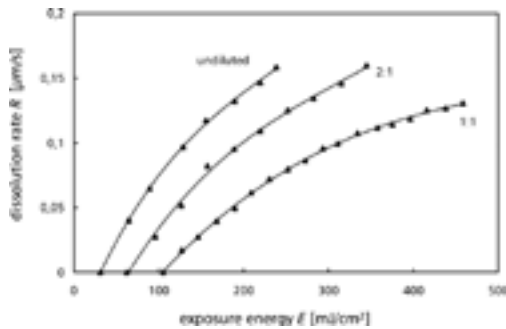


Fig. 2: $R(E)$ -curves for different developer concentrations.

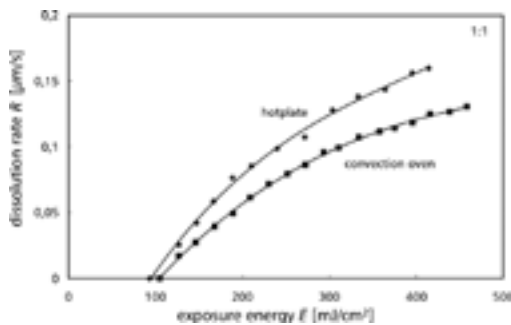


Fig. 3: $R(E)$ -curves for different prebake conditions.

As one can see from the $R(E)$ -curves a threshold energy must be exceeded before a photochemical reaction occurs. If this energy is not reached at all positions of the exposure pattern, plateaus of undeveloped resist are formed. Increasing developer concentrations primarily shift the threshold energy towards lower values while the prebake mode mainly changes the slope of the curves. Compared to standard photoresists optimized for the recording of binary structures the dissolution rate of the evaluated resist system raises more slowly with increasing exposure energy. Thus, the energy range where a linear $R(E)$ -

curve can be assumed is sufficiently broad for a precise control of the surface profile. Neither surface inhibition nor dark development were observed during the experiments.

Based on the $R(E)$ -curves we chose the processing and illumination parameters to transfer first analog structures into the resist (prebake: 20 min , 105°C , convection oven; developer concentration: 2:1). We generated a sinusoidal intensity pattern of fringes by the coherent superposition of two plane wavefronts that were slightly tilted to another.

For the given experimental setup, we applied two different methods to assure the threshold energy to be exceeded:

1. contrast reduction by unequal intensities in both wavefronts so that the minimal intensity in the fringes increases, and
2. exposure in two steps: background exposure to exceed the threshold followed by the pattern exposure.

The profilometer scan of a fabricated analog resist surface profile is shown in figure 4.

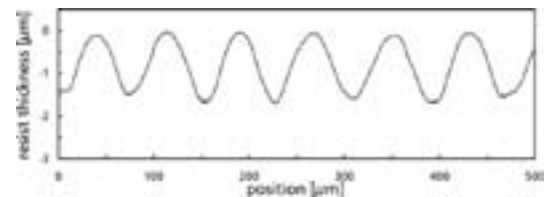


Fig. 4: Profilometer scan of the resist surface.

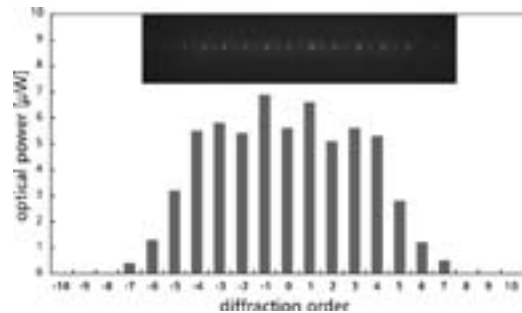


Fig. 5: Distribution of the optical power within the diffraction orders for the resist profile in figure 4.

Finally, we investigated the diffraction behavior of the recorded gratings. In figure 5, one can see the highly symmetrical distribution of optical power within the diffraction orders of the sinusoidal phase grating that mirrors its symmetric shape.

In conclusion, we have shown that the photoresist "SX AR-P 3500/6" is suitable for the use in holographic lithography. We succeeded in the realization of first phase-gratings with continuous surface profiles.

The authors gratefully acknowledge the financial support of the Thüringer Ministerium für Wirtschaft, Technologie und Arbeit (project "KOMPHOR").

[1] S. Sinzinger, J. Jahns: Microoptics, Wiley, 2003.

[2] www.allresist.de

[3] Ch. Zanke, A. Gombert, A. Erdmann, M. Weiss: Fine-tuned profile simulation of holographically exposed photoresist gratings, Optics Comm. 154 (1998) 109-118.

[4] B. de A. Mello, I. F. da Costa, C. R. Lima, L. Cascato: Developed profile of holographically exposed photoresist gratings, Appl. Opt. 34 (1995) 597-603.

[5] F.H. Dill, W.P. Hornberger, P.S. Hauge, J.M. Shaw: Characterization of positive photoresist, IEEE Trans. Electron Devices 22 (7) (1975) 445-452.

Holographic Lithography Based on Copying of Computer-Generated Holograms

M. Teschke* and S. Sinzinger
Department of Optical Engineering

Motivation

Holographic lithography enables the fabrication of continuous surface profiles within one single exposure. The concept is based on the superposition of at least two coherent wavefronts (object and reference), which leads to a greyscale intensity pattern. The resolution of the intensity pattern is merely defined by the angle between the incident wavefronts. Therefore, high frequency profiles can easily be realized for large substrates [1]. However, conventional holographic lithography systems are limited to two kinds of wavefronts (planar or spherical). That results in limited interferometric intensity patterns. To achieve more complex interference patterns complex wavefront must be created by real existing objects (see Fig.1).

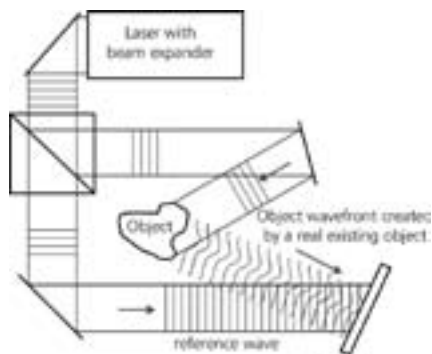


Fig. 1: Holographic interferometry with complex wavefronts.

A new approach to form complex wavefronts was presented by Bartelt and Case [2]. They suggested the copying of computergenerated holograms (CGH), which enables the production of an artificial object and hence a complex wavefront (see Fig. 2).

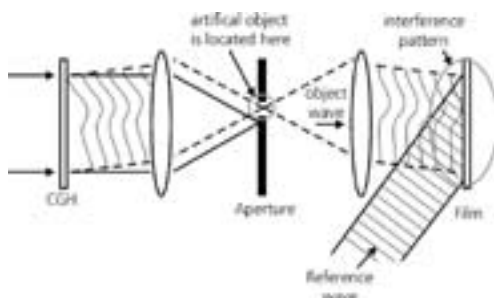


Fig. 2: Holographic lithography by copying a CGH.

Technology

Computergenerated holograms (see Fig. 3) can be calculated using the Iterative Fourier Transform Algorithm (IFTA).



Fig. 3: Computer-generated hologram (CGH).

By passing a CGH, a wavefront is modulated in such way that a required intensity pattern occurs in the diffraction image as an artificial object (see Fig. 2). This diffraction image includes a complex wavefront, which can be used for holographic lithography. A setup for holographic lithography is presented in figure 4.

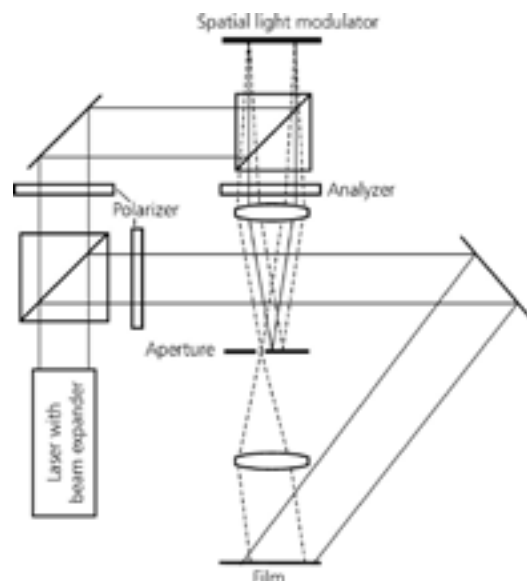


Fig. 4: Setup for holographic lithography with a complex wavefront.

We used a spatial light modulator (SLM) to create the CGH (see Fig. 5). With this technique we are able to provide an infinite number of different wavefront geometries without modifying the setup.

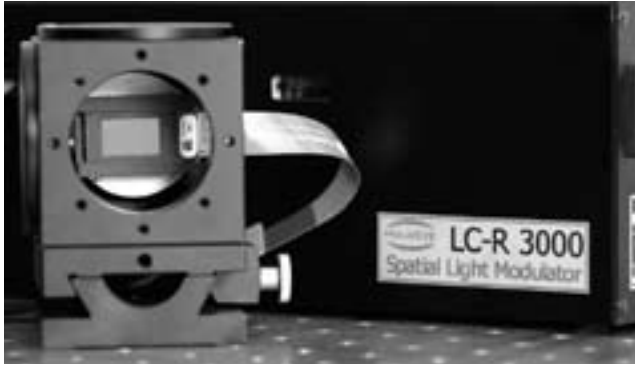


Fig. 5: Spatial light modulator.

As a consequence of the mode of operation, the spatial light modulator alters the polarization direction. This fact is considered by applying several polarizers (see Fig. 4). The two interfering wavefronts have to be in the same polarization state for optimal interference. Furthermore, an aperture is needed to blind out other artificial objects, which are also generated by the CGH (see Fig. 6).

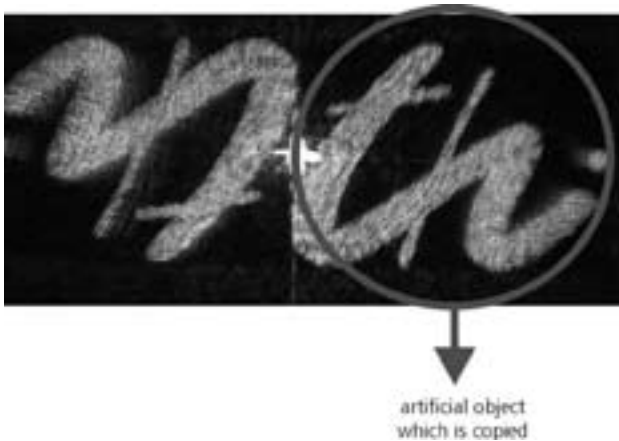


Fig. 6 : Artificial objects generated by CGHs.

Experiments

Figure 7 shows a result of the copying technique. The artificial object (Fig. 6), which was generated by the spatial light modulator, has been exposed to a holographic film. After the development process, the object could be reproduced and photographed by a CCD camera.

The copying technique was very successful to create an arbitrary object wavefront and to interfere it with a planar reference wavefront. The next step within this work is to replace the holographic film by a substrate coated with a layer of the photoresist SX AR-P 3500/6 [3]. The performance of this photoresist was investigated extensively [4]. The mapping of the development rate R against the exposure energy E showed a linear relation for the operating wave-length of 457.9 nm. Thus, the requirements for optimal holographic lithography are satisfied.



Fig. 7: Reconstructed object by illuminating the holographic film.

This work was part of the project KOMPHOR. We thank the Thüringer Ministerium für Wirtschaft, Technologie und Arbeit for financial support.

[1] R. Brunner, R. Steiner, H.-J. Dobschal, K. Rudolf: Hybride diffraktive - refraktive Optik: Vom Design zum System. Photonik 4/2004, 50-53.

[2] H. Bartelt, S. K. Case: High-efficiency hybrid computer-generated holograms. Appl. Opt. (1982) 2886-2890.

[3] www.allresist.de

[4] M. Hoffmann: Lithographische Herstellung analoger Oberflächenprofile für mikrooptische Anwendungen. Diploma thesis, TU Ilmenau, Department of Optical Engineering, 2005.

Prism-Coupling into a Planar Integrated Free-space Optical System

M. Amberg*, H. Baitinger, and S. Sinzinger
Department of Optical Engineering

Motivation

Planar integrated free-space optics [1] combine the advantages of free-space optics and the precise alignment possibilities of planar fabrication technology.

The concept is to fold the optical system into a thick glass substrate (Fig. 1). Optical elements, either diffractive or refractive ones, are integrated onto the surfaces of the substrate. The light travels between the reflection-coated surfaces of the substrate on a zigzag-path. It was shown by different authors that these optical systems, e.g., applied in optical inter-connections, relay systems and security applications, can be optimized in terms of optical properties [2].

However, the overall efficiency of purely diffractive systems is low, i.e. in the range of a few percent. We show that it is possible to raise the efficiency significantly by the use of refractive prisms for coupling into the substrate (see Fig. 1) [3].



Fig. 1: Setup of (a) a purely diffractive and (b) a refractive/diffractive system.

Integration of refractive elements to a planar integrated free-space optical system

Integrating prisms changes the optical properties of such prism-coupled setups (Fig. 2b) compared to a purely diffractive (Fig. 2a) implemented system as seen in the spot diagrams generated by raytracing simulations with the optical design software ZEMAX™.

The overall efficiencies for a purely diffractive and a prism coupled system are:

$$\begin{aligned}\eta_{\text{diffractive}} &= \eta_{\text{prism}}^2 \cdot \eta_{\text{Dk.1/Dk.2}}^2 \cdot \eta_{\text{diffractive}}^7 \\ &= 0.405^2 \cdot 0.81^2 \cdot 0.98^7 \\ &= 0.09 \\ \eta_{\text{prism_coupled}} &= \eta_{\text{prism}}^2 \cdot \eta_{\text{Dk.1/Dk.2}}^2 \cdot \eta_{\text{diffractive}}^7 \\ &= 1^2 \cdot 0.81^2 \cdot 0.98^7 \\ &= 0.57\end{aligned}$$



Fig. 2: Results of the raytrace: (a) spot diagram of a purely diffractive integrated and (b) spot diagram of a prism-coupled system.

Fabrication

The whole system was fabricated at the ZMN. The diffractive lenses are four phase level elements and were made by a two step fabrication process. First, the structures of layer 1 were generated by mask lithography into a photoresist layer and were subsequently etched into a fused silica substrate by RIE etching leading to a binary structure. Layer 2 with the structures needed to generate a four phase level element was processed afterwards with the same technique. The additional edges needed for the alignment of the off-the-shelf prisms were made by a structured photoresist layer. For our setup, we used AR-P 3210 and spun it onto the wafer with a thickness of about 18 μm . The edge pattern was aligned to the diffractive lenses by marks on the glass wafer that have already been used to align the diffractive lenses and made by an additional litho-graphic step.

Developing the illuminated resist leads to the eight alignment structures surrounded by two integrated systems as shown in figure 3 [4].

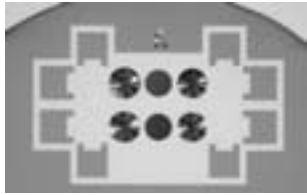


Fig. 3: Two integrated systems surrounded by eight alignment marks.

Experiments

In an experimental setup, we could show good optical imaging properties of the prism-coupled system. For the setup the BK7-prisms needed to be aligned to the diffractive lenses. Controlled by a camera with a microscope objective the prisms were set by hand to the resist edges (see Fig. 4).

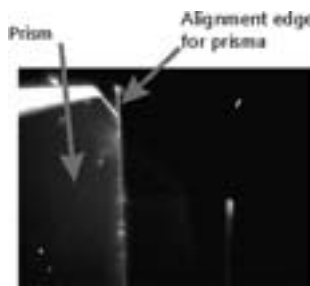


Fig. 4: Microscope image of prism aligned to resist edge.

The design wavelength of the system is 632.8 nm. Therefore, we used a red HeNe laser for coupling into a single mode fiber. The fiber was aligned right upon the prism for coupling in (see fig. 5) and acted as a point source for the tests. Attached to micrometer stages in x- and y- direction it was possible to scan the whole object field. The spot image of the fiber in the image plane was captured by a CCD-camera setup with a Nikon 20x microscope objective which can be seen on the right hand side in figure 5. Due to the small dimensions of the whole setup, it was necessary to fold the optical path between the image plane and the microscope objective by an extra mirror.



Fig. 5: Lab setup for testing imaging quality.

The imaging quality for an object field of $480 \mu\text{m} \times 360 \mu\text{m}$ is shown in figure 5. The images are captured with the same camera settings for shutter speed and gain control for all five spots. The shutter speed was set to image the brightest spot, which is the left spot in the middle column in figure 6, without being overexposed. Thus, due to tilt and misalignment the spot intensities are not constant over the whole image field.

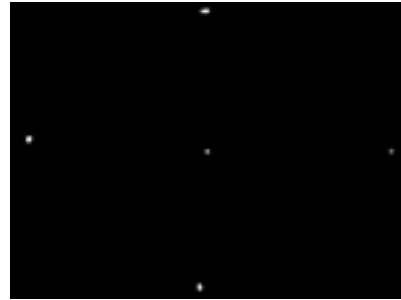


Fig. 6: Image spots of the single mode fiber (five spots copied into a single frame, field size is $480 \mu\text{m} \times 360 \mu\text{m}$).

Figure 7 shows an intensity plot of the spot in the center of figure 6. The Gaussian shape of the spot can be seen clearly and the diameter is approximately $7.5 \mu\text{m}$.

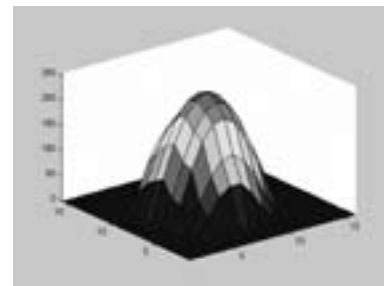


Fig. 7: Plot of the spot at $x=0 \ y=0$ (center of object field) the diameter of the spot is approximately $7.5 \mu\text{m}$.

Conclusions

In this paper, we demonstrated a planar integrated free-space optical system with prism coupling for higher efficiency compared to a purely diffractive implemented one. The whole system was fabricated in the ZMN facilities. Laboratory tests show excellent optical properties of the system.

This work, as part of the European Science Foundation EUROCORES Programme SONS, was supported by funds from the Deutsche Forschungsgemeinschaft DFG and the EC Sixth Framework Programme.

- [1] J. Jahns, "Planar packaging of free-space optical interconnections", IEEE Proc. 82 (1994) 1623-1631.
- [2] S. Sinzinger, und J. Jahns, "Microoptics", Wiley-VCH, Berlin (2003).
- [3] M. Amberg, und S. Sinzinger, "Design consideration for efficient planar integrated free-space optical systems", Opt. Comm. accepted.
- [4] H. Baitinger, "Prozessoptimierung für die Herstellung planar-optischer Mikrosysteme "Studienarbeit TU Ilmenau (2006).

Fabrication of Microstructured Glass Components by Drawing Technology

A. Hesse*, S. Belau, S. Mrotzek, and D. Hülsenberg
Department of Glass and Ceramics Technology

Introduction

The fiber drawing process allows very long devices with small cross sections. Consequently the most applications of components fabricated by the drawing process are optical waveguides or other photonic devices. But it's also possible to use the drawing process to fabricate elements with small and long capillaries (high aspect ratio) for other applications (e.g. fluidic devices, filters).

The glass characteristics allow a relatively simple fabrication of the glass components by simultaneous fusing and forming of the preforms.

Technology

The fabrication of microstructured glass components by drawing geometrically similar glass preforms is comparable with the fabrication of glass fibers. This principle assumes the laminar flow of glass. The method is characterized by the feed velocity of the preform into the heating zone of the furnace (v_1), the viscosity of glass inside the furnace and the drawing velocity of the fiber (v_2).

The fabrication of microstructured glass fibers is subdivided into two steps. First of all some single preforms will be stacked to a preform bundle with the wanted structure. After this, the bundle will be placed into the furnace, heated and drawn down to a microstructured glass fiber. During the drawing process the several preforms were fused together and formed to a composed fiber with the wanted cross-section and defined micro channels [1].

Experiments

There were two intentions for the experiments. The first one was to fabricate various fiber structures. On the other hand openings with the smallest possible size should be manufactured. For the fabrication of microstructured glass components many different preforms or preform bundles can be used. Examples for geometries of single preforms are round rods, tubes or hexagonal preformed elements. For the shown experiments only round rod and tube preforms were used. All preforms had an outer diameter of 3 mm and the glass tubes had an inner diameter of 2 mm.

Figure 1 shows examples for the fabrication process of a micro structured fiber of 90 tubes and 1 rod.

The 91 elements were packed into the hexagonal structure, placed into the furnace, heated and drawn down to the fiber as shown in figure 1a. Figure 1c displays an onion, where the single preforms fused together and reduced in their cross section. Further the cross section of the drawn fiber is presented in figure 1b.

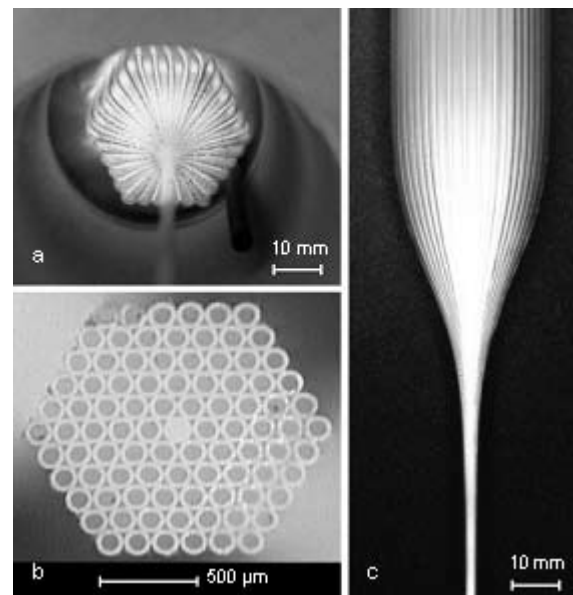


Fig. 1: Example of the drawing process for a bundle of 90 tubes and 1 rod. a) tapering structure in the furnace after cooling down the bundle; b) cross section of the microstructured fiber, c) tapering structure of the bundle (onion).

The inner diameters of the tubes are in the range of 100 μm . Further there are clearly visible triangular openings between three tubes. If the fiber was drawn to a smaller diameter or with a slower velocity, the triangular openings are getting smaller until they collapse. This effect is caused by the surface tension.

For the fabrication of smaller tube openings it is necessary to draw down the fiber a second time.

A SEM picture of one of the twice drawn fibers is shown in figure 2. The openings are about 1 μm wide and the small triangles have a side length of about 400 nm.

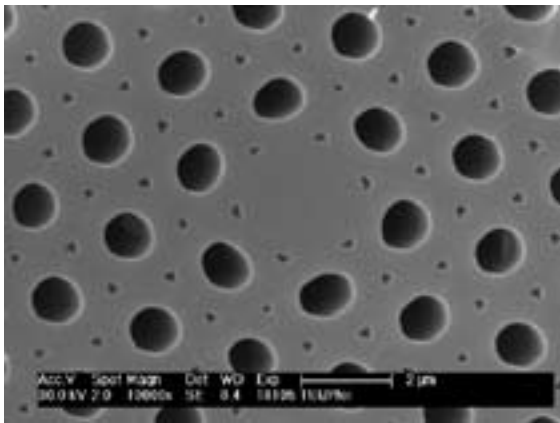


Fig. 2: SEM picture of a twice drawn fiber.

Another possibility for producing fibers with holes is to draw a bundle of rods with regions of removed rods. Figure 3 shows a bundle of 72 rods.

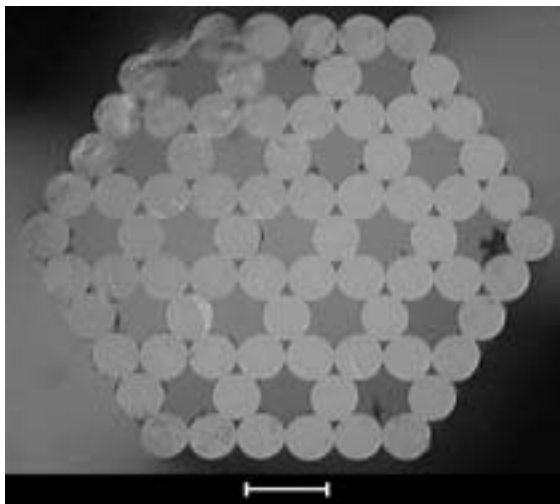


Fig. 3: Microscopy picture of a fiber with 72 rods (the fields between the rods are filled in with air).

In this figure the openings of the removed rods have no round geometry. But if this fiber is drawn a second time or by a slower drawing velocity, the triangular openings between three rods collapse and the other openings get a round geometry due to the surface tension. Figure 4 shows a fiber with collapsed triangular openings and round holes.

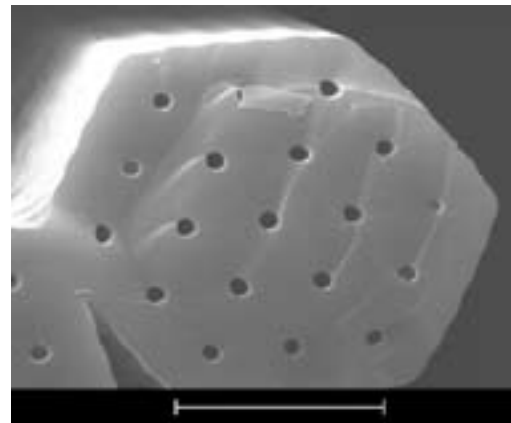


Fig. 4: SEM picture of a fiber of 72 rods with collapsed triangular openings and round openings at the places of the removed rods.

Another possibility to modify fibers is to draw compressed air-enhanced. This offers a wide range to vary the fiber structure. It is possible to get structured fibers with big hexagonal holes, additional smaller triangles, massive points and very thin walls (Fig. 5). The surface tension plays a very important roll, and only by different combining the rods and the tubes many diverse geometries are realizable.

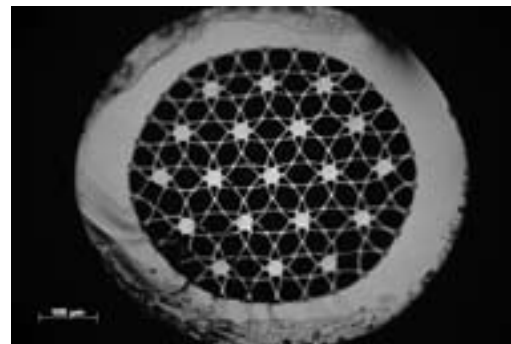


Fig. 5: Microscopy picture of a fiber with a small wall thickness as a result of compressed air-enhanced drawing.

- [1] Russell, P.: Photonic crystal fibers. Science Vol. 299, p. 358 – 362, 2003.
- [2] Beloglazov, V.I.; Skibina, Yu.S.; Chtcherbakov, A.V.; Lebedev, N.F.; Soukhoveev, S.P.: Technologie des mikrostrukturierten Glases. 44th International Scientific Colloquium. Technische Universität Ilmenau, 1999.
- [3] Beloglazov, V.I.; Soukhoveev, S.P.; Suetin, N.V.: Three-dimensional micron and submicron structures based on fiber glass technologies. Proc. Indo-Russian Workshop on micromechanical systems. SPIE proc. Vol. 3903, p. 134-140, 1999.
- [4] Wiedererwärmen und Ziehen von Glas für Interferenzsysteme und Mikrobauteile Fraunhofer-Institut für Silicatiforschung Würzburg, Jahresbericht S.47-48, 2000.

Glass as a Material for Gravure Printing of Electric Functionalised Inks

U. Brokmann*, K. Sönnichsen, and D. Hülsenberg
Department of Glass and Ceramic Technology

Introduction

Current trends in the development of flexible electronic systems for the information and communication technology show that a provision of materials and manufacturing procedures for thin mechanically flexible components and semiconductors plays an important role. New functional polymers with conductive, semi-conductive or insulating properties facilitate the fabrication of different electronic devices using typography. Due to the possibility of high resolution prints and the processing of low viscous inks, gravure printing is an appropriate procedure to create structured layers for electronic applications. Table 1 shows a comparison of different master coupled print techniques.

	Screen printing	Gravure printing	Letterpress printing (flexo print)	Lithography (offset print)
lateral resolution [μm]	> 100	> 15	> 40	>10
average layer thickness [μm]	3 – 15	0.8 – 8	0.8 – 2.5	0.5 - 2
viscosity of print material [Pas]	0.5 - 50	0.05 – 0.2	0.05 – 0.5	30 - 100

Tab. 1: Comparison of different typographies.

For gravure printing (Fig. 1), the surface of a printing plate with recessed elements (cells) will be covered with low viscosity ink. After the doctor blade which removes all the excessive material, the ink is residual only in the recesses. A flexible substrate which is fixed on a rotating cylinder will be pressed onto the horizontal moved printing plate and takes up the ink from the recesses. Thin flexible glass sheets (thickness < 100 μm) and also printing plates made from glass are in the centre of interest due to the transparency, chemical, mechanical and thermal stability of this material.

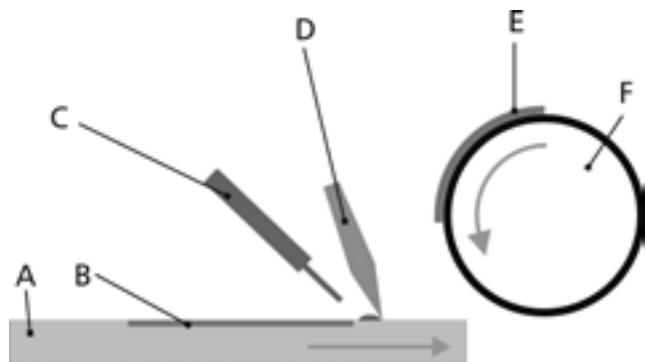


Fig. 1: Scheme of a gravure print device with printing plate (A: printing plate (metal), B: glass cliché with cells, C: spreading of ink on the printing plate, D: doctor blade to fill in the ink in the cells of the glass plate, E: mechanically fixed flexible glass substrate, F: printing roll).

Mechanical behavior of thin glass sheets

During the gravure printing process glass substrates will be mechanically stressed by fixing and extracting in the printing machine, during the transport in the printing machine and during the printing procedure in contact with the printing plate. Therefore the mechanical strength of an display glass D263T (thickness: 30 μm) was determined by 3-point bending tests. For the untreated glass foil D263T the maximum bending strength s_{max} amounts 139 N/mm². The sample treatments, spincoating of a polymer film and laminating of an adhesive plastic foil lead to a significant increase of s_{max} (spincoated polymer: 245 N/mm², laminated plastic film: 255 N/mm²), similar to the results of [Cra2005]. The main reason for the uncontrolled brittle breaking of glass samples are damages in the surface by cracks. Such cracks will be induced during the manufacturing process, an incorrect storage and handling and significantly during the separation/cutting process. An increasing of reproducible results can be achieved if glass foils have a minimal surface roughness of <1 nm, the surface is covered by a spincoated polymer with a thickness of 20 μm or a laminated plastic film with an adhesive strength of < 0.1 N/20 mm and the tensile bending stress acts on the so called top side of the glass sheets. The top side is the surface which was used for an implementation of defined cracks

(using a diamond tool) during a separation process. It was determined a minimal bending radius of around 10 mm for the display glass D263T independent on the treatment.

Rheological behavior of glass substrates and printing plates

A successful gravure print implies an adjustment of contact angles between the printing plate and the substrate material regarding the used inks. The surface with the smaller contact angle retains the ink volume. Therefore the minimum difference of the contact angles against the ink has to be $DCA > 10^\circ$ [Dar2000]. For instance P3HT (20% chlorobenzene) has a contact angle of $CA < 22^\circ$ against the untreated substrate materials D263T and also PE films. For photo structurable glass, contact angles of $CA > 33^\circ$ were measured depending on the treatment (exposure, thermal treatment, etching). Further material combinations will be investigated for the optimization of the printing process.

Gravure printing using glass printing plates

Printing plates for gravure printing were made from the photo structurable glass FS21 by the 3 step photo form procedure [Har2001]. Due to the high requirements regarding the flatness of the printing plates ($ttv < 10 \mu\text{m}$), an additional grinding and polishing step was necessary after the thermal treatment of UV exposed glass plates. To achieve cells with defined depths a single side etching was realized. Figure 3 shows a typical gravure pattern realized by the photo structuring procedure of glass. Figure 4 shows gravure printed dots of P3HT on a PE film. The thickness of the P3HT layer is around $2.5 \mu\text{m}$.

Amongst others, the lateral size and the thickness of printed layers depend on parameters of the pattern in the glass plate (lateral cell size, cell depths, pitch in form of lines/cm, surface properties etc.). The investigation of relations between quantitative and qualitative properties of different printed layers and structuring parameters of glass plates are subject of further works.

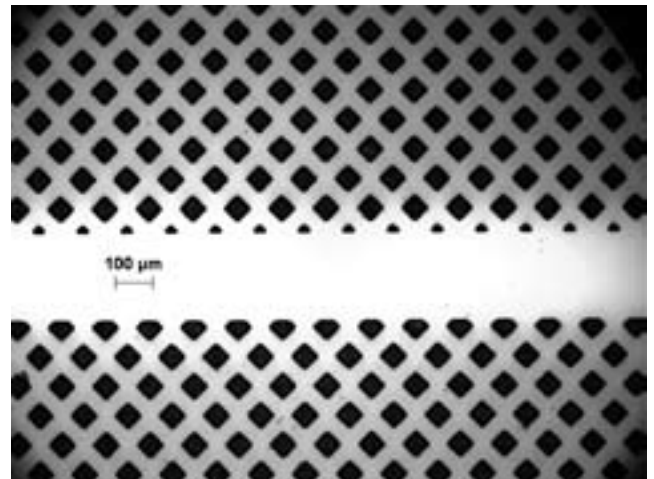


Fig. 3: Gravure printing pattern in photo structured glass, cell depth: $8 \mu\text{m}$.

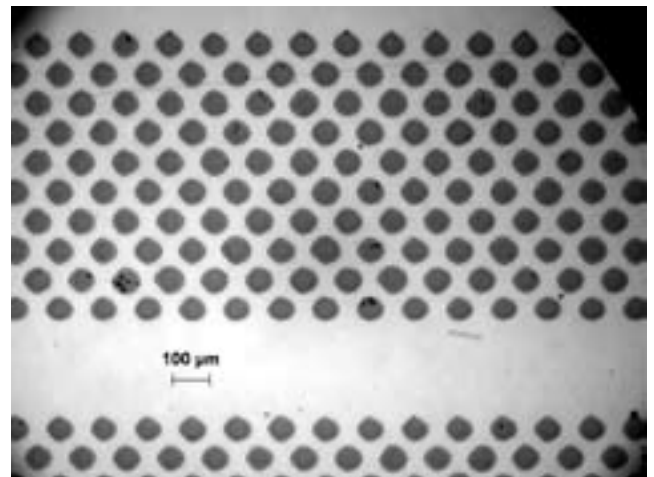


Fig. 4: Gravure printed P3HT dots on a PE film, printing plate: photo structured glass (Fig. 3), layer thickness: $\sim 2.5 \mu\text{m}$.

This work was funded by the European Commission, IST/STREP programme in FP6, EU-Project: CONTACT, Contract No.: 51156

[Dar2000] A. A. Darhuber, S. M. Miller, S. M. Troian, S. Wagner: Process Simulation for Contact Print Microlithography. Proceeding of MSM2000 at San Diego, 2000.

[Har2001] Harnisch, A.; Hülsenberg, D.; Hecht-Mijic, S.; Mrotzek, S.; Brokmann, U.: UV-microstructurable glasses – an overview. Proceedings XIX. Int. Congr. Glass, Edinburgh, July 2001, Glass Technol., 2002, 43C, 259-64.

[Cra2005] G.P.Crawford: Flexible Flat Displays. John Wiley & Sons. 2005.

Composite Layers through the Combination of Electrophoretic Deposition and Galvanic Processes

A. Knote^{1,*}, H. G. Krüger¹, S. Selve², Th. Kups², H. Kern¹, and L. Spieß²

¹ Department of Metallic Materials and Composite Materials

² Department of Materials for Electronics

Motivation

There is a continuous need for coated metallic components, e.g. for wear and corrosion protection, as well as for applications at high temperatures. These coatings are expected to exhibit both, a high wear and corrosion resistance as well as a good adhesive bonding to the metallic component, excellent thermal shock resistance and high damage tolerance during mechanical stress.

As an alternative to pure ceramic coatings, attempts have been made to develop metalceramic composite layers in which the favorable properties of metals, for example ductility, can be combined with the hardness and wearresistance of ceramics. These processes include, for example, electrolytic dispersion deposition, in which small ceramic particles are dispersed in the electrolytes and deposited together with the metal [1]. Dispersion composite coatings with nanoscale ceramic powders are promising to significantly increase the hardness, wear resistance and maximum application temperature [2]. However, the high specific surface of fine ceramic particles and the tendency associated with this to form particle agglomerates allow only low particle concentrations.

Current studies focus on a combination of electrophoretic deposition and electroplating technology [3]. In the present study an improvement of the method has been developed. It is based on the application of a galvanic metal intermediate coating onto the metal substrate for improvement of the coating adhesive bond.

It was possible to achieve both nickel/zirconium oxide as well as a copper/zirconium oxide coatings with strong adhesive bonds on stainless steel.

Experimental Methods

The tests were carried out on stainless steel X6Cr17. For production of the metal ceramic composite layers, the metal substrate was first degreased and then electroplated with a thin metal layer (5–10 μm). For this process, the substrate surface was first activated and roughened in a preliminary nickel-plating bath.

The ceramic powder used was zirconium oxide TZ-8Y (Tosoh Corporation, Japan). This powder was electrophoretically applied onto this primary electroplating coating. For this, it is necessary to prepare the fine powder into an agglomeratefree, electrostatically stable suspension. The zirconium oxide

powder was dispersed ultrasonically with the addition of 4-hydroxybenzoic acid in ethanol and a small part of water.

The electrophoretic deposition was realized at current densities of 0.2–2 mA/cm^2 with 2–5 s coating time.

After drying the layer in air, the specimen was sintered in vacuum at temperatures of 1050°C–1150°C for 3 hours, resulting in an open-porous layer of ~50% porosity.

The open porosity in the ceramic layer was then galvanically filled with metal.

A final heat treatment of one hour at 800°C in vacuum enabled the positive bonding of the composite layer onto the substrate via diffusion processes.

Results and discussion

The ceramic layers were electrophoretically deposited on the metal surface using an optimized suspension. The layer thickness which can be obtained, depends on the current density and coating time. Figure 1 shows the relation between the layer thickness and the coating time for various current densities.

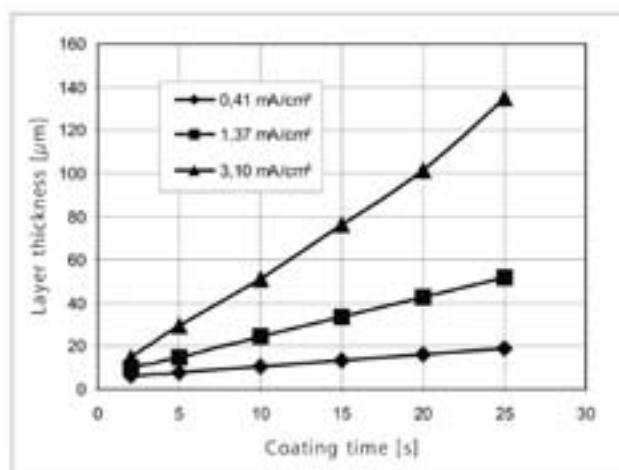


Fig. 1: Relation between coating time and layer thickness achieved at various current densities.

The zirconium oxide layers produced electrophoretically were sintered in a vacuum of 10^{-1} mbar after drying at temperatures of 1150°C for creating nickel-zirconium oxide layers and at 1050°C for the copper-zirconium oxide layers. The porosity of the layers was determined

to be 40-50%. The sintering in vacuum is necessary in order to prevent oxidation of the metal. An oxide layer would prevent contacting of the surface and hence it would impede the coating development both in electrophoretic layer production and in galvanic infiltration.

In the layers sintered at 1150°C, an openporous ceramic layer with clearly pronounced sintering necks resulted. The sintering of the ceramic layer for production of the copper/zirconium oxide layers was carried out at significantly lower temperatures. The lower sintering temperature was necessary owing to the low melting point of copper.

The sintering on a galvanic intermediate layer leads to a considerable improvement in the bonding of the ceramic layer onto the stainless steel.

Material transport through diffusion occurred between the substrate and the galvanic intermediate layer during sintering. At the same time, nickel or copper partially dissolves in the metal substrate. The remaining galvanic layer improves the contacting of the substrate during galvanic filling of the open-porous layer after sintering.

The practical implementation of the galvanic filling did not present any problems, despite the very narrow pore channels. The open porosity of the ZrO_2 layer could be completely filled. The metal extends through the ZrO_2 layer beginning from the substrate surface, forming effectively an interpenetrating metalceramic compound layer.

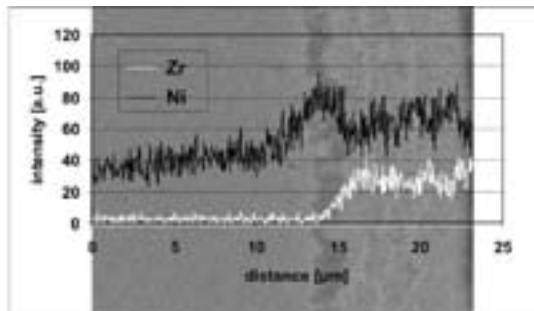


Fig. 2: EDX line scans with distribution of the elements zirconium and nickel over the sample crosssection.

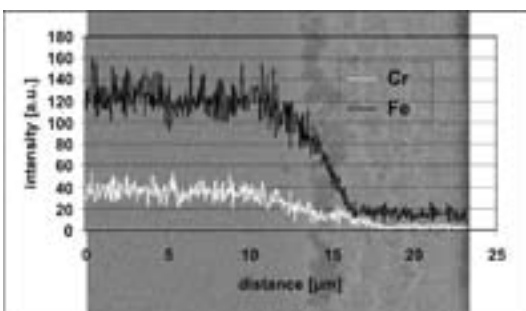


Fig. 3: EDX line scans with distribution of the elements chromium and iron over the sample crosssection.

An improvement in the layer formation can be achieved through subsequent annealing in vacuum. The final annealing process enables a strong material bonding of the composite layer with the substrate through reciprocal diffusion of the metal components. Overlapping SEM images with EDX line scans, which represent the distribution of the individual elements in the transition zone from the substrate to the composite layer, revealed the distribution of the individual elements after heat treatment. It is clearly discernible that nickel has diffused very deeply into the metal substrate (Fig. 3). At the same time, chromium and iron from the stainless steel substrate diffused into the nickel layer. As figure 4 shows, it is interesting that both, iron and chromium, can even be detected in the composite layer after the final annealing.

The same characteristics were observed when manufacturing the copper/zirconium oxide layers. After infiltration of the ceramic layer and subsequent thermal treatment at 800°C, the metal diffusion is also discernible through EDX line scans for these samples. In addition to the copper intermediate layer, figure 4 also reveals copper in the steel substrate. In the copper zirconium oxide composite layers, the EDX line scans in figure 5 show that both iron and chromium have diffused into this layer.

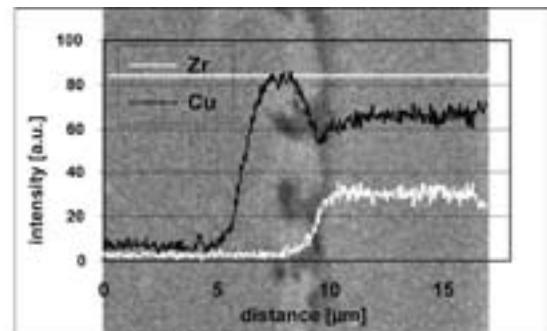


Fig. 4: EDX line scans with distribution of the elements Zirconium and copper over the sample crosssection.

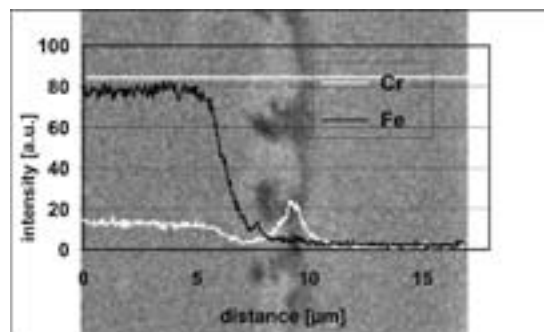


Fig. 5: EDX line scans with distribution of the elements Chromium and iron over the sample crosssection.

This work was financially supported by Deutsche Forschungsgemeinschaft (reference KE 359/7-1).

- [1] C. Karayianni and P. Vassiliou, *J. Mater. Sci. Letters*, 17(1998) 389.
- [2] G. Maurin and C. E. Barchichi, in *Proceedings of the 50. ISE Conference 1999*, p. 284.
- [3] H. G. Krüger and A. Knöte and U. Schindler and H. Kern and A. R. Boccacini, *J. Mater. Sci.* 39(2004) 839.

Magneto-hydrodynamic effects on electrodeposition of nickel composite coatings with nano-particles of oxidic ceramic

F. Erler, C. Jakob*, and F. Petzoldt

Department of Electrochemistry and Metal Finishing

Introduction

There is widespread use in engineering of electrodeposited nickel composite coatings, which conventionally have particles of a diameter ranging between 1 and 100 μm [1]. There is now a trend of using solid powder of a primary particle diameter below 100 nm as the additional ingredient of the nickel composite. This kind of nano nickel composite coating may find application in micro-technology and in thin film coatings.

The properties of the material can be improved by varying the type, size, amount and distribution of the incorporated particles. The optimum dispersion hardening effect in composite materials, calculated theoretically, appears when a ductile matrix contains 10-nm-particles spaced 100 nm apart. In this case, there are only 0.86 vol-% particles in the composite material, a "low" quantity of incorporated particles. The literature, indeed, predicts this low quantity, attributing it to physical and chemical effects between particle and growing surface.

The very high surface energy and agglomeration tendency of the nanoparticles in high conductive metal electrolytes will tend to impede uniform distribution of the particles. Furthermore, the compression of the double layer by the high-conductivity electrolyte together with the low particle surface charge (three orders of magnitude less in comparison to nickel ions) will render any transport of particles by means of electrophoresis or their migration within the electrolyte highly unlikely [2]. Uniform co-deposition would then appear to be well-nigh impossible in microstructures with a high aspect ratio. The very presence of particles in the metal electrolyte will, furthermore, affect the metal deposition process itself.

The even and high as possible incorporation of ceramic particles on the micro scale basically depends on the convective movement between electrolyte and electrode. In contrast to that, a convective influencing of the deposition is not possible in microstructure substrates, especially with high aspect relation. The thickness of the diffusion layer approximately corresponds with the height of the structure. Nickel composite coatings containing an amount up to 2 vol-% of nanoscaled oxidic ceramic particles have, notwithstanding, been subjected to examination by a number of methods, all focusing on the interface between the particle and the nickel matrix.

Proportion of particles in composite coatings measured by Photon Correlation Spectroscopy (PCS)

The proportion of incorporated particles in deposited nickel layers increases with increasing particle content of the electrolyte and decreasing current density (see Fig. 1). Above and beyond this, the agglomerate size in the electrolyte prior to deposition has a marked influence on the incorporation rate and thus also any mechanical treatment (ultrasound) and the hydrodynamic conditions. All these factors have to be kept constant during plating experiments. Larger and "denser" agglomerates facilitate a higher incorporation rate.

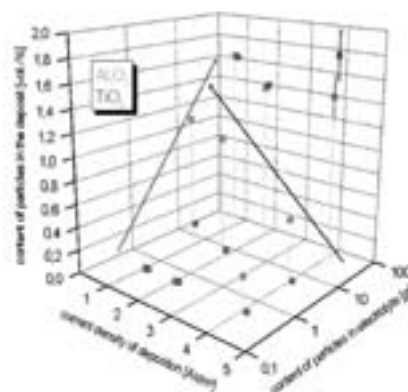


Fig. 1: Particle content in nickel layers in relation to current density and particle content in electrolyte [4]

Another field of interests is the variation in the amount of particles incorporated in the depth of a microstructure. In order to compare the results with regard to the incorporation amount and the distribution of the particles at smooth and structured surfaces, a model cell was used which guarantees analogue convective flow conditions at the structured wafer and the smooth special-steel.

For microstructures with a high aspect ratio the gentle vertical flow of the deposition cell was not sufficient to enhance the mass transport and remove hydrogen bubbles.

For example an EDX-measurement series is mapped in figure 2. The sample was deposited at 2 A/dm² from an electrolyte containing 50 g/l TiO₂ for 20 h. The structure was overgrown to provide a comparison between the incorporation rate inside and outside the structure.

No clear dependency of incorporation rate on depth of the structure was observed. Outside the structure, a slightly higher amount of particles was incorporated in the nickel coating. This might be due to the hydrodynamic transport conditions for the particles.

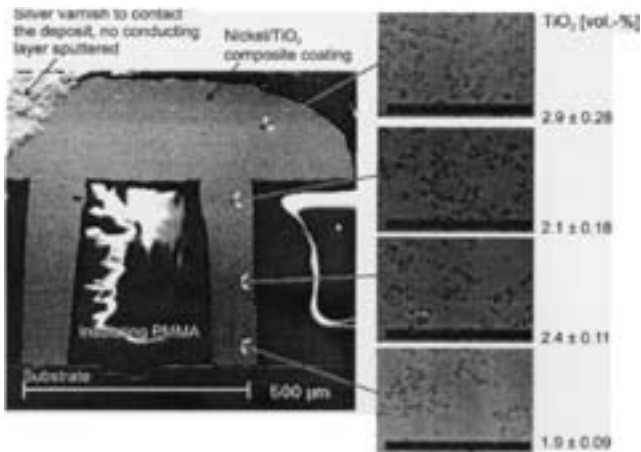


Fig. 2: Proportion of incorporated TiO_2 particles in the depth of a micro-structure with an aspect ratio of 5:1 measured by EDX [4]

MHD-effect on a model-electrolyte system

A high magnetic field applied perpendicular to the ion current induces a Lorentz force $F_L = I \times B$, which causes an additional convection in the hydrodynamic layer δ_H . For diffusion-limited systems a decreasing thickness of the diffusion layer δ_D and an increasing deposition rate is the consequence [3].

Magnetohydrodynamics (MHD) as kind of "micro-convection" was studied with a model-electrolyte-system to avoid influences from changing electrode surfaces.

To analyse the magneto-convection effect the limiting current i_L at several magnetic flux densities B was measured. With an increasing electromagnetic field a rising limiting current, caused by the classical MHD effect, was examined (Fig.3).

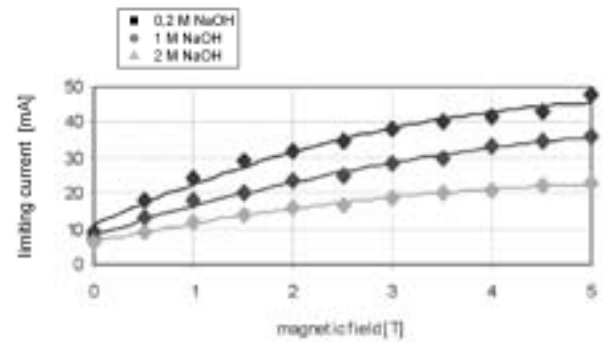


Fig. 3: Dependence of the limiting current on magnetic field for the cathodic branches

The results are currently attributed to the Lorentz force F_L exerted by the electromagnetic field B on the charged ions moving at the velocity I within an electric field. It is generally admitted that i_L is proportional to $B^{1/3}$ [4]. Aogaki et.al. [5] has demonstrated, that so called micro vortices appear in the vicinity of the electrode. This phenomenon is attributed to micro-MHD-cells and leads to magneto-convective effects in the diffusion layer usually being free of convection.

This micro-MHD-effect should be used to increase the convection in microstructures with high aspect ratio. First measurements were taken with a micro structured gold electrode in the same electrolyte system. Furthermore the effect of the magnetic field on the movement of nano-particles should be analysed. Tendencies of increasing convection in microstructures and influences on the particle incorporation must be assayed in future.

[1] C. Jakob, F. Erler, R. Nutsch, S. Steinhäuser, B. Wielage, A. Zschunke, *Metalloberfläche* 54 (2000) 50.

[2] A. Krause, M. Uhlemann, A. Gebert, L. Schultz, *The 15th RIGA and 6th PAMIR Conference on fundamental and applied MHD 2005*.

[3] O. Devos, A. Olivier, J.P. Chopart, O. Aaboubi, G. Maurin, *J. Electrochem. Soc.*, Vol. 145, No. 2, 1998.

[4] F. Erler, C. Jakob, H. Romanus, L. Spiess, B. Wielage, T. Lampke, S. Steinhäuser, *Electrochim. Acta* 48 (2003), S. 3063-3070.

[5] R. Aogaki, A. Tadano, K. Shinohara, *Transfer Phenomena in Magnetohydrodynamic and Electroconducting Flows*, Kulwer, Netherlands, 1999.

Strain Relief and Formation of Dislocations in InN Thin Films

V. Lebedev*, V. Cimalla, J. Pezoldt, Ch. Mauder, and O. Ambacher
Department of Nanotechnology

Motivation

Recent studies of the narrow band gap InN semiconductor [1] show increasing interest to investigate its fundamental properties and evaluate potential applications. InN was predicted to have the lowest effective mass for electrons among all III-nitride semiconductors [2], resulting in high mobility and high saturation velocity suitable for high-frequency field effect transistors. Recently reported results reveal the promising applications of InN epilayers for chemical and biological sensors [3].

The most valuable problem of the InN heteroepitaxy is related to large lattice mismatches between the epilayer and any available substrate material. This raises the question of strain relaxation even for very thin epilayers, since the misfit dislocation density in InN is initially $> 10^{11} \text{ cm}^{-2}$ [4]. In order to achieve high optical and electronic quality, misfit relaxation defects in InN should be avoided within the constituting layers. The purpose of this work is to study the strain relief, including the formation of dislocations in (0001) InN/AlN heterostructures grown by plasma induced molecular beam epitaxy (PIMBE).

Experimental

The samples were grown in a Balzer's PIMBE system described elsewhere [5]. The growth process was monitored by digitized patterns of reflection high energy electron diffraction (RHEED). The (0001) AlN/Al₂O₃ epitaxial templates were overgrown in situ by 2H-InN epilayers (0.35-2.2 nm) at $T_{\text{sub}} \sim 380^\circ\text{C}$ under stoichiometric (1:1) conditions to prevent a surface metal accumulation. Structural analysis was performed by high resolution x-ray diffraction (XRD)

using a Bruker D8 diffractometer. The samples for crosssection and planview transmission electron microscopy (TEM) were prepared by mechanical thinning and ionmilling. The micrographs obtained in brightfield (BF) and darkfield (DF) modes by conventional two-beam (2B) conditions and high resolution TEM (HRTEM) were analyzed.

Room temperature mobility in excess of $1500 \text{ cm}^2\text{V}^{-1}\text{s}^{-1}$ were obtained by Hall measurements for $\sim 800 \text{ nm}$ thick InN layers with dislocation densities of $\sim 3 \times 10^9 \text{ cm}^{-2}$.

Results and Discussion

The in situ RHEED observations allowed us to distinguish at least three different growth phases characteristic for any highly-mismatched heterosystem: (i) nucleation and subsequent growth of slightly misoriented 2H-InN islands up to a thickness of $\sim 10\text{-}15 \text{ nm}$, (ii) a partial coalescence of the islands into a continuous film, and (iii) a long-term epitaxy followed by gradual improvements of the surface morphology (Fig. 1(a)).

In the InN/Al_xGa^{1-x}N heterostructures, most of the lattice mismatch is accommodated by geometrical misfit dislocations (GMDs), which are 60° dislocations with a Burger's vector \vec{b} and line parallel to $\langle 2\bar{1}10 \rangle$ directions and lying in the (0001) basal plane. Statistical HRTEM analyses demonstrate an approximate ratio, m:n, InN{01 $\bar{1}0$ }:AlN {01 $\bar{1}0$ } of $\sim 57:64$ resulting in a residual mismatch of $f = |(n \times d_{\text{AlN}} - m \times d_{\text{InN}}) / n \times d_{\text{AlN}}| = -0.012$. A line density of dislocations near the AlN/InN heterointerface of $D \sim (4 \pm 0.5) \times 10^6 \text{ cm}^{-1}$ was extracted from HRTEM images. During the coalescence (Fig. 1(a)), 2H-InN domains come into contact forming a partially

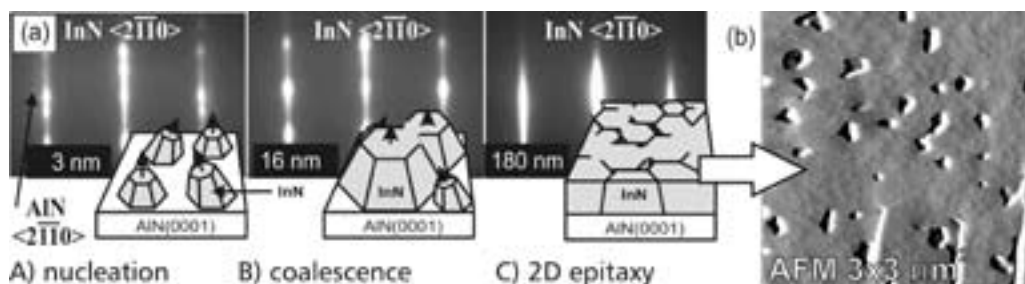


Fig. 1: (a) $2\bar{1}\bar{1}0$ RHEED patterns and schematic representation of the growth of 2H-InN on highly mismatched templates: (A) early formation of the slightly misoriented flat InN platelets with elastic relaxation at the edges, (B) partial coalescence of the platelets, and (C) further growth and formation of a continuous layer. (b) AFM reveals a small surface roughness of $\sim 2 \text{ nm}$ for a 2.2 nm InN epilayer.

disordered phase. The small in-plane misorientation, $\Delta\phi$, will give rise to a low-angle domain boundary which consists of an array of dislocations with a spacing

$D = |\vec{b}| \times \tan(\Delta\phi)$. For $\vec{b} = 1/3 \langle 11\bar{2}0 \rangle$ threading dislocations (TDs) and $\Delta\phi \sim 0.3^\circ$, the dislocation density of $D_c \approx 7.7 \times 10^{10} \text{ cm}^{-2}$ can be derived.

These $|\vec{b}| = 1/3 \langle 11\bar{2}0 \rangle$ TDs are pure edge dislocations with no dislocation glide, produced by the domain structure of the film (see Fig. 2).

At a certain critical thickness, it may become possible that the strain energy is partially released by the generation of a new dislocation network of secondary misfit dislocations (SMDs) which glide to the island/substrate interface.

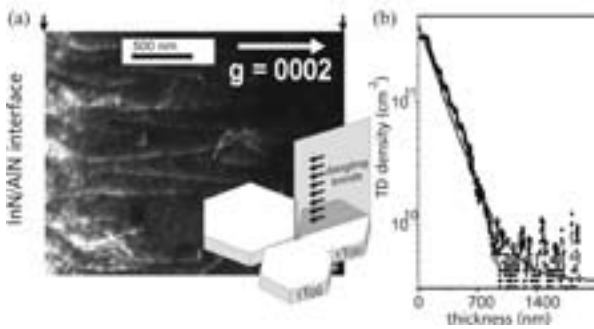


Fig. 2: (a) DF-TEM micrograph taken in 2B conditions using the 0002 reflection for

pure screw $\vec{b} = \langle 0001 \rangle$ or mixed $\vec{b} = 1/3 \langle 11\bar{2}3 \rangle$ TD detection; (Inset: a schematic view of the grain boundary TDs at the contact plane of the 2H-InN islands);

(b) TDs density vs. distance from the interface for a 2.2 μm thick InN epilayer derived from TEM.

The following slip systems: (a) $\{1\bar{2}2\} \langle 11\bar{2}3 \rangle$; and

(b) $\{1\bar{1}01\} \langle 11\bar{2}3 \rangle$ were found to be the only possibility to form SMDs, more and less probable, respectively to relieve the biaxial strain. If we assume

that each SMD could be related at least with one

secondary $\vec{b} = 1/3 \langle 11\bar{2}3 \rangle$ TD and its length is limited by the mosaic structure, a secondary planar TD density of $D_2 \sim 3.26 \times 10^{11} \text{ cm}^{-2}$ can be deduced.

Finally, we can estimate the total density of TDs after the coalescence phase as follows:

$D = D_c(\mathcal{S}) + D_2(\mathcal{S}) \sim 4 \times 10^{11} \text{ cm}^{-2}$. GMDs have not been taken into account so as they do not create dislocation lines propagating along the $\langle 0001 \rangle$ direction. The calculated total density of TDs fits well to the value obtained by the TEM observations; for example for dislocations with pure edge or mixed character at a thickness $\sim 7.5 \text{ nm}$ (experimental: $3 \times 10^{11} \text{ cm}^{-2}$, extrapolated: $4 \times 10^{11} \text{ cm}^{-2}$).

Figure 2 shows a DF-2B-TEM micrograph using the

0002 reflection of InN near the $[\bar{1}\bar{1}00]$ zone axis to display pure screw and mixed TDs. Similarly, TEM micrographs were taken in 2B conditions using the

$11\bar{2}0$ reflection for pure edge $\vec{b} = 1/3 \langle 11\bar{2}0 \rangle$

or mix $\vec{b} = 1/3 \langle 11\bar{2}3 \rangle$ TDs detection. From the intensity profiles of these images, the reduction in the dislocation density is seen to follow an exponential decay law up to a thickness of $\sim 1 \mu\text{m}$ (Fig. 2(b)). The main mechanism of TDs annihilation in 2H-InN has been found similar to those observed in 2H-GaN [6] and 2H-AlN [5] epilayers.

Conclusions

The proposed growth model emphasizes a determinant role of the residual strain relief and coalescence processes in the formation of $\vec{b} = 1/3 \langle 11\bar{2}0 \rangle$ TD network in 2H-InN as revealed by RHEED and TEM measurements. It has been shown that the TD density decreases exponentially during film growth due to annihilation of the dislocations reaching $\sim 1.3 \times 10^9 \text{ cm}^{-2}$ in $\sim 2.2 \mu\text{m}$ thick InN films.

This work was supported by the DFG grant AM105/1-1/2 (Germany). The authors also thank Dr. F.M. Morales for TEM analyses.

[1] V. Davydov et al., phys. stat. sol. (b) 229, R1 (2002); 230, R4 (2002).
 [2] S. N. Mohammad and H. Morkoc, Prog. Quantum Electron. 20, 361 (1996).
 [3] H. Lu, W. J. Schaff and L. F. Eastman, J. Appl. Phys. 96, 3577 (2004).
 [4] E. Bellet-Amalric, C. Adelman, E. Sarigiannidou, J. L. Rouvière, G. Feuillet, E. Monroy and B. Daudin, J. Appl. Phys. 95, 1127 (2004).
 [5] V. Lebedev, F. M. Morales, H. Romanus, S. Krischok, G. Ecke, V. Cimalla, M. Himmerlich, T. Stauden, D. Cengher and O. Ambacher, J. Appl. Phys. 98, 093508 (2005).
 [6] S. Tanaka, M. Takeuchi and Y. Aoyagi, Jpn. J. Appl. Phys., Part 2 39, L831 (2000).

Flow-rate dependent formation of gold nanoparticles in micro fluid segments

K. Ritter, J. Wagner, and J.M. Köhler*

Department of Physical Chemistry and Microreaction Technology

Microreactors are under investigation for homogenous and heterogeneous chemical processes. Furthermore micro flow-through systems are successfully applied for the preparation of inorganic micro and nano particles, e.g. continuous processes for the preparation of carbonate nanoparticles [1] as well as gold nanoparticles [2] using static micro mixers. Micro fluid segments are of particular interest for the preparation of nanoparticles. At first, they convert the laminar flow transport behaviour of liquids in microchannels and tubes in an ideal plug flow behaviour [3,4]. Secondly, shear forces induce an intensive convection inside fluid segments resulting in a fast mixing of educt solutions after coalescence of segments [5]. Thirdly, high contact angles between the process liquid and the channel walls can be realized and, therefore, the adsorption and deposition of solid material at the walls (reactor fouling) can be avoided. Here, the preparation of gold nanoparticles (GNPs) by a miniaturized continuous flow-through process using fluid segments is reported. The influence of reaction conditions and flow rates on the product quality was investigated.

Experimental arrangement and materials

A system of PTFE and PEEK tubes and a 7-port manifold out of PEEK were used for the preparation of GNPs. Both the carrier solution and the educt solutions were carried by a Cetoni[®] syringe pump. Total flow rates of educt solutions were varied between 250 and 750 $\mu\text{L}/\text{min}$. We used tetradecane or PP9 (perfluorinated alkane) as water-immiscible carrier liquids. The formation of fluid segments was realized by injection of the aqueous educt solutions into the streaming carrier liquids using the 7-port manifold (Fig. 1).

The GNPs are formed by reduction of HAuCl_4 (1 mmol/l) with ascorbic acid. The pH-value was varied between 3 and 9 by using a carbonate buffer solution.

In addition, the effect of macromolecules on nanoparticle formation in the fluid segments was tested. It is known from previous investigations that polymers lead to a reduction of the growth rate of nanoparticles [6]. Here, the water-soluble polymer polyvinylpyrrolidone (PVP) was applied as additive in some flow-through synthesis experiments in micro fluid segments. The product solutions were collected

in Eppendorf cups. The optical characterization occurred after separation of the aqueous phase from the carrier liquid. The product quality was further characterized with a CPS-System (DC 20000) by Differential Centrifugal Sedimentation.

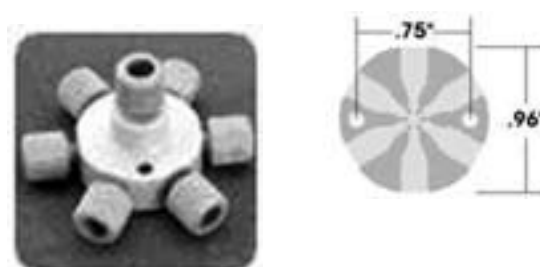


Fig. 1: Photograph and cut of the 7-Port-Manifold from Upchurch.

Segment formation, mixing and influence of chemical reaction conditions

Micro fluid segments can be generated easily in the fluid system. Size and distance of segments are quite regular. The mixing of educt solutions inside the segments is sufficient and leads to a good reproducibility of nanoparticle formation. An increase of pH-value causes a significant reduction of the mean diameter of GNPs (Fig. 2).

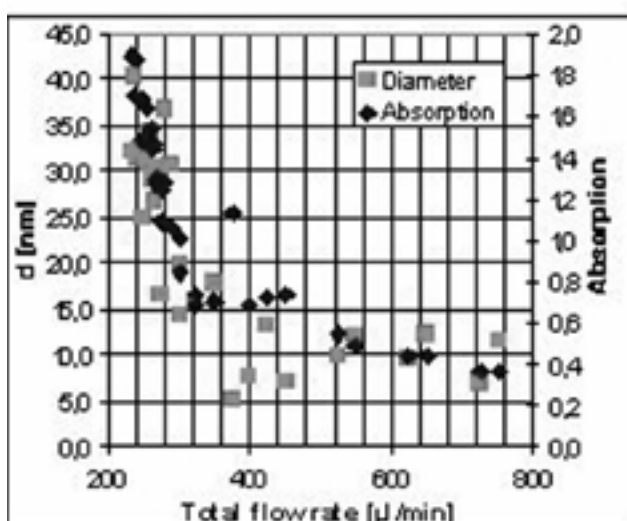


Fig. 2: Size distributions for different pH-values.

This effect corresponds with the behaviour in batch synthesis and with flow-through synthesis in homogenous phase. It can be explained by the increase of reduction power of ascorbic acid with increasing pH. The increasing reduction power leads to a higher nucleation rate. In result, the ratio of seed formation and particle growth increases with increasing pH. At lower pH a lower number of gold seeds is formed in the nucleation process. Therefore, particles grow up to larger diameters. At higher pH, most of the tetrachloroaurate is consumed in the nucleation process, the growth of seeds is limited and the high nucleation rate results in smaller GNPs.

Polymer addition effects the nanoparticle formation significantly. In comparison to polymer-free educt solutions, smaller particle diameters resulted when PVP is used. This behaviour was observed in the whole pH-range investigated. It is to assume that polymer molecules are adsorbed at the surface of the primarily formed gold seeds and inhibit the particle growth. In consequence, the ratio of seed formation to particle growth becomes higher, resulting in a higher concentration of smaller particles.

Influence of flow rate on the product quality

In contrast to pH-value, polymer additions, and educt concentrations, the total flow rate represents a global process parameter for the chemical process, which cannot influence the kinetics of a chemical process directly. In all synthesis a significant decrease of mean particle size with increasing flow rate was observed (Fig. 3). The predominant diameters are reduced from about 40 nm at lower flow rates to about 10 nm at higher flow rates.

An increase in the total flow rates causes an amplification of shear forces inside the whole fluidic system. Two effects can be discussed for the reduction of particle sizes by increasing shear forces:

1. The tendency of temporal adsorption of particles

at the wall as well as the tendency of aggregation are reduced by shear forces. 2. Increasing shear forces lead to an increase of segment-internal convection, which is responsible for the fast mixing of educts. It is to assume, that the second effect is the dominating factor for the observed reduction in particle size. Fast mixing leads to optimal conditions for high nucleation rates. Therefore, it can be expected, that higher concentrations of gold seeds are achieved, if high flow rates are applied.

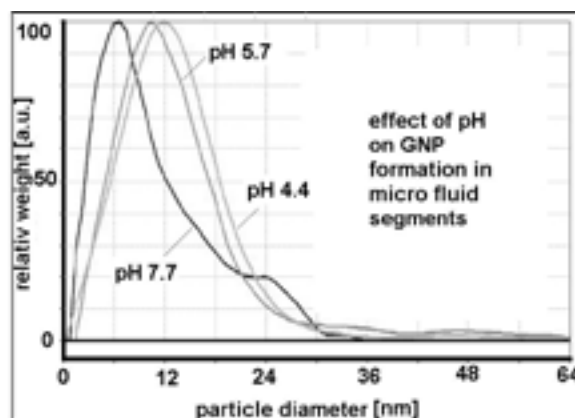


Fig. 3: Particle size and absorption of product solution in dependence on total flow rate.

Conclusions

The investigations show, that the synthesis of gold nanoparticles can be established in micro fluid segments. The reduction of tetrachloroaurate by ascorbic acid results in colloidal gold solutions of GNPs with diameters between about 10 and 40 nm. The mean size and the size distribution can be controlled by the composition of educt solutions and by the mixing speed. The addition of water-soluble polymers, the application of different pH-values and the selection of suited flow rates represent possibilities for controlling reaction parameters and product quality.

[1] Schenk, R., Hessel, V., Werner, B., Schönfeld, F., Hofmann, Ch., Donnet, M., Jongen, N., 2002, Proc. 15th Symp. on Ind. Crystallization (Sorrento 2002).

[2] Wagner, J.; Kirner, T.; Mayer, G.; Albert, J.; Köhler, J.M. Chem. Eng. J. 2004, 101, 251.

[3] J.M. Köhler, U. Dillner, A. Mokansky, S. Poser and T. Schulz, Proc. 2nd Internat. Conf. on Microreaction Technology (New Orleans). 1998, 2, 241.

[4] Burns, J.R., Ramshaw, C., Lab on a Chip 2001, 1, 10.

[5] Song, H., J.D. Tice, J.D., Ismagilov, R.F., Angew. Chem. 2003, 115, 792.

[6] Wagner, J.; Köhler, J.M., Nanoletters 2005, 685.

Carbon Nanotube Peapods – Insertion of C₆₀ into Multi-Wall Carbon Nanotubes

P. Scharff^{1,*}, U. Ritter¹, T. Fröhlich¹, W. Schliecke², O. Ambacher², H. Romanus³, and L. Spiess⁴

¹ Department of Chemistry

² Department of Nanotechnology

³ Center for Micro- and Nanotechnologies

⁴ Department of Materials for Electronics

Motivation

With the discovery of the fullerenes and carbon nanotubes, carbon science had a remarkable renaissance: Discrete spherical carbon molecules, being soluble in many conventional organic solvents, offered a broad variety of possible reactions to the chemists, whereas the nanotubes stand out because of their unique physical properties.

A unique possibility for an endohedral functionalization of nanotubes is to encapsulate fullerenes inside, as was first done with C₆₀ in single-wall carbon nanotubes (SWCNTs) by Smith et al. [1]. A lot of interesting questions arise concerning their physical properties and possible applications. In yet another small step towards building nanoscale devices, scientists have determined that the so called nanotube peapods have tuneable electronic properties. The findings published by Hornbaker et al. [2], suggest that stuffing the straws provides greater control over the electronic states of single-walled carbon nanotubes (SWNT). So far the fullerene encapsulation was reported with SWCNTs but not with MWCNTs. Here we show the insertion of C₆₀ into MWCNTs.

Results

During the formation of encapsulated fullerenes in-side SWCNTs (peapods), fullerenes enter via sidewall defects as well as via open tube ends. For MWCNTs only the second way exists. For the experiments we used high quality multi-wall carbon nanotubes prepared by the arc discharge method. Multi-wall nanotubes are obtained as cathode deposit in an arc vaporisation process of graphite in the absence of transition metal catalysts.

Because of the mostly carbonised impurities and the fact that all MWCNTs are closed, we have to develop a cleaning and opening strategy.

Figure 1 shows a sample of a MWCNT before oxidation (cleaning) and afterwards. Most of the carbon impurities (amorphous carbon, graphite and fullerenes) are removed.

Figure 2 showed a MWCNT after the acid treatment procedure. The inner graphene layers are partly reordered and all the MWCNT are closed caps. Therefore we have to remove all caps via a treatment with concentrated nitric acid [3].

Figure 2 shows that the acid preferably attacks the caps, where non-six membered carbon rings are located.

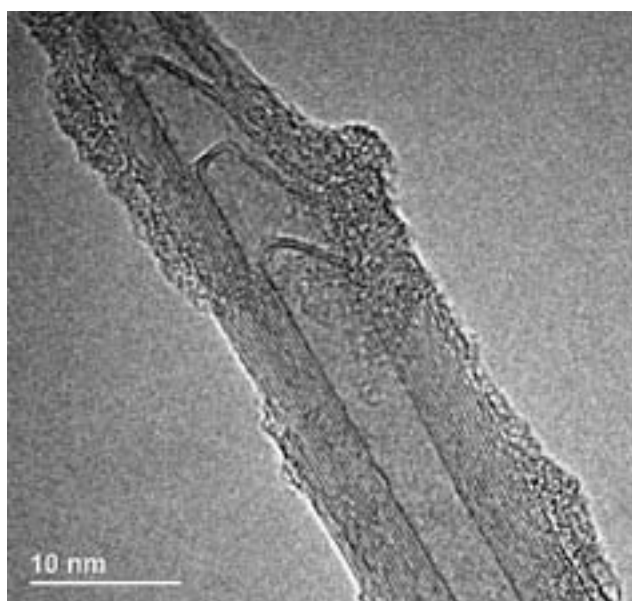


Fig. 1: HRTEM image of a MWCNT before the oxidation procedure.

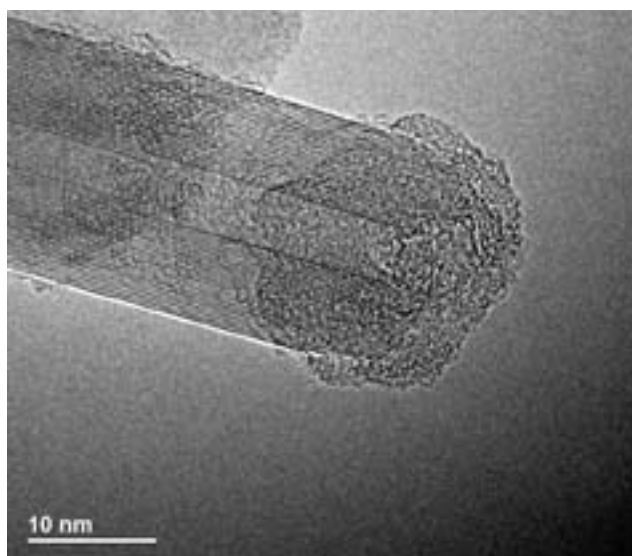


Fig. 2: HRTEM image of a MWCNT after the acid treatment.

The weight loss upon this procedure proved to be about 27% and several TEM images showed an average of 30-40% uncapped nanotube ends. We added C_{60} to the opened MWCNTs in a weight ratio of 1 to 7. Afterwards the mixture was sonicated in toluene and air-dried. Then the C_{60} -nanotubes mixture was placed onto a silicon wafer lying on an ordinary heating desk. The silicon wafer was covered loosely by a quartz glass hood and transferred via load lock into the main chamber, in which a turbo pump was providing a dynamic vacuum. All necessary prearrangements were followed by a 3 h annealing step at 650°C and a pressure of $200\ \mu\text{Pa}$. Such a high vacuum is important as we could not find any encapsulation of C_{60} in MWCNTs at higher pressure. Afterwards the prepared sample was directly dispersed in ethanol and imaged by a Tecnai 20 S-TWIN HRTEM instrument. In figure 3 inside of a MWCNT circles with a diameter of approximately $0.7\ \text{nm}$, corresponding to C_{60} fullerenes, can be seen.

Generally, there are two kinds of arrangements which are shown in figure 4: the first one consists of irregularly arranged C_{60} clusters together with some residual amorphous carbon which can be found at the tube end with a higher inner diameter ($3.4\text{-}4.4\ \text{nm}$) due to the acid treatment. In the second one, the innermost graphitic tube is still intact. Its diameter was determined from the HRTEM image to be $d_{\text{inner}} = 2.04 \pm 0.07\ \text{nm}$. This diameter is smaller than the sum ($2.3\ \text{nm}$) of twice the C_{60} molecule size ($0.7\ \text{nm}$) and three times the graphitic van der Waals separation ($0.3\ \text{nm}$). The fullerenes attach to the innermost tube and, therefore, tend to form zigzag chains.

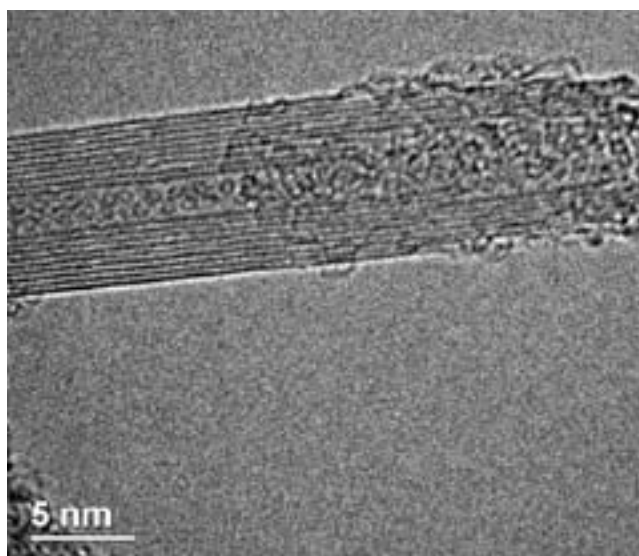


Fig. 3: HRTEM image of opened MWCNT filled with C_{60} molecules.

Two different nanotubes filled with C_{60} molecules are shown in the next two images.

In figure 4a ($d_{\text{inner}} = 2.25 \pm 0.1\ \text{nm}$) the sidewalls of the nanotube became wavy and most of the fullerenes were already fused during the observation, and, therefore, can hardly be seen here. In figure 4b the MWCNT with a very wide inner diameter ($8.1 \pm 0.2\ \text{nm}$) contains a composition of C_{60} which is obviously neither a bulk crystalline order nor any other ordered arrangement. In our sample we could not find any C_{60} filled nanotubes with closed caps, whereas we observed C_{60} molecules inside every open tube.

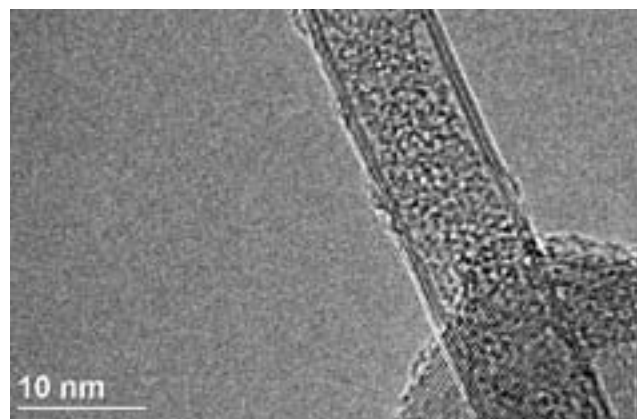


Fig. 4: Two filled MWCNTs with different inner diameter. Their inner diameter was measured to be $2.25 \pm 0.1\ \text{nm}$ (a) and $8.1 \pm 0.2\ \text{nm}$ (b).

Conclusion

In this short report we have demonstrated the insertion of fullerenes (C_{60}) into MWCNTs. The diffusion of C_{60} only takes place through open tube ends, and therefore an effective opening of MWCNTs is a precondition. In conclusion, insertion of C_{60} molecules inside nanotubes is realized and the formed inner structure is dependent on the tube radius. Both, zigzag structures and higher structures were found. When the diameter of the innermost graphitic tube is about $2\ \text{nm}$ the fullerenes attach to the inner wall and tend to form zigzag chains. In this study, we focused on the structural properties only. But as one can imagine, other properties of fullerene-filled nanotubes also change with changing fullerene configuration. For example, the phonon modes will be different for the linear and zigzag configurations. As a result, thermal conductivity will be different in the two configurations. Thus it should be possible to tune properties of filled nanotube materials by changing the radii of the host nanotubes. In future, it could be interesting to study further on the geometrical arrangements depending on the inner diameter of the tube and on the filling rate.

- [1] Smith B.W., Monthieux M., Luzzi D.E., Nature, 396, p. 323, 1998.
 [2] Hornbaker D.J., Kahng S.-J., Misra S., Smith B. W., Johnson A. T., Mele E.J., Luzzi D.E., Yazdani A., Science, 295, p. 828, 2002.
 [3] Tsang S.C., Chen Y.K., Harris P.J.F., Green M.L.H., Nature 372, p. 159, 1994.

New Results in the Crystallization Behaviour of Amorphous Material in the System $\text{BaO-Fe}_2\text{O}_3\text{-B}_2\text{O}_3$

U. Schadewald^{1,*}, B. Halbedel¹, H. Romanus², and D. Hülsenberg¹

¹ Department of Glass and Ceramic Technology

² Center for Micro- and Nanotechnologies

Introduction

Modern applications like high-frequency absorption, perpendicular recording, micro actuators or medical applications for hyperthermia require special properties of magnetic powders like certain aspect ratios, particle size or special occupations of the lattice sites. These properties can not be achieved by conventional sintering processes. The crystallization of hexagonal barium ferrite ($\text{BaFe}_{12}\text{O}_{19}$, BHF) by the "glass crystallization method" [1] offers a large potential to influence these properties. Former investigations of the crystallization of BHF often resulted in contradictory statements. In some works ([2], [3]) the first crystallizing phases are identified as borates (BaB_2O_3 , BaB_4O_7) whereas other authors ([4], [5]) found that first hexagonal barium ferrite appears.

In this work new results of the crystallization of BHF in glass of the composition 40 BaO-33 B_2O_3 -27 Fe_2O_3 (mole - %) are shown. Thermoanalytic methods like differential scanning calorimetry (DSC) and thermo gravimetric analyses (TGA) are used to obtain information about the crystallization process. X-ray powder diffraction measurements (XRD) are performed to analyze the crystalline phases. The morphology and size of the nuclei and crystals are investigated using the transmission electron microscopy (TEM) and scanning electron microscopy (SEM).

Experimental

The materials used in this work are amorphous flakes of the above mentioned composition, obtained by the rapid quenching process [1]. For further treatment the material is ground to $<63 \mu\text{m}$ and thermoanalytically analysed with a STA 409 PC "Luxx" (Netzsch) using a heating rate of 5 K/min. As a result of these measurements two curves are obtained. From the DSC-curve important temperature dependent information for the following tempering process (glass transformation temperature and temperatures of exothermic and endothermic reactions) can be obtained. The TGA-curve contains information about possible mass gains or mass losses caused by oxidation or reduction processes. To find out which phases crystallize at certain peaks of the DSC-curve tempering experiments in a high temperature furnace (ZZ 40-360/13, Gero Hochtemperaturöfen GmbH) are performed. Therefore the sample is heated to the

selected (DSC-) onset-temperature with a heating rate of 5 K/min, remained for 10 min and then cooled down to room temperature. After that the sample is ground again ($<63 \mu\text{m}$) and then analysed by XRD (Siemens AXS "D5000", wavelength: 1.540598 nm). To analyze appearing ferrite crystals it is necessary to solve off other phases (surrounding borates) by a weak acid (acetic acid: CH_3COOH). The unsolvable ferrite powders are analysed again by XRD. The estimation of the crystal morphology and size is done with a transmission electron microscope (Phillips Tecnai S20). Magnetic measurements are performed with a vibrating sample magnetometer (VSM). The real chemical composition of the sample material is obtained by wet chemical analyses (titration, ICP-OES).

Results and discussion

The results of the thermoanalytic measurements are shown in figure 1. Beside the glass transformation temperature at 490°C four exothermic peaks with onset temperatures of 524°C , 560°C , 606°C and 669°C are present.

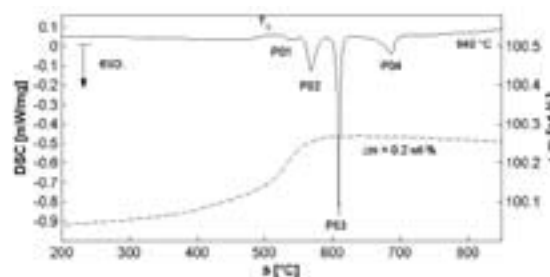


Fig. 1: DSC- and TGA-curves of the amorphous flakes (5 K/min, $m_{\text{sample}} = 326,166 \text{ mg}$).

The thermo gravimetric curve shows a mass gain of ca. 0.2 wt-% starting at about 200°C . This mass gain is caused by the oxidation of Fe^{2+} to Fe^{3+} which was also confirmed by chemical analyses. The XRD diagrams of the tempered material are shown in figure 2. The diffractograms of the untreated flakes and the material tempered at 524°C show no peaks which could indicate a precipitation of crystalline material, but halos which show the amorphousness of this samples. After tempering at a temperature of 560°C the intensity of these halos decreases and a small broad peak appears at $2\theta = 62^\circ$ (Fig. 2

marked circle). At a tempering temperature of 606°C characteristic peaks of BaB₂O₄ and first small peaks of BHF appear and remain also at higher tempering temperatures. At 669°C further peaks appear.

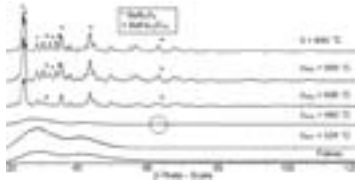


Fig. 2: XRD diagrams of the sample material tempered at the onsets of the peaks obtained from the DSC-measurement.

These peaks can be associated with crystalline BaFe₁₂O₁₉. The amorphous flakes, as well as the material tempered at 524°C leave no residue after solving in the weak acid. The first crystalline material can be obtained only after solving the sample tempered at 560°C. Due to the very low intensity and strong broadening of the peak this material can not be clearly identified by XRD. The diffraction diagrams of the material obtained after the solving process is shown in figure 3.

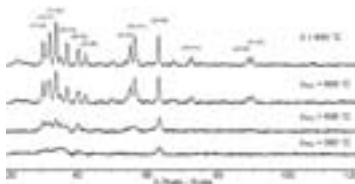


Fig. 3: XRD-diagrams of the residues remaining after solving the tempered samples.

After tempering at 606°C and dissolving the surrounding phases the remaining powder can clearly be identified as BaFe₁₂O₁₉. With rising tempering temperature the peaks become more intense and more narrow which can be attributed to the increasing perfection of the crystals. This can also be approved by TEM investigations of the tempered and suspended material. At low tempering temperatures the images of the residue show nuclei with a diameter of about 5 nm (see Fig. 4 left). When tempered at a temperature of 606°C the nuclei grow and become crystals (Fig. 4 right). They reach diameters of about 50 nm (Fig. 5 left). An increase of the tempering temperature to 840°C results in a further growth of the crystals to diameters of about 200 nm (Fig. 5 right) and a morphology transformation from a hexagonal bipyramidal into a hexagonal plate-like form (see Fig. 6).

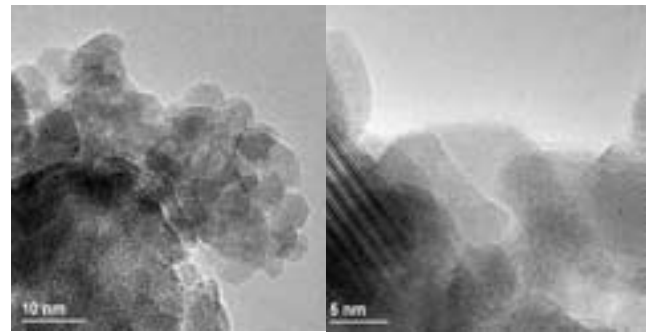


Fig. 4: TEM images of the material tempered at 560 °C (left) and 606 °C (right).

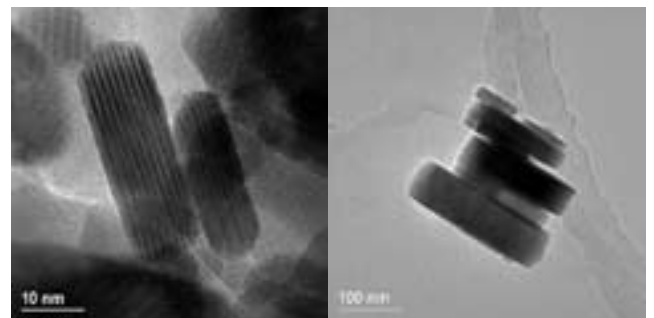


Fig. 5: TEM images of the material tempered at 669 °C (left) and 840 °C (right).



Fig. 6: Schematic drawing of the morphology change from a hexagonal bipyramidal to a hexagonal plate-like form.

Conclusions

The crystallization of BHF in amorphous flakes of a composition of 40 BaO - 33 B₂O₃ - 27 Fe₂O₃ (mole-%) was analysed. Thermoanalytic measurements showed, beside the glass transformation temperature, four exothermic reactions, which were investigated by XRD and TEM (Tab. 1). Investigations in progress focus on the evaluation of chemical composition and magnetic properties of the crystalline material.

Tempering Temperature	occurring reactions
490°C	glass transformation temperature
524°C	oxidation of Fe ²⁺ to Fe ³⁺
560°C	precipitation of a crystalline phase not yet clearly identifiable, D≈5 nm)
606°C	precipitation of BaB ₂ O ₄ , growth of ferritic particles (BaFe ₁₂ O ₁₉ , D≈20 nm)
669°C	further growth of BaFe ₁₂ O ₁₉ (D≈50 nm) crystals within BaB ₂ O ₄ matrix: crystals of hexagonal bipyramidal morphology
840°C	BHF-particle sizes D=100 nm ... 200 nm morphology of BaFe ₁₂ O ₁₉ particles changes to hexagonal plate-like form

Tab. 1: Tempering temperatures and reactions.

Stress Modification in Wide Gap Heteroepitaxy on Silicon

J. Pezoldt^{1,*}, Ch. Zgheib^{1,2}, Th. Stauden¹, Ch. Förster¹, F. M. Morales¹, and P. Masri³

¹ Department of Nanotechnology

² Department of Sciences, Notre Dame University, Zouk Mikayel, Lebanon

³ Groupe d'Etude des Semiconducteurs, Université de Montpellier, France

Introduction

The stress state in heterostructures is one of the important design parameters in the technology of heterostructures. The residual stress affects the manufacturability of the processed wafers as well as the defect densities and, therefore, the device related properties of the grown heterostructures. Generally, different types of defects are generated if the stress in the heterostructure exceeds a critical value. The defects formed during the relaxation of the lattice distortion have a detrimental impact on the material properties. For example, they led to a lowering of the carrier mobility, the diffusion length of the minority carriers and the breakdown voltage. The optical properties are influenced due to the impact of the defects on the band structure and, therefore, on the absorption coefficient as well as on the recombination velocity of the minority carriers in the regions where defect are existing. The mechanical properties are affected by the internal elastic fields formed by the zero (point defects), one dimensional (dislocations), two dimensional (stacking faults surrounded by dislocations) and three dimensional defects (voids or secondary phases). They change the elastic moduli and causes additional losses due to internal friction. The stress in heterostructures can be reduced by applying the following methods: (1) low deposition temperatures, (2) compliant substrates: for example, thin Si, buffer layers, SOI, porous layers, intentional and unintentional voids; (3) local or selective epitaxy: for example, checkerboard substrates, lateral overgrowth, nanoheteroepitaxy; (4) micro- and nanostructured surfaces in form of undulant surfaces, porous layers, nanostructuring; (5) buffer layer and dislocation filtering; (6) annealing of the heterostructures: for example, thermal and flash lamp annealing.

It will be demonstrated that germanium modified silicon substrates are a suitable alternative technique to reduce the internal stress in SiC/Si heterostructures independent on the growth method.

Experimental

To investigate the influence of the surface modification by germanium deposition 3C-SiC was grown on Si(111) and Si(100) p-type boron doped substrates. The wafer resistivity was 10 Ω cm. All 3C-SiC layers were grown using a two step method. The first step consists in a carbonization procedure allowing

the incorporation of germanium into the SiC/Si hetero-interface. The second growth, i.e. the growth of the thick 3C-SiC epitaxial layer, was realised by using four different methods: (1) solid source molecular beam epitaxy (SSMBE) on Si(111) substrates at low temperatures (*method 1*), (2) chemical vapour deposition at low temperatures in an ultra high vacuum chamber on Si(100) substrates (*method 2*), (3) atmospheric pressure chemical vapour deposition at high temperatures resulting in compressive stressed layers on non modified Si(100) wafers (*method 3*), (4) atmospheric pressure chemical vapour deposition at high temperatures leading to tensile stressed layers on non modified Si(100) wafers (*method 4*).

Results

Method 1 [1]

The tensile strain shows a linear decrease in dependence on the Ge coverage prior to the carbonization of the Si(111) substrate. At the same time the FWHMs of the TO phonon peaks decreases with increasing Ge coverage indicating an improvement of the 3C-SiC crystallinity for both thicknesses.

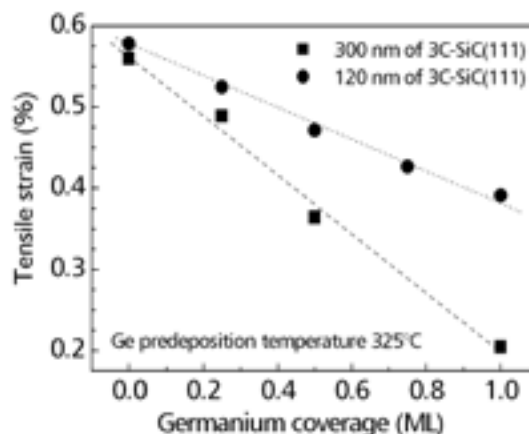


Fig. 1: Tensile strain versus Ge coverage prior to the carbonisation and epitaxial growth on Si(111).

Figures 1 and 2 illustrate that the modification of the Si substrate with Ge adds an additional strain relaxation path to the common observed improvement of the 3C-SiC quality with increasing layer thickness. Furthermore, the strain reduction is not associated with a reduction of the crystalline quality caused by an enhanced plastic relaxation by dislocation

generation. This is evidenced by the slightly decrease of the FWHMs in figure 2.

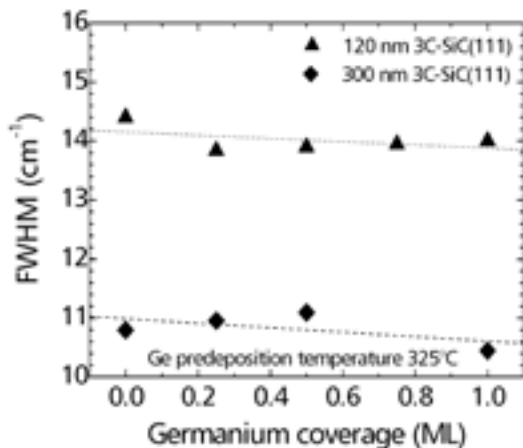


Fig. 2: FWHM of the TO phonon peak versus Ge coverage prior to the carbonization and epitaxial growth on Si(111) [1].

Method 2 [2]

Figure 3 shows the strain in the 3C-SiC layers grown by UHVCVD on Si(100) substrates versus the Ge pre-coverage.

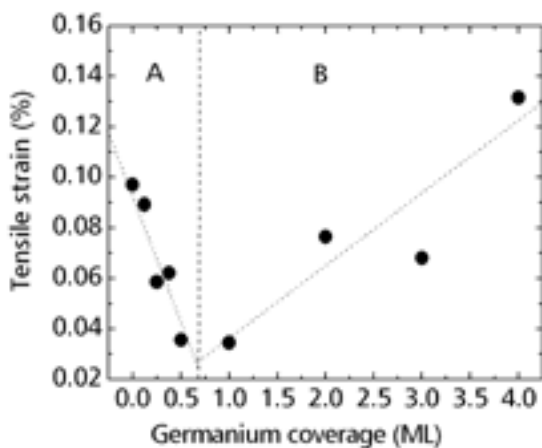


Fig. 3: Residual strain variation versus Ge predeposition prior to the carbonization process and growth on Si(100) [2].

As in the case of the SSMBE grown layers the strain state in the 3C-SiC layers is always tensile. Two strain regions, A and B, can be observed. In region A the strain decreases linear with increasing Ge precoverage and approaches a minimum at 0.5 to 1 ML Ge. If the predeposition exceeds 2ML Ge (region B) the residual strain in the 3C-SiC epitaxial layer starts to exceed the value of the sample without Ge modification. The strain value determined for

the reference sample is comparable to the strain obtained for thick layers grown at temperatures above 1300°C [3].

Method 3 [4]

The results obtained indicate an increase of the compressive in-plane strain for Ge precoverages prior to the carbonization up to 1 ML. If the predeposited amount exceeds this value the compressive strain decreases. The Raman intensity ratio I_{LO}/I_{TO} of the LO and TO phonons of the 3C-SiC epitaxial layers increases with increasing stress relaxation. The increase of the intensity ratio indicates an improvement of the crystalline properties of the grown 3C-SiC(100) layers when the compressive stress is decreasing.

Method 4 [5]

In the case of on-axis wafers Ge incorporation led to a decrease of the tensile strain, where as in the case of off-oriented wafers the tensile strain increases. Off oriented wafer normally led to a more pronounced stepped structure on the surface and to larger step heights due to step bunching. Higher step heights can be interpreted as an increase in surface roughness which in turn may led to an increase of stress if germanium is incorporated into the interface as shown in the case of SSMBE (*method 1*) grown samples on smooth and rough silicon substrates [6]. The FWHMs values of all epitaxial layers are nearly identical.

Conclusion

An alternative type of substrates for the heteroepitaxy of 3C-SiC(100) on Si(100) and 3C-SiC(111) and Si(111) has been developed. These substrates consist of a silicon wafer with a chemically modified surface. Here germanium was used.

It allows to reduce the stress and to improve the crystalline quality of the grown 3C-SiC layer in a comparable way to SOI substrates, if the Ge coverage is in the range between 0.5 to 1 ML, especially in the case of thin layers. Independent on the growth method and the growth temperatures used the residual stress is shifted towards compressive strain if the initial surface roughness prior to the carbonization process is not to high. This allows to reduce the residual strain in tensile strained layers. These results can provide a promising route towards the optimization of heteroepitaxial growth of wide band gap semiconductors on silicon substrates.

This work was supported by the European Union under grant No. G5RD-CT-2002-00704. F.M. Morales would like to thank AvH (SPA/1114640 STP)

- [1] Ch. Zgheib, L.E. McNeil, M. Kazan, P. Masri, F.M. Morales, O. Ambacher, J. Pezoldt, Appl. Phys. Lett. 87 (2005) 041905.
- [2] Ch. Zgheib, L.E. McNeil, P. Masri, Ch. Förster, F.M. Morales, Th. Stauden, O. Ambacher, J. Pezoldt, Appl. Phys. Lett. 88 (2006) 211909.
- [3] J. Camassel, J. Vac. Sci. Technol., B16 (1998), 1648.
- [4] J. Pezoldt, Ch. Zgheib, F.M. Morales, Ch. Förster, Th. Stauden, Ch. Wang, P. Masri, A. Leycuras, G. Ferro, O. Ambacher, Electrochem. Soc. Proc., 2005-09 (2005) 707.
- [5] J. Pezoldt, Ch. Zgheib, Ch. Förster, F.M. Morales, G. Cherkachinin, Ch. Wang, A. Leycuras, G. Ferro, Y. Monteil, I. Cimalla, O. Ambacher, P. Masri, Wiss. Techn. Ber. FZR-433 (2005) 20.
- [6] P. Weih, V. Cimalla, Ch. Förster, J. Pezoldt, Th. Stauden, L. Spiess, H. Romanus, M. Herrmann, M. Eickhoff, P. Masri, O. Ambacher, Mater. Sci. Forum 433-436 (2003) 233.

Pyrolysed lignin and cellulose based polymer compounds as novel material for applications in fuel cells

S. Krischok^{1,*}, M. Himmerlich¹, S.-I.-U. Ahmed¹, A. Kauffmann², J. Pfitzer³, M. Huber⁴, W. Bengel⁵, and J.A. Schaefer¹

¹ Department of Technical Physics

² Fraunhofer-Institute for Chemical Technology, Pfinztal

³ TECNARO Gesellschaft zur industriellen Anwendung nachwachsender Rohstoffe mbH, Eisenach

⁴ SFC Smart Fuel Cell AG, Brunenthal

⁵ Biomasseprojekt GmbH, Radolfzell

Fuel cells are rapidly gaining importance in mobile and portable applications such as cell phones and laptops. This is due to their high efficiency and low emissions, particularly CO₂.

One of the main components of a fuel cell is the bipolar plate. Nowadays, they contribute with up to 80% to the total volume and weight and are responsible for up to 50% of the stack costs. Therefore, the design of novel materials, which match the specifications needed for bipolar plates, is an important issue. The essential restrictions of the material are:

- specific conductivity > 10 S/cm
- working temperature range: 60°C-100°C
- compatibility with media
- mechanical stability
- adequate reaction chamber sealing.

At the same time the material has to be as inexpensive, easily available and suitable for fast production processes.

Currently we are actively working on the development of novel bipolar plates based on the pyrolysis of native materials, within a collaborative BMBF funded project. The basic material, a standard compound with the trade name "Arboform® F45", is provided by one of the partners (Tecnaro GmbH, Eisenach). It is a thermoplastic material based entirely on renewable resources (Fig. 1). First experiments with this material have shown that pyrolysis of the compound leads to a material with a

conductivity of about 90 S/cm and a comparatively low mass density. During pyrolysis the material shrinks. This is an effect that has to be compensated for eventual applications. However, more critical effects also occur during pyrolysis. One is that the material bends and the other that bubbles are formed on its surface as a result of gases escaping from the material (Fig. 1). These effects are not easy to compensate and would limit the successful implementation of this material. Therefore, it is important to understand their origins and, based on this understanding, to tune the material properties as well as the pyrolysis process in order to avoid the occurrence of such effects in the first place. This is an important goal in this project.

The analysis of the surface composition is performed by X-ray photoelectron spectroscopy (XPS). In Fig. 2 a survey spectrum of a typical pyrolyzed sample is shown. As expected, the two main components observed by XPS are carbon and oxygen. In addition, some sodium is found together with traces of nitrogen and calcium. A quantitative analysis shows that the chemical composition of the near surface region is: 81% C, 13% O and 5% Na, while the amount of N and Ca is below 1%. The detected amount of Na differs significantly for different samples and might result from the compound preparation as well as an impurity resulting from the production process. The observed Na and Ca impurities have to be removed from the bipolar plates since they

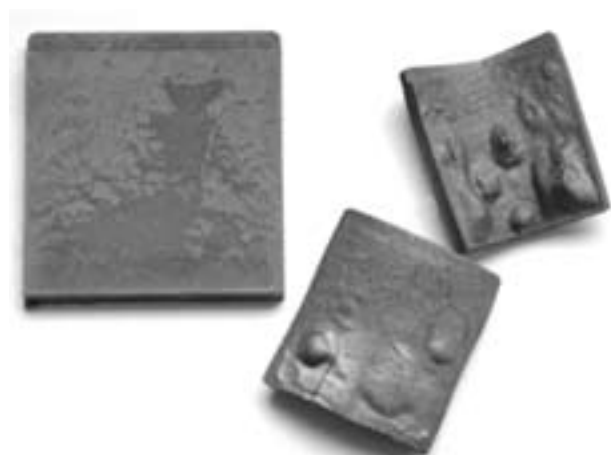


Fig. 1: Arboform®-plates before (50x50x6 mm³) and after (appr. 35x35x4 mm³) pyrolysis.

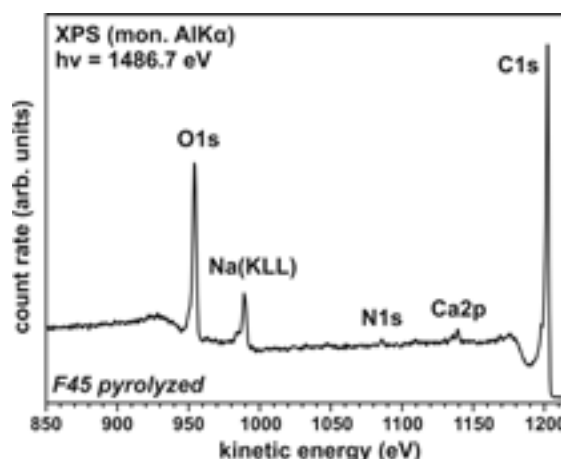


Fig. 2: Typical example for a pyrolyzed Arboform® sample measured by XPS.

are known to poison the methanol used in fuel cells, which will cause failure of the complete device.

The observed C:O ratio of about 5 is higher than that of the unpyrolyzed compound as well as cellulose, lignin and wood. This means that during pyrolysis a C-rich material is formed. Furthermore, an inspection of the high resolution spectrum of the C1s region (Fig. 3) reveals that, besides the C-C bonding attributed to graphitic species, other species such as C-O and C=O are also present. This indicates that the pyrolysis in this case did not lead to complete graphitization.

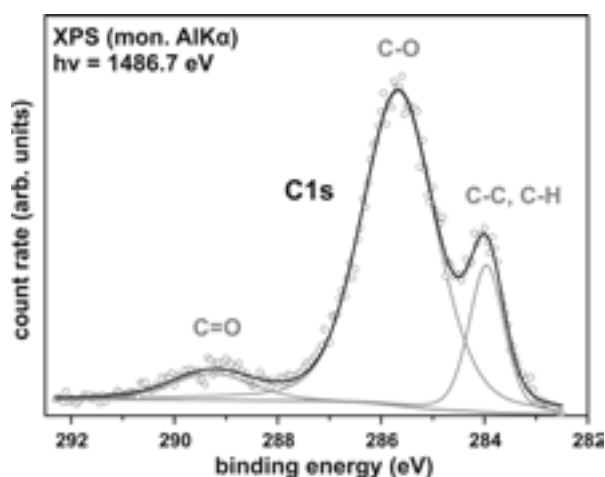


Fig. 3: C1s spectrum for a pyrolyzed Arboform® sample measured by XPS.

In order to gain information on the gases formed during the pyrolysis, we performed mass spectrometry during controlled annealing of the Arboform® samples under vacuum conditions.

The corresponding mass spectra of the desorbing gases are shown in Fig. 4 for 20°C, 60°C and 300°C, respectively. It is important to note that the background of residual gases in the ultra high vacuum system is negligibly low. The magnification of the 20°C and 60°C with respect to the 300°C spectrum is indicated in the figure.

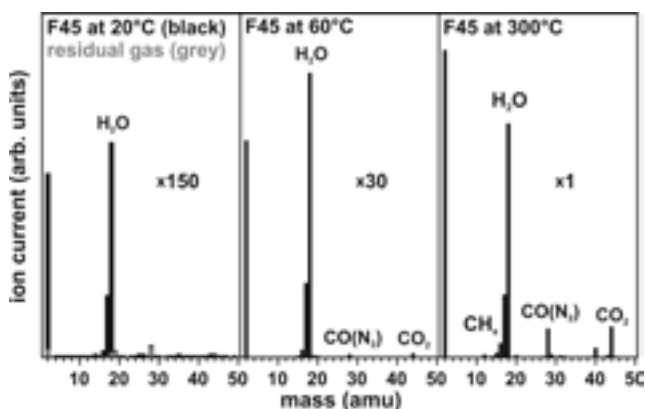


Fig. 4: Mass spectra of Arboform® at different annealing temperatures.

From the mass spectra it can be concluded that water vapor desorbs almost exclusively at low temperatures. At about 300°C, water is still the main desorbing species. However, with rising temperature the mass spectra become increasingly complicated due to the fragmentation of several desorbing species (see Fig. 5 for a mass spectrum of Arboform® at 300°C, note the partial pressure is shown on a logarithmic scale). The spectrum shows considerable quantities of CO and CO₂ as well as hydrocarbons. In addition, the spectrum also exhibits desorption of other molecules.

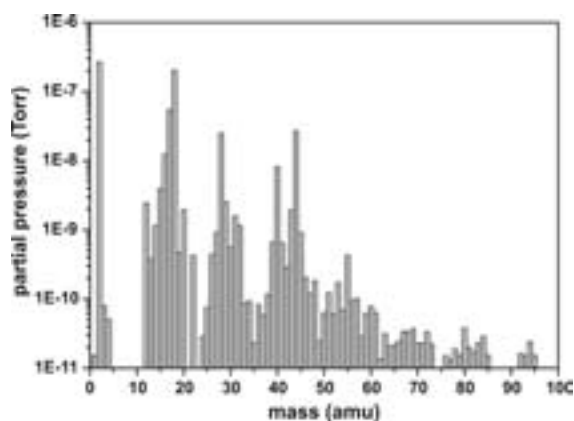


Fig. 5: Mass spectrum of Arboform® at 300°C in the logarithmic scale showing complex fragmentation products.

Their identification is not possible at present due to complexity of the recorded mass spectra. The measurements by mass spectroscopy provide insight into the pyrolysis process and enable the identification of critical temperature regimes where high amounts of gases are formed, which results in the undesired bubble formation. The identification of such critical temperatures has a direct impact on the eventual process parameters used in industry. For example, a minimization of bubble formation can be expected if, during pyrolysis, the temperature is kept constant for a certain time at a point where the gas formation is still at a tolerable level before heating further above the critical temperature.

In summary, first studies on the pyrolysis of native materials (polymers, fibers and additives) have been performed. The obtained material exhibits promising properties for use in fuel cells. However, problems such as bending and bubble formation during pyrolysis need to be addressed. Investigations into the chemical surface composition as well as thermal desorption properties provide useful information on the fundamental processes occurring during pyrolysis. This knowledge can be applied for optimizing the pyrolysis process parameters and, thus, reducing the unwanted effects during pyrolysis.

Microtechnical Challenges Miniaturising Valves

M. Kallenbach*, A. Albrecht, and M. Hoffmann
Department of Micromechanical Systems

Introduction

Up to now, magnetic actuators are rarely applied in small-size systems and MEMS. As limiting causes, in contrast to piezo and electrostatic actuators, unfavourable scaling rates, nonmature fabrication techniques of the microrange, and the complicated configuration of the magnetic circuit are listed. In this article, strategies to design and implement powerful miniaturized magnetic actuators are represented, and the specific advantages of the magnetic drive principle in small-size environments are shown. Considering the guidelines of the design process, the behaviour of different miniaturized neutral and polarized magnetic circuits is to be investigated for the use in low-power industrial pneumatic microvalves of small valve arrays for automatization.

This research work is embedded in an innovative regional growth core VERDIAN which is a cooperation intention of 12 small- and medium-size business companies within the bounds of the BMBF-Initiative "Entrepreneurial Regions", the BMBF Innovation initiative for the New German Länder. The intention is successfully vindicated at the project executing organisation.

Magnetically driven MEMS

The development of micromechanical drive systems and their successful insert in different industrial applications gain more and more significance. Examples are electrostatic mirror plate arrays for video projection beamers, piezoelectric injection valves, and magnetic mini- and microactuators for gas valve control. Whereas magnetic systems are often used in the macro world, in miniaturized actuators, their successful application is limited for the following reasons:

- the complex configuration of magnetic drives to fulfil the special demands of the magnetic circuit for source-free curl fields,
- the special features to structure soft- and hard magnetic bulks and the interlinking of the field coils with the magnetic fluxes,
- the scaling laws for magnetic actuators and
- the strong dependence of power controllability on the armature position and current of the MMF (magneto motive force).

The mechanical work generated by the magnetic actuator can be described with following equation:

$$W_{\text{mech}} = B_s A_{\text{Fe}} A_w j k_{\text{Cu}} k_m \quad (1)$$

in which B_s means the magnetic saturation flux density, A_{Fe} the iron area, A_w the winding area, k_{Cu} the copper (filling) factor, k_m the degree of utilization and j the current density. Taking into account the micro-scaled behavior of functionally important structures, the mechanical work capacity dramatically drops when actuators are scaled down, because the actuator work is given by the product of two areas. The use of the best magnetic materials (B_s maximum) and of an geometrically optimized magnetic circuit (k_m maximum) is the prerequisite for the design of small powerful drives.

coil variation	(a)	(b)	(c)	(d)
max. current [A/mm ²]	500	50	23	10
coil copper filling factor	0.005	0.15 .. 0.25	0.1 .. 0.23	0.65
conductor height [μm]	some	70 μm	50 μm	wire
Multilayer	no	yes	yes	yes

Tab. 1: Different technological solutions for microcoils.

The current density respectively the ampability of the coil is the most important lever for the design.

In order to minimize the coil shape, the current density through the coil is increased by the use of short-time pulses (short on-time cycles).

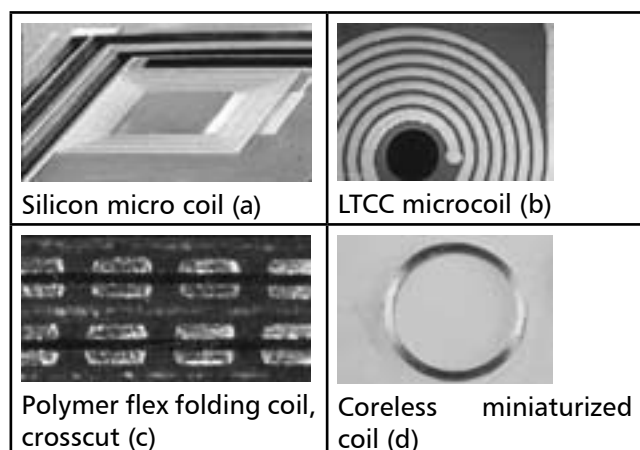


Fig. 1: Microtechnical coil possibilities.

Methods for lowering the holding currents or the alternative use of permanent magnetic circuits make possible the reduction of the active coil volume. Thinking of novel coil configurations made of polymers or ceramics is another solution to increase current densities in MEMS (Fig. 1). The parameters of the different coils are listed in table 1.

Design of a miniaturized valve actuator

Consequent miniaturization can only be realized by using volumetric and functional integration with the help of mechatronic design methodology. With this approach, a new magnetic valve for small industrial valve cluster could be realized. The magnetic system, made of two parallel circuits is shown in figure 2 and allows a displacement range (valve nominal width) of the armature of some 100 μm (Fig. 3).

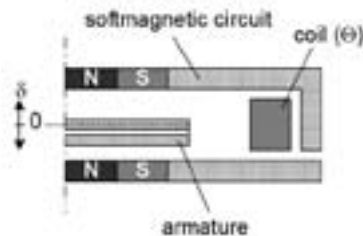


Fig. 2: Valve actuator working principle.

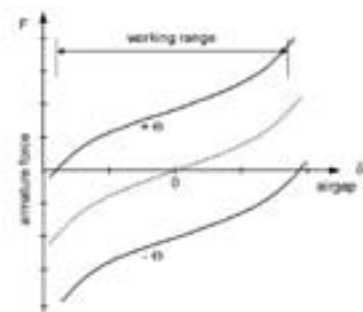


Fig. 3: Principle of an actuator force-displacement-characteristic (middle: without MMF).

Because of the two permanent magnets, no force acts on the armature in the middle position. Outside the middle position, the difference of the forces generated by the permanent magnets in dependence on the position (Fig. 3, middle characteristic) acts on the armature. In order to move the force-displacement-characteristic up and down, a current is applied to the coil.

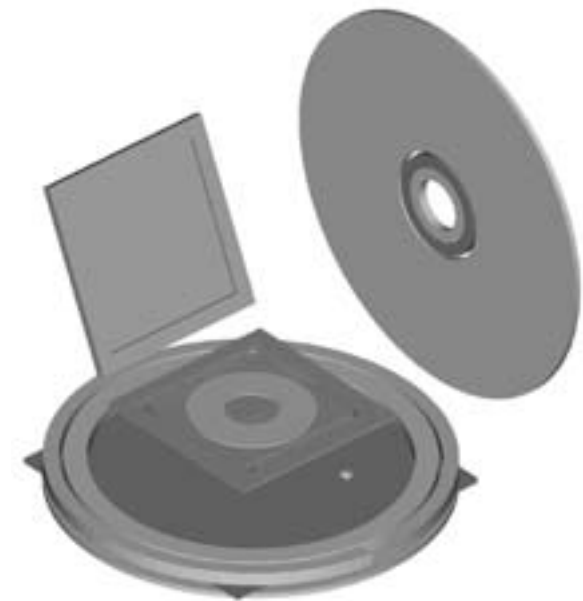
A testing assembly (Fig. 4 and Fig. 5) was realized in microtechnologies. The armature is made of silicon and the soft magnetic domains are laser-cut and embedded in etched cavities. On the same way, the iron parts are fabricated. In this concept, the coil is coreless.



Fig. 4: Assembling test of a flat minivalve for small valve clusters.



(a)



(b)

Fig. 5: Conceptual state for measuring, (a) view to the armature, (b) CAD explosion.

Future works will include design and the fabrication with galvanofarming, MIM (metal injection molding), and etching technologies with the step to wafer-level integration of magnetic microvalves.

Summary

The design of an magnetic microvalve with a small valve cluster adding size and a large nominal width in a concept state is shown. The consequent miniaturization of the valve is only possible by the use of an optimized magnetic circuit, special coils with high ampability in combination with intermittent duty and permanent magnets, and special fabrication technologies.

[1] Kallenbach, M.: Entwurf von magnetischen Mini- und Mikroaktoren mit stark nichtlinearem Magnetkreis. ISLE Verlag Ilmenau, 2005.
 [2] Bonitz, Björn: Konstruktive Umsetzung eines magnetischen Mikroventils. Unveröffentlichte Projektarbeit, TU Ilmenau, 2006.
 [3] Kallenbach, M.; Bussinger, F.; Kallenbach, E.; Herrmann, R.: Miniaturisation of magnetic actuators for small and powerful industrial pneumatic valves. Actuators 2006 – 10th international conference on new actuators, Conference proceedings, Bremen, Germany, Seite 116.

Thermal Design Aspects for LTCC Microwave Packages

J. Müller* and M. Mach

Junior Research Group Functionalised Peripherals, MacroNano® – Centre for Innovation Competence

Introduction

LTCC materials offer thermal conductivities in a range from 2 to 5 W/m²K which is insufficient for the thermal management of a variety of applications. Typical RF-power amplifiers have a power dissipation of about 2-5 W. In order to prevent overheating the MMIC, the substrate underneath should provide the highest thermal conductivity possible. For satellite or avionic applications considered here, it should also be hermetic to protect the inner assembly (bare dies). Thermal vias in LTCC are able to improve the integral value of the thermal conductivity. Depending on the array formation (diameter of vias and pitch), values comparable to or even better than alumina have been practically achieved [1] [2]. However, typical MMICs have no equally distributed heat source(s). Though silver has the best thermal performance, gold conductors and vias are often required for satellite use.

As boundary condition the package itself will be mounted on a printed circuit board with a metal core to transfer the heat from power modules assembled (Fig. 1). Two cases can be taken into account. For low or medium power dissipation no heat sink is necessary on the package. Larger power dissipation requires an attached metal plate acting as a heat spreader and heat sink.

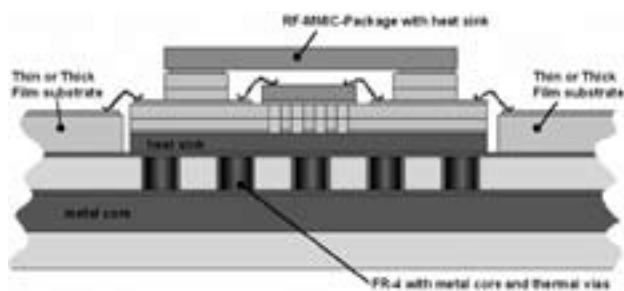


Fig. 1: Potential mounting scheme of the RF package on a metal core printed circuit board.

Thermal via coverage

In production, the use of different via sizes is often restricted due to manufacturing concerns. Therefore, the impact on via density or diameter was investigated. At the given area of 3 x 3 mm², 36 vias were arranged in a 6 x 6 matrix with 500 micron pitch (4 layers 951AX). The via diameter was varied from 50 μm to 300 μm at a constant power dissipation of

10 W (metal coverage 0.78% - 28.3%). Figure 2 depicts the graphs for simulated junction temperature and thermal resistance. The useful range for via diameters in terms of manufacturability at 500 μm pitch and 254 μm tape thickness (green) is between 125 μm and 300 μm (approx. 260 μm sintered). For thinner tapes, often required for low profile packages, the maximum via diameter will be smaller. However, the pitch can be reduced as well. A via coverage of about 20% is close to the technological limit for standard processing. Higher coverage was achieved with Ag foil by special manufacturing steps [3].

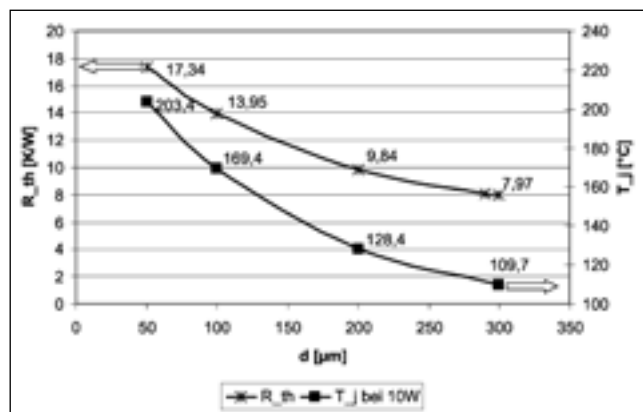


Fig. 2: Thermal resistance and junction temperature at 10 W vs. thermal via diameter.

Thermal via position

An increase of via density in combination with hot spots may not improve the thermal conductivity. Figure 3 shows two cases with 36 and 25 vias respectively (vias are drawn as squares with same area to speed up the simulation).

The heat sink was set to fixed ambient temperature. Remaining simulation parameters were:

- LTCC thickness: 400 μm,
- Via material: Au/Ag thick film, Ø = 130/87 μm
- Thermal interface material: 10 μm, λ = 51 W/mK,
- Heat spreader: 1 mm x 1 mm x 40 μm, λ = 70 W/mK for Au-System, λ = 250 W/mK for Ag-System,
- Heat source: 50 x 50 μm², 0.25 W and
- Free convection.

Figures 4 and 5 show thermal images of simulated structures according to figure 3 b and c. The higher via density (Fig. 4) just compensates the misalignment

between heat source and thermal via. A similar result was obtained with 130 micron vias either for a 9:16 or 1:4 via number ratio. The difference in thermal resistance was surprisingly small between one via directly under the hot spot and 4 vias surrounding it. A direct path between hot spot and via is therefore recommended.

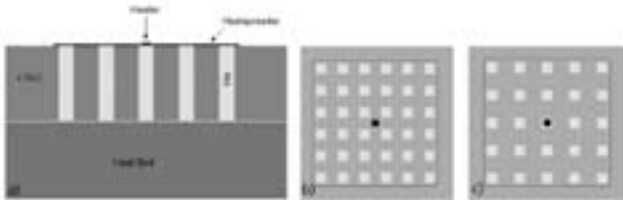


Fig. 3: Thermal via array under a small heat source a) cross section of structure c) via pitch = 2x via size; b) via pitch = 2.5 x via size.

The findings are in good agreement with the results obtained for a RF front end circuit [4]. The optimum design should have a large via under the hot spot. Table 1 contains all simulated results. Without vias, the junction temperature increases to about 82°C.

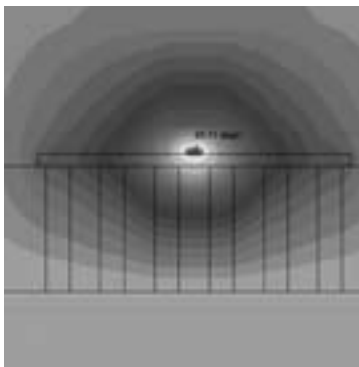


Fig. 4: Temperature distribution for an array of 36 vias (Ø = 87 µm) with a heat source between vias.

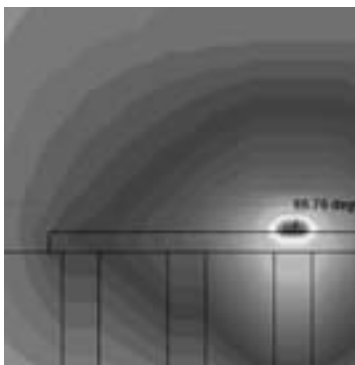


Fig. 5: Temperature distribution for an array of 25 vias (Ø = 87 µm) with a heat source directly over the central via.

Via diameter [µm]	Number of Vias	Via pitch [µm]	Heat Source to Via Position	Tj [°C]	R _{th} [K/W]	R _{th} /R _{th, no via} [%]
-	-	-	-	82.45	245.8	100
130	1	-	direct	72.94	207.7	84.5
130	4	260	between	70.87	199.5	81.1
130	9	325	direct	65.91	179.6	73.1
130	16	260	between	66.25	181	73.6
87	25	218	direct	66.76	183	74.5
87	36	174	between	65.71	178.8	72.7
130 (Ag)	9	325	direct	36.52	62.08	25.3
130 (Ag)	16	260	between	36.12	60.48	24.6

Tab. 1: Simulated junction temperatures and thermal resistance for various via pitches and via numbers.

Gold vias and a gold heat spreader reduced the thermal resistance by about 27% (compared to LTCC without vias). For two scenarios gold was replaced by silver. The superior thermal conductivity of silver vias drastically decreased the effective thermal resistance (approx. 75% reduction). A further reduction is only possible by thinning the substrate. The contribution of convection was below 1% for all cases investigated. Summary and conclusions

The best thermal solution with vias requires constant, large via diameters. However, this approach is in contrast to potential hermeticity demands. The contribution of radiation and convection on the thermal management can be neglected for hermetic packages in space applications. Due to this, covers and lids have only a minor impact on the thermal resistance. A maximum via coverage of about 20% can be achieved (practical limit). Since the position of thermal vias is critical for hot spots a close coordination with chip design is necessary.

The project MultiSysTeM is funded by the BMBF under the initiative "Centres for Innovation Competence".

[1] M. Ray Fairchild et al.: LTCC Technologies for Harsh-environment Automotive Applications Utilizing Soldered Interconnections, Proc. of the 37th International Symposium on Microelectronics, Nov. 14-18, 2004, Long Beach, CA.
 [2] Dan Amey, Mimi Keating: Thermal Performance of 943 Low Loss Green Tape LTCC with Thermal Via and Internal Metallization Enhancements, Proceedings of the 2004 Ceramic Interconnect Technology Conference, April 26-28, 2004, Denver/CO, USA.
 [3] Marc A. Zampino, Ravindra Kandukuri, W. Kinzy Jones: High Performance Thermal Vias in LTCC Substrates, 2002 Inter Society Conference on Thermal Phenomena, pp. 179-185.
 [4] Victor A. Chiriac, Tien-Yu Tom Lee: Thermal Assessment of RF-Integrated LTCC Front End Modules, IEEE Transactions on Advanced Packaging, Vol. 27, No. 3, August 2004.

EM-Simulation of Physical Properties of LTCC RF Inductors

J. Müller*, S. Rentsch, and R. Perrone

Junior Research Group Functionalised Peripherals, MacroNano® – Centre for Innovation Competence

Introduction

High-Q-inductors play an important role in passive integration of filters, baluns and matching networks in RF System-in-Packages (SiP). Typical implementations are based on spiral and helical designs. The former has been widely used on top of ceramic substrates or printed circuit boards. It can, however, be also embedded into a multilayer structure to save area for components without integration potential. Inductance is determined by the inner diameter of the spiral, number of windings, line width and line spacing. Adjacent ground planes have a considerable impact on resulting inductance values. 3D or helical inductors offer more design degree of freedom in terms of area vs. number of layers or number of turns respectively. Additional design parameters are layer thickness, line width and ground plane distance.

LTCC Inductor Designs

Figure 1 shows typical inductor designs which are applied in a variety of applications. Spiral inductors (Fig. 1a) need only one layer (two if a series connection to the inductor center is required). However, each additional turn in the spiral design over-proportionally adds conductor line resistance. 3D- or helical designs (Fig. 1b and c) show a linear increase of line length vs. number of turns. Type c), as described in [1] has a transversal magnetic field orientation related to type a) and b). In order to achieve high inductance values, the area penetrated by the magnetic flux needs to be large, thus, increasing the substrate thickness which is often in conflict with package thickness requirements. Similar considerations apply also for design b), but layer thicknesses as thin as 40 μm allow low profile multilayer inductors.

3D Inductor Analysis

Simple two-port-circuits can be described by the classic models shown in figure 2. Such a device is completely characterized by the full set of S-parameters (s_{11} ... s_{22}). In reality it is rather difficult to realise just a single series or shunt element. Due to parasitics associated to the package or interconnection, further elements are added to the schematic. The result is usually a Π - or T-circuit. Inductors comply either with the Π -model (Fig. 2c) or the transmission line model (Fig. 2e) which is explained later. Electrical simulation of scattering parameters was applied to identify inductor design parameters. Depending on

the simulation tool and resolution used, it provides a cheap and fast solution for evaluating numerous design options.



Fig. 1: Typical LTCC inductor designs [a) spiral, b) helical-z, c) helical-x-y].

The complete inductor structure analysis is performed in the following steps:

- 1) Full 2-port S-Parameter simulation
- 2) De-embedding of feeding lines (if necessary)
- 3) Transformation into ABCD-matrix
- 4) Calculation of model elements based on Pi- or line-model

The entire procedure is explained in [2].

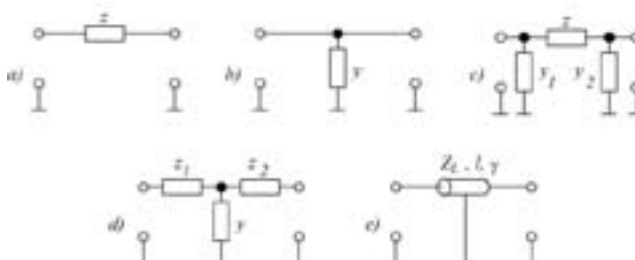


Fig. 2: Typical two-port circuits a) series impedance; b) shunt admittance; c) Π -circuit; d) T-circuit; e) transmission line.

Model calculation results do not include second order effects (e.g. higher resonances). Therefore, the model is only valid up to the first self resonance frequency. S-parameter simulation was performed with SONNET EM Release 10. For better confidence this simulator was compared to measured results of the test structure as well as to simulation results of two other full 3D electromagnetic field solvers. Figure 3 shows the comparison of simulation results for a 3.5 turn helical inductor. Differences at the resonance points (s_{21}) may derive from the different interpretation of the conductor thickness in the simulators. Extracted

model parameters, however, show no significant deviation.

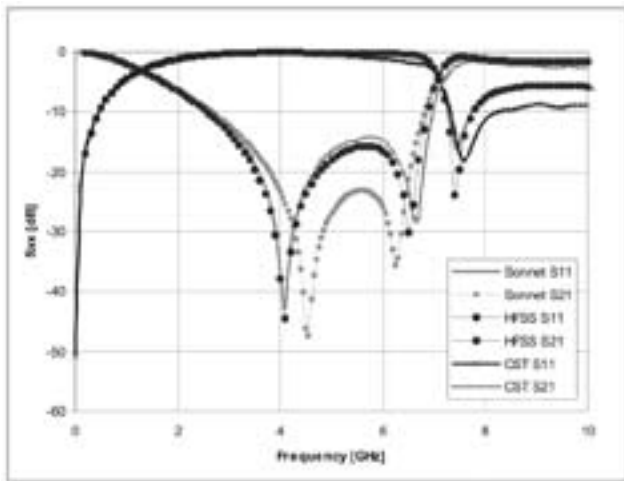


Fig. 3: Comparison of simulation tools for inductor analysis (line width $w=150 \mu\text{m}$).

Free air inductance

Free air inductance was selected for the evaluation since it reduces the impact of parasitic ground capacitances and delivers the maximum possible inductance value for the structure. These inductance values were used for normalization. As expected, the inductance is proportional to coil diameter, number of turns and inversely proportional to the layer thickness or coil length respectively. The line width influences the inductance considerably ($> \pm 10\%$). For a given diameter and number of turns, the highest inductance is achieved with the minimum line width and the thinnest tape available. However, both will have an impact on the quality factor and the self resonance frequency. The inductor with the highest self resonance frequency is made with a $50 \mu\text{m}$ line (higher series resistance). Its maximal quality factor is considerably lower compared to the inductor made with $150 \mu\text{m}$ lines (50 vs. 75).

Ground plane influence

In general, a ground plane below an inductor shows two effects. Firstly, a reduction of inductance caused by mutual inductances associated with mirror currents in the ground plane and secondly, large parasitic capacitances between coil and ground. Both effects are increased with reduced ground plane distance. The induced negative mutual inductance in the ground plane might influence the inductance by as much as 50 % [3].

Two procedures addressing the ground plane effects are known. The patterned ground shield approach [4] reduces mutual inductances. This effect can be utilized for trimming purposes [5]. An air cavity between inductor and ground plane minimizes the capacitance to ground [6].

The higher the ground plane distance, the more the inductor will behave as a lumped element. The self resonance frequency becomes smaller with increased ground plane spacing (Fig. 4). However, the reduction is higher than expected based on increased inductance. Therefore, also the coupling capacitance between windings is influenced by the ground plane layer.

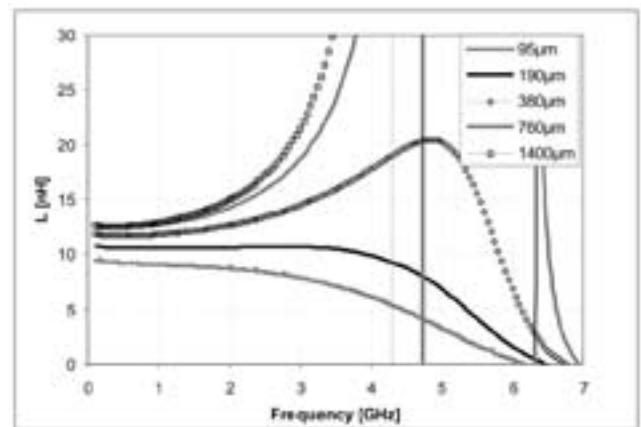


Fig. 4: Inductance vs. frequency for various ground plane distances [3].

Summary and Outlook

LTCC offers a variety of options to design inductors for rf applications. An optimum design is very complex due to interacting impact of all relevant parameters. The principal influence of the ground plane on inductance and wide band behavior was demonstrated.

The project MultiSysTeM is funded by the BMBF under the initiative "Centres for Innovation Competence".

- [1] Michael D. Phillips, Raghu K. Settaluri: New Toroidal Inductor Configurations for LTCC Applications, Proc. of the Conference on Ceramic Interconnect Technology, April 26-28, 2004, Denver/CO.
- [2] Drüe K.-H., Thust H., Müller J.: RF Models of Passive LTCC Components in the Lower Gigahertz-Range, Applied Microwave & Wireless, April 1998.
- [3] Jens Müller, Rubén Perrone: Physical Model Based Design Optimization for LTCC RF Inductors, 2nd Ceramic Interconnect and Ceramic Microsystems Technology (CICMT), April 2006, Denver.
- [4] Inder Bahl: Lumped Elements for RF and Microwave Circuits, Artech House, Norwood/MA, 2003.
- [5] Müller J., Thust H., Drüe K.-H.: Laser Structuring and Trimming of RF-Elements in Multilayer Thick Film Circuits, Proceedings of the International Conference on Electronics Technologies, Windsor, Juni 1994.
- [6] Rubén Perrone, Heiko Thust: Progress in the integration of Planar and 3D Coils on LTCC by using Photoimageable Inks, Proceedings 2004 International Symposium on Microelectronics, 14-18 November 2004, Long Beach/CA.

Methods to Calculate the Resonant Frequencies of Multi-layer MEMS by Means of Analytical Models

F. Will^{1,*}, J. Weber², V. Cimalla¹, K. Tonisch¹, K. Brückner³, R. Stephan³, M. Hein³, and O. Ambacher¹

¹ Department of Nanotechnology

² Department of Max Planck Institute for Solid State Research, Stuttgart

³ Department of RF and Microwave Techniques

Introduction

One of the most important parameters for NEMS (nanoelectromechanical system) and MEMS (micro-electromechanical system) is the resonant frequency which is dependent on both material and geometrical properties. Various sensing applications are based on modifications of the resonant frequency in such systems. This work shows an easy calculation method which provides an evaluation of the resonant frequency of different material systems and variable geometries. For standard geometries like single and doubly-clamped beams with a multi layer structure it was possible to calculate the resonant frequencies without a time consuming simulation as can be performed by ANSYS.

Theoretical Considerations

Nanomechanical doubly-clamped resonators can be considered as one-dimensional damped harmonic oscillators. The resonant frequency f_{10} of the fundamental vibration mode of the beams can be described by the Euler-Bernoulli theory:

$$f_{10} = 3.56 \sqrt{\frac{EI}{\rho A}} \cdot \frac{1}{L^2} \quad (1)$$

Here, EI is the flexural stiffness and ρA the mass load per unit length of the resonator beam. To account for the shift of the resonant frequency, if the beam is subjected to an axial force N , equation (1) has to be enhanced by a square-root term [1]:

$$\begin{aligned} f_1 &= f_{10} \sqrt{1 + 0.295 \frac{NL^2}{12EI}} \\ &= 3.56 \sqrt{\frac{EI}{\rho A}} \cdot \frac{1}{L^2} \cdot \sqrt{1 + 0.295 \frac{NL^2}{12EI}} \end{aligned} \quad (2)$$

which represents an approximation of the exact solution of the related differential equation. The error of f_1 is smaller than 0.5 % if

$$0.295NL^2 / (12EI) < 1 \quad (3)$$

For beams of uniform material, equation (2) can be related easily to the strain ε inherent to the active resonator layers:

$$f_1 = 1.028 \sqrt{\frac{E}{\rho}} \cdot \frac{t}{L^2} \sqrt{1 + 0.295 \frac{L^2}{t^2} \varepsilon} \quad (4)$$

with E being the Young's modulus and ρ the mass density of the resonator material. Numerous studies have revealed that the influence of the metallization on the resonant frequency cannot be neglected [2]. Therefore, for multilayer beams, the terms EI and ρA in equation (3) have to be replaced by the sums of the flexural stiffnesses and mass loadings per unit length of the individual resonator layers:

$$EI \leftrightarrow \sum_{j=1}^n E_j I_j, \quad \rho A \leftrightarrow \sum_{j=1}^n \rho_j A_j \quad (5)$$

Here, n is the total number of layers, and j is the layer index. It has to be taken into account that the moment of inertia I_j of each layer depends on the location of that layer with respect to the neutral axis (Steiner's law). Resonator beams of various dimensions and materials were also investigated numerically using the commercial finite-element software ANSYS®. The simulations agreed fairly well with the results obtained from the analytical approach.

Experimental

Single and doubly-clamped (Fig. 1) resonators of different geometries were realized using active layers of silicon carbide (SiC) and aluminum nitride (AlN). The electrically conductive top-layer which is necessary for a magneto-dynamic actuation is patterned by a lift-off process. At the same time, this top-electrode serves as etching mask for the subsequent patterning of the resonator bar. Anisotropic etching of the bars is realized by fluorine or chlorine based dry etching for SiC [3] or AlN, respectively, while freestanding resonator structures are realized in both systems by undercutting via isotropic, fluorine based silicon etching. The resonators were excited by magneto-motive actuation, where the oscillation is caused by an

applied alternating voltage in a permanent magnetic field resulting in an oscillating Lorentz force. A measurement setup which separates the excitation signal and the response signal in the time domain allows the determination of the resonant frequency and quality factor by observing the free decay of the oscillations [4]. The resonant frequencies of the processed AlN and SiC-beams were determined to be 0.32 to 8 MHz, the quality factor reached 350 and 50000 in air and in vacuum ($2\text{-}5 \cdot 10^{-5}$ mbar), respectively.



Fig. 1: Schema of doubly-clamped and coupled single-clamped beam designs.

Results

The comparison of ANSYS simulations and analytical results applied to several material and metallization systems showed a deviation of 0.5% to 4% confirming the analytical model as time saving alternative (Fig. 2). The deviation rises with decreasing the beam length. This is caused by the influence of the clamping conditions which become more relevant for shorter beams, where the clamping stiffens the beam resulting in higher resonant frequencies. Whereas the ANSYS simulation takes these clamping conditions into account, the analytical model still has to be modified to account for related effects.

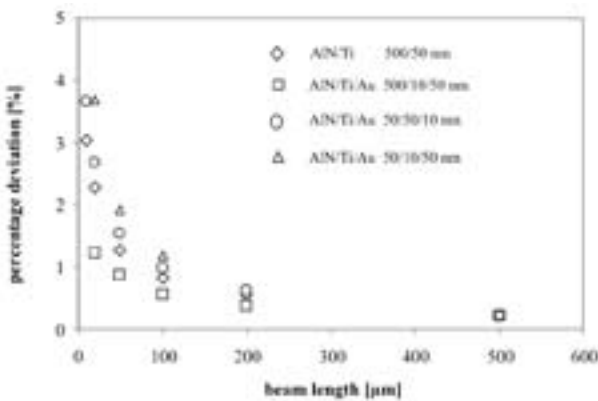


Fig. 2: Percentage deviation of calculated results to ANSYS simulations for different metallization systems.

From equation (4) in dependence on the internal strain a transition at a strain and geometry dependent transition length L_{trans} can be estimated

$$\left(0.295 \cdot \frac{L_{trans}^2}{l^2} \epsilon \ll 1\right)$$

For $L < L_{trans}$ the $1/L^2$ -dependence can be expected according equation (4), while for $L > L_{trans}$ the strain related term becomes dominant resulting in a $1/L$ law. The measured dependence of the resonant frequency for doubly-clamped SiC and AlN beams on L is shown in figure 3 along with the theoretical curves following equation (5).

$$f_1 = 1.028 \sqrt{\frac{\sum_{j=1}^n E_j I_j}{\sum_{j=1}^n \rho_j A_j}} \cdot \frac{t}{L^2} \sqrt{1 + 0.295 \frac{L^2}{l^2} \epsilon} \quad (6)$$

To consider for internal strain equations (4) and (5) were combined in equation (6) and allow the fitting of the measured resonant frequencies if $c(\epsilon)$ is given.

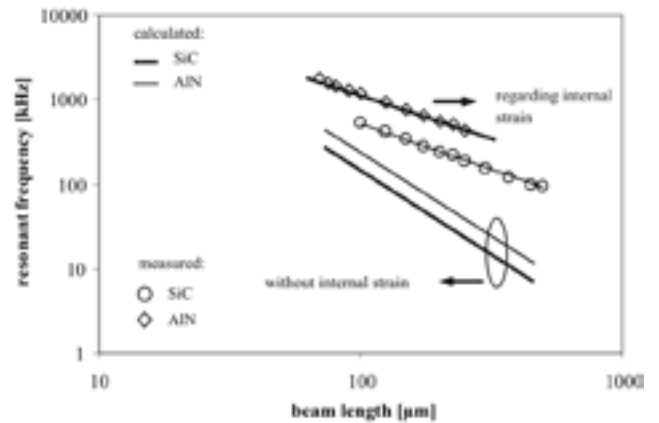


Fig. 3: Calculations according equation (5) (lower dotted and solid line) and equation (6) (upper dotted and solid line) were compared to measured resonant frequencies.

In conclusion the analytical model of multilayer systems has been confirmed as easy method to calculate resonant frequencies of different material systems and variable geometries comparable to simulation results obtained by ANSYS.

This work has been funded by the Deutsche Forschungsgemeinschaft, SPP 1157 contract AM 105/2-1 and SPP 1157 contract CI 148/2-1 and the European Union projects "FLASIC" (G5RD-CT-2002-00704) and "GaNano" (NMP4-CT2003-505614).

[1] S. Bouwstra et al., IEEE 1991 int. conf. on solid-state sensors, actuators and micro-systems, Transducers '91, San Francisco, CA, 24-27 June 1991, pp. 538-542.
 [2] N. Cleland et al., Single-crystal aluminum nitride nanomechanical resonators, Appl. Phys. Lett., 79 (2001) 2070-2072
 [3] Ch. Förster et al., Group III-nitride and SiC based micro- and nanoelectromechanical resonators for sensor applications, phys. stat. sol. (a) 203 (2006) 1829-1833.
 [4] V. Cimalla et al., Pulsed mode operation of strained microelectromechanical resonators, Appl. Phys. Lett., 88 (2006) 253501.

Electron Transport in Wurtzite InN

V. M. Polyakov and F. Schwierz*

Department of Solid-State Electronics

Introduction

The effect of negative differential mobility (NDM) in the steady-state drift velocity-field characteristics and the transient velocity overshoot in semiconductors are the subject of extensive investigation. The NDM can dominate the performance of electron devices in which high electric fields promote the population of the satellite valleys, whereas velocity overshoot can enhance high-speed operation of nanoscale devices. These phenomena have been studied in many semiconductors, such as Si, GaAs and GaN. As has been already discussed in the literature, there are several possible reasons for the NDM and velocity overshoot. Intervalley electron transfer to the heavier effective mass satellite valleys of the conduction band is the conventional explanation of these effects. However, depending on the transport regime (temperature, doping, electric field) as well on as the parameters of the band structure and of the scattering processes, other mechanisms can be crucial for the appearance of NDM and overshoot.

In recent years, InN has attracted much attention due to the substantial progress in the growth of monocrystalline wurtzite samples with improved quality, low free electron concentrations, and high mobilities. The current work is aimed to investigate the steady-state and transient electron transport in bulk wurtzite InN by the ensemble MC method giving the main emphasis to the origin of NDM and velocity overshoot.

Model Description

In the present work, the band structure of wurtzite InN is approximated by the three lowest conduction band minima (Γ_1 , Γ_3 , and $M-L$ valleys). Parameters such as effective masses m^* for the different valleys, nonparabolicity factors α , and valley separation energies have been extracted from a conduction band structure recently calculated by the empirical pseudopotential method [1]. The satellite valleys Γ_3 and $M-L$ are assumed to be parabolic (i.e., $\alpha = 0.0$), while the main Γ_1 valley is characterized by the isotropic nonparabolic dispersion relation as follows:

$$\frac{\hbar^2 k^2}{2m^*} = \varepsilon(1 + \alpha \varepsilon) \quad (1)$$

Here, ε denotes the electron energy, m^* the effective mass, and α is the nonparabolicity factor

of the valley. The Γ_1 valley has been fitted using (1) to evaluate the conduction band edge effective mass $m_{\Gamma_1} = 0.04 \times m_0$ (m_0 is the electron rest mass) and the nonparabolicity factor $\alpha_{\Gamma_1} = 1.43 \text{ eV}^{-1}$. The electron scattering mechanisms are the other major ingredient of the MC technique. All relevant phonon scattering mechanisms, such as intravalley (acoustic, polar optical) and intervalley (non-polar optical) phonon scatterings have been included. Apart from the band structure, several additional material parameters of InN required for calculating the scattering rates have been recently refined. In particular, we use the

optical phonon energy $\hbar\omega_{LO} = 73 \text{ meV}$ instead of 89 meV as taken in previous MC calculations [2-3]. We consider the InN to be uncompensated and the donor concentration is 10^{17} cm^{-3} . The interaction of electrons with ionized impurities is accounted for in the Conwell-Weisskopf formulation [4].

Results and Discussion

Fig. 1 shows the calculated steady-state electron drift velocity and valley occupancies in InN as function of the applied electric field [5-6].

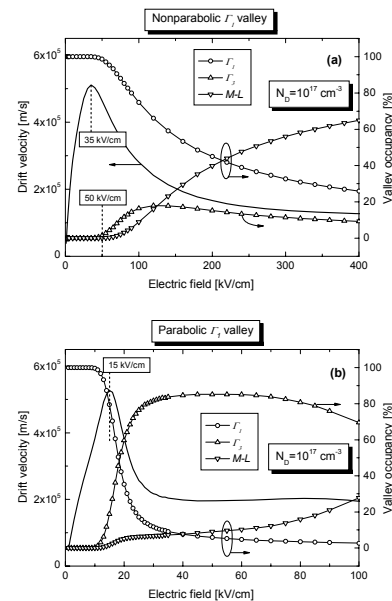


Fig. 1. Steady-state drift velocity and valley occupancies in InN as a function of the applied electric field calculated at room temperature: (a) nonparabolic and (b) parabolic cases.

First, the central Γ_1 valley is considered to be nonparabolic with $\alpha=1.43 \text{ eV}^{-1}$. As clearly observed in Fig. 1a, the NDM onset at $E=35 \text{ kV/cm}$ is not pinned to the intervalley repopulation which sets in at $E=50 \text{ kV/cm}$. Instead, the peak velocity occurs at an electric field where all electrons still reside in the central valley. Even at $E=60 \text{ kV/cm}$, only less than 5% of the electrons have been transferred to the satellite valleys and, correspondingly, more than 95% of electrons are still confined in the central valley. The drift velocity, however, has already dropped to 80% of the peak value. Therefore we state that the onset of the NDM in InN at $E=35 \text{ kV/cm}$ is associated with the strong nonparabolicity of the Γ_1 valley rather than with intervalley transfer. It is worth mentioning that the nonparabolicity influences the steady-state transport in two aspects. First, the nonparabolicity itself provides a saturation of the electron group velocity by increasing the electron energy without any electron collisions. Secondly, the dominant polar optical phonon scattering is strongly modified by taking into account the nonparabolicity in a way that the scattering rate steadily increases with an increase of the electron energy (this is in contrast to the parabolic case). The combination of these two effects leads to the NDM onset prior to the intervalley transfer. Our conclusion is supported by the results presented in Fig. 1b. Here, the nonparabolicity of the central valley is intentionally neglected and we observe that the NDM onset at $E=15 \text{ kV/cm}$ is strictly associated to the intervalley repopulation.

Hence, one can conclude that for a parabolic central valley the NDM onset is solely attributed to the intervalley transfer, whereas a strong valley nonparabolicity favors attaining the steady-state peak velocity prior to the intervalley repopulation. It should be noted that at higher fields intervalley transfer contributes to the NDM also for the case of a strongly nonparabolic central valley.

Next, the influence of the nonparabolicity on the transient drift velocity is illustrated in Fig. 2. As expected, the peak velocity substantially decreases for larger nonparabolicity factors. We also observe that the shape of the velocity overshoot drastically changes by increasing the valley nonparabolicity. For the parabolic case and for small nonparabolicity factors, the transient peak velocity is associated with the onset of the intervalley transfer. However, for $\alpha=0.5 \text{ eV}^{-1}$ the overshoot shape flattens without revealing a pronounced peak structure.

For the strong nonparabolicity $\alpha=1.43 \text{ eV}^{-1}$ we observe a less pronounced velocity peak that, however, occurs prior to the intervalley transfer.

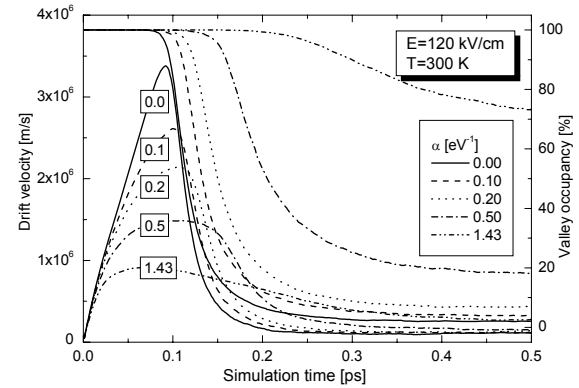


Fig. 2. Transient drift velocity and valley occupancies calculated for different nonparabolicity factors of the central Γ_1 valley at $E=120 \text{ kV/cm}$ and $T=300 \text{ K}$.

Conclusion

In this work we have investigated the steady-state and transient electron transport properties in bulk wurtzite InN applying the ensemble Monte Carlo technique. The main emphasis is given to the origin of the negative differential mobility for the steady-state transport and of the drift velocity overshoot for the transient transport. We found that the nonparabolicity of the central Γ_1 valley strongly influences the transport properties in InN. By neglecting the nonparabolicity of the central valley, the NDM is strictly pinned to the intervalley repopulation. By taking into account the valley nonparabolicity, on the other hand, the peak drift velocity occurs at considerably lower electric fields compared to the onset of intervalley transfer. In polar semiconductors with a weak nonparabolicity of the main valley, such as GaAs, the overshoot effect is dominated by intervalley transfer. In wurtzite InN, however, the drift velocity overshoot is mainly caused by the strong nonparabolicity of the central valley. The nonparabolicity can be a dominant mechanism of the drift velocity overshoot also in other semiconductors where the electron group velocity in the central valley saturates or even decreases at energies well below the threshold energy for electron transfer to the heavier effective mass satellite valleys.

- [1] D. Fritsch, H. Schmidt, and M. Grundmann, Phys. Rev. B 69, 165204 (2004).
- [2] S. K. O'Leary, B. E. Foutz, M. S. Shur, U. V. Bhapkar, and L. F. Eastman, J. Appl. Phys. 83, 826 (1998).
- [3] B. E. Foutz, S. K. O'Leary, M. S. Shur, and L. F. Eastman, J. Appl. Phys. 85, 7727 (1999).
- [4] E. Conwell and V. P. Weisskopf, Phys. Rev. 77, 388 (1950).
- [5] V. Polyakov and F. Schwierz, Appl. Phys. Lett. 88, 032101 (2006).
- [6] V. Polyakov and F. Schwierz, J. Appl. Phys. 99, 113705 (2006).

Construction Including Bionic Algorithm

C. Schilling¹, R. Fetter¹, J. Mämpel¹, J. Schade¹, W. Kempf¹, D. B. Hill², and H. Witte^{1,*}

¹ Department of Biomechatronics

² Institut of Technics and their Didactics, Westfälische Wilhelms-Universität Münster

ABSTRACT

Systematic construction and design in Germany have a tradition of more than half a century. Since bionics (or biomimetics) nearly exists for about the same period, but in the perspective of engineers works rather unsystematically, Ilmenau as a place with a tradition in both fields just from the beginning of their methodologies seems the right place to bring biologists and engineers together in their scientific approaches closer than before. In preparation of the conference "AMAM 2005" we made a proposal for structuring a "Bionic Algorithm".

SYSTEMATIC CONSTRUCTION

In most design processes in engineering sciences at least 80 % of the costs of products are determined by the designer – not surprisingly a systematic approach in this field could show up economic benefits, leading to the consequence that in the long lasting German tradition of standardization the developing rules of systematic, rational construction processes were condensed in national standards: VDI-R 2221 "Methodology for the development and construction of technical products" and VDI-R 2225 "Construction under technical and economical aspects". Current trends drive an opening towards psychology, to give room to creativity while not neglecting the helpful character of standards.

BIONICS

The idea of "Bionics" in Germany both East and West co-evolved with international developments. In East Germany (GDR), at Ilmenau bionic concepts were centered around the term "Biocybernetics". In West Germany (FRG), Werner Nachtigall drove the concept of "Technical Biology" mirroring "Bionics" as equivalent prerequisite. It has to be pronounced, that bionics does not claim to be a new science – it is a method to intertwine two fields of science with different history and culture in research and education. For engineers grown up in the tradition of systematic construction Bionics with its focus on intuition, inspiration, and association remains suspect, a field for creative inventors, not for "real" engineers. Engineers widely admire "constructions" nature provides in living systems, but there are principal doubts that a systematic transfer of

principles derived from inspection into nature into technical construction is possible. Now that the insight into the meaning of the individual for the success of construction processes grows and terms like "Autogenetic construction" take up aspects of evolution theory, we dare to propose a compromise strategy for biologically inspired construction, hopefully acceptable to engineers as well as to life scientists: "Bionic algorithm".

BIONIC ALGORITHM

Engineers often look into the living world drawing conclusions by spontaneous analogies. The follow-up of successful bionicbased technical developments intrigued us under heuristic strategies of "biomechatronics" to make the experiment to formalise this approach. Herein, differences between technical and biological systems usually occurring may not be ignored (biological objects: dynamic, multifunctional, nonlinear). Main goal is the extension of our technical know-how by making biomedical knowledge accessible.

The principles of the "Bionic Algorithm" proposed here is shown in the flow diagram given in the figure. Though it should be self-explaining, some terms have to be clarified or defined since they are used in different sciences in a different manner:

Analogy:

- has to be drawn between a technical demand (goal-directed "task") and biological functions sustaining the survival of a biological system (in nature "goals" and "tasks" do not exist).
- may be based on different levels of abstractions, from copies of nature ("biomimetics") to transfer of principles into quite different technical purposes ("bionics" sensu strictu).

Biological paragons:

- complete ecological (supra-organismic) systems.
- complete organisms (animals, plants, protists – "organismic approach")
- organs and cells (always multifunctional!)
- molecules
- processes of development
- processes of material, information, energy transfer.

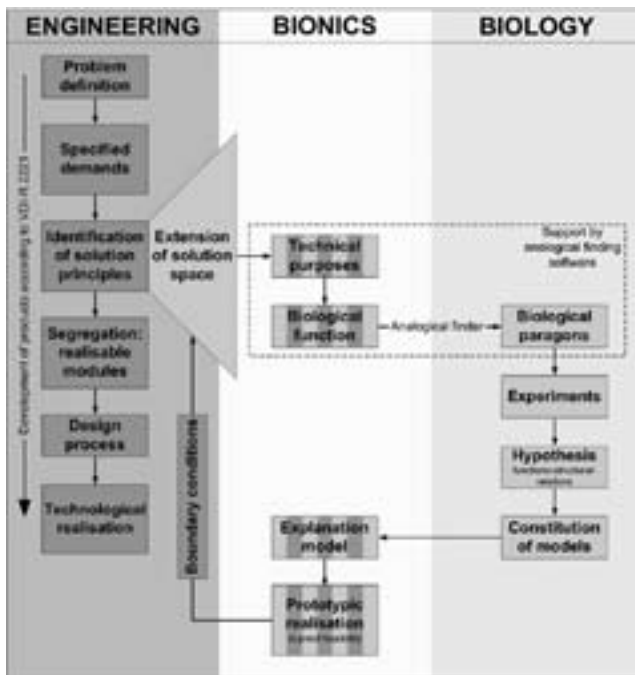


Fig. 1: Bionic algorithm. Core element is the finding of analogies between biological and technical systems, may they be morphological, structural, and/or functional. This task has to be fulfilled by humans, but may be supported by data bases, knowledge bases, and software algorithms.

Modelisation:

- increasing the level of abstraction by leaving out features which are irrelevant for the technical purpose.
- interpreting biological phenomena using technical terms and symbols

Explanatory model:

- experimental test of functionstructural relations hypothesised for the biosystem.

Design model:

- constructive realisation under the restriction of user demands, based on technological possibilities.

Extension of solution space:

- to conquer paradigms („we always did it this way“).
- to create completely new ideas derived from other areas of knowledge, under the motivation of “synectics”, a common term in construction theory.
- to systematically abstract the generation of ideas.

Boundary conditions:

- critical check of transferability, referring to criteria of geometric similarity, availability of other types of materials, and different production processes.

The flow diagram not only illustrates the sequence and order of tasks to be fulfilled, but also states logical interdependencies.

To make accessible biomedical knowledge to engineers, at present we realise a software to identify biological paragons and functionstructural solutions embodied by them, to synectically propose alternate solutions. The correlation of modules (structure, function) in an organism and a machine requires a high level of abstraction – this process may be founded on schemes like the one proposed by B. Hill.

GERMAN BIONICS COMPETENCE NETWORK BIONKON

Bionics holds promise of genuine innovations. The combination of tested principles and optimized structures demands the attention of business and industry. Investments in bionics thus are an investment in the future. Sustainability is an explicit goal of the two German Competence Networks “BioKoN” and “Biomimetik”. Nature has had an incomparable amount of time and resources to develop convincing solutions – it is up to bionics to harvest these ideas.

The work underlying this publication partially was granted by Bundesministerium für Bildung und Forschung (BMBF) / Projektträger Deutsches Forschungszentrum für Luft- und Raumfahrttechnik (DLR), and BMW AG München.

3rd International Symposium on Adaptive Motion in Animals and Machines (AMAM): Program/Abstracts, Verlag ISLE, Ilmenau, 2005, p. A-C.

Information System about Medical- and Microtechnical Relevance of Chemical Elements

C. Schilling^{1,*}, R. Müller³, W. Kempf¹, M. Stubenrauch², and H. Witte¹

¹ Department of Biomechatronics

² Department of Micromechanical Systems

³ Gesellschaft für Ökologie und Umweltchemie mbH, Erfurt

Summary

At present there is a drastic increase of technical structures that are applied in biological systems, especially in humans. Therefore the requirements for the materials and substrates used in these products and components grow. The material compounds of complex implant systems have to fit the needs of the higher functionality as well as the biocompatibility. Furthermore, disposal considerations have to be taken into account before manufacturing products. An internet based consulting service software will gather all these information and present them in a user friendly way.

“How toxic is Neodymium?”

The public negative image of some chemical elements shifts the point of view on the risk potential for the group of users. In many cases it is not easy to get objective statements about toxicity and toxicity conditions, synergy effects in physiology, therapeutical broadness or the relationship to the biosphere.

Challenge and intention of the information systems presented here, is the easy access to a variety of information on the base of the table of the elements from Mendeleev (PSE). It is structured into chemical, biological and application aspects, especially in the field of microsystem technologies. The system is flanked by references, cross-references and internet links. This network of information will lead to binding statements about the requested element as a component of a technical product with medical or ecological relevance.

Access- and Selection Page for Elements

The standard color index for the table of elements was disregarded (like for the acid-base state of oxides), see figure 1. Groups of elements were pooled taking into account the effects or applications. Practicability and self-explanatory groups were other focuses. Clicking on an element opens a page with monographic, divided short description.

Instable isotopes like Actinoides have not been implemented into the data base yet.

Fig. 1: Grouping and indexing in the PSE, ordered by functional criteria.

Legend (gray values):

a: I. main group („alkali metals“, except H)

b: II. + III. main group („light metals“)

c: III. – VI. main group („Metalloids“)

d: V., VI. main group (biotroph elements, nutrition)

e: VII. main group („halogens“)

f: VIII. main group („noble gases“)

g: II.- IV. main group; II. side group („heavy metals“)

h: III. side group + Lathanoids („rare earth metals“)

i: V. – VIII. side group („steel alloy metals“)

k: IV. + V. side group. („Ti-Ta-Group“)

m: I. + VIII. side group. („noble metals“).

Target Groups

The selection of elements and their compounds as part of technological compound materials and the basic knowledge of material properties is a problem of many manufacturers and users who do not have sufficient chemical experience. Using the information system will contribute to the commercial funding policy by scientific support for engineers especially in R&D. Excellent effects on companies working in the field of medicine, medical technologies or implanting systems are targeted. Furthermore it can be used

as a preinformation instrument in the context of certifications on environmental compliance. It is also relevant for the approval of production lines with potentially toxic chemical elements. Post gradual education can also be supported with the information system esp. for technicians, medical staff or people working in environmental surveillance. Even chemistry lectures in schools can have a benefit. The texts are made primarily scientific correct and beside that also easy to understand. So even people without special chemistry knowledge have the opportunity to get themselves informed about risks and possible cross effects of chemical elements or construction materials on health and environment.

Software Implementation

The following requirements had to be implemented into the software: it should be a locally independent, accessible from a high number of parallel users, with flexible presentations, various linking possibilities, and easy publication. So, an internet based simple content management system (CMS) was chosen on HTML, PHP and CSS. Due to its open structure it can be easily adapted to future requirements. Special attention was paid to an easy and intuitive program code. The syntax is supported by several integrated help texts. The consequent usage of existing standard internet technologies for data acquisition and presentation and the simple linking options will play an important role for future enhancements of the system and allows changes in the software without special experiences in web page design. An additional routine for transforming the data base into static HTML-pages enables parallel usage and actualizations. This option also provides a publication and distribution on a CD-ROM.

Microsystem Aspects

The range of materials in micro system technologies is not restricted to the commonly known palette but it can be easily systematized. There are substrate materials like single crystalline silicon and compound semi-conductors, functional oxide or nitride layers, metallization layers, ceramics like lead-titanate-zirconate, high energy magnets, glasses like photo patternable heavy metal doped Foturan® and polymers like PMMA. In individual cases, they have already been under investigation regarding their interaction with biogenous media in vitro, but a negative interaction of normally bioinert materials can lead to critical situations. These uncertainties have to be implemented and shown for documented cases. For other possible compounds the user has to be warned against such effects.



Fig. 2: Screen shot of a content page for an element with general chemical and technical facts as well as its biological functions.



Fig. 3: Screen shot of a page with information about the interaction of an element to the environment and the human body.



Fig. 4: Screen shot of a page about biocompatibility of an element with information about application fields and purposes in the medical context.

However, a big problem of all synoptical overviews is a suitable limitation concerning the total broadness of all information. The system presented cannot and shall not replace a toxicological council. We only address indications with the target of biocompatibility of materials with a medical, biotechnical and ecological context. For high risks, the user is forwarded to relevant Websites or official councils.

Properties of Micro-Electromechanical RF Resonators for Sensor Applications

K. Brückner^{1,*}, R. Stephan¹, K. Blau¹, K. Tonisch², F. Will², V. Cimalla², O. Ambacher², and M. A. Hein¹

¹ Department of RF and Microwave Techniques

² Department of Nanotechnology

Using appropriate semiconductor production processes, the fabrication of free-standing micro- and nanomechanical resonators has been demonstrated by several groups [1,2]. Coupling to electrical circuits can be achieved by metallization layers, allowing magnetomotive actuation of the resonators. The mechanical oscillation is affected by various physical parameters like the geometrical dimension, mass, friction, tension, temperature, and ambient pressure. Electrical detection of these parameters would make accessible a variety of sensor applications, especially in connection with functionalized surfaces for the detection of chemical and biological species [3]. In all cases, high resonant frequencies and high quality factors are beneficial for high sensitivity. Compared to vacuum, sensors working under ambient conditions or even in liquids, exhibit strongly reduced Q-factors, necessitating optimized geometries and materials.

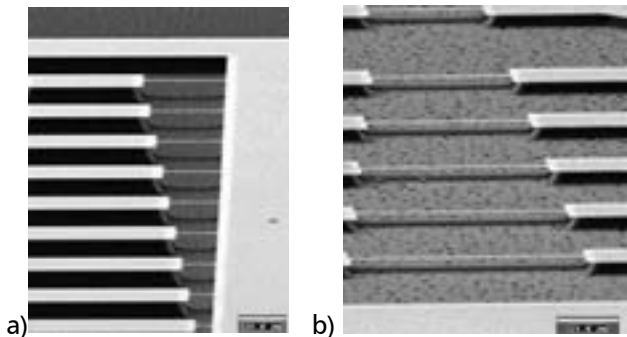


Fig. 1: Scanning-electron microscope (SEM) images of the doubly clamped resonators. (a) Set of 150-nm thick AlN-beams with lengths from 8 to 40 μm . (b) Set of 250-nm thick SiC-beams with lengths from 40 to 100 μm .

To fabricate doubly clamped beam resonators, as the ones shown in figure 1, aluminum nitride (AlN) and silicon carbide (SiC) layers were deposited onto silicon substrates by reactive sputtering and high-vacuum chemical vapor deposition, respectively [4]. The resonators were patterned by combined isotropic and anisotropic dry etching. The metallization consisted of an evaporated Ti/Au or a Cr/Ti multilayer. The geometric dimensions of the resonator beams varied from 10 μm to 500 μm in length L , from 1 μm to 8 μm in width w , and from 50 nm to 250 nm in thickness t .

The resonant frequency f_1 of the fundamental vibration mode of the beams can be described by the Euler-Bernoulli theory, here enhanced by a second square-root term to account for the influence of the strain ϵ inherent to the active resonator layers [5]:

$$f_1 = 1.028 \sqrt{\frac{E}{\rho}} \cdot \frac{t}{L^2} \cdot \sqrt{1 + 0.295 \frac{L^2}{t^2} \epsilon} \quad (1)$$

In this equation E represents the Young's modulus and ρ the mass density of the resonator material.

The beams were placed in a permanent magnetic field of about 0.5 T. A RF current set the beam in oscillation, due to the Lorentz-force. The induced response of the resonators is smaller than the exciting signal by 4 to 6 orders of magnitude and, therefore, challenging to detect. For the experimental characterization of the beams, we used a pulsed-measurement technique, where excitation and response signal can be separated in the time domain [6]. In this technique, the microelectromechanical resonator is excited by short voltage pulses and after amplification (Stanford Research SR560) the response is monitored by a digital oscilloscope (Agilent DSO6102A). Synchronized pulse-suppression protects the amplifier from the strong exciting signal. A typical decay curve is shown in figure 2.

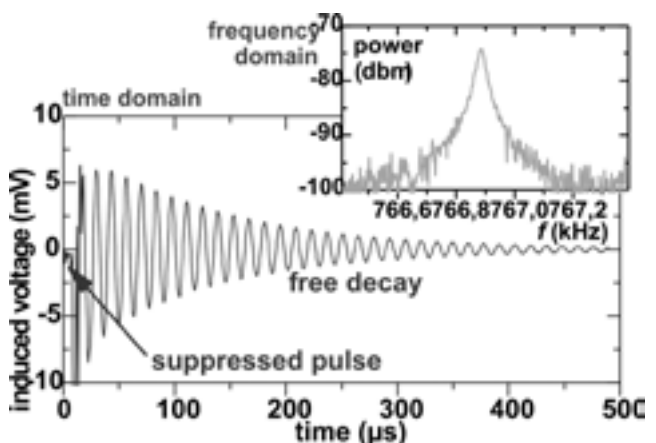


Fig. 2: Typical decay signal of a 200- μm long AlN resonator. Inset: Measurement of the response of a similar resonator in frequency domain.

From such data, the period of oscillation T and, hence, the resonant frequency, $f_{res} = 1/T$, as well as the quality factor Q can be easily determined:

$$Q = \frac{\pi \cdot f_{res} \cdot (t_2 - t_1)}{\ln(U_1/U_2)} \quad (2)$$

Recently, we have been successful in monitoring the frequency response of our resonators also in the frequency domain (inset to figure 2). We have applied a bridge measurement similar to the one described in [2]. The comparison of data measured in time and frequency domains will provide additional insight into the dynamics of the resonant beams. However, in the following we focus on the data obtained in the time domain.

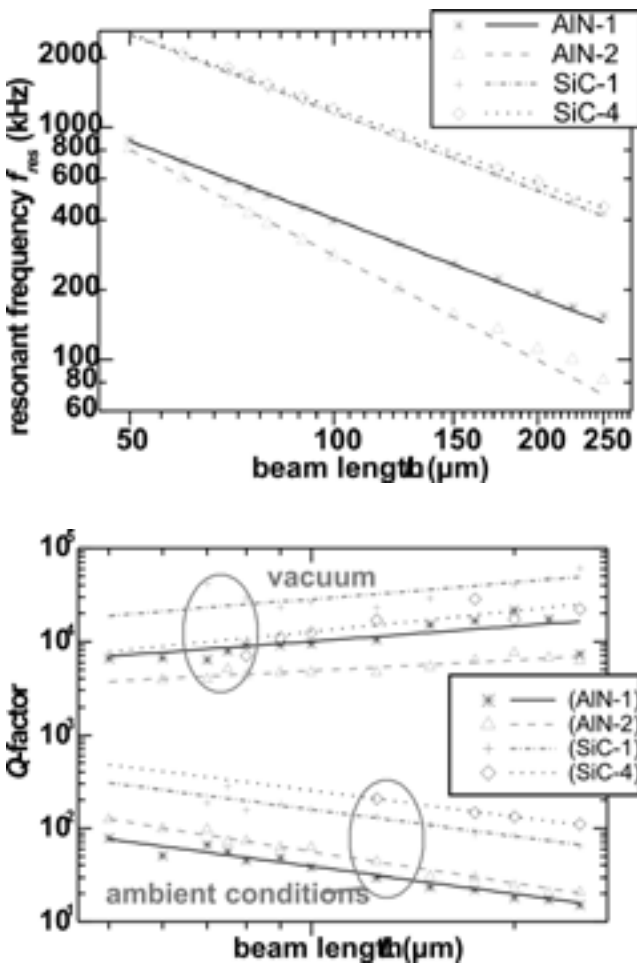


Fig. 3: (a) Resonant frequency versus beam length for the doubly clamped AlN and SiC beams. (b) Measured quality factors versus beam length, under ambient conditions (lower set of curves) and under vacuum (upper set). Beam widths: 1 μm (AlN-1, SiC-1), 2 μm (AlN-2), and 4 μm (SiC-4).

The measured resonant frequencies f_{res} ranged from 81 to 885 kHz for the AlN beams, and from 430 to 2100 kHz for the SiC beams. Figure 3a shows in double logarithmic scaling the dependence of f_{res} on the beam length L for both material systems, with curves for two different beam widths for each material. According to equation (1), the L -dependence

of f_{res} follows a power law: $f_{res} \sim L^b$, where b increases from -2 to -1 for increasing strain. In agreement with equation (1), the exponent b is not exactly constant but exhibits a weak dependence on L , as indicated by the deviation between data and fit for long beams. The slope b ranges from -1.07 (i.e., highly strained) for the 4-μm wide SiC beams to -1.51 for the less strained 2-μm wide AlN beams.

For the same resonator beams used to draw figure 3a, the quality factors have been measured, both under ambient conditions and vacuum ($p = 10^{-3}$ Pa), with the results displayed in figure 3b. In vacuo, the Q -factors are higher than those obtained under normal pressure by more than two orders of magnitude.

This pronounced difference identifies the viscous damping in air as the dominant loss mechanism for the operation under ambient conditions. A vibrating sphere represents one of the few geometric bodies for which viscous damping can be described analytically. This result can be used to approximate the quality factor $Q_{viscous}$ associated with the viscous damping of the beam resonators [7]. In such a model, the beam is represented by a chain of vibrating spheres, with a chain length identical to L , and with sphere diameters according to the beam width w . For composite beams, one gets:

$$Q_{viscous} = \frac{c \cdot w \cdot \sum_{i=1}^n \rho_i t_i}{\eta_0 / f_{res}(L, \epsilon) + w \cdot \sqrt{\rho_0(p)} \cdot \sqrt{\eta_0 / f_{res}(L, \epsilon)}} \quad (3)$$

with η_0 being the viscosity and ρ_0 the mass density of the ambient air, where ρ_0 is proportional to the ambient pressure p . To derive $Q_{viscous}$ from experimental data, the relation $1/Q_{air} = 1/Q_{viscous} + 1/Q_i$ has been used to eliminate the contribution of the losses Q_i inherent to the material and given by the residual Q -values in vacuum. Equation (3) provides excellent agreement with the data compiled in figure 3b, where the widest SiC beams ($w=4 \mu\text{m}$) with the highest resonant frequencies display the highest Q -factors under ambient conditions. From the measurement data, the constant factor c has been found to be about 1.2.

In summary, we have performed a systematic study of the resonant properties of doubly-clamped AlN and SiC microelectromechanical resonators and obtained resonant frequencies from 100 kHz to 2100 kHz and Q -factors up to 60,000 kHz in vacuo. Consistent descriptions of the dependences of f_{res} and Q on resonator geometry, material strain, and ambient pressure pave the way for an optimization of the devices for sensor applications in viscous environment.

This work has been funded by the German Science Foundation (DFG), Priority Program 1157: Integrated Electroceramic Functional Structures.

- [1] Cleland et al., App. Phys. Lett., vol. 79, no. 13, pp. 2070-2, 2001.
- [2] Ekinci et al., Appl. Phys. Lett. 81, no. 12, pp. 2253-5, 2002.
- [3] Will et al., Proc. Eurosensors XX, Göteborg, Sept. 17-20, 2006, will be published.
- [4] Förster et al., physica status solidi (a) 202, no. 4, pp. 671-6, 2005.
- [5] Bouwstra, Geijselaers, Transducers '91, San Francisco, CA, June 24-27, pp. 538-42, 1991.
- [6] Brueckner et al., Proc. 35th European Microwave Conference, Paris, Oct. 4-6, pp. 1531-4, 2005.
- [7] Hosaka et al., Sensors and Actuators A 49, no. 1-2, pp. 87-95, 1995.

Characterization and modelling of the electrical behaviour of SPM sensors

J.-P. Zöllner^{1,*}, A. Frank¹, M. Netzel², and I. W. Rangelow¹

¹ Department of Micro- and Nanoelectronic Systems

² SEDIX Elektronik GmbH, Ilmenau

Introduction

Scanning probe microscopy (SPM) is a powerful method to characterize surface properties in nanoscale dimension. The SPM sensor (a flexible cantilever with an extremely sharp tip mounted on it) is passed over a sample surface, its tip follows the surface profile and the vertical deflection of the cantilever is measured.

Especially Wheatstone bridge-type piezoresistive cantilevers with integrated actuator are of relevance because opposite to optical detection no external components are needed and the cantilevers are easy to use. Moreover, this type of cantilever includes an integrated bimorph actuator. Its vertical position is thermally controlled in a feedback loop by the actuator. On the other hand the actual position of the probe tip is determined by measurement of the cantilever bending with the integrated piezoresistive sensor. The elegance of this concept is that by using an almost identical detection principle and differently functionalized tips or cantilever surfaces, it is possible to detect subtle sample interactions (mechanical, electrical, thermal, and chemical) with a significantly more compact system than with optical beam deflection techniques. A possibility to increase the SPM throughput is the application of multiple probes in an array arrangement on a single chip for parallel operation. Each probe is individually controlled by a vertical interconnected application specific integrated circuit (Fig. 1). Cross-talking effects and parasitic coupling between the sensors and actuators as well as between neighbouring SPM sensors are possible.

Therefore the electrical characterization of the sensor and sensor arrays includes the measurement of parasitics and the determination of cross-talking effects, as well as the development of suitable models to describe such effects. These are important tasks for the optimization of the probes and probe arrays and their operation conditions including the adjustment of the controlling and measuring electronics.

Characterization and Modelling

For the characterization of the electrical behaviour of micro- and nanosensors semi-automatic wafer probers are available. Together with a control unit (PC) it can be used for on-wafer characterization of

semiconductor devices, sensors and ICs. Furthermore, we can determine parasitics (C, L, and R), even in the case of extremely small values.

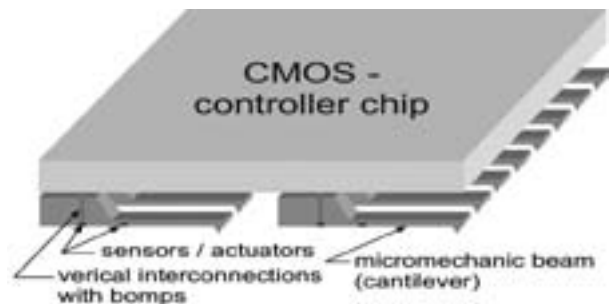


Fig. 1: M(N)EMS – sensor array direct connected with a controller integrated circuit

By means of IC-CAP (a software package) it is possible to extract complete model parameter sets for a number of Spice models. The Fig. 2 shows a cantilever structure under test. The detected device parameters and parasitics are utilized in the circuit simulator PSpice to model the electrical behaviour of the device. By means of parameter variation the optimization of the sensor device is carried out. The extracted device model of the sensor is used as a part to design the full electrical circuit for sensor signal detection.



Fig. 2: On-wafer test of a nano-structure

Simulation Environment

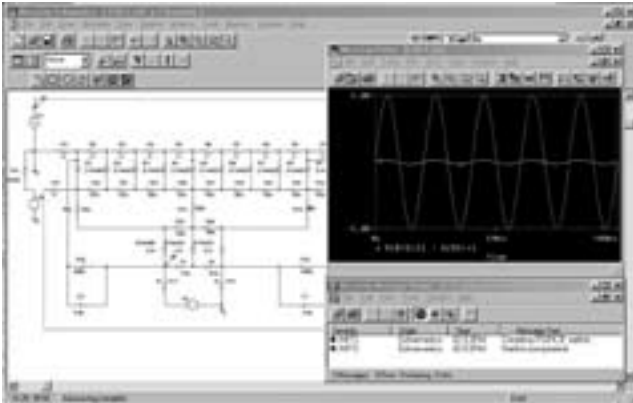


Fig. 3: Screen shot of the equivalent network of a resistance structure in silicon and the simulated voltage behaviours.

PSpice is an advanced, native mixed-mode simulator, which is used to simulate complex mixed-signal circuits with analog and digital parts.

To explore the circuit behaviour it can be used for DC, AC, noise, and transient analysis. The circuit behaviour variation can be investigated via parametric, Monte Carlo, temperature and worst case analysis.

The tool allows the implementation of new internal models and the adaptation of existing models. The large variety of models ensures a flexible simulation (Fig. 3).

The electrical model is used to optimize the sensitivity and signal-to-noise ratio of the sensor. Crosstalk between the actuator and the sensor of active self-actuated SPM sensors is minimised by investigating and optimizing the parasitic coupling. Also an accurate model is useful in the development of better feedback-algorithms and optimization of the measurement. With a thoroughly understanding of the electrical behaviour it is possible to simulate sensor, sensor arrays and ASIC together and detect mismatches at an early design level.

- [1] I.W. Rangelow, Scanning proximity probes for nanoscience and nanofabrication *Microelectronic Engineering*, Volume 83, Issues 4-9, April-September 2006, Pages 1449-1455.
- [2] T. Schenkel, J. A. Liddle, J. Bokor, A. Persaud, S.J. Park, J. Shangkuan, C.C. Lo, Kwon, S.A. Lyon, A.M. Tyryshkin, I.W. Rangelow, Y. Sarov, D.H. Schneider, J. Ager and R. de Sousa Strategies for integration of donor electron spin qubits in silicon *Microelectronic Engineering*, Volume 83, Issues 4-9, April – September 2006, Pages 1814-1817.
- [3] I.W. Rangelow, P. Grabiec, T. Gotszalk and K. Edinger Piezoresistive SXM sensors *Surface and Interface Analysis*, Vol. 33, pp. 59-64, (2002).

SAW-Resonators at High Temperature

S. Klett^{1,*}, W. Buff², and F. Krispel³

¹ Department of Micro- und Nanoelectronic Systems

² senTec Elektronik GmbH, Ilmenau

³ Piezocryst GmbH Graz, Austria

For several years it has been known that SAW devices (surface acoustic wave) are able to perform the task of rf remote wireless sensing. In particular, they are operating passively without own electronic circuitry for signal transmission and without own power supply. This makes them suitable for measurement tasks which are not possible to be solved otherwise. At the moment, there exist several SAW-based principles with the capability of passive remote sensing [1]-[4]. Compared to other solutions the usage of resonators takes the advantage of narrow band operation.

In particular, the temperature restriction of standard semiconductor applications or batteries ($T_{\max}@150^{\circ}\text{C}$) is not given. In this way, the limitation in the working temperature of the sensor unit is only given by the SAW element itself.

It has been demonstrated that quartz substrates with a metallization of aluminum can be used for temperatures up to 300°C . This temperature range is important for many industrial applications. However, for a wide range of practical applications, many measurements have to be done under extreme conditions. So the more challenging temperature range is above 300°C .

In addition to the reported improved electric and elastic properties [5], the high temperature behaviour of gallium orthophosphate (GaPO_4) and langasite ($\text{La}_3\text{Ga}_5\text{SiO}_{14}$) is important. Furthermore, it is necessary to have a high Q-factor for the rf interrogation.

Sample Design

A SAW device consists of a piezoelectric substrate with a metalization. Every part of such a system has to be optimized and adapted to the high temperature conditions.

The demands for the piezoelectric crystal over the entire temperature range are mainly the following:

- mechanical and chemical stability,
- stable piezoelectric and elastic behavior,
- no appearance and migration of contamination,
- no pyroelectric behavior.

Both, gallium orthophosphate and langasite, meet these conditions and are available in good qualities nowadays.

The demands for the metallization are:

- stable without oxidation over the entire temperature range,

- good adhesiveness of the of the metallic layer over the temperature range,
- low resistivity also at high temperatures,
- well known elastic behavior,
- possibility to pattern metal layer for the production of interdigital transducers,
- uniform thickness over the wafer,
- not too high specific mass.

Platinum in combination with a capable adhesion layer emerged to be a convenient material to fulfill the demands.

As for the crystal structure, gallium orthophosphate belongs to the same point group as quartz (32 or D_3), possesses similar physical properties (piezoelectric effect, no pyroelectric effect) and can be used up to 970°C because of the absence of the a-b phase transition of quartz [6]. The doubled piezoelectric effect compared to quartz and the high stability of the most physical properties up to 900°C make the crystal a good choice for SAW applications at high temperatures [7].

The used crystal cuts are in the range $\lambda=90^{\circ}$, $m=0\dots90^{\circ}$, $\theta=0^{\circ}$.

As metallization for the finger structures, Pt is used. The adhesive layer consists of indium tin oxide (ITO) or Ti.

The interdigital transducers and the reflectors are produced by lift off process. This technological step is commonly used in the manufacturing of SAW devices. However, in the case of platinum there are some difficulties. If we have thicker layers (here 210 nm), the ductile properties of platinum result in very uneven tear-off edges after the lift off process (Figs. 1, left and Fig. 2). When using thinner layers (here 120 nm), the devices' homogeneity is improved.

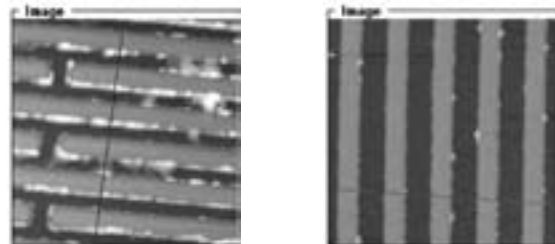


Fig. 1: AFM scan of metallization thickness 210 nm (left) and 120 nm (right). Experimental results

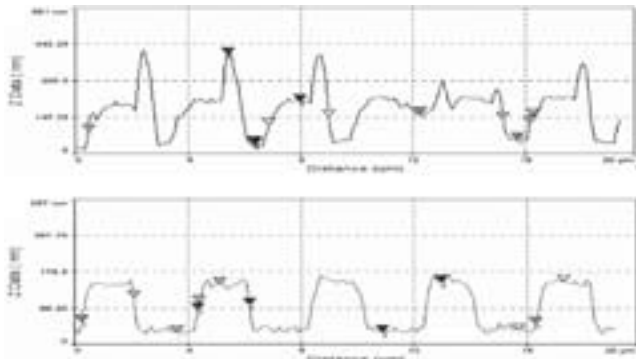


Fig. 2: Line scan of GaPO4 devices with the thicker Pt layer and with optimized technology.

Experimental results

The aim of the first SAW tests was to yield high temperature stability between 500°C and 600°C. Figure 3 shows the 1st order temperature coefficient on frequency (TCF) T1 and the SAW velocity v_0 of GaPO₄ for SAW applications.

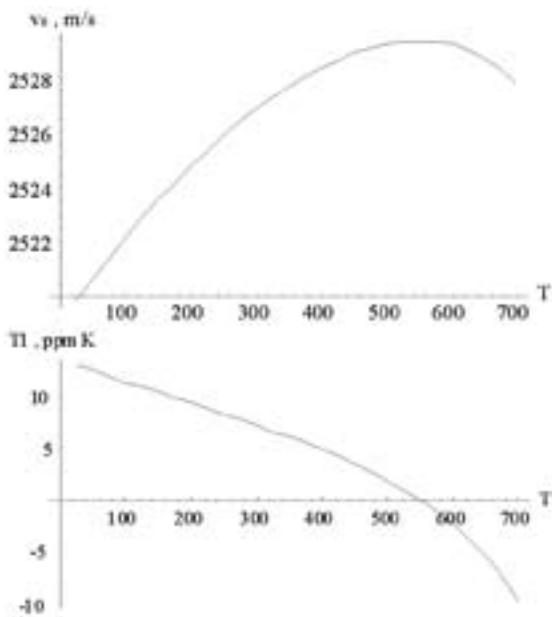


Fig. 3: Free surface velocity (v_0) and 1st TCF (T1) of GaPO₄ at $m=11^\circ$ depending on temperature.

The calculated temperature behavior of the SAW velocity v_0 is parabolic with the inversion temperature at 550°C.

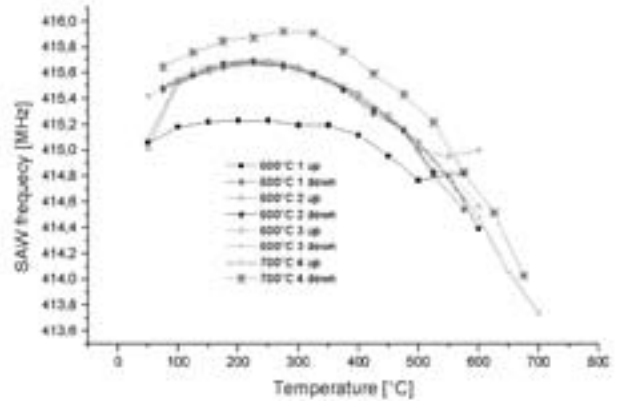


Fig. 4: Measured SAW frequency of a GaPO4 sample, depending on temperature.

Figure 4 shows the first measurements with high temperature SAW devices made of GaPO₄. With the calculated free surface velocity a SAW frequency of 415 MHz is achieved for the chosen IDT finger width of 1.468 μm and a gap of 1.431 μm . The metallization was 20 nm ITO and 190 nm Pt.

Figure 4 shows the SAW frequency after several cycles of heating up and cooling down. The first heating up causes an initializing process, then the frequency temperature curve is stable until a higher maximum temperature is chosen. Then a new initializing process is observed. A comparison with the predicted values shows a strong shift of the resonance frequency with temperature and a lower value of the absolute frequency. This discrepancy can be attributed to a strong mass loading effect caused by the physical properties of the Pt layer.

Part of this work was supported by the European Commission under grant G1RD-CT-2001-00541 "WIREGONE". Many thanks to Dr. V. Skarda and his team from the University of Southampton for the preparation of the samples on GaPO₄.

[1] Reindl, L., Pohl, A., Scholl, G., "SAW-based Radio Sensor Systems", IEEE Sensors Journal, Vol. 1, 2001, pp. 69-78.
 [2] Buff, W., "SAW Sensors for Direct and Remote Measurements", Proc. 2002 IEEE Ultrasonics Symp., pp. 420-428.
 [3] Pohl, A., "A Review of Wireless SAW Sensors", IEEE Transactions of Ultrasonics, Ferroelectrics and Frequency Control, Vol. 47, 2000, pp. 317-331.
 [4] Beckley, J., Kalinin, V., Lee, M., Voliansky, K., "Non-Contact Torque Sensors Based on SAW Resonators", Proc. 2002 IEEE Freq. Control Symposium, pp. 202-213.
 [5] Krempl, P., Stadler, J., Wallnöfer, W., Ellmeyer, W. "Present State of GaPO₄ Research", Proc. European Time and Frequency Forum, 1991, pp. 143-147.
 [6] Jacobs K., Hofmann P., Klimm D., Reichow J., Schneider M., "Structural Phase Transformations in Crystalline Gallium Orthophosphate", J. Sol. Stat. Chem. 149 (2000), pp. 180-188.
 [7] Bigler, E., Ballandras, S., Bonjour, C., Palmier, D., Philippot, E., "Experimental Study of SAW Propagation on Gallium Orthophosphate", Proc. 1994 IEEE Ultrasonic Symposium, pp. 385-389.

SiGe-Core Circuit for Ultra-Wideband Sensors

J. Sachs* and R. Thomä

Department of Electronic Measurement

Introduction

Ultra-wideband (UWB) technique is an emerging sensor and communication technology. Particularly innovative ultra-wideband sensors will open new applications and perspectives for non-destructive testing, medical imaging, supervision and emergency applications, localisation and radar systems, and many other more.

Ultra-wideband sensors use a low power (typically less than 1 mW) electromagnetic wave for sounding the scenarios under test. The sounding signal occupies a spectral band of several GHz bandwidth within the lower GHz range. From this a high spatial resolution of radar images respectively positioning devices and a good wave penetration of most substances results which evokes the large interest in this new sensor technology.

The key-component of an UWB-sensor is its wideband RF-electronics. The paper deals with a new and worldwide unique approach [1] which not only permits an integrated solution of the UWB-sensor electronics, but also provides excellent technical parameters, such as a high short term stability, a high measurement speed and scalability concerning different applications.

The measurement approach

An UWB-sensor has to provide a very wideband sounding signal in order to stimulate the scenario under test and it has to capture one or more response signals gained from antennas or applicators. In the concerning case, a very wideband pseudo-random code acts as the sounding signal.

Figure 1 demonstrates the principle of the measurement electronics. A stable RF-clock, typically in the range of 10 GHz, pushes a fast shift-register. If this shift-register is equipped with an appropriate internal feedback, it provides a special pseudo-random code, which is called M-Sequence. Its usable bandwidth corresponds to approximately half the clock rate, i.e., about 5 GHz. In the case of the basic concept, this M-Sequence acts directly as sounding signal, i.e., it will stimulate the scenario under test. The measurement signal which results from the behaviour of the test objects is captured by an interleaved sampling approach. As a result of the sampling theorem, the enormous bandwidth of the sounding signal would suppose a data capturing

rate beyond 10 GHz. This would require a technically challenging and power hungry system causing extremely high costs. Fortunately, the applied M-Sequence stimulus is periodic, so that a sub-sampling approach, e.g., interleaved sampling may be applied. This drastically reduces the data rate without violation of the sampling theorem. Consequently, the system cost and power dissipation decrease.

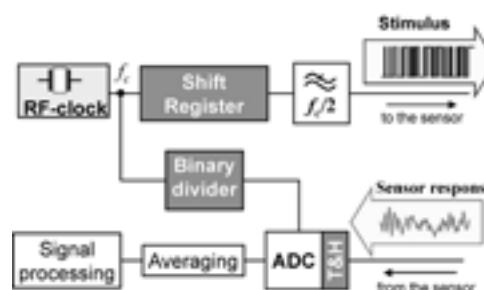


Fig. 1: Schematics of the UWB-electronics. The emphasised blocks represent the RF-core circuits.

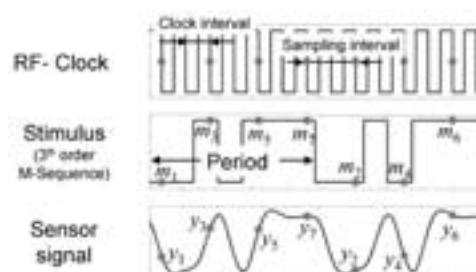


Fig. 2: Sampling rate reduction by binary division of the clock rate

The basic idea of subsampling is to distribute the gathering of the required data samples over a number of periods. In the considered case, one data sample per chip of the M-Sequence is required (see [1] for details). Following the example in figure 2, this can be done in a very effective and stable way by controlling the data gathering via a binary divider. The larger the dividing factor, the slower the measurement rate will be. Since the minimum measurement speed is given by the actual application scenario, an optimum solution concerning measurement speed and system costs (power dissipation) can simply be found by programming the divider without any change in the RF-hardware.

Even if the low measurement rate allows the use of on the shelf AD-converters, a wideband Track-and-Hold (T&H) circuit has to be in front of them since the incoming signal is still of huge bandwidth. The processing of the digitised data depends on the actual application. It will not be discussed here. Several modifications of the basic concept have been introduced already. For details the reader is referred to ([2], [3]).

RF-Core Circuit

The key components of the RF-part are the shift register, the T&H circuit and the binary divider. Figure 3 shows a layout example of such a circuit which was manufactured by IHP Frankfurt in SiGe:C BiCMOS technology [4]. The currently available designs operate up to a clock rate of about 15 GHz. The analogue bandwidth of the T&H is about 12 GHz and its sampling rate can be between a few KHz and 2 MHz.

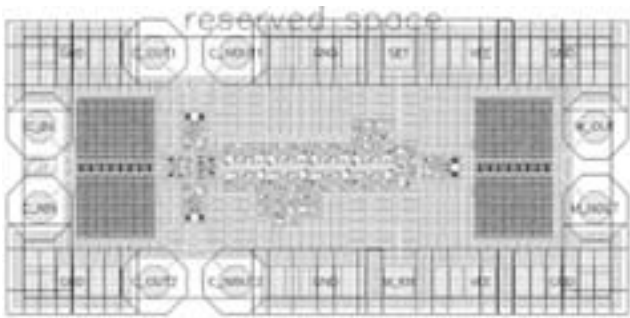


Fig. 3: Layout of the M-Sequence generator in 0,25 μ SiGe:C BiCMOS technolo

The chip design was not only aimed for a high operational frequency but also for a moderate power dissipation per square mm chip area. For this reason, both wire bonding and flip chip wiring was used to connect the chips with the remaining parts of the electronics. Flip chip wiring results in less effective heat transport than wire bonding since the chip is not in direct contact with the carrier substrate. On the other hand, flip chip connections cause lower inductivities which is of great advantage at high operation frequencies.

Figures 4 and 5 show the two methods of chip wiring. Figure 4 refers to wire bonding on Rogers material and figure 5 shows the cut through a SiGe chip mounted on LTCC. In the considered case, performance degradation due to wire bonding could not be observed. However, for future applications in the 60 GHz band, the flip-chip technique will be the method of choice.

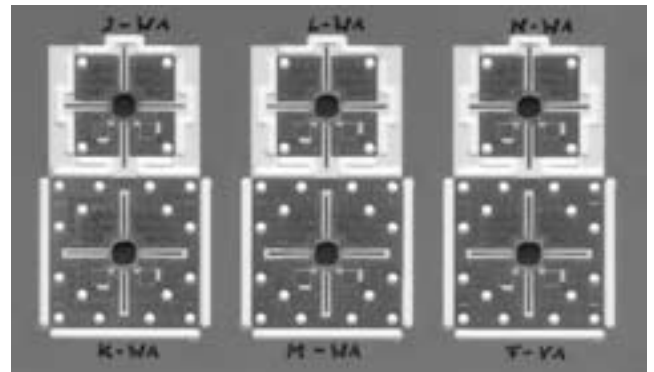


Fig. 4: Standardises RF PCBs with assembled SiGe chips. The PCBs open a great deal of flexibility to configure the actual sensor electronics.

The flip-chip wiring corresponding to figure 5 is based on a multilayer LTCC substrate. The top layer covers the RF-connections. It was built in thin-film technique in order to reach small tolerances. The remaining layers (ground, control lines, power supply) are manufactured in classical thick film technique. For future designs, it is intended to replace the thin-film layer also by a thick film one.

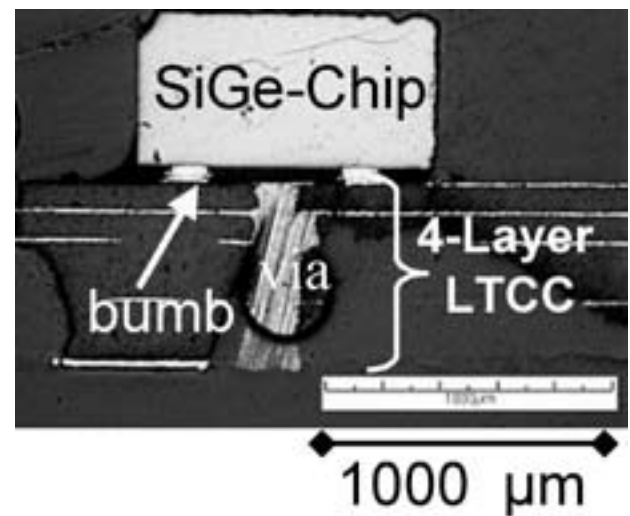


Fig. 5: Cut of a SiGe chip flipped on a 4 Layer LTCC.

The authors wish to thank all colleagues and project partners for their engagement and support. Primarily, they appreciate the contributions and engagement from F. Bonitz; K. Borkowski; R. Herrmann; M. Kmec; P. Rauschenbach; F. Tkac; S. Wöckel and R. Zetik. The close cooperation with MEODAT GmbH, Stephen Crabbe Consulting and IHP Frankfurt is also emphasized which enables technical implementation and project management. The diverse UWB projects were partly funded by the State of Thuringia, the German Federal Government and the European Commission.

[1] J. Sachs: M-sequence radar. In Ground Penetrating Radar 2nd edition, D.J. Daniels ed., IEE Radar, Sonar, Navigation and Avionics Series 15, pp. 225-237, 2004.
 [2] M. Kmec, J. Sachs, P. Peyerl, P. Rauschenbach, R. Thomä, R. Zetik: "A novel Ultra-Wideband real-time MIMO Channel Sounder Architecture", XXVIIIth General Assembly of URSI, October 23 -29, 2005, New Delhi, India.
 [3] M. Kmec, J. Sachs, P. Peyerl, P. Rauschenbach, R. Thomä, R. Zetik: "A novel Ultra-Wideband real-time MIMO Channel Sounder Architecture", XXVIIIth General Assembly of URSI, October 23 -29, 2005, New Delhi, India.
 [4] M. Roßberg, J. Sachs, P. Rauschenbach, P. Peyerl, K. Pressel, W. Winkler, D. Knoll: 11 GHz SiGe Circuits for Ultra Wideband Radar. Bipolar/BiCMOS Circuits and Technology Meeting BCTM-2000, 25 -26 September, Minneapolis, MN.

Investigation of Organic Field Effect Transistors with Different Design

A. Herasimovich*, S. Scheinert, and I. Hörselmann
Department of Solid State Electronics

Motivation

Organic materials have been proposed for many applications in electronics due to their low cost and simple device fabrication processes. However, there are some unsolved problems for the field effect transistors (OFETs), such as stability and performance increase. The OFETs performance can be improved by the carrier mobility increase or the channel length decrease. The latter one causes restriction on the processing technology or/and transistor design. We have investigated the influence of the contact material and design on the current characteristics of OFETs based on poly (3-hexylthiophene) (P3HT).

Technology

The OFETs were fabricated on a highly doped n-Si wafer (Fig. 1). The backside of a n-Si wafer was coated with Ti by sputter deposition and used as gate. A 30 nm thick thermally grown SiO₂ served as gate dielectric. It is well known, that the surface treatment of the silicon dioxide layer by hexamethyldisilazane (HMDS) increases the carrier mobility in OFETs [1]. Therefore, after an initial cleaning step, the silicon wafer was baked in an oven for 26 hours at 60°C in a HMDS atmosphere. Afterwards the wafer was rinsed with acetone and diethyl ether.

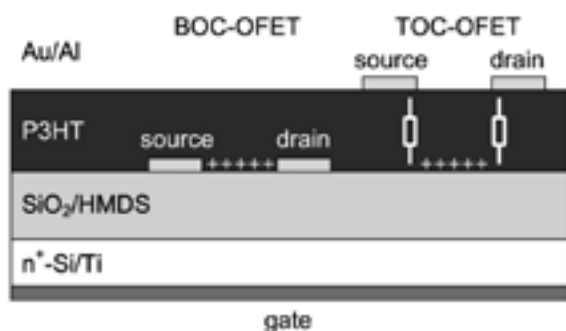


Fig. 1: Schematic cross section of the OFETs in "bottom contact" (BOC) and "top contact" (TOC) geometry with P3HT as active semiconductor layer.

In the next step, source and drain electrodes of gold (Au) and aluminium (Al) were deposited on one half of the substrate by evaporation through a shadow mask for the BOC-transistors. The channel length and width were 25 mm and 1000 mm respectively.

The active polymer film was deposited by spin casting from a solution of P3HT in chloroform with a weight concentration of 0.45%. Then the wafer was annealed at 100°C for 5 minutes. Finally, source and drain electrodes of Au and Al were evaporated through a shadow mask for the TOC-transistors. All technological steps were carried out under dry nitrogen atmosphere.

Electrical measurements were made in a nitrogen environment using a KEITHLEY 4200 semiconductor parameter analyzer.

Results and discussion

At first, the output characteristics of the TOC-transistors with the gold (work function 5.1 eV) and aluminium (work function 4.3 eV) source/drain contacts are shown in figure 2. The drain current for transistors with Au contacts is higher than for transistors with Al contacts due to the higher work function of gold. Below we will discuss that in more detail together with the comparison of OFETs with TOC- and BOC-designs, respectively.

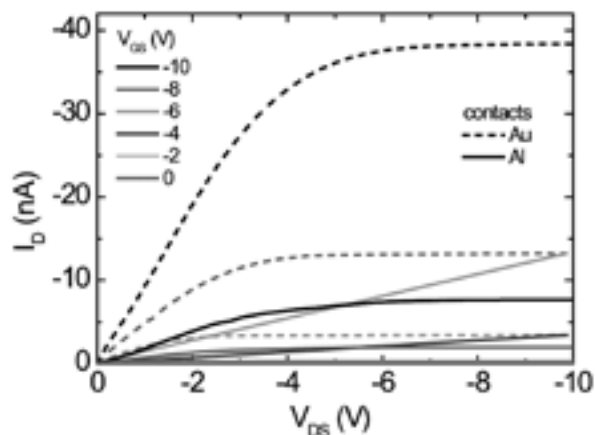


Fig. 2: Output characteristics (I_D vs V_{DS}) of the TOC-OFETs with Au- (dashed) and Al- (solid) source/drain contacts.

The measured output characteristics of the TOC-transistors with Au and Al source/drain contacts show a nonlinearity at small drain voltages and high gate voltages, which is absent at small gate voltages. Such nonlinearity was attributed in [2] to the field dependence of the mobility due to the Poole-Frenkel effect, whereas in [3] series resistances are described

as the reason. The main difference between the TOC- and BOC-designs of OFETs is the presence of additional paths for current (in figure 1 labelled with resistances) from the source/drain to the channel in the TOC-structures (in figure 1 labelled with "+"). In BOC-structures the carriers are injected directly from the source/drain contacts to the channel. Therefore, the Poole-Frenkel effect becomes more efficient in BOC-transistors while series resistances are more pronounced in TOC-structures. For this reason we have carried out investigations of both OFET designs on one substrate.

The comparison between the output characteristics of the BOC- (solid) and TOC- (dashed) OFETs with Au source/drain contacts is presented in figure 3. It can be seen that the TOC-transistor has a slightly greater drain current than the BOC-transistor in spite of the long path of the carriers. 2D calculations have shown that such behaviour takes place if the work function of source/drain contacts is less than 4.8 eV. In addition, the current doesn't flow through BOC-transistors for the work function equal 4.3 eV. We have observed such behaviour of the BOC-transistors for OFETs with Al-contacts.

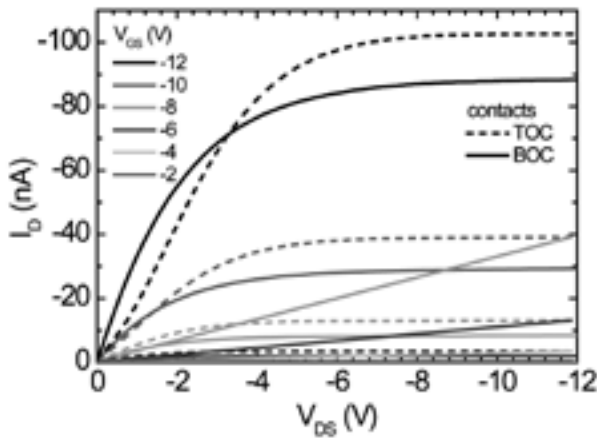


Fig. 3: Output characteristics of the BOC- (solid) and TOC- (dashed) OFETs with Au source/drain contacts.

The non-linearity in output characteristics exists only for TOC-OFETs. This can be seen more clearly in figure 4. The drain conductance has a maximum for TOC-transistor, in contrast to the BOC-transistor. Therefore, the Poole-Frenkel effect does not dominate over other effects in both OFET-designs. In our opinion, possible reasons for the observed non-linearity in the output characteristics of the TOC-transistors are: i) traps or/and ii) the anisotropy of the carrier mobility in P3HT, resulting in increased series resistances. It is difficult to separate these effects because of the absence of additional information about the P3HT layers, regarding, e.g., trap concentration, trap energy level/distribution, doping level, work function of P3HT.

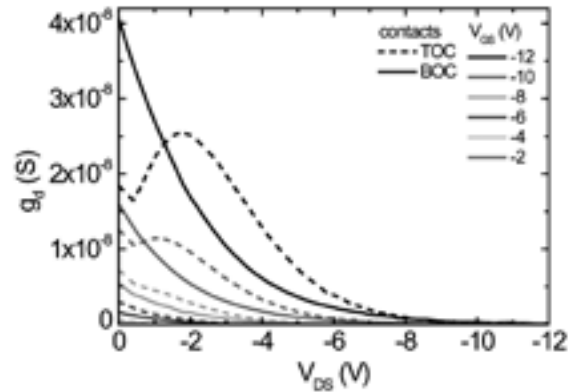


Fig. 4: Drain conductance of the BOC- (solid) and TOC- (dashed) OFETs with Au source/drain contacts.

As a result of this investigations we conclude, that the contact material and design change essentially electrical properties of the OFETs: i) BOC-transistors with Alcontacts do not work because of Schottky contact formation and ii) BOC-transistors with Audrain/source contacts do not have any non linearity in output characteristics.

[1] Janos Veres, Simon Ogier, and Giles Lloyd, Chem. Mater. 16, 4543 (2004).

[2] P. Stallinga, H. L. Gomes, F. Biscarini, M. Murgia, and D. M. de Leeuw, J. Appl. Phys. 96, 5277 (2004).

[3] Gilles Horowitz, Mohsen E. Hajlaoui, and Riadh Hajlaoui, J. Appl. Phys. 87, 4456 (2000).

A New Type of Highly Sensitive Portable Ozone Sensor Operating at Room Temperature

Ch. Y. Wang*, V. Cimalla, C.-Ch. Röhlig, Th. Stauden, and O. Ambacher

Department of Nanotechnology

Motivation

Air pollution sensors are highly demanded for environmental protection. Highly sensitive, easy-to-operate and low-cost ozone (O_3) sensors are required for two reasons. The first one is the usage of ozone as a sterilization and deodorization gas in industry. Another one is the detection of O_3 in atmosphere, especially, in life environment (e.g. in the case of office photocopiers and laser printers) [1]. Furthermore, in the last decades, O_3 usage is expanding rapidly in various fields such as water supply, fish farming, food storage and air sterilization. On the other hand, ozone is harmful to humans due to its strong oxidizing power [1]. Thus, the spatial and time control of ozone concentration in the life environment is on demand requiring effective O_3 sensors operating at room temperature.

Conventional ozone sensors operate at high temperatures of more than 200°C requiring a heating system causing high cost and high power consumption [1]. If one thinks of a large area ozone registration or miniaturized portable systems, high temperature sensors are not an optimal solution for such applications. Recently, room temperature monitoring of ozone has been achieved by usage of indium oxide (In_2O_3) thin films as a sensing material. Instead of thermal energy provided by a heating system, the sensing thin films are activated by ultraviolet (UV) light [2]. With such concept, the ozone sensors with less power consumption leading to low cost can be miniaturized with integrated UV light emitting di-odes (LED).

In this work, we use In_2O_3 thin films grown by metal organic chemical vapor deposition (MOCVD) as the ozone sensitive material. Such sensors are exposed to ozone with concentrations from 15 ppb to 90 ppm. The temperature dependence of the sensitivity to ozone is tested.

Technology

The films were grown in a horizontal MOCVD reactor (AIXTRON 200) at 600°C . Trimethylindium and water vapor were used as indium and oxygen sources, respectively. The films were characterized *ex situ* by X-ray diffraction (XRD, θ - 2θ scans) and scanning electron microscopy (SEM). The ozone sensing experiments were carried out in self-build vacuum equipment consisting of two separated parts: a chamber for ozone generation provided by UV

irradiation of oxygen flow at $\lambda \sim 254$ nm and a chamber for ozone detection where the In_2O_3 sensors were mounted on a ceramic substrate holder. To conduct the temperature dependence measurement a heat-ing-chip were mounted on the backside of the In_2O_3 sensor.

Experiments

Highly textured $\text{In}_2\text{O}_3(100)$ films were obtained by using a low temperature In_2O_3 nucleation. Cu $K\alpha$ x-ray diffraction pattern of the as deposited In_2O_3 films (Fig. 1 (a)) revealed two peaks at 35.49° and 54.46° , corresponding to the (400) and (600) diffraction peaks of body-centered cubic indium oxide. In the SEM micrographs (Fig. 1 (b)), well developed grains ($>1 \mu\text{m}$) with misorientations are visible. Such grains are in-plane rotated by 30° with respect to each other. Details related to the formation mechanism of such 30° in-plane rotated grains are described in the previous publication [3].

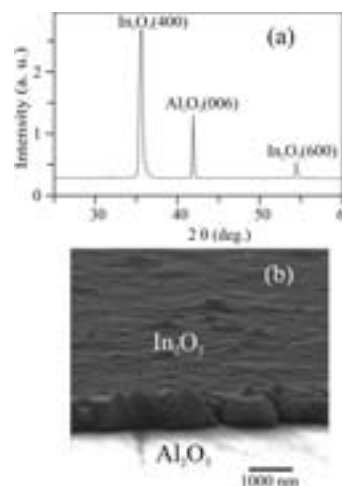


Fig. 1: (a) Cu $K\alpha$ X-ray diffraction pattern of In_2O_3 films. (b) SEM image of 80° tilted In_2O_3 film.

To improve the In_2O_3 resistivity, the films were annealed in the oxygen atmosphere at 1200°C for 1 minute. The photoreduction/oxidation cycles shown in figure 2 (a) were performed by an exposure of the sensor to Xe lamp radiation and varying the O_3 concentration from 15 ppb up to 92 ppm, respectively. The recovery time after UV light exposure (defined as the time from 90% to 10% of the final values) was about several ten seconds.

But the response time (defined as the time from 10% to 90% of the final values) after introducing O_3 into the chamber was about several hours at low O_3 concentrations (Fig. 2 (a)). The slow response was caused by the slow absorption-desorption process at room temperature. In order to develop an O_3 sensor for practical applications, we have just stopped the oxidation measurements after twenty minutes. The sensitivity ($S=R_{\text{ozone}}/R_{UV}$) was calculated with the resistance after 5-minutes oxidation (R_{ozone}) and the final resistance value after photoreduction (R_{UV}). The corresponding sensitivity (Fig. 2 (b)) revealed a linear dependence on the O_3 concentration (C_{O_3}) in double logarithmic scale ($S \propto C_{O_3}^{1/4}$). The response time after O_3 exposure in dependence of O_3 concentration ($\tau_{\text{response}} \propto C_{O_3}^{-1/2}$) is shown in figure 2 (c). At low O_3 concentrations, the sensors need several tens of minutes to response, whereas at high O_3 concentration, the response time is only about one minute. Furthermore, such dependence like, $S, \tau_{\text{response}} \propto C_{O_3}^{-1/m}$ can be explained by the law of mass action [4].

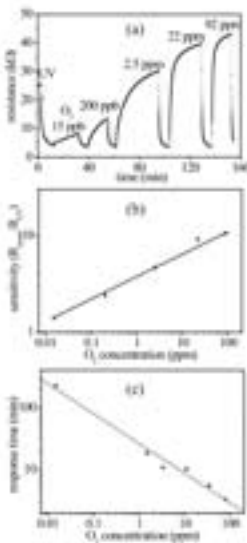


Fig. 2: (a) Resistance change of In_2O_3 films at different O_3 concentrations. (b) O_3 sensitivity at different concentrations. (c) Response time at different O_3 -concentrations.

The dependence of the sensitivity on operating temperature is plotted in figure 3. The sensitivity reduces from ~ 13 to ~ 6 by increasing the operating temperature from $20^\circ C$ to $250^\circ C$. The observed reduction of the film sensitivity is directly related to an increase of the resistance after UV light illumination. The film resistance after oxidation, however, did not exhibit significant temperature dependent changes. These observations can be explained by the following two facts. Firstly, the lattice scattering resulting from thermal vibrations of the lattice atoms

leads to a decrease of electron mobility by increasing temperature ($\mu \propto T^{-3/2}$) [5]. As a consequence, the resistance ($R \propto 1/en\mu$) increases with increasing temperature after electron generation by UV illumination. But, the resistance remains constant notwithstanding the temperature variation after oxidation due to lack of oxygen vacancies. Secondly, the physisorbed oxygen molecules can be ionized by absorbing thermal energy. The chemisorbed ionized oxygen molecules can absorb the thermal energy to be bound to a lattice site by overcoming the related energy barrier at high temperatures [1]. Thus, on one hand, the number of free electrons decreases at high temperatures than at low temperatures after illumination. On the other hand, less oxygen vacancies can be generated by UV irradiation due to existence of less unstable oxygen molecules at high temperatures. From these observations, it can be concluded that such In_2O_3 films show their largest response to ozone at room temperature indicating that In_2O_3 based sensors can be operated at ambient temperatures without additional heating.

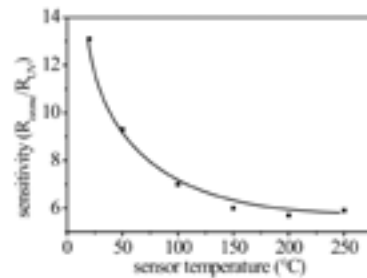


Fig. 3: Temperature dependence of the sensitivity to 90 ppm O_3 .

Conclusions

In summary, by using the MOCVD method, we synthesized highly textured $In_2O_3(100)$ thin films as an active material for ozone sensors. The ozone sensing properties were evaluated. The minimal detected ozone concentration was about 15 ppb. Ozone with a wide range of concentration (about 4 orders of magnitude) was measured with a sensitivity dependent on ozone concentration ($S \propto C_{O_3}^{1/4}$). The temperature dependence of the sensitivity revealed that such sensors should be operated at room temperature resulting in low cost and low power consumption. It is feasible to develop a portable ozone sensor by using In_2O_3 .

This work was supported by Thüringer Ministerium für Wirtschaft, Technologie und Arbeit (TMWTA) within the project "INOZON" under grant no. 2011420176.

[1] T. Seiyama, Chemical Sensor Technology, Vol. 2, Kodansha LTD., Tokyo, 1988.
 [2] M. Bender, N. Katsarakis, E. Gagaoudakis, E. Hourdakis, E. Douloufakis, V. Cimalla, and G. Kiriakidis, J. Appl. Phys. 90 (2001) 5382.
 [3] Ch. Y. Wang, V. Cimalla, H. Romanus, Th. Kups, G. Ecke, Th. Stauden, M. Ali, V. Lebedev, J. Pezoldt, and O. Ambacher, Appl. Phys. Lett. in press.
 [4] G. Heiland, Sensors and Actuators, 2 (1982) 343.
 [5] J. Bardeen and W. Shockley, Phys. Rev. 77 (1950) 388.

SiC-Based MOSFET for the Detection of NO_x , D_2 , and O_2 -Gases using $\text{In}_y\text{V}_x\text{O}_x$ as a Gate Material

M. Ali^{1,*}, Ch. Wang¹, V. Lebedev¹, Th. Stauden¹, V. Cimalla¹, G. Ecke¹, V. Tilak², P. Sandvik², and O. Ambacher¹

¹ Department of Nanotechnology

² General Electrics, Niskayuna, USA

Introduction

In recent years much attention has been focused on the role of NO_x containing gases and their detection and measurement in urban air quality due to automotive and industrial emissions. Nitrogen oxides, especially NO_x (mixture of NO and NO_2) which are found in the combustion exhaust of automobiles and oil-burning power plants are acutely toxic gases that cause problems such as acid rain, and the formation of photochemical smog. Hence, detection and emission control of toxic NO_x is of great importance. SiC-based sensors that can be used at high temperature and in corrosive atmosphere have been under development for this purpose. Electronic devices based on SiC can function as chemical sensors after deposition of a catalytic material as well as a thin insulating layer on their surfaces. The catalytic material can be a metal such as Pt, Pd, Ir, or combinations of these [1-3]. Metal oxides can also be used as catalytic layers on these devices [4-5]. The field effect transistor (FET) is the most complicated device design tested to date. However, it has a highly reliable design for gas sensors applications. In traditional FETs, small voltages applied to the gate contact can control large currents that pass through the channel between the source and drain contacts. In the case of sensor applications, the small changes induced in the catalytic metal by the reactant gases can cause large changes in the source-drain current, which makes this device a very sensitive sensor. In this paper the NO_x sensing properties of SiC-based FETs with $\text{In}_y\text{V}_x\text{O}_x$ metal oxides as a catalytic gate have been investigated as a function of the operation temperature and partial pressure. In order to study the selectivity to NO_x the cross sensitivity to other oxidizing gases such as O_2 and reducing gases such as D_2 is investigated. By choosing the appropriate temperature, devices with optimized selective sensitivity to certain gases have been realized.

Experiments

The design of the sensor is shown in figure 1. The structure includes a SiC-based FET with $\text{In}_y\text{V}_x\text{O}_x$ gate as a gas sensitive layer. The sensor was realized using n-type 4H-SiC substrates, a 4 μm p-type ($N_A=5\times 10^{15} \text{ cm}^{-3}$) epitaxial layer, and a 0.25 μm

n-type ($N_D=1\times 10^{17} \text{ cm}^{-3}$) epilayer. The device fabrication process utilized mainly conventional process steps, including mesa isolation, source and drain implantation, and a field oxide deposition using a thermal oxidation. Ohmic contacts were fabricated using Ni metal followed by a rapid thermal annealing. Finally, a 100 nm thick $\text{In}_y\text{V}_x\text{O}_x$ gate electrode was deposited by simultaneous co-sputtering of indium and vanadium oxides. Detailed information on the fabrication process can be found elsewhere [6-7]. For gas sensing tests, the sensors were placed into a quartz tube which was evacuated to a base pressure of 4×10^{-8} mbar. Current-voltage (I-V) characteristics have been carried out at different concentrations of test gases (NO_x , O_2 , and D_2) above the sensors which were heated during operation at different temperatures using a furnace. The temperature was measured by a thermocouple placed a few millimetres above the sensor. In all cases, the applied source-drain voltage varied between 0 V and 20 V in steps of 40 mV, while the respective values of the current were measured.

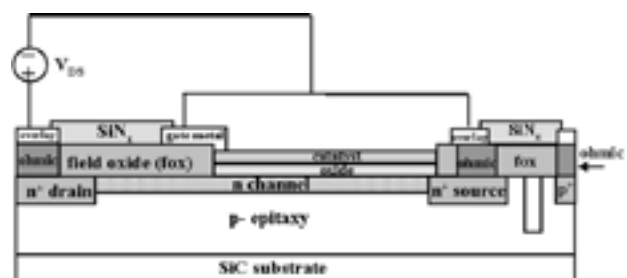


Fig. 1: Design of the SiC-based FET. The active and total area are $450 \times 9 \mu\text{m}^2$ and 1 mm^2 , respectively.

Results and Discussion

In the first step the sensors were tested for the response to NO_x gas with concentrations starting from 2 ppm and going up to 2010 ppm (pure NO_x) in vacuum at temperatures between 230°C and 400°C . Figure 2 shows the I-V characteristics of a SiC-based FET sensor in vacuum and in the presence of 2 ppm of pure NO_x at 300°C . It is obvious that the exposure of the sensor to the oxidizing gas NO_x results in a

decrease of the source-drain current. The response to NO_x can be understood by considering the interaction between NO_x and InV_yO_x . NO_x molecules will affect the effective work function of the gate and thus change the current through the transistor. If NO_x molecules are introduced between the catalyst and insulator, the difference of work function of the catalyst (metal oxide) and the semiconductor, $\Phi_{MS} = \Phi_M - \Phi_S$, changes upon chemical reactions on the surface interface, causing a shift in the threshold voltage V_T . This would affect the source-drain current I_{SD} in the linear region of the transistor ($V_G \ll V_{SD}$) according to:

$$I_{SD} = \mu C_i \frac{W}{L} (V_G - V_T) V_{SD} \quad (1)$$

where μ is the electron mobility in the channel, C_i is the insulator capacitance per unit area, W/L is the channel width-to-length ratio, V_G and V_{SD} are the applied gate-source and source-drain voltages, respectively, and V_T is the threshold voltage. The increase of work function will cause a decrease in source-drain current. This is because the threshold voltage depends on the difference between the Fermi level in the semiconductor and the catalyst. As the work function increases the threshold voltage increases and the current decreases as the $(V_G - V_T)$ value gets lower.

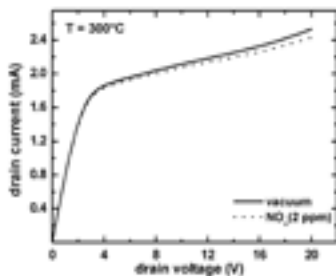


Fig. 2: I-V characteristics of the sensor operated at 300°C in vacuum (solid line) and in the presence of 2 ppm of pure NO_x (dotted line).

In order to study the selectivity to NO_x the sensors were tested for the response to other gases such as deuterium with concentrations between 12 ppm and 5180 ppm (pure D_2) at temperatures between 25°C and 350°C, and O_2 with concentrations starting from 2 ppm going up to 3030 ppm (pure O_2) at temperatures between 250°C and 400°C. The exposure of the sensor to reducing gases such D_2 results in an increase of the source-drain current due to a decrease in the work function of the catalytic gate. As a consequence a decrease in the threshold voltage of the FET is measured.

The dependence of the sensitivity towards 100 ppm, 500 ppm and 1000 ppm of pure NO_x , O_2 , and D_2 on the operating temperature is presented in figure 3. In this work, we have defined the sensitivity as the relative current variation at constant voltage expressed in percent:

$$S = \frac{I_g - I_v}{I_v} \times 100 \quad (2)$$

Whereby I_g and I_v are the current of the sensor in the presence of gas and in vacuum, respectively.

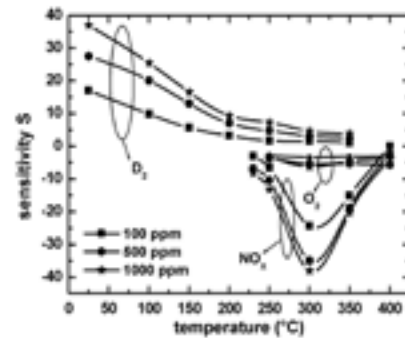


Fig. 3: The dependence of the sensitivity towards 100 ppm, 500 ppm and 1000 ppm of pure NO_x , O_2 , and D_2 on the operating temperature. The measurements were performed at a constant voltage of $U_{SD} = 14$ V.

It becomes obvious from figure 3 that the optimum detection temperatures occur in the range of 275°C-325°C for NO_x . In this range the cross sensitivity to O_2 and D_2 is very low indicating that the sensor is very suitable for selective detection of NO_x . The optimum temperature for detection of deuterium is determined to be between 25°C-100°C, considering the sensitivity and the response time. In this range no significant response to O_2 and NO_x is observed indicating that the sensor is very suitable for selective D_2 detection at very low temperatures.

This work was supported by TKM, project InOzon, and the European Union (project GaNano) NMP4-CT-2003-505641.

[1] H. Wingbrant, P. Salomonsson, D. Kubinski, J. H. Visser, M. Löfdahl, and A. Lloyd Spetz, IEEE Sensors Journal, 5 (2005) 1099.
 [2] C. K. Kim, J. H. Lee, S. M. Choi, I. H. Noh, H. R. Kim, N. I. Cho, C. Hong, and G. E. Jang, Sensors and Actuators, B 77 (2001) 455.
 [3] A. Lloyd Spetz, M. Eriksson, L.-G. Ekedahl, and I. Lundström, Conference proceeding of TAFT 2000, Nancy, France, 27-30 March (2000).
 [4] G. W. Hunter, L. Y. Chen, P. G. Neudeck, D. Knight, C. C. Liu, Q. H. Wu, H. J. Zhuo, D. Makel, M. Liu, and W. A. Rauch, NASA/TM-1998-208504.
 [5] Z. Fan, J. and G. Lu, Appl. Phys. Lett. 86 (2005) 123510.
 [6] P. Sandvik, M. Ali, V. Tilak, K. Matocha, Th. Stauden, J. Tucker, J. Deluca, and O. Ambacher, Conference proceeding of ICSCRM 2005, Pittsburgh, Pennsylvania, 18-23 September (2005).281-285.
 [7] M. Ali, V. Cimalla, V. Lebedev, Th. Stauden, G. Ecke, V. Tilak, P. Sandvik, and O. Ambacher, Sensors and Actuators B, accepted.

Photometric Measurements in Micro- and Nanoliter Droplets

B. Lübbers^{1,*}, G. Kittler¹, V. Cimalla¹, M. Gebinoga², C. Buchheim³, D. Wegener⁴, A. Schober², and O. Ambacher¹

¹ Department of Nanotechnology

² Junior Research Group Microfluidics and Biosensors, MacroNano[®] – Centre for Innovation Competence

³ Department of Experimental Physics I

⁴ Institute for Physical High Technology, Jena

Motivation

The analysis of liquids represents one of the most important fields in clinical and pharmaceutical laboratory everyday work and research. Optical detection is mainly performed using photometry. Common analysis systems utilize cuvettes with a typical volume of a few 100 μl or are based on closed fluidic systems (lab-on-a-chip). With regard to cost and analysis efficiency the reduction of sample volume is of great interest [1].

We present a setup for photometric measurements in an open fluidic system for micro- and nanoliter droplets. The setup is part of a novel integrated GaN-based system for physical, biological and chemical analysis. Combined with a transparent AlGaIn/GaN-based pH-sensor [2] it will allow simultaneous electronic and optical analysis of droplets.

Theory

Photometry is based on the Lambert-Beer-Law and is used to determine substance concentration in liquids, gases and solids. The concentration c can be calculated by:

$$c = \frac{-\log\left(\frac{I}{I_0}\right)}{\alpha_\lambda \cdot d} \quad (1)$$

with I being the transmitted light intensity, I_0 the incident intensity, α_λ the absorption coefficient at wavelength λ and d the optical pathlength.



Fig. 1: Model of droplet geometry.

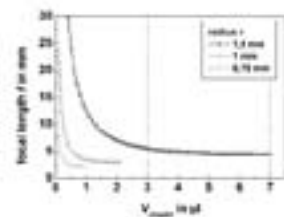


Fig. 2: Calculated focal length for different droplet volumes V_{droplet} and radius r .

The main difficulty when measuring absorption in droplets arises from the shape of the droplet influencing the light path due to refraction. To account for this influence a model (Fig. 1) for describing the focal length as a function of droplet volume V_{droplet} and radius r is derived. The height of the droplet and therefore the optical pathlength is given by:

$$h = \frac{r^2}{\sqrt{\frac{3 \cdot V_{\text{droplet}}}{\pi} + \sqrt{\frac{9 \cdot V_{\text{droplet}}}{\pi^2} + r^4}}} - \sqrt{\frac{3 \cdot V_{\text{droplet}}}{\pi} + \sqrt{\frac{9 \cdot V_{\text{droplet}}}{\pi^2} + r^4}} \quad (2)$$

With this the focal length of a water droplet is calculated by:

$$f = \frac{3 \cdot (h^2 + r^2)}{2 \cdot h} \quad (3)$$

where h is the height of the droplet. This relationship is shown in figure 2.

Experiments

A combination of an InGaIn laser diode emitting at 415 nm and a novel selective sensitive InGaIn photodetector [3] is used to measure optical absorbance by droplets (Fig. 3). The sample droplet is pipetted and positioned manually in the collimated laser beam. The detector optics were adjusted for each droplet volume to focus the transmitted light onto the detector.

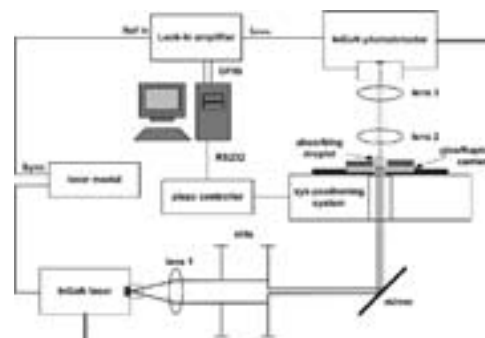


Fig. 3: Experimental setup for optical analysis of water based droplets.

Positioning accuracy, droplet evaporation and the regulation of humidity as well as the influence of light, temperature and electromagnetic fields limit the accuracy and sensitivity of the setup. To guarantee reproducibly formed droplets a polyimide film with a thickness of $125\ \mu\text{m}$ was structured onto a glass carrier (Fig. 4). The positioning of the droplet with respect to the laser beam was performed by a piezodriven xyz-positioning system. Droplet evaporation was limited by installing the setup into a glove-box and increasing the humidity to 70%rH. Ambient light had no influence on the detector signal due to bandpass like sensitivity of the employed InGaN photodetector. Changes in ambient temperature resulted in fluctuations of the measured signal as the laser diode was not stabilized. They were minimized by the temperature control of the glove-box. High frequency electromagnetic interference from the pulsed laser diode could only be suppressed partially and turned out to be the limiting factor for measuring high absorbance. The temporal stability of the detector signal was measured for different droplet volumes over several minutes and was determined to be $\pm 1\%$ (Fig. 5). The reproducibility of the measurements was approximately $\pm 2\%$. This is mainly due to manual dosing and the fluctuations in droplet volume connected to it. Future measurements will be carried out with an ink-jet like dosing system and should improve reproducibility.

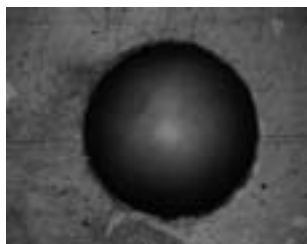


Fig. 4: Structured polyimide film with a $5\ \mu\text{l}$ droplet of water.

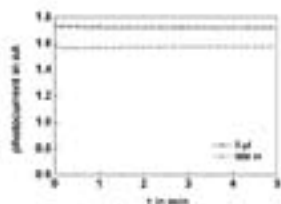


Fig. 5: Stability of detector signal for different droplet volumes.

Paranitrophenol (Sigma-Aldrich) was used as a model system for photometric measurements. This dye is released in various enzymatic assays and can also be used as a pH indicator. $2\ \mu\text{l}$ droplets of paranitrophenol dissolved in a citric acid/tris-bis propane buffer were measured for different concentrations. To calculate the concentration the absorption coefficient at $415\ \text{nm}$ was measured with a spectrophotometer and the optical pathlength was estimated using equation 2. It was noticed that the error in calculated concentration increases dramatically for absorbance lower than 0.1 (Fig. 6). Therefore, the working range of this experimental

setup is from 0.1 to 1 absorbance with an error of less than 10%. It could be noticed that in this range the measurements agreed very well with values obtained by a state-of-the-art photometer (Fig. 7).

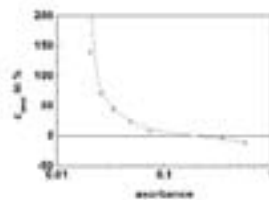


Fig. 6: Error in measured concentration with regard to droplet absorbance.

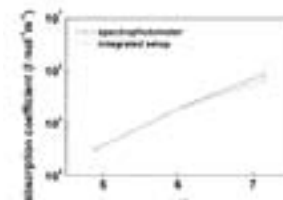


Fig. 7: Measured absorption coefficient of paranitro-phenol for different pH-values of the droplets.

The setup was sufficiently stable to observe the dynamic of chemical reactions. The release of paranitrophenol in an enzymatic assay was measured and the reactivity of the enzyme was determined (Fig. 8).

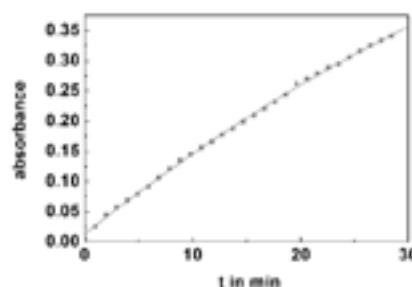


Fig. 8: Increase of absorbance due to release of paranitrophenol during enzymatic conversion of acetylparanitrophenyl-phosphat.

Conclusions

The developed fluidic setup is capable of measuring absorbance in μl - and sub- μl -droplets. Stable and reproducible measurements of dye concentration were made between 0.1 and 1 absorbance. Dynamic chemical reactions in μl reaction volumes could be monitored.

This work was supported by the Thuringian Ministry of Culture (TKM) and the European Union (EFRE program: B 678-03001, 6th framework program: GaNano NMP4-CT2003-505614).

- [1] N. Lion, F. Reymond, H.H. Girault and J.S. Rossier, *Current Opinion in Biotechnology*, 15, 31 (2004).
- [2] R. Neuberger, G. Müller, O. Ambacher, and M. Stutzmann, *phys. stat. sol. (a)* 185, 85 (2001).
- [3] C. Rivera, J.L. Pau, F.B. Naranjo and E. Munoz, *phys. stat. sol. (a)* 201, 2658 (2004).

Monitoring of Bioreactions by GaN-Based pH-Sensors

G. Kittler^{1,*}, A. Spitznas¹, B. Luebbers¹, V. Lebedev¹, D. Wegener², M. Gebinoga³, A. Schober³, and O. Ambacher¹

¹ Department of Nanotechnology

² Institute of Physical High Technology, Jena

³ Junior Research Group Microfluidics and Biosensors, MacroNano[®] – Center for Innovation Competence

Introduction

Group-III nitrides are known to be a suitable material system for microelectronic devices and sensors. Their outstanding properties like high chemical stability, optical transparency in the visible range, and high spontaneous and piezoelectric polarization offer a huge variety of applications like surface sensitive sensors, high electron mobility transistors (HEMT), and light emitting diodes (LED) or lasers (LD) [1].

The gradient of spontaneous and piezoelectric polarization at the AlGaN/GaN-interface leads to a two-dimensional accumulation of electrons with high sheet carrier concentration. In our experiments we used the feasibility to manipulate the carrier density within the two-dimensional electron gas (2DEG) by changing the surface potential caused by different concentrations of ionic solutions. The principle of such ion-sensitive field effect transistor (ISFET) was described by Bergveld [2]. First pH-measurements with GaN-based structures were reported by Steinhoff [3] and theoretical described by Bayer [4]. According to the site dissociation theory [5] amphoteric hydroxylgroups are responsible for the ion-sensitive response of sensor structures. These groups can be either protonated or deprotonated leading to a change in surface potential. In recent years GaN-based sensors were used for measuring cell action potential [6] or to detect proteins [7]. We describe the use of such AlGaN/GaN heterostructures for monitoring a lipase based enzymatic reaction by measuring the pH. Lipases are the most versatile biocatalysts used for many biotransformation reactions such as alcoholysis, acidolysis, and hydrolysis. [8]

Experimental

The AlGaN/GaN-heterostructures were grown by plasma-induced molecular beam epitaxy. A 25 nm thick Al_{0.25}Ga_{0.75}N barrier layer was grown on a GaN bulk layer. These heterostructures were capped by 2 nm GaN. Metal contacts consist of 20 nm Ti, 80 nm Al, 30 nm Ti, and 100 nm Au. Contacts were passivated by solder stop resist to avoid electrochemical reactions. The schematic view of this sensor structure is depicted in figure 1. The sensors were placed in Petri dishes and passivated by a silicone glue. A Ag/AgCl reference electrode were connected by an ion-conducting gel with the liquid.

The experiments were performed in constant current mode, i.e. during an experiment the drain current I_{DS} was kept constant by controlling the reference potential V_{Ref} . The sensor calibration and determination of sensitivity were carried out by recording transfer characteristics in buffer solution at pH=4 and 7 before and after each experiment series. All measurements were done at room temperature.

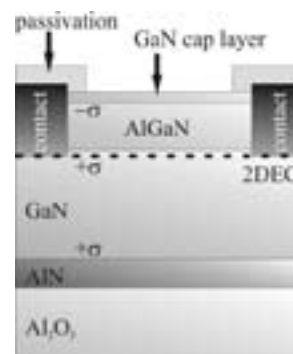


Fig. 1: Schematic view of an AlGaN/GaN-based pH-sensor.

In our experiments 5 μ l lipase from *pseudomonas fluorescens* reacted with 30 μ l 4-nitrophenyl caprylate solution (1 mM in 1 mM BES buffer) as a substrate, which was cleaved by the enzyme to produce caprylic acid and para-nitrophenol. The increase of caprylic acid leads to a drop of pH-value.

In order to investigate the reaction kinetics we used different diluted lipase solutions (1:20 and 1:40). The lipase assay was cross checked at equal conditions with denaturated lipases and buffer without the lipase enzyme, respectively.

Results and discussion

The pH-sensor was calibrated by measuring the transfer characteristic at $V_{DS} = 0.3$ V for pH buffer solution with pH=4 and pH=7. The sensitivity was constant at $S=50.15 \pm 0.05$ mV/pH, calculated from the shift of transfer characteristics parallel to the V_{Ref} -axis. The characteristics are presented in figure 3.

The 4-nitrophenyl caprylate solution was pipetted onto the active area of pH-sensor. After 1 minute, 5 μ l of lipase from *pseudomonas fluorescens* were added. After a short increase of pH value the concentration

of oxonium ions started to increase resulting in a decrease of pH as expected.

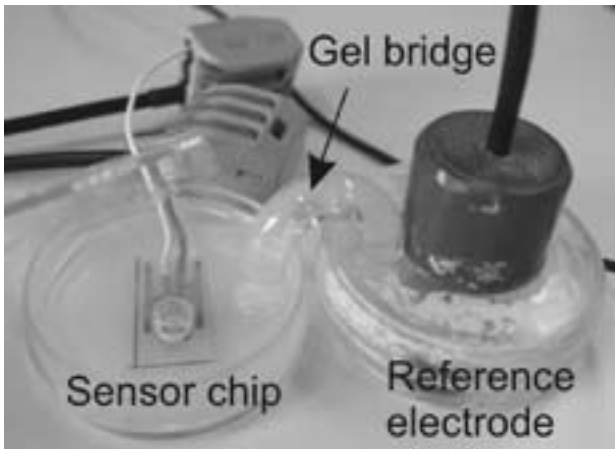


Fig. 2: Measurement setup for lipase assay.

The measurements were reproducible as shown in figure 4. The curves were normalized for easy comparison. The pH change was about 0.9. A further dilution of the lipase from 1:20 to 1:40 resulted in a slower reaction kinetics. The flatter slope of the measured characteristic is clearly seen in figure 4.

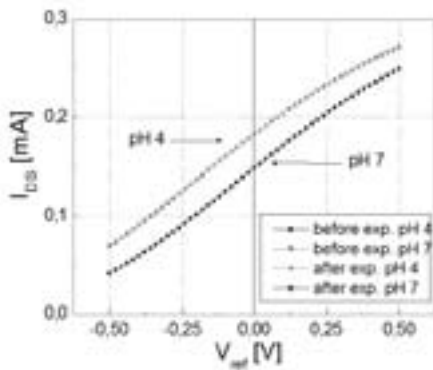


Fig. 3: Transfer characteristics of pH-sensor to determine sensitivity.

The experiment was cross checked by adding denatured lipase. Therefore the lipase was heated up for 10 min to 95 °C. No characteristic decrease in pH was observed, but also a short signal increase after adding heat inactivated lipase was measured indicating that this is caused most likely by the buffer solution of lipase.

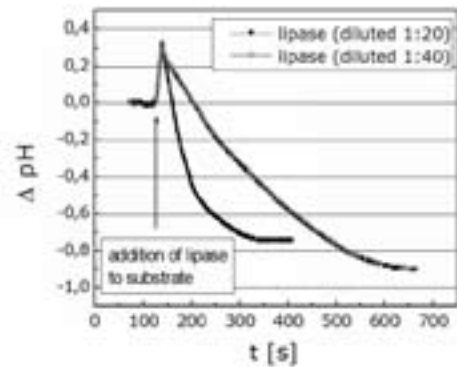


Fig. 4: Change of pH after adding lipase.

Besides acid this assay simultaneously produces the pH-sensitive dye para-nitrophenol, which allows monitoring the same reaction by the change in colour of the reaction solution. Absorption measurement with this assay showed a decreased photocurrent of about 50%. Because of the change in absorption and the optical transparency of the material system at visible wavelength it is possible to monitor the lipase reaction by a combined optical and electrical measurement.

Conclusion

We used AlGaIn/GaN-heterostructures with a 2 nm thick GaN cap layer to measure the change in pH-value during a lipase bioreaction. The change in pH was about 0.9. Time depending measurements showed different reaction kinetics for different lipase concentrations. GaN-based pH-sensors are well suited for monitoring lipase related bioreactions and offer the possibility to combine electrical and optical measurements.

This work was supported by the Thuringian ministry of culture (TKM) and the European Union (EFRE program: B 678-03001, 6th framework program: GaNano NMP4-CT2003-505614).

[1] O. Ambacher, J. Phys. D: Appl. Phys. 31, 2653–2710, (1998).
 [2] P. Bergveld, IEEE Trans. Biomed. Eng. 17, 70, (1970).
 [3] G. Steinhoff, M. Hermann, W. J. Schaff, L. F. Eastman, M. Stutzmann, and M. Eickhoff, Appl. Phys. Lett. 83, 177 (2003).
 [4] M. Bayer, C. Uhl, and P. Vogl, J. Appl. Phys. 97, 033703, (2005).
 [5] P. Bergveld, A. Sibbald, Compr. Analyt. Chem. Vol. 23, Elsevier (1988).
 [6] G. Steinhoff et al., Appl. Phys. Lett. 86, 033901, (2005).
 [7] B. S. Kang et al., Appl. Phys. Lett. 87, 023508, (2005).
 [8] K. E. Jaeger, T. Eggert, Curr. Opin. Biotechnol. 13 (4), (2002).

Design, fabrication and test of a 3D biosensor for impedance spectrometry

M. Fischer^{1,*}, D. Kloß², and A. Robitzki²

¹ MacroNano® - Center for Innovation Competence

² Division of Molecular Biological - Biochemical Processing Technology, Leipzig University

Introduction

To establish a representative model for effective drug testing *in vitro*, tumour cells are cultured as multicellular aggregates. Thereby the 3D structure of primary tumours and metastases is mimicked *in vitro*. Because of the spheric shape they are called tumour spheroids. Cellular membranes display electric charges in a range of about 60 kHz to 5 MHz that cause β -dispersions [1]. Within this frequency range modifications in dielectric properties of cells such as alterations in proliferation, differentiation and apoptotic processes can be measured. It has been shown in a number of previous studies that changes in cell membranes [2], cytoskeleton [3] or formation of cellcell contacts [4] are detectable independently from the size of the spheroids [5].

The noninvasive monitoring subsequently allows for the collection of tumour spheroids for molecular biological analysis which enables the correlation of impedimetric data with cellular processes, especially in terms of external signals.

To optimise impedance spectrometry- based non-invasive realtime measurement of 3D cellular cultures a new biochip was designed by the department of Prof. A. Robitzki at Leipzig University. The Center for Innovation Competence was assigned to realize the fabrication of the chip mentioned above.

Figure 1 illustrates a microcavity with four gold electrodes (size 100 x 40 μm). The complete biosensor chip comprises of a silicon substrate with 15 squared microcavities of three different sizes (200, 300, and 400 μm) and a depth of 100 μm .

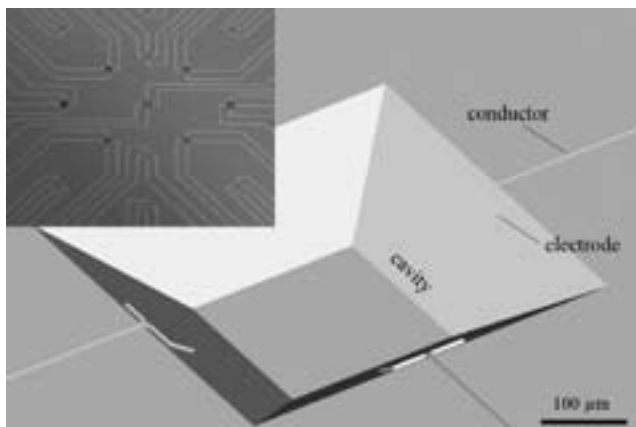


Fig. 1: Schematic drawing of a micro cavity with gold electrodes. The small image shows 15 cavities etched into a silicon substrate and gold conductors.

Technology

For an optimum yield of biochips and due to the given dimension of the test system a silicon chip size of 20 mm x 20 mm x 0.5 mm was chosen.

The mechanical fixing of the silicon chip in the carrier frame was realized by a precise silicone adhesion (Loctite 5366), which guarantees an excellent stability and tolerance at the demanded surrounding parameters (121°C, 1bar pressure, steam atmosphere etc.). The construction scheme of the test system is shown in figure2.

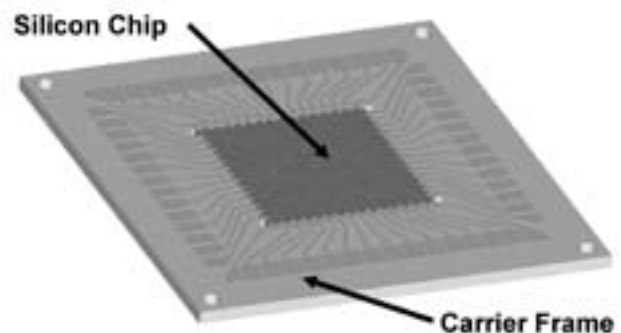


Fig. 2: Schematic of biochip test system

The electrical connection between silicon chip and carrier frame was done by wire bonding.

The silicon chip, which contains different sized cavities, is fabricated with standard MEMS technologies (see Fig. 3).

A 4"-silicon wafer is structured by wet chemical anisotropic etching (etching speed depends on the crystal direction) in a 40% KOH-solution at 90°C. The cavity structure mapped in a chrome mask was transferred into the masking material (SiO_2) by a lithography step and a SiO_2 -etching process (buffered HF-solution). Due to the crystal orientation of the silicon (100) the square holes are etched under an angle of 54.7° into the substrate (like a pyramid stump). For a good electrical insulation of the contacts which are produced afterward, the wafer is oxidized thermally after the structuring (O_2 -atmosphere, 1050°C) to obtain an 1800 nm SiO_2 -coating over the complete wafer structure. The contact pads on the side

wall of the cavities, as well as the chip conductor paths were realized with a lift off process. A special thick layer resist (All Resist GmbH) allowing lithography on structured wafer surfaces was spin coated, exposed, and developed. Afterwards a combined metal layer (10 nm titanium, 500 nm gold) was sputtered. After resist stripping good quality side wall contact pads were obtained (see figure 4). For upward passivation a silicon nitride layer (700 nm) was deposited on the complete wafer surface by a PECVD process (Plasma Enhanced Chemical Vapour Deposition) on a STS 310 (Surface Technology Systems Ltd.) at 350°C with SiH₄ and NH₃.

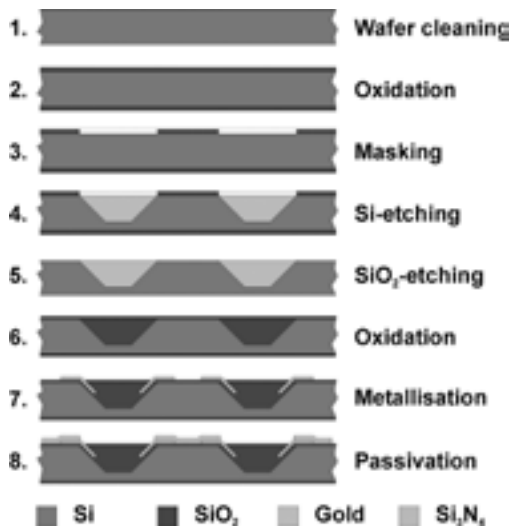


Fig. 3: Fabrication scheme of the wafer

For cell connection it is necessary to bare the cavity contact pads and the bond pads from silicon nitride. This etching step is done by a RIE process (Reactive Ion Etching) on a STS 320 (Surface Technology Systems Ltd.) with CHF₃ and CF₄ and a premanufactured resist mask.

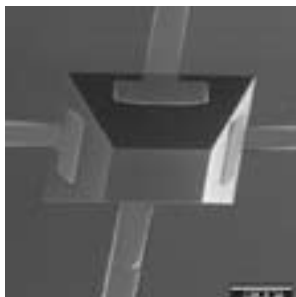


Fig. 4: Etched cavities with contact pads on the side walls

After batch processing the 4"-Wafer will be sawed to obtain 12 silicon chips. In order to connect the silicon chips to an established measuring system a

carrier system with milled cavities, goldplated pads and circuit paths made of circuit board material (FR4) was developed. After wire bonding the electrical junctions and the gap between chip and frame was sealed with silicone (Loctite 5366) by means of the commercial available dosing system dotmaster (DIMA SMT Systems) (see Fig. 5). This kind of final passivation is leak proof and stress stable during all cell cultivation operations necessary.

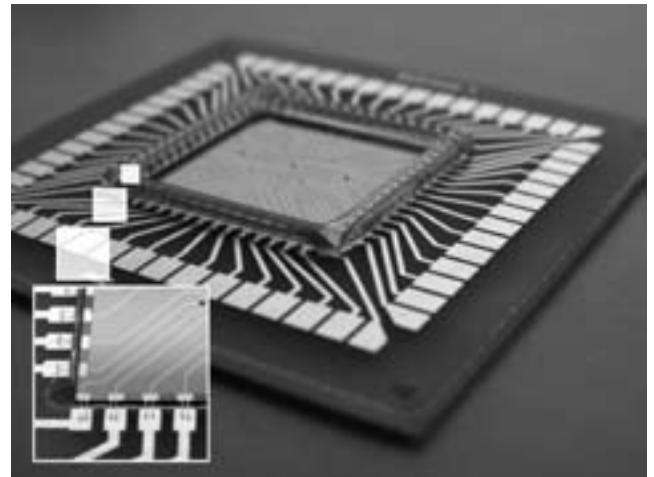


Fig. 5: Wire bonded and sealed biochip

Characterization and Discussion

Spheroids have been positioned quickly into different microcavities according to their size. Treatment of the surface to promote cell adherence was not necessary since a close contact of the tumour spheroids to the electrodes was established by forces of gravity whereby spheroids drop into the cavities. The positioning was controlled via microscopy. Thus spheroids were exactly positioned between two pairs of measurement electrodes. In this way impedance for each spheroid could be measured from two directions (between two opposite electrodes) which displayed similar values. Detectable changes in impedance signals occurred in a frequency range of 10 to 500 kHz. Due to the fact that impedimetric measurements always include summary effects over the entire cell-aggregate it is a big challenge for future work to distinguish between those multiple cellular interactions.

The current system is a time- and cost- effective diagnostic tool to distinguish between healthy and pathological tumour tissue and to provide a basis for high-content drug screening tests to specify effects of substances on cell and tissue cultures.

[1] Borkholder D.A (1998). Cell based biosensors using microelectrodes. Dissertation, Stanford University.
 [2] Paunescu T.G., Helman S.I. (2001). PGE2 activation of apical membrane Cl-channels in A6 epithelia: impedance analysis. *Biophys. J.* 81: 852-866.
 [3] Moy A.B., Van Engelenhoven J., Bodmer J., Kamath J., Keese C., Giaever I., et al. (1996). Histamine and thrombin modulate endothelial focal adhesion through centripetal and centrifugal forces. *J. Clin. Invest.* 97: 1020-1027.
 [4] Moy A.B., Winter M., Kamath A., Blackwell K., Reyes G., Giaever I., et al. (2000). Histamine alters endothelial barrier function at cell-cell and cell-matrix sites. *Am. J. Physiol. Lung Cell. Mol. Physiol.* 278: L888-L898.
 [5] Reininger-Mack A., Thielecke H. and Robitzki A. (2002). 3D-biohybrid systems: applications in drug screening. *Trends in Biotechnology* 20: 56-61.

Optical and Tactile Probing with a Focus Sensor

R. Mastyló*, E. Manske, and G. Jäger
Department of Process Measurement

The development and the wide variety of applications has already been shown for a focus sensor in combination with a nanopositioning and nanomeasuring machine (NPM) and some measurement results have been presented [1, 2]. Since then, experiments have been performed to determine the volume of a drop of fluid using the "Sessile Drop Method". Initial measurements have shown that the laser beam of the focus sensor is additionally reflected by the substrate surface starting at a critical water drop height of about $30\ \mu\text{m}$, which greatly influences the measuring signal (effect of focus carrying through to other layers). This effect caused a minimum measurable droplet volume of 20 nl. The focus carry-through could not be prevented even for anti-reflective surfaces of the droplet carrier, because of the disruptive reflections of the carrier plate. For this reason, investigations were done to reduce or eliminate these reflections. First, a droplet of immersion liquid with an index of refraction of 1.515 was analysed. This means that the carrier plate and the droplet both possess the same refractive index and it therefore demonstrated that the focus carry-through effect could be effectively suppressed. Figure 1 shows a 3D measurement of the immersion liquid droplet.

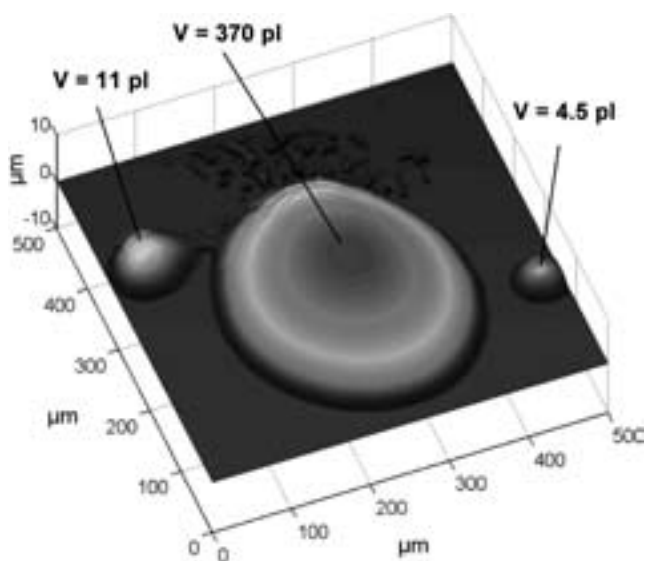


Fig. 1: Surface form and volume determination of a droplet with the help of the Nanomeasuring machine.

If water droplets are to be analysed, the carrier plate's index of refraction must be reduced to a value as close as possible to $n=1.33$. This prerequisite can be achieved using materials like artificial crystals (sodium fluoride (NaF , $n=1.32$) and magnesium fluoride (MgF_2 , $n=1.32$)).

However, a disadvantage arises when using these crystals: their good solubility in water (4.22 g and 0.002 g per 100 g, respectively). In this respect additional investigations are necessary under climate-controlled conditions (especially with high humidity).

The focus sensor is very flexible in use. As another example we built up a tactile stylus prober for application in the NPM-Machine. A MarSurf Pick-up unit MFW 1250 without internal measuring system was used. On the backside of the stylus we bonded a small piece of a polished Si-wafer. The stylus is arranged under the focus sensor which acts as zero indicator of the mechanical stylus (Fig. 2). We used a standard diamond tip ($2\ \mu\text{m}/90^\circ$) and a constant measuring force of 0.9 mN. The big advantage of this stylus arrangement is the perfect realisation of Abbe comparator principle. The deviation of the stylus is measured by the focus sensor in line to the measuring axis. We have no influence due to backlash of the pivot and we measure only in one zero position of the lever.

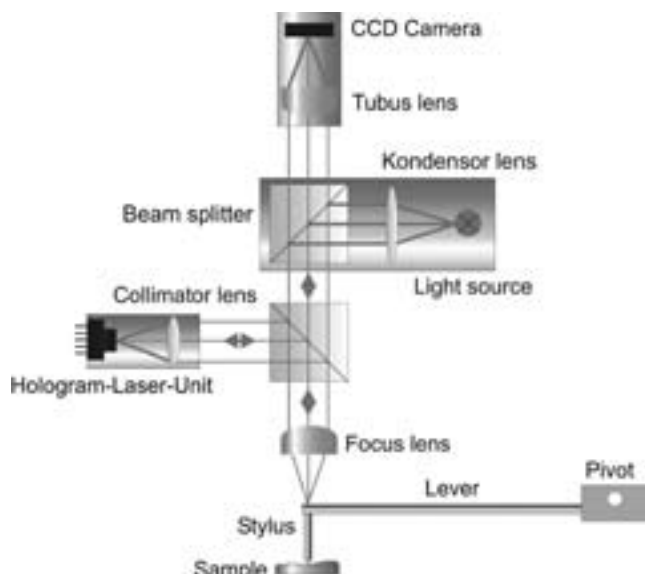


Fig. 2: Principle of the tactile stylus sensor.

Therefore, it is possible to achieve highest measurement accuracy independent of the influence of measuring force and tip geometry.

In figure 3 and 4 the measuring results of a step height standard (69 nm) and of a glass scale with a period of 8 μm is shown. In both figures no batwing effects can be seen. Furthermore the glass scale consists of coated areas with high reflectivity and uncoated glass areas with low reflectivity. The distance between the edges is 4 μm . It was nearly impossible to measure these structures with a focus sensor alone. Only the application of the stylus sensor enables such measurements. We tested different scanning speeds. Since this arrangement is a passive mechanical system the scanning speed depends on the damping of the lever and the structure geometry. We achieve normally good results with a scanning speed of 100 $\mu\text{m/s}$. To improve the measurement accuracy a next step should be the evaluation of the influence of stylus tip geometry.

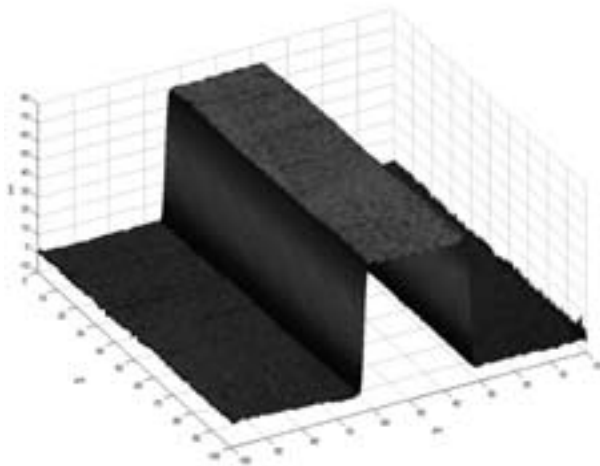


Fig. 3: Measuring of a step height standard (69 nm).

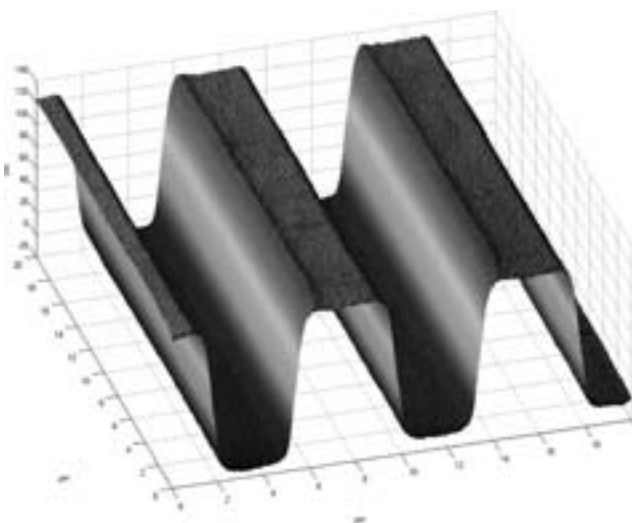


Fig. 4: Measuring of a glass scale (8 μm period).

We have also improved the behaviour of the focus probe. The NPM-Machine is able to move the measuring stage 5 mm in vertical direction. But the working distance of the existing focus sensor is only 1.8 mm. The short working distance results from the short focal length combined with a high numerical aperture. As a result step heights or contours of more than 1.8 mm height could not be measured because of the risk of collisions between specimen and objective of the focus sensor.

The laser of the focus sensor [1] is optimised for DVD-application with $\text{NA}=0.6$ and $f=3.3$ mm. The only way out is the use of a long working distance objective. This objective is characterised by a lens group that the principal plain of the objective is outside of the objective. We have chosen an objective with a working distance $\text{WD}=10.1$ mm and a numerical aperture of $\text{NA}=0.55$. Therefore, the focal spot size is 0.59 μm and only insignificant larger than the standard objective. With this objective we can use the full positioning range of the NPM-Machine of 5 mm with sufficient safety against collision.

We integrated the objective into the NPM-Machine and measured some large step heights in the millimetre range and the roughness of the surfaces in the nanometre range in one step. Besides the determination of large step heights, this objective enables also the measurement of large contours like, e.g. aspheres, contour standards, high-precision mechanical parts etc.

Another option is a combination of the focus sensor with a white-light interferometer. The white-light interference microscope is based on the CCD microscope including white light illumination of the focus sensor with a special Mirau type objective. The disadvantage of most common white light microscopes is the limited measuring range of some 100 μm and the measuring system to determine the localisation of the zero order path difference. If a white light microscope is working in the NPM-Machine the measuring range grows up to 5 mm. The fringe evaluation is based on laser interferometer accuracy in the whole range. In the next time we want to realise such kind of a white-light interferometer. However, every kind of focus sensor (tactile or optical) shows different advantages and disadvantages. The selection of the best probe depends on several parameters of the measuring task. An interesting field for the next time should be the comparison of the different optical non-contact probes and the tactile stylus as well as scanning force microscopes at different measuring specimen with the NPM Machine.

- [1] Rostyslav Mastylo, Denis Dontsov, Eberhard Manske, Gerd Jäger: A focus sensor for an application in a nanopositioning and nanomeasuring machine, Proc. SPIE Vol.5856, 2005, pp. 238-244.
 [2] Mastylo R., Manske, E.; Jäger, G.: New investigations with the nanopositioning and nanomeasuring machine in combination with a high resolution focus sensor, Jahresbericht ZMN 2004.

Micro Segmented-Flow PCR in a Helical Tube System with Asymmetric Temperature Zones

A. Brösing*, R. Hartung, and J. M. Köhler

Department of Physical Chemistry and Microreaction Technology

Introduction

Polymerase chain reaction (PCR) has emerged as a powerful tool in genetic analysis, medical diagnostics, drug discovery and biomedical screening applications. The increasing demands in these fields for analyzing a large number of samples have encouraged the development of high-throughput PCR-techniques [2, 3, 5, 7]. Based on the development of a tube-PCR-system [1, 6], we modified this system with a changed time residence of the PCR-mixture in the different temperature-zones for a high-throughput-segmented-flow application.

Design of the flow-trough system

The basic idea of this system is a circular arrangement of a teflon tube, surrounding a three-part heating element (Figs. 1a, b, and 2). The circulation of the segmented PCR-solution through the different temperature zones is effected by computer-controlled syringe-pumps. The segmentation process of the DNA-solution is carried out by a cross-shaped TEFZEL-modul. The inner diameter of the used teflon tubes range from 0.25 up to 0.5 mm.

Furthermore, there is the possibility to extend the span of the different temperature zones according to individual requirements. Otherwise the system allows the integration of a fluorescence-DNA-detection unit.

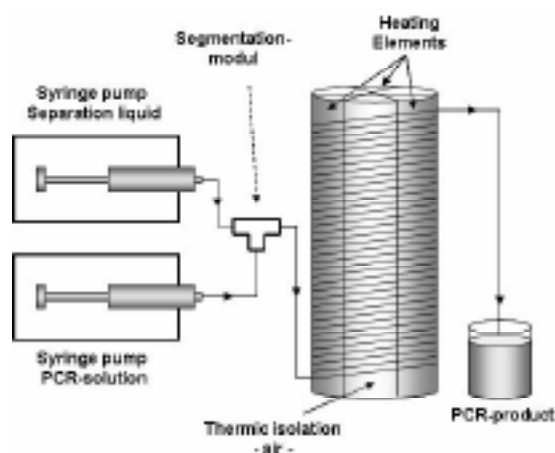


Fig. 1a: Schematic view of the experimental setup.

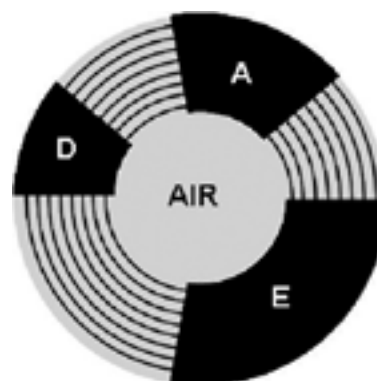


Fig. 1b: Modified ratio of the heating elements, D=Denaturation, A=Annealing, E=Elongation.

Based on this experimental setup it is possible to generate high-frequently large scaled reproducible results with a minimum of time and amount of chemicals.

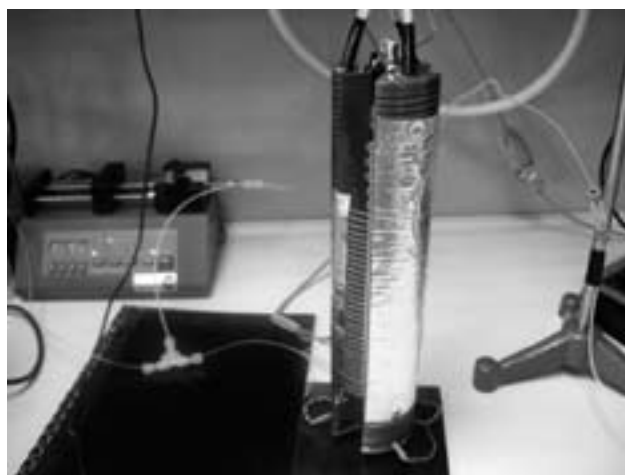


Fig. 2: Modified helical tube-PCR-system.

Material and methodes

DNA and primer:

For the PCR-approach we used a DNA-template from phage Lambda. The used primer amplifies for a 292bp-fragment, as well as a 1025bp-fragment.

The volume of the PCR-mixture was 50 μ l. It consists of:

- 2 mM MgCl₂,
- 200 μ M of each dNTPs,
- 30 ng template,
- 0.4 nM of each primer,
- 10 ng/ μ l BSA,
- 2.5 units polymerase

Temperatures:

The temperatures was set at:

- denaturation 94°C
- annealing 42°C
- elongation 72°C

For the Segmentations-process we used PP9 (Perfluormethyldecalin).

Results

The work with the modified tube-PCR-system clearly showed the possibility to amplify small and also large templates within very short time scales (Tab. 1) and 30 cycles. The ratio of the residence time in the different temperature zones was 2:3:5 (Denaturation: Annealing: Elongation).

flow rate (μ l/min)	residence time in the temperature zones			amplification
	Denat.	Anneal.	Elong.	
10.5	22''	33''	55''	(1025 bp)
14.0	18''	27''	45''	(292 bp)
30.0	8''	12''	20''	(292 bp)

Tab. 1: Residence time distribution.

A flow speed of 2.3 mm/s results in a flowrate of 30 μ l/min at an inner diameter of the tube of 0.5 mm. The whole residence time of one segment with DNA-mixture within the tube (length of the tube: 697.5 cm; volume of the tube: 1.37 ml) was 46.5 min. Finally, both templates were amplified with a large product yield (Fig. 3).

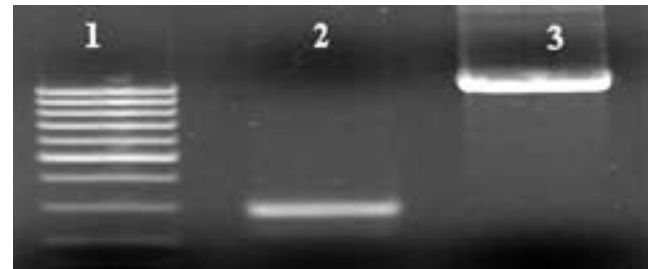


Fig. 3: Amplification products, trace 1 standard, trace 2 292 bp-fragment, trace 3 1025 bp-fragment.

Conclusions

The investigations show, that the helical tube-PCR-system with a new calculated residence time ration of 2:3:5 is well suited for DNA amplification. The application of PTFE-tubes as well as TEFZEL-Segmentation-modules assure a large stability of the segments during the whole process. It was shown that DNA inside segments with volumes down to about 100nl can be amplified. Cycle times below one minute can be achieved. This leads to total processing times below 30 minutes. Series of segments were transported without undesired unification or splitting of segments. Otherwise stronger cross-talk effects were not observed. The system represents an adequate solution for fast serial DNA analytics in medical diagnostics, drug development and screening operations.

- [1] Curcio, M. and Roeraade, J. 2003. Continuous segmented-flow Polymerase Chain Reaction for high-throughput miniaturized DNA amplification. *Anal Chem* 75: 1-7.
- [2] Hashimoto, M., Chen, P.-C., Mitchell, M.W., Nikitopoulos, D.E., Soper, S.A. and Murphy, M.C. *Lab on a Chip* 2004, 4, 638-645.
- [3] Köhler, J.M.; Dillner, U.; Mokansky, A.; Poser, S. and Schulz, T. 1998. Micro channel reactors for fast thermocycling. *The American Institute of Chemical Engineers (AIChE), Spring Meeting, New Orleans, LA.* 241-247.
- [4] Lee, J.Y.; Kim, J.J.; Park, T.H.; *Biotechnol. Bioprocess Eng.* 2003, 8/4, 213-220.
- [5] Manz, A. and Becker, H. 1999. *Microsystem Technology in Chemistry and Life Science.* Springer: Berlin, 1999.
- [6] Park, N.; Kim, S.; Hahn, J.H.; *Anal. Chem.* 2003, 75, 6029-6033
- [7] Schneegaß, I.; Bräutigam and Köhler, J.M. 2001. Minaturized flow-through PCR with different template types in a silicon chip thermocycler. *Lab on Chip* 2001, 1, 42-49.
- [8] Verpoorte, E. 2002. *Electrophoresis.* 23: 677-712.

Fast determination of matrix polarity of ternary organic solvent mixtures using a micro segmented flow assembly

G. A. Groß^{1,*}, P. M. Günther¹, C. Hamann¹, Th. Frank², and J. M. Köhler¹

¹ Department of Physical Chemistry and Microreaction Technologie

² Little Things Factory, Ilmenau

We used the advantages of the segmented flow principle to generate nanoliter fluid segments with individual composition, inside a micro fluidic system in a serial manner [1, 2]. The polarity of the mixture was monitored by the absorbance wavelength of Reichardt's betaine dye. Matrix polarity is important for the rate and selectivity of chemical reactions [3]. Therefore, the control of solvent polarity as well as the polarity of gels is of particular interest for miniaturized combinatorial and microanalytical chemistry. The polarity of a reaction supporting matrix is determined by solvent composition and dissolved additives. But the effect of concentration changes on the resulting matrix properties is not linear and thus, the prediction in case of complex matrices is difficult.

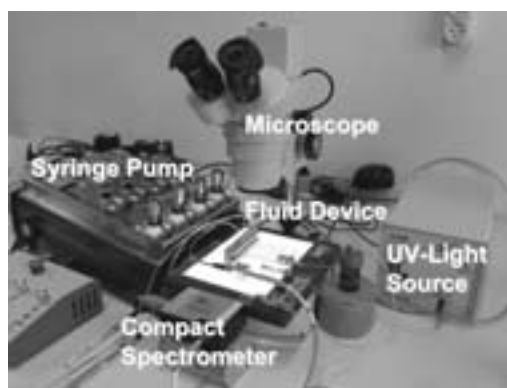


Fig. 1: Experimental Assembly.

Experimental

Three different solvents were delivered with syringe pumps [4] varying dispensing volumes to form individually composed fluid segment. A common fluid manifold was used as segment generation device. A perfluorinated solvent was used to separate the individual composed segments. The formation, transport and spectral analysis of the fluid segments were controlled automatically by a LabView application. The segment volume was adjusted to a minimum solvent consumption. Reproducible results were obtained using only 150 nl per segment and the same amount of separation liquid. Hence, this method is of advantages in terms of environmental sustainability. At least less than 5 ml of all solvent were used.

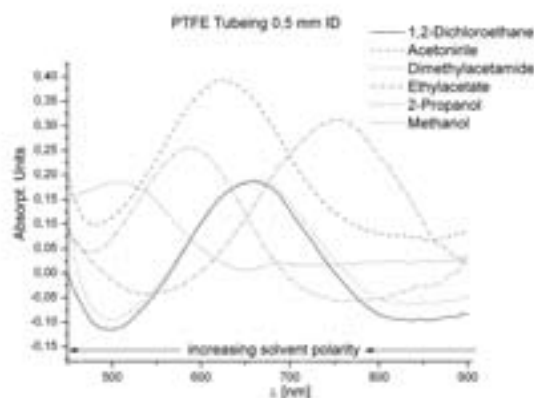


Fig. 2: Absorbance Spectra of Reichardt's Betaine dye solutions recorded in segments.

The solvent polarity was monitored by dissolved Reichardt's betaine as solvatochromic indicator dye [6]. This dye was always used in a concentration of 5 mmol/L. The optical readout was realized by means of a glass fiber system connected with micro apertures using a common 1/16''-PTFE-tubing (0.5 mm i.D.). A white light LED or UV-Lamp was used as light source. Optical spectra were recorded in the range of 400 - 900 nm with a frequency of 50 Hz by means of a compact UV-Vis spectrometer. The maximum absorbance wavelength was measured with an accuracy of about 3 nm in each segment spectrum (Fig. 2).

Theory

The empirical solvent polarity E_T [kJ/mol] of Reichardt's betaine dye solutions was calculated from the long wavelength UV/Vis absorbance band λ_{\max} [nm] by equation 1. Normalized ETN values were calculated by equation 2 using water and tetramethylsilane (TMS) as references solvents [5].

$$E_T = \frac{11962}{\lambda_{\max}} \quad (1)$$

$$E_T^N = \frac{E_T(\text{solvent}) - E_T(\text{TMS})}{E_T(\text{water}) - E_T(\text{TMS})} = \frac{E_T(\text{solvent}) - 30.7}{32.4} \quad (2)$$

Results and Discussion

Ternary polarity diagrams as shown in figure 4 were obtained within two minutes. Different mixtures of protic polar, aprotic polar and nonpolar solvents were analyzed. Resulting ETN values measured in the micro segments were compared with manually composed reference mixtures. The present injector device allows the polarity determination of individually composed segments with an accuracy of about 0.02 ETN numbers.

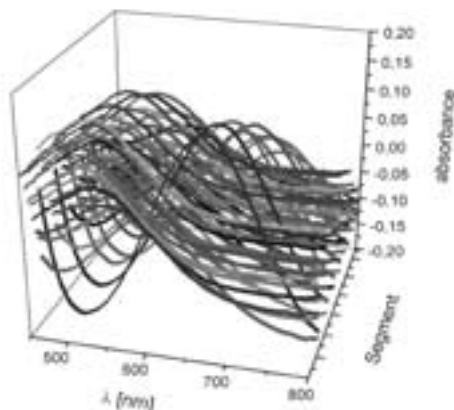


Fig. 3: Collected UV-Vis Spectra of 66 ternary solvent mixtures (CH_3OH , DMF, 1,4-Dioxane). Recorded within 2 minutes.

The segment formation process starts with the simultaneous delivery of appropriate solvent volumes followed by the fluorinated separation liquid. If no or only low volumes of one component are delivered, the programmed volumes were exceeded by washing small solvent portions out of the other injectors. This perturbing wash out effect was minimized by

variation of the flow rates, total segment volumes and delay times. At least the deviation of the segment composition was lower than 2% of the programmed volume.

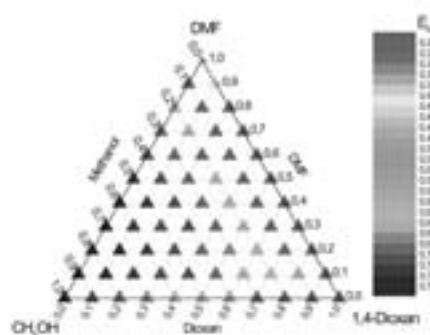


Fig. 4: Relative polarity of ternary solvent mixtures taken in the micro segmented flow assembly.

Conclusions

The set-up and procedure is well suited for the screening of complex matrix compositions. Three dimensional polarity diagrams consisting of 66 measurement points (Figs. 3 and 4) were generated within two minutes with a very low solvent consumption ($<10 \mu\text{l}$). The solvent polarity was measured with an accuracy of about 0.02 ETN numbers. Fluorinated separation liquids were reused consistently. The described method is advantageous in terms of environmental sustainability. The described method extends the micro segmented flow principle for physico-chemical applications which need anhydrous solvent conditions and enables the fast analyses of complex mixtures in a systematical way.

The financial support of the German Federal Environmental Foundation (DBU) is gratefully acknowledged. The authors thank Dr. T. Frank, Dr. K.-H. Drue and Dr. A. Albrecht for helpful discussions and excellent technical support.

- [1] J.M. Köhler, Th. Henkel, A. Grodrian, Th. Kirner, M. Roth, K. Martin, J. Metzke, Digital reaction technology by micro segmented flowcomponents, concepts and applications, *Chem. Eng. J.* 101, 2012 6, (2004).
- [2] H. Song, J. D. Tice, R. F. Ismagilov, A microfluidic system for controlling reaction networks in time, *Angew. Chem., Int. Ed.*, 42 (7), 768772, (2003).
- [3] e.g. P. M. E. Mancini, A. Terenzani, C. Adam, L. R. Vottero, Solvent effects on aromatic nucleophilic substitution reactions. Part 9. Special kinetic synergistic behavior in binary solvent mixtures, *Journal of Physical Organic Chemistry*, 12 (6), 430440 (1999).
- [4] Syringe pump system "ceDOSYS" was received from www.cetoni.de.
- [5] C. Reichardt, *Solvents and Solvent Effects in Organic Chemistry*, 2nd. Ed. VCH Weinheim, ISBN 3-527-26805-7, (1988).

Micro Flow-through Processes for the Continuous Generation of Polymer Minirods and Polymer Nanoparticles

G. A. Groß*, P. M. Günther, C. Hamann, J. Wagner, and J. M. Köhler

Department of Physical Chemistry and Microreaction Technology

Microreactors were introduced in several chemical synthesis and analytical procedures during the last decade [1]. Microreactors were also used for the generation of inorganic dielectric [2], semiconductor and metal nanoparticles [3-5]. Here, two methods for the generation of polymer particles by means of microreaction technology are reported, one for the generation of nanoparticles and the second for the generation of minirods as an example for larger particles.

Polystyrene nanoparticles generated by micro flow-through emulsion polymerization

The well known principle of emulsion [6] polymerization was transferred into a continuous process with a micro flow-through arrangement using static micro mixing for the generation of an emulsion containing the organic monomer and the aqueous solution of initiator [7]. Syringe pumps were applied for fluid actuation. After mixing, the reaction emulsion is streaming through a residence loop at elevated temperature in order to complete polymerization. The arrangement is shown in figure 1.

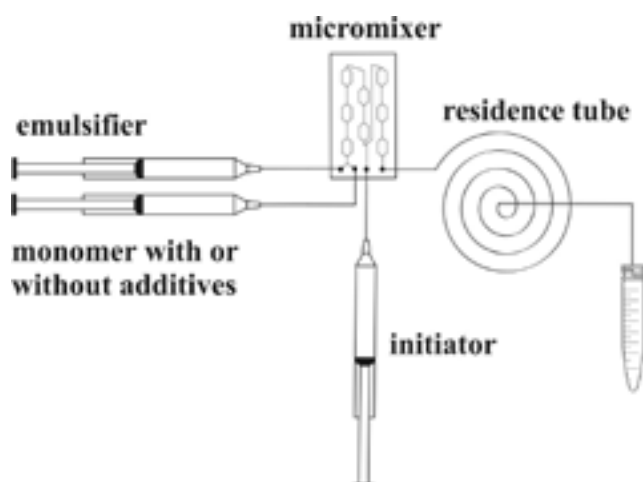


Fig. 1: Experimental arrangement for the formation of polymer nanoparticles by micro flow-through polymerization of styrene in aqueous emulsion.

The emulsifier (sodium dodecylsulfate) was applied with a concentration of 8.7 mmol/L.

Under the experimental conditions, micelles are formed in which the polymer chains are growing. In result of the chain growth, each organic core of the micelles is converted to a polymer particle during the polymerization processes. A suspension of these particles in the aqueous reaction solution is obtained after completing the reaction in the residence loop. The polymer particles can be isolated by separation from the product suspension and cleaned by washing. They were characterized by scanning electron microscopy (SEM). The typical particle sizes are in the range of about 30 to 85 nm (Fig. 2). In some cases, comparatively narrow size distribution of nanoparticles with a maximum at about 72 nm was obtained. Frequently, aggregates of nanoparticles were observed.

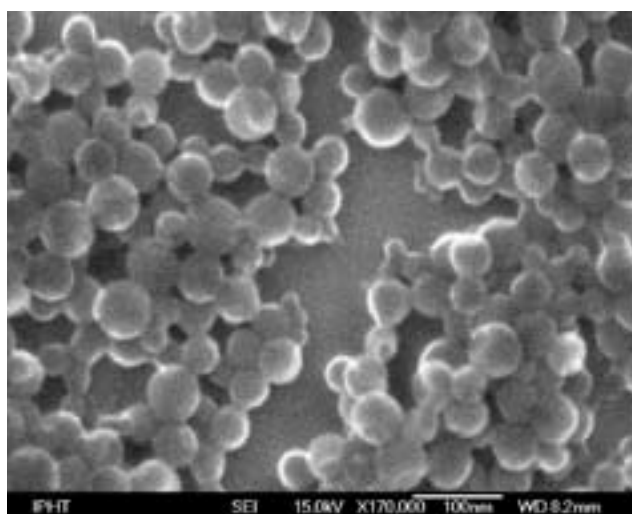


Fig. 2: SEM image of polymer nanoparticles obtained by micro flow-through emulsion polymerization.

Nanoparticles with special properties can be generated by introduction of functional components in the polymerization process. For example, lipophilic dyes can directly be incorporated in polymer nanoparticles during the polymerization process. Metal nanoparticles can also be introduced into the micelles for polymerization. Normally, the metal particles are obtained in form of an aqueous colloidal solution. For incorporation in organic micelles, the hydrophilic metal particles must be converted into lipophilic particles by an exchange of functional

groups at the particle surface. The introduction of hydrophobized metal nanoparticles leads to a certain decrease in the polymerization rate due to radical quenching. It was found that metal nanoparticles with hydrophobic shells can be enriched by the lipophilic micelles (Fig. 3).

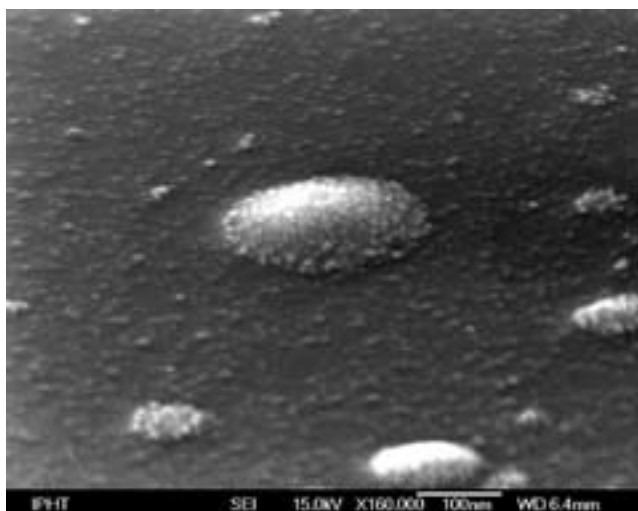


Fig. 3: Nanospots of polymers from micelles containing metal nanoparticles with hydrophobic shells obtained by micro flow-through polymerization of an emulsion of styrene nanosuspension containing small gold nanoparticles (SEM image after deposition on a monocrystalline Si surface).

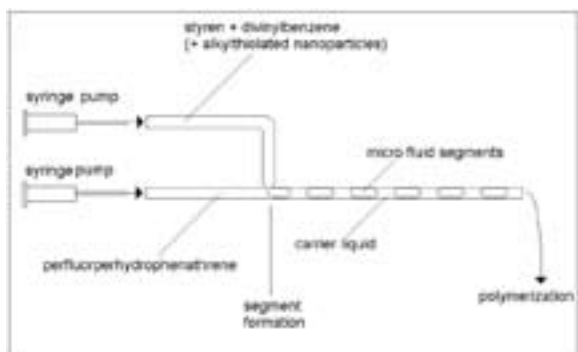


Fig. 4: Experimental arrangement for the formation of polymer mini rods by in-situ polymerization of styrene/divinylbenzene mixtures in micro fluid segments.

Dye-doped cross-linked polystyrene minirods generated in a flow-through system using the principle of micro segmented flow

Micro fluid segments attract increasing interest due to their specific advantages for serial micro fluidic processes [5, 8]. A micro segmented flow is formed, when two immiscible liquids are injected together in a micro channel. The segmentation is dependent on the flow rates, on viscosity, on the wetting of the

wall by both liquids and on the liquid/liquid interface tension.

Polymer particles in the shape and size of fluid segments can be synthesized by injection of a monomer mixture into a carrier stream of an inert liquid immiscible with the monomers [10]. Therefore, perfluorinated alkanes were applied as carrier liquid. The monomer mixture (styrene and divinylbenzene) as well as the carrier liquid were actuated by syringe pumps. Segments of monomer mixtures are formed at the injector (arrangement in figure 4). Segment series are stored in a PTFE tube and polymerization was initiated by thermal treatment. As a result, the segments became solid and can be isolated from the tubes and cleaned by washing.

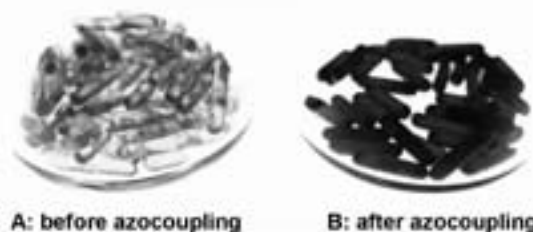


Fig. 5: Undyed and dyed polymer mini rods: particles obtained by a segmented-flow processes and subsequent polymerization; azo coupling by reaction between polymer matrix and diazonium salt DAS-4 after diffusion into the cross-linked polymer matrix

The size of polymer minirods is determined by tube diameter and the fluidic conditions for segment formation. The segment diameter is nearly given by the internal tube diameter in case of comparatively low flow rates. The segment length is mainly dependent on the flow rates of carrier liquid and monomer mixture. Typically, rod diameters between 0.25 mm and 1.0 mm and rod lengths between one and some millimeters are obtained.

The cooperation of the IPHT staff (mixer development and preparation by J. Albert, G. Mayer, M. Sossna, SEM images by F. Jahn and A. Assmann) are gratefully acknowledged.

The investigations were supported by the German Environmental Foundation.

- [1] W. Ehrfeld, V. Hessel, H. Löwe: Microreactors (Wiley VCH 2000)
- [2] Schenk, R.; Hessel, V.; Jongen, N.; Buscaglia, V.; Guillemet-Fritsch, S.; Jones, A.G. Encyclopedia of Nanoscience and Nanotechnology, 2004, 7 287-296.
- [3] Sönnichsen, C.; Alivisatos, A.P.: Nanoletters 2005, 5, 301-304.
- [4] Link, S.; El-Sayed, M.A. J. Phys. Chem. 1999, 103, 8410-8426.
- [5] Schmid, G.; Chi, L.F.: Adv. Mat. 1998, 10, 515-526.
- [6] Hunkeler, D., et al.; „Heterophase Polymerizations - A Physical and Kinetic Comparison and Categorization.” BERLIN: SPRINGER-VERLAG BERLIN, 1994, 115-33.
- [7] P. M. Günther, J. Wagner, G. A. Groß and J. M. Köhler, Micro Total Analysis Systems 2005; Vol. 2; Proceedings of μ TAS 2005; edited by Klavs F. Jensen, Jongyoon Han, D. Jed Harrison and Joel Voldman, Boston, MA, USA; pp. 918-920.
- [8] Nakamura, H.; Yamaguchi, Y.; Miyazaki, M.; Uehara, M.; Maeda, H.; Mulvaney, P. Chemistry Letters 2002,(10), 1072-1073.
- [9] Grodrian, A., J. Metze, T. Henkel, K. Martin, M. Roth, and J. M. Köhler. 2004 Biosensors & Bioelectronics 19:1421-1428.
- [10] Köhler, J. M., Gross, G. A., Hamann, C., Wagner, J., Günther, M.; Proceedings of AIChE Spring National Meeting Orlando 2006, pp. 50.

Microfluidics and Biosensors for the Examination of Cell Differentiation

M. Gebinoga¹, C. Kremin¹, M. Fischer¹, Frank Weise¹, K. Lilienthal¹, I. Cimalla¹, G. Kittler², A. Spitznas², E. Gottwald³, C. Augspurger^{1,3}, Thomas Friedrich¹, Dennis Wegener⁴, A. Schwienhorst⁴, O. Ambacher², and A. Schober¹

¹ Junior Research Group Microfluidics and Biosensors, MacroNano[®] – Center for Innovation Competence

² Department of Nanotechnology

³ Research Center Karlsruhe

⁴ University of Göttingen, Institute for Microbiology and Genetics

Introduction

It has been shown that microfluidic properties are important for the cultivation of advanced three dimensional cell cultures [1]. In this way medium and gas supplies are realized. In addition, surface modifications and patterning of the culture substrate [2] are important for defined cell cultures morphology and differentiation. Recently it has been shown that micro-fluidic properties play a dominant role for the cultivation of stem cells [3]. Furthermore, those microreactors with advanced cell culture systems are suitable tools for the examination of the effect of drugs to the differentiation of cells. Cell culture systems are discussed as tools for “High-Content-Screening” approaches [4]. The parallelization of these approaches together with the integration of advanced cell culture systems and different sensor principles is subject to recent research [5]. Here we describe the combination of advanced cell culture systems with new biosensor concepts for examining cells.

Among other factors, the regulation of the chromatin by the HDAC enzyme which belongs to the hydrolases is a key in cell differentiation. Thus, this enzyme family plays a dominant role in cancer research. Therefore our sensor approach was utilized for the determination of the HDAH activity in the μl range down to the nI volume. In addition different HDAC inhibitors were tested with regard to their effect onto differentiation of HepG2 cell cultures [6].

In a proof of concept experiment another hydrolase, the enzyme lipase, was examined by an AlGa/GaN sensor system. The substrate conversion could be monitored [5]. As a conclusion this approach was transferred to the HDAH enzyme system.

In this way a new experimental platform for basic research and applications for the drug discovery process is under development.

Technology

By optimising the properties of the sensors an experimental set-up for testing the AlGaN/GaN heterostructure sensor system has been realized. The set-up allows for the continuous optimisation

of different components as sensors or fluidic devices which is useful for the applications described in this paper, but for the development of sensors measuring in the the sub μl - or even pI-volume range (see Fig. 1), as well.

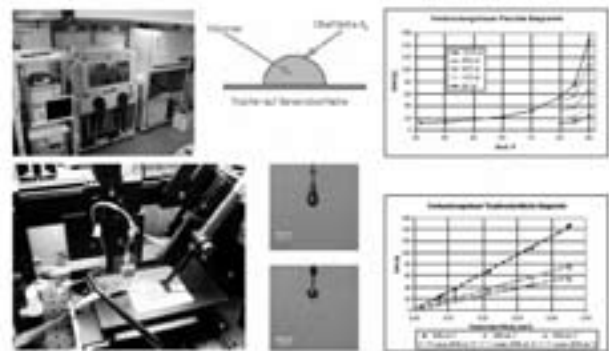


Fig. 1: Experimental set-up for the testing sensors in the picoliter measurement range. Control of humidity, pressure and temperatures is realized within the chamber. With the drop-on-demand system (e.g., application of potential drugs onto cells or tissues) volumes down to the picoliter volume can be realized.

The sensor system utilized for different applications is based on a ChemFet architecture realized with the AlGaN/GaN system originally developed for HEMT transistors. The basic principle and the realization for parallel sensor arrays are shown in figure 2 (left). At the interface between the two materials a two dimensional electron gas (2DEG) is induced by spontaneous and piezoelectric polarisation. Electronic and material properties can be controlled by the composition of the material. A barrier layer with a band gap of 4.1 eV is transparent for radiation with a wave length above 300 nm. This allows the simultaneous monitoring of optical and electrophysiological measurements. In figure 2 the induced positive bound charge caused by the polarisation discontinuity is indicated with δ^+ which is compensated by electrons from surface donors forming a 2DEG at the interface. Such 2DEGs

react very sensitively to changes of the surface potential induced, e.g., by chemical solutions with different pH values measurable by variation of the source drain current.

Possible applications of such structures are the measurement of the pH value in enzymatic studies (Fig. 2, right) or of cell cultures for metabolism studies.

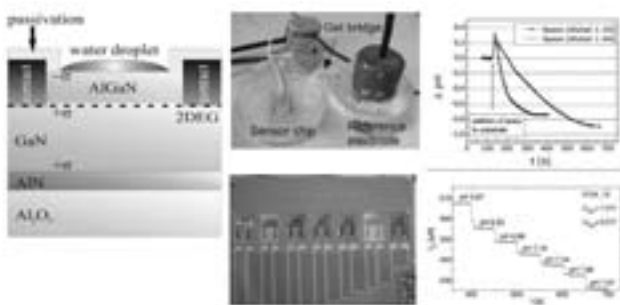


Fig. 2 (Left): Sensor principle. (middle): Set-up with reference electrode and sensor array. (right): Lipase enzyme kinetics and titration of pH Values.

Figure 3 (right) shows the realization of a traditional pH measurement set-up adapted for the measurement in 100 μ l volume containing an embryoid body of P19 cells (pluripotent mouse carcinoma cell line-age).

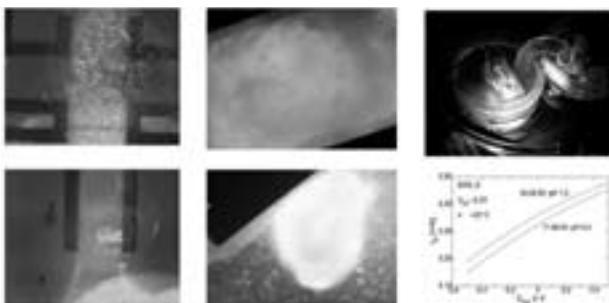


Fig. 3 (left): P19 myocardial cells adherent to AlGaIn/GaN sensor structures. (middle): P19 bodies on transparent Al-GaN/GaN sensor structures. (right): Microbioreactor for the P19 cells with reference electrode, measurement of the pH value.

Such a sensor set-up can also be used in the sub μ l range. Another layout of the sensor was realized for incorporation in a microbioreactor for the cultivation of liver cells (Fig. 4). Here, the length of the sensor has to be adapted according to the size of the microbioreactor.

Experiments

The biocompatibility of the AlGaIn/GaN material was examined and the results for the fibroblasts and the P19 lineage [5] could be confirmed with CHO and Hek cells [8].

Different experiments have been performed with the microbioreactor designs described above. Hep G2 cells were cultivated successfully in the CellChip-based microbioreactor shown in figure 4.

P19 cells differentiated into myocardial bodies have been cultivated in a special microreactor with an implemented transparent AlGaIn/GaN heterostructure sensorsystem for online optical observation (Fig. 3, left, bottom). Thus simultaneous measurement of metabolism, e.g. the change of pH, and the optical/microscopical monitoring (Fig. 3, right) was realized successfully for a 20 hour period.

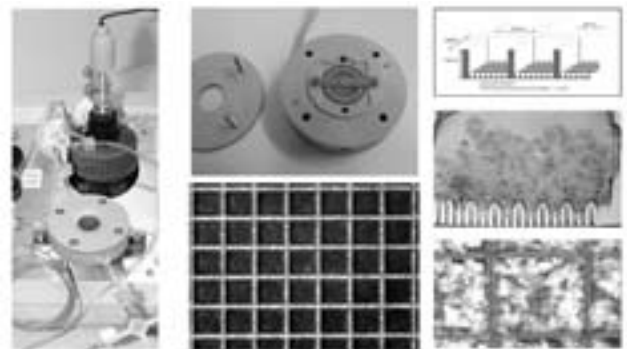


Fig. 4 (left): Microbioreactor with cellchip and cellchip populated with HepG2 cells. (right): CellChip array (Source: Forschungszentrum Karlsruhe).

Summary and Outlook

The sensors are tested with respect to long term stability and sensitivity. Biological measurements in the range of several hours meet the necessary requirements. Optimization with respect to sensitivity, signal to noise ratio and long term stability (>24 hours) is the aim of further research.

The described integrated system modules are utilized for the following examination strategies:

- 1) Characterization of CellChip cultures in microfluidic and biosensoric systems
- 2) Characterization of enzyme activity together with the determination of enzyme inhibitors with our measurement platform in the sub μ l volume range.

This work was supported by the BMBF-Project "MacroNano*", the European Union, and the Thuringian ministry of culture (TKM) (FKZ 032IK062 and EFRE program: B 678-03001, 6th framework program: GaNano NMP4-CT2003-505614).

- [1] Eschbach, et al; Microstructured scaffolds for liver tissue cultures of high cell density: morphological and biochemical characterization of tissue aggregates. *Journal of Cellular Biochemistry*, 95(2005) S.243-55.
- [2] Welle, A., Gottwald, E.: UV-based patterning of polymeric substrates for cell culture applications. 2002; *Biomedical Microdevices* 4: 33-41.
- [3] Zhao, F et al. Effects of Oxygen Transport on 3-D Human Mesenchymal Stem Cell Metabolic Activity in Perfusion and Static Cultures: Experiments and Mathematical Model, *Biotechnol. Prog.* 2005, 21, 1269-1280.
- [4] L. A. Kunz-Schughart, J.P. Freyer, F. Hofstaedter, R. Ebner, The use of 3-D Cultures for High-Throughput Screening: The multicellular Spheroid Model, *Journal of Bio-molecular Screening* 9(4); 2004.
- [5] A. Schober et al, „Neue Sensoren für mikro- und nanofluidische Systeme und ihre biotechnologischen Anwendungen“ 143 – 146, 7. Dresdner Sensor Symposium, 2005.
- [6] G. Kittler, et al, , Optimized GaN based pH-Sensors and their Applications, *International Symposium on Compound Semiconductors (ISCS)*, Rust, 2005.
- [7] C. Augspurger; et al., Effects of HDAC-inhibitors on proliferation and differentiation of the human hepatoma cell line HepG2. 2nd International Conference "Strategies in Tissue Engineering" Würzburg 2006.
- [8] I. Cimalla, et al, Impact of the device technology processes on the surface. properties and biocompatibility of group III nitride based sensors submitted to EMRS (2006).

Method and microfluidic systems for handling and cultivation of valuable biological specimen

D. Voges^{1,*}, M. Stubenrauch², J. Burgold², C. Schilling¹, M. Knoblauch³, H. Witte¹

¹ Department of Biomechatronics

² Department of Micromechanical Systems

³ Institute for General Botany, Justus-Liebig-University Giessen, Germany

I. INTRODUCTION

Handling and cultivation of biosamples in microfluidic structures is the crucial part of most experiments in the field of Bio-MEMS. A simple way is the use of structured substrates like glass or silicon chips to bring the sample into cavities on the surface, and consecutively covering it with a piece of glass for microscopy. The alternative is to manufacture fully enclosed microfluidic structures that can be filled through external connections such as tubes or capillaries. Our new approach is a semiclosed fluidic structure with capillary force enhanced guiding of liquid currents through channels and sample chambers. The system consists of microfluidic channels for liquid supply into the observation chamber. Constriction elements, in analogy to internal structures in water guiding vessels of plant stems, enclose the chamber to prevent the loss of biomaterial. An orifice to the outside near the observation chamber allows easy handling of the valuable specimen. During operation capillary forces keep these small holes closed to allow a flow of liquids through the system.

II. TECHNOLOGY

A special combination of existing standard silicon MEMS processes including anodic bonding of structured glass lids is used (see Fig. 1).

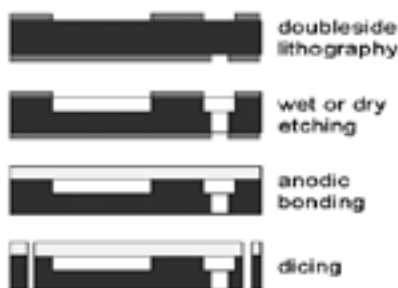


Fig. 1: Schematic of the process flow

All assembly technologies for MEMS are incompatible with living specimen. Therefore they have to be implemented after the complete manufacturing process. For structures with toploding, the glass wafer is structured with holes using comparable processes as for the silicon substrate before anodic

bonding. Sideloding systems are made by a special dicing regime.

Special care is required to avoid contamination of the microchannels and constriction elements with particles. Figure 2 shows the principle of placing biological specimen into the microstructures.

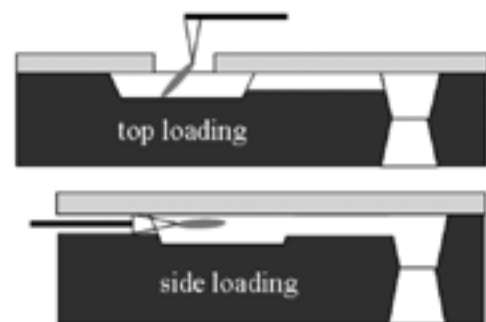


Fig. 2: Methods for loading of the specimen

Depending on the manipulators available in the laboratory, side- or toploding into the observation chamber can be done. The specimen can be positioned into the fluidic chamber by manipulators or sucked into the chamber by pressure pulses from external fluidic connections. The micro-channels are completely filled with aqueous solution before the loading step.

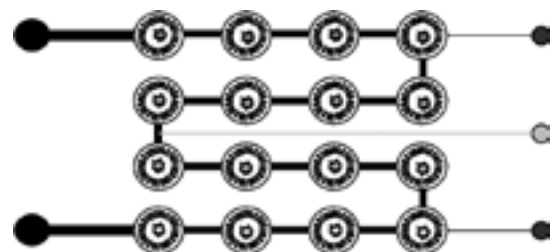


Fig. 3: Cascaded assay for monitoring tests

In the chamber, the specimen will be kept by constriction elements and capillary forces. Different solutions and drugs can be delivered to the samples by adding them to the water flow through the systems (see fig. 3). Additional manipulation is possible via the loading orifices. Complex experiments can be set up by cascading or parallelisation of different

structures with several compartments for multiple cells or specimen.

III. DESIGN

A series of different designs for observation chambers have been created. Some of them are shown in fig. 4 and 5. Channel and chamber sizes from 10 μm to 200 μm have been developed for different living organisms, cells or cell organelles.

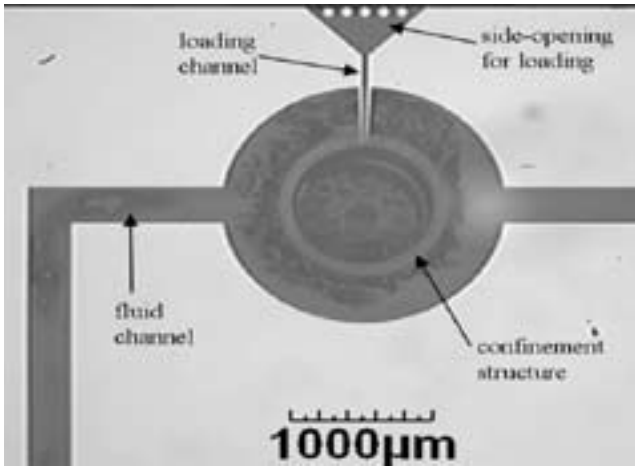


Fig. 4: Structure for side loading

The pitch of the constriction structures scales down to 1 μm . To minimize the loss of bio-specimen due to sticking at the side walls the loading orifices are very close to the observation chambers.

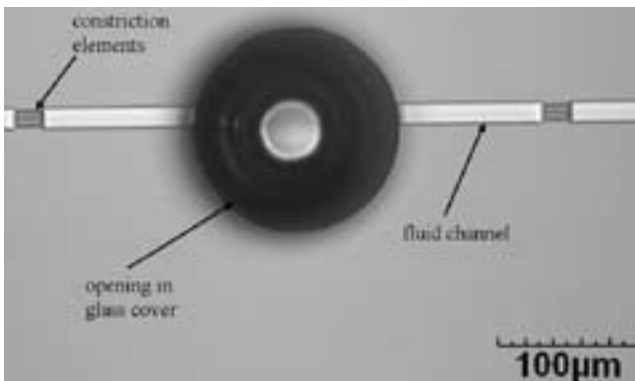


Fig. 5: Structure for top loading

III. APPLICATION

Our microfluidic chips can easily be used for the improvement of various experiments in basic biological research. Single cells or cell components can be picked with manipulators and brought into the chip. The samples can be kept under controlled conditions for long term experiments while having the opportunity of continuous flows through the sample chamber, as well as, access for further manipulations.

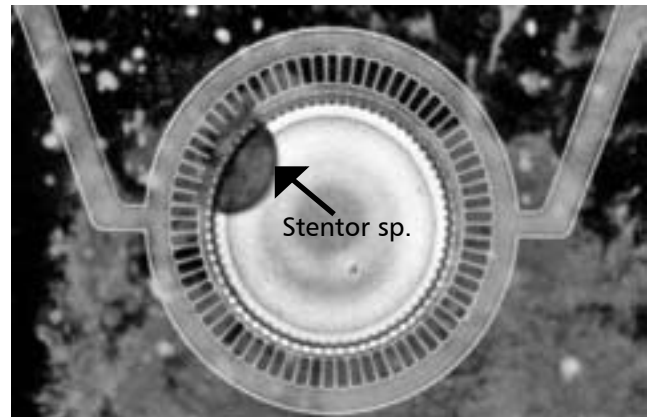


Fig. 6: *Stentor sp.* in a fluidic microchip

First experiments (see fig. 6) were carried out with organisms such as rotifers, *Stentor sp.* and *Paramecium sp.* to study their behavior in artificial environments. Following these efforts, an artificial micro-ecosystem can be set-up as a biomimetic approach (see fig. 7)[1].

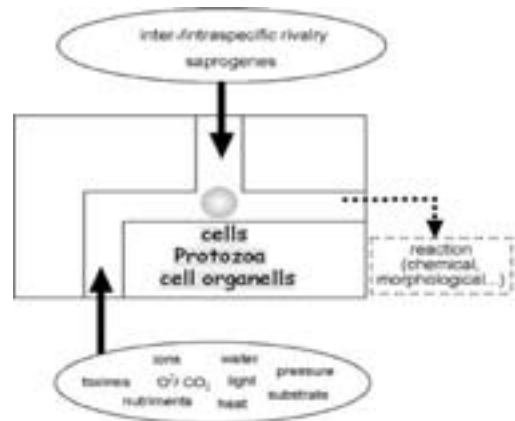


Fig. 7: Artificial micro-ecosystem [1]

Different environmental conditions can be simulated in such devices. Future Applications could be the environmental protection (e.g. for monitoring of fresh- and drinking water), the medical research and cell physiology (e.g. cultivation of single cells for neuro-MEMS and for the tissue engineering of human histoblastes) an the cyto-"bionical" approach by the intention of mimicking the mechanical features of cells and their organelles in micro- an nanotechnological systems.

This work was supported by the BMBF under contract number 0312014C. We gratefully acknowledge valuable contributions from K. Bley and M. Koch at -4H- JENA engineering GmbH. [1] VOGES, D., et al.: Wie können Einzeller oder Motorproteine in technischen Systemen "überleben"?, p 461-465 in 12. Heiligenstädter Kolloquium, "Technische Systeme für Biotechnologie und Umwelt", 2004.

Electrochemical Micro Reactor Based on LTCC Ceramics with Integrated Platinum Micro Electrodes

P. M. Günther¹, T. Thelemann², M. Hintz³, M. Fischer², L. Abahmane¹, G. A. Gross^{1,*}, and J. M. Köhler¹

¹ Department of Physical Chemistry and Microreaction Technology

² Junior Research Group Functionalised Peripherals, MacroNano[®] – Centre for Innovation Competence

³ Department of Microperipherals

Electrochemical micro devices have been investigated for a lot of microanalytical purposes in the last decades [1]. Later, electrochemical microreactors were introduced in chemical synthesis [2]. Here, we describe the design, preparation and the basic characterization of a flow-through micro reactor based on Low Temperature Co-fired Ceramics (LTCC).

LTCC is an interesting material for the preparation of microreactors. This material adds to the advantages of ceramics (high chemical, mechanical and thermal stability) a high flexibility in the design and in the preparation. A particular advantage is the possibility of inclusion of functional layers of different additional materials. Both the LTCC matrix material and the additional functional layers can be micropatterned by mechanical as well as optical methods. Therefore, it is particularly easy to develop special micro channel structures equipped with micro electrode systems.

Design of the electrochemical microreactors

The LTCC electrochemical cell consists of one channel possessing three electrode arrangements. Six electrodes are introduced from the upper side of the electrochemical cell. Four electrodes having a surface area of 0.4 mm² are located near the inlet and outlet of the cell. The other two electrodes with surface area of 1 mm² and 24.8 mm² are centrally located in the cell. Additionally, from the lower surface of the cell another three electrodes are introduced. Two smaller electrodes with a surface area of 1 mm² each are separated by the larger third electrode with a surface area of 26 mm². These electrodes are positioned opposite to each other as shown in figure 1.

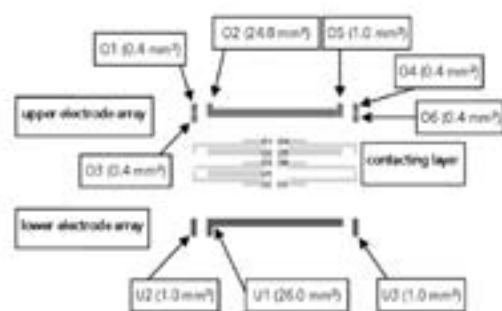


Fig. 1: The micro-electrode positioning in the LTCC-electrochemical cell.

The electrode arrangement was configured in order to realize either a two-electrode or a three-electrode measurement technique. The electrodes situated at the inlet and outlet of the cell were available for analytic investigations, e.g. cyclic voltammetry. The electrodes with the larger active surface were intended for synthetic applications whereas the upper electrode served as working electrode. All electrodes are prepared of platinum. The contacts between electrodes and ceramics were realized by a silver/palladium alloy. The channel of the electrochemical cell has a height of approx. 0.64 mm and a width of 1 mm.

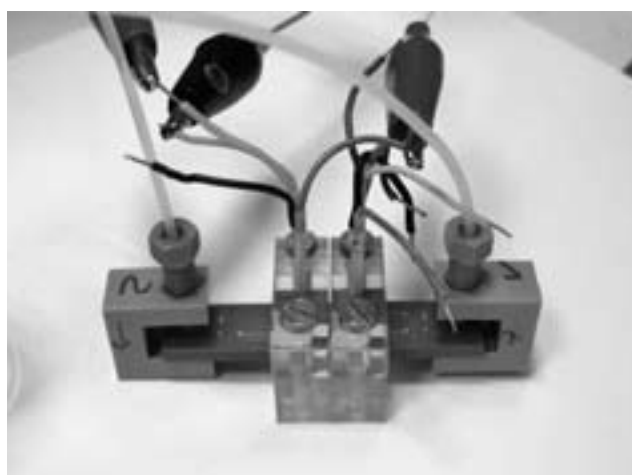


Fig. 2: The LTCC-electrochemical cell.

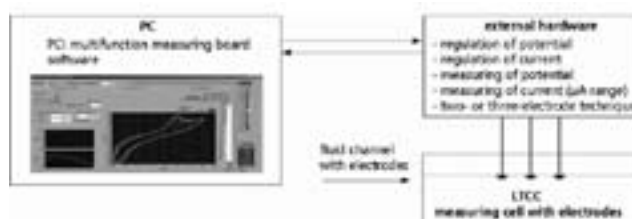


Fig. 3: Experimental arrangement.

Experimental arrangement

The potentiostat/galvanostat-system consists of a PC with a PCI multifunction measuring board. This consists of 16-bit-AD converter with 200 kHz sampling rate and two 16-bit-digital converters with 10 kHz actualization rate. This configuration gives

the possibility of potentiostatic (potential regulation) and/or galvanostatic measurements.

Preparation of reference electrode

1) Reference electrode:

An Ag/AgCl pseudo reference electrode was prepared in order to realize measurements with defined potentials. 0.1 M silver nitrate solution was pumped through the cell with a flow rate of 2.4 ml/h (passed through electrochemical cell for 25 min) and silver was galvanostatically deposited ($I=0.2 \mu\text{A}$). After rinsing the cell with distilled water 1 M HCl solution was applied with a flow rate of 2.4 ml/h.

2) Electrochemical cell testing:

The cyclic voltammetry (CV) is an experimental, electro-chemical analytical method [3]. A cyclic voltammogram gives information about the thermodynamics of redox processes as well as knowledge about the kinetics of heterogeneous electron transfer coupled with chemical reactions. In the cyclic voltammogram the current in the system is plotted as a function of its voltage [4].

The redox system $\text{Fe}^{2+}/\text{Fe}^{3+}$

An electrolyte mixture of 0.1 M Fe^{2+} -solution (yellow prussiate of potash), 0.1 M Fe^{3+} -solution (red prussiate of potash) and 0.1 M K_2SO_4 solution was cyclic voltammetrically investigated. The K_2SO_4 solution was used as supporting electrolyte.

The obtained cyclic voltammogram (Fig. 4) demonstrates that our pseudo reference electrode Ag/AgCl is suitable for further analytics and/or synthesis.

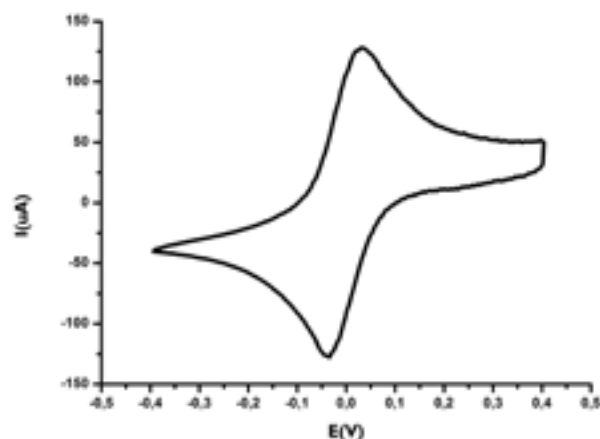


Fig. 4: Cyclic voltammogram of the redox system $\text{Fe}^{2+}/\text{Fe}^{3+}$; scan rate: 100 mV/s; potential vs. pseudo Ag/AgCl electrode.

Conclusions

The investigations show, that the LTCC technology is well suited for the preparation of micro flow-through reactors for electrochemical applications. The concept of the three-electrode system consisting of a counter electrode, a working as well as a pseudo reference electrode, was realized for analytical purposes. A micro-channel reactor equipped with an electrode system including at least one large electrode could be used for electro-organic synthesis.

The development of a PC-controlled potentiostat for electrochemical characterization was realized by S. Schneider. The investigations were supported by the State of Thuringia (project KRAFEMA) and by the German Environmental Foundation.

- [1] R. de Vivie-Riedle, *Physikalische Chemie* <Magazin> 2003.
- [2] M. R. Gongora-Rubio et al. *Sensors and Actuators A* 89 (2001) 222-241.
- [3] C.H. Hamann und W. Vielstich, *Elektrochemie*, VCH-Wiley, 3. Auflage, Weinheim (1998).
- [4] F. Beck, *Elektroorganische Chemie*, VCH-Wiley, Weinheim (1974).
- [5] J. Heinze, *Angew. Chemie* 96 (1984) 823.
- [6] T. Shono, *Electroorganic Synthesis*, Academic Press (1991).

Peristaltically Activated Device for Minimally Invasive Surgery

M. Lang, R. Löw, P. Meier*, S. Oberthür, N. Vasev, C. Wystup
Junior Research Group "PADeMIS"

I. MOTIVATION

The aim of this project is the development of a Peristaltically Actuated Device for Minimal Invasive Surgery (PADeMIS). The device moves actively like an earthworm and carries a hollow tube behind its back. The tube and PADeMIS are providing a canal to insert endoscopic tools towards the invasive location of surgery. The first application of PADeMIS is the minimal invasive spine surgery. A possible progress of a spine surgery with PADeMIS is the insertion of the device at the sacral bone (os sacrum), crawling to, e.g. a herniated disc (see Fig. 1) inside the epidural space, removal of herniated disc through the inner opening, crawling to a second herniated disc, and so on, and at the end extraction of the device. Due to anatomical conditions the outer diameter of PADeMIS must be alterable from 4 to 10 mm and in order to insert the endoscopic instruments an inner diameter of 2 mm must remain. PADeMIS consists of serially arranged segments. Each segment contains cushions, which can be filled hydraulically. Filling the cushions of different segments periodically results in a deformation of the entire worm and leads to the desired peristaltic locomotion (see Fig. 2). For this purpose the filling of the cushions has to result in axial and radial expansion of the segment, but in addition, the inner canal has to remain hollow.

II. MATERIAL AND METHOD



Fig. 1: PADeMIS (head) way in the vertebral channel. The device runs a tube (tail) for endoscopic tools.



Fig. 2: Schematic illustration of PADeMIS, based on the FEA simulation of one segment.

Due to the ambient conditions large deformations and large strain are required. Therefore, PADeMIS has to be produced from rubberlike material. The MED 49XX liquid injection moulding silicone elastomer made by NuSIL® Technology is used. XX indicates the shore hardness of the silicone rubber and varies from 10 to 70. The constitutive law of the material is experimentally determined by uniaxial and equibiaxial tension tests. The life time of the material is controlled by uniaxial tension tests.

Each segment is built up from two thin cylinders of silicone rubber. The cylinders are separated in the area of the cushions and connected at the rest of the structure. The design of the segment is calculated and improved by finite element analysis (FEA) using Ansys® and MSC.Marc. The filling of the cushions is simulated by increasing the pressure in the areas of the cushions. To improve the deformation in the required direction the number of cushions, the geometry of the segment, and the shore hardness of the silicone rubber are varied in the simulations. A typical deformation – pressure curve is shown in Fig 3.

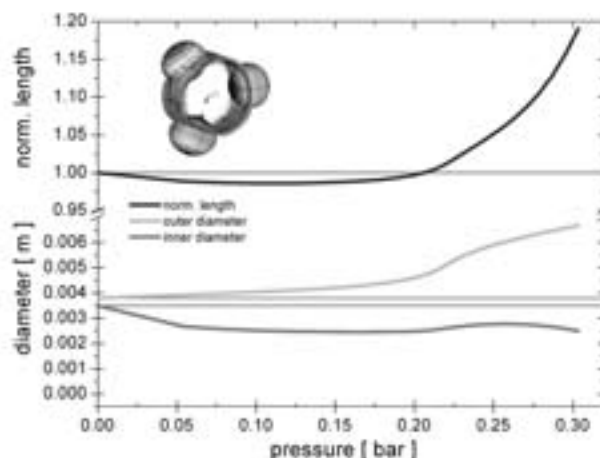


Fig. 3: Deformation in dependence on the pressure. The inset shows the corresponding design.

A facility adapting a lithographic process (see Fig. 4) to silicone rubber is build up.

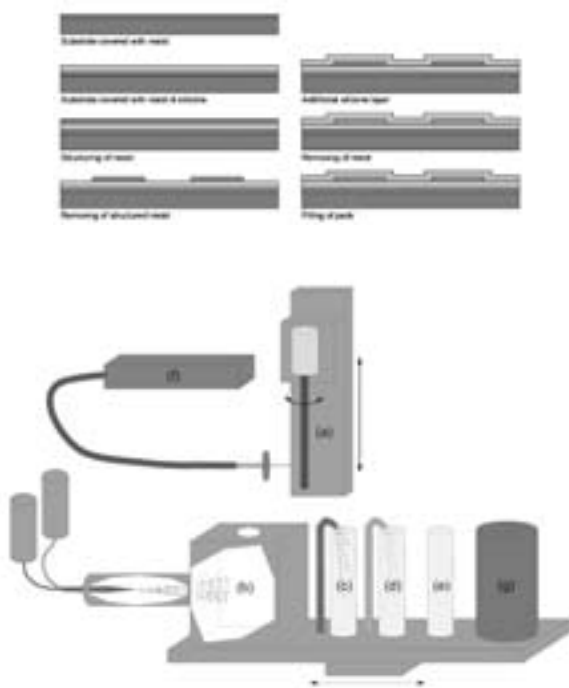


Fig. 4. Top: Lithographic process for manufacturing PADeMIS. Bottom: Schematic setup of the lithography facility: a) Substrate; b) Spray-coating PR; c) Developing PR; d) Rinsing; e) Dip coating LSR; f) Exposing; g) Tempering.

For production of PADeMIS the following steps have to be performed:

1. Alignment of the substrate
2. Measuring the diameter of the substrate
3. Application of separating photo resist (PR) layer to the substrate
4. Tempering of the PR layer
5. Measuring the thickness of the PR layer
6. Application of liquid silicone rubber (LSR) layer
7. Tempering of the LSR layer
8. Measuring the thickness of the LSR layer
9. Application of a photo resist (PR) layer
10. Measuring the thickness of the PR layer
11. Exposing and developing of the PR layer to obtain cushions and supply tubes
12. Application of the LSR layer
13. Tempering of the LSR layer
14. Measuring the thickness of the LSR layer
15. Solving of resist of the separating layer and inside the cushions
16. Filling of the cushions

Due to the cylindrical design of the device a rod with 3.5 mm diameter is used as a substrate. PR and LSR coating, tempering, solving and rinsing are performed actuated by another linear motor performing a horizontal movement. The exposing unit is moved by a pressure cylinder toward the substrate. An optical

measuring unit allows the determination of the tilting of the substrate to determine the actual diameter of the coated substrate during the process, and the measurement of the distance between coated substrate and focusing lens.

The cushions of PADeMIS will be filled with physiological infusion solution to avoid injuries of the patient in the case of leakage. For the same reason the control unit works volume controlled and measures the pressure. To allow steering of the device, at least 3 cushions per segment are needed. For the peristaltic locomotion at least 3 segments in serial arrangement are needed, but an arrangement of six segments moves twice as fast (assuming same time for filling). This 3 or 6 segment unit can be repeated serially to improve the wall contact of the device. Therefore a control unit piloting 18 ducts is built up. The controller is shown in Fig. 5.



Fig. 5: Controller for a device with 18 ducts.

III. CONCLUSION

For a couple of incisions in MIS a compliant structure replacing the common rigid trocars would be preferable. Therefore, a self crawling device is developed primarily to replace herniated discs. For fabrication of the device a lithographic facility is built up, allowing the fabrication of cylindrical structures with medical proven materials. For a short time, all process steps work satisfactory. Therefore, the first devices will be fabricated soon and have to prove PADeMIS practicability in animal tests.

Furthermore, the technology allows the fabrication of similar devices for other applications, e.g. surgery inside the bronchia and other devices like grippers, bending elements, etc., made up from cylindrical basic form.

[The authors thank Dipl. Ing. Mike Stubenrauch for some ideas in the beginning. Alike we thank Dr. H. Böhm, MD (Spine surgery, Zentralklinik Bad Berka GmbH), for his inspirational input towards the project. Furthermore we would like to thank the TKM (Ministry of Education of Thuringia) for financial support of the Junior Research Group PADeMIS.

"Syn&Sort": A Chip Based Tool for Combinatorial Synthesis and Biological Screening

M. Gebinoga^{1,*}, A. Albrecht², G. Schlingloff³, T. Lübeck¹, T. Henkel³, and A. Schober¹

¹ Junior Research Group Microfluidics and Biosensors, MacroNano[®] – Center for Innovation Competence

² Department of Micromechanical Systems

³ Institute of Physical High Technology, Jena

Summary

We present a new method for combinatorial solid phase libraries synthesis. The new method called "Syn&Sort" combines the advantages of the directed sorting technique with those of miniaturized parallel synthesis. Directed sorting steps were realized by combination of two encoding principles: spatially resolved encoding was used for a carrier chip, bearing 60 solid phase units and an individual barcode marker for each carrier. Solid phase supports were made of glass with a magnetic core coated with synthesis polymer. 60 synthesis units were arranged on each carrier chip using the magnetic "clip board" principle. No special synthesis equipment is necessary and all carriers were used in standard laboratory equipment. "Syn&Sort" was applied to the synthesis of a pentamer-peptide library.

Description

The "Syn&Sort" technology is a miniaturized parallel synthesis system which uses the directed sorting technique at two hierarchical levels.

"Syn&Sort" utilizes chemical solid-phase synthesis using planar polymer films coated on magnetic handling devices. Therefore, functionalized films were polymerized onto small magnetic glass chips. 60 of these chips were arrayed on one magnetic glass carrier. The "Syn&Sort" technology enables an easy spatial rearrangement of the single solid support chips between the different carriers.

The carriers itself are used for directed sorting synthesis encoded by their barcode marking (see Fig. 1). For subsequent synthesis steps the glass chips are rearranged each time. Afterwards the carriers are placed in appropriate reaction solutions following the combinatorial synthesis strategy. After all synthetic and washing steps, each glass chip contains a single compound which can be identified by recording the starting position inside the array and the following rearrangement / reaction steps (see Fig. 1).

Mechanical and magnetical system

The preparation of glass chips is performed in a sandwich like structure of glued glass plates with a

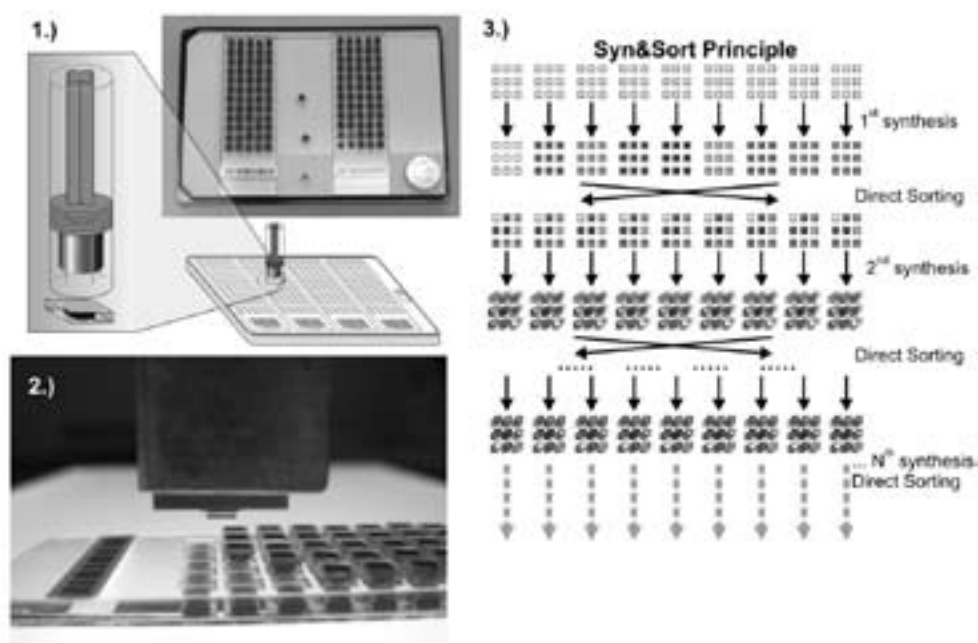


Fig. 1: "Syn&Sort": 1.): Scheme of a microtiterplate (MTP) bearing chip carrier with the magnetic pen to move the magnetic glass chips. insert: photograph of a MTP carrier with two of four chip-carriers. 2.): Photograph of the magnetic pen gripper above a chip-carrier (some chips are removed to visualize the chip wells). 3.): Principle of the combinatorial "Syn&Sort" technology for directed sorting library synthesis.

magnetic core. Micro structuring of appropriate glass sources was carried out by micro powder blasting. The magnetic powder was filled into resulting wells and two glass plates were sealed using two-compound-adhesive and thermal curing.

A xyz-positioning system with a special constructed magnetic gripper was developed for the sorting operations. The basic idea of this system consists of a moveable ferro-magnetic pen inside a mechanical guidance (see Fig. 1). This system is positioned on the chip to be gripped and the magnetic pen was activated. The activation causes a magnetic force for taking off the chips.

Chemical system

The glass chips were coated with a PEGA film that provides free amino groups for amino acid attachment by polymerization. As starting material 4,7,10-trioxa-1,13-tridecanediamine was transformed to an aminocarbonic acid by treatment with dihydro-

2,5-furandion. Conversion with acryl-chloride leads to the acrylamido-carbonic acid which enables the introduction of the carboxy functionality into the polymer support during polymerization. Activation of remaining polymer bound carboxylic groups using TSTU as coupling reagent yields the active ester which was transformed into immobilized amine-groups using an excess of ethylene-diamine.

The single chips were then employed to the peptide synthesis according to our protocol. A library of 16 different peptides was synthesized and then analysed by mass spectrometry (Fig. 2).

With chips of the surface size 14.4 mm² the release of 70 nmol substance was possible. This is sufficient for a detailed mass spec analysis. The MS Spectra shows that the desired peptides were synthesised at the chips.

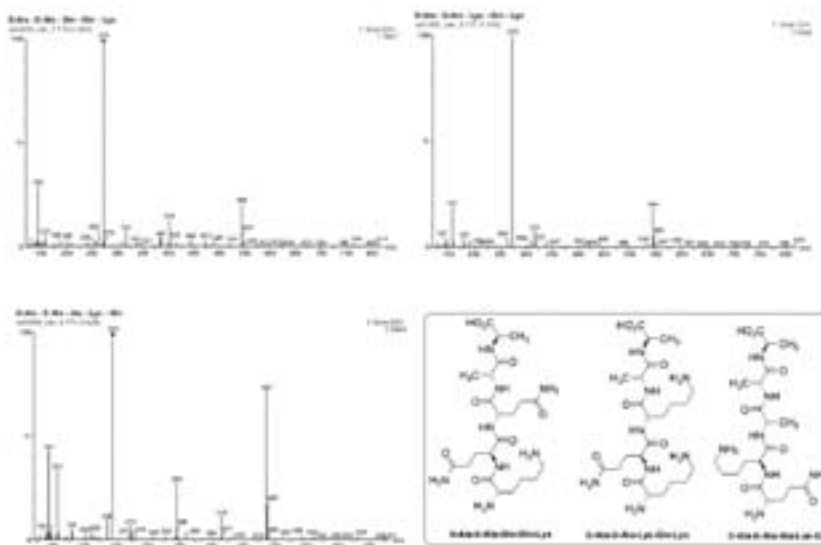


Fig. 2: Selected mass spectra of three synthesized peptides.

Thermally driven microgripper as a tool for micro assembly

B. E. Volland^{1,*}, K. Ivanova², T. Ivanov¹, I. W. Rangelow¹, D. Andrijasevic³, W. Brenner³, and I. Kostic⁴

¹ Department of Micro- and Nanoelectronic Systems

² Institute of Nanostructure Technologies and Analytics (INA), University of Kassel, Germany

³ Institut für Sensor- und Aktuatorssysteme, Technische Universität Wien, Austria

⁴ Institute of Informatics, Slovak Academy of Sciences, Bratislava, Slovakia

Introduction

Microgrippers are needed for handling and assembly of microparts, for manipulation of biological samples, and for microassembly. In general, microgrippers consist of a pair of tweezers that grab the objects, and an actuator that provides the required force.

Amongst the most popular types of microactuators are shape-memory alloys, electrostatic actuators, piezoelectric, or thermal actuators. Shape-memory actuators operate as on-off actuators, so the control of the gripping force is complicated. Electrostatic actuators generate the force by electrostatic attraction of comb finger electrodes at different electric potential.

Thermal actuators rely on thermal expansion of an electrically heated so-called 'hot arm' attached to a lever mechanism. They are usually made from SU-8, with thin metal layers serving as a conductive layers for the electrical current. They can operate in atmosphere or vacuum, as well as in dusty environment.

The present work uses single crystal silicon as mechanical material, and a so-called 'two-hot-arms' design.

Design

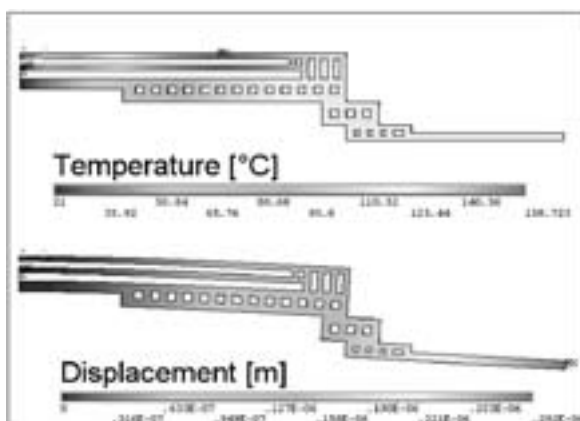


Fig. 1: Design and simulations of the microgripper. Current passes through the two thin 'hot arms' and causes Joule heating. Due to thermal expansion, the gripper tweezer bends. The dissipated power was 30 mW, and the arm length is 200 μm .

The microgripper consists of a pair of electrothermal actuators driving a pair of tweezers. The opening of the tweezers is 5 μm wide, while the tweezers are 20 μm long. The electrothermal actuator is based on the bimorph effect. A current is fed through two so-called 'hot arms' (275 μm long), heating them due to ohmic resistance, which, as a consequence, expand due to thermal expansion. A so-called cold arm, that is not heated and therefore is not subject to thermal expansion, is attached in parallel to the hot arms. The thermal expansion of the hot arms in connection with the not expanding cold arm creates a torque. It is this torque which causes the tweezers to close (Fig. 1).

In the conventional single hot arm design, the current passes through the hot and cold arm. In order to avoid heating of the cold arm, the cold arm must be wide and short for low resistance, thus interfering with the demands for mechanical elasticity. With the two-hot-arm design, the current passes through the hot arms only, not heating the cold arm.

The base material is single crystalline silicon, which is coated by thermally grown silicon oxide serving as an insulating layer. The current is fed through a metal layer (Cr/Au) on top of the oxide. Joule heating appears in the metal layer, which heats up the underlying oxide and silicon.

The voltage required for full closing is relatively low (5 V approx.), with a current draw of only a few tens of Milliampères (50-60 mA). Therefore, the gripper device can be driven by standard TTL logic chips without the need for additional voltage or power amplifiers.

The design was optimized employing finite element simulations of the thermal and mechanical response of the device (Fig. 1).

Fabrication

The devices are made from single crystalline silicon (100) wafers. The fabrication sequence is a combination of modified SCREAM and LIRIE process. The structures are transferred into an oxide layer (1.2 μm) on top of the wafer by means of contact

print lithography and RIE. After resist stripping, the structures are etched ($70\ \mu\text{m}$ typical) into the bulk silicon by means of gas chopping DRIE (deep reactive ion etching). The sidewalls are passivated by means of thin (100 nm) dry oxidation. The passivation at the trench floors is removed by reactive ion sputtering.

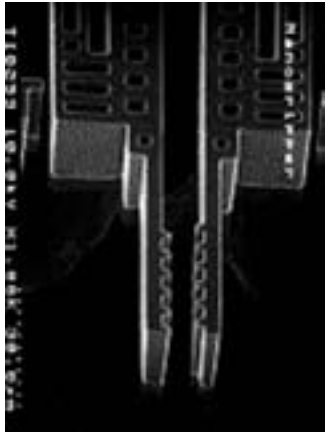


Fig. 2: SEM image of a fabricated microgripper

The movable structures are released by means of isotropic dry etching. Metalization for electrical contacts completes the fabrication sequence. This fabrication process is self-aligned and requires only one lithographic mask.

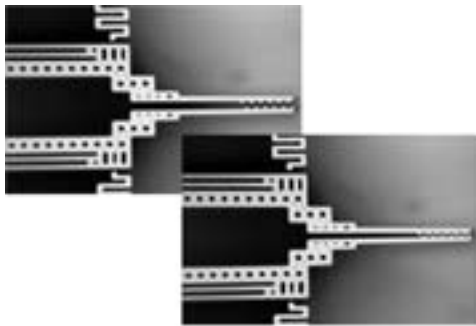


Fig. 3: Microgripper operation under atmosphere (viewed through optical microscope)

After separation, the devices were mounted and bonded to ceramic holders. The total dimensions of the device including the holder are approximately $10 \times 5 \times 1.5\ \text{mm}^3$. Figure 2 shows a fabricated microgripper.

Experiments

The devices were operated under normal atmosphere, and the gripping motion was observed by an optical microscope (Fig. 3). DC voltage was supplied to the gripper, and the voltage and current for fully closed grippers were recorded. Typical values are 4.5-5.5 V at 50-60 mA, in agreement with the calculated power of 240 mW. Destruction due to overheating appears at driving voltages above 7 V. Dynamic measurements were not done, however, the grippers open and close within much less than 1 second.

Gripping experiments

For gripping experiments, the devices were mounted inside a scanning electron microscope (SEM) on a x-y-z stage. Even in the vacuum of the SEM, the operation parameters were not noticeably altered, indicating that heat transfer through air or convection can be neglected for such devices.

For the gripping experiments, a second passive gripper was used as the target. The active microgripper approaches the target microgripper and grabs a piece of delaminating metal layer. By moving the stage backwards, the active gripper pulls at the metal film. As a consequence, the bonding between the film and the target microgripper breaks, and the micro part is picked up by the active microgripper.

The taken metal part is then transferred to the tweezers of the passive gripper, and put down. Figure 4 shows the pick-up sequence.

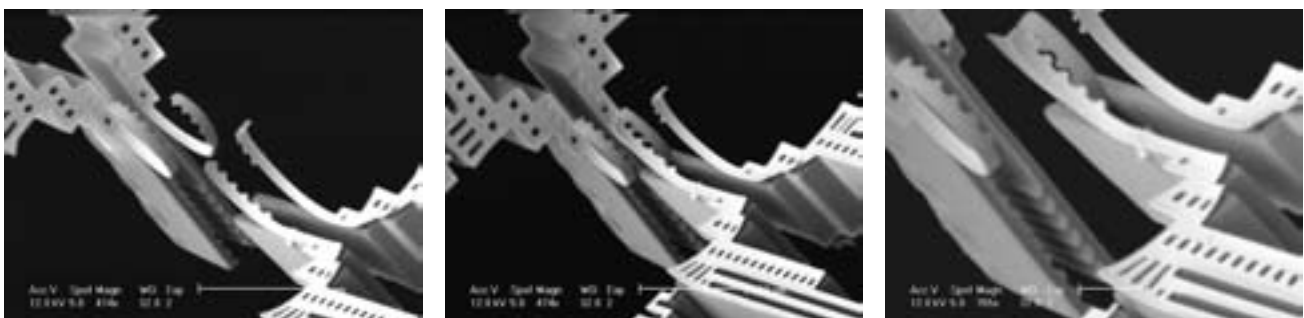


Fig. 4: Pick-up sequence under vacuum in a SEM. The active microgripper (right) approaches the passive target microgripper (left), grabs the delaminating metal film, and picks it up.

Equipment for the Crystallization of Glass and Glass Melts at High Temperatures in Strong DC Magnetic Fields

B. Hamann*, C. Kraffert, Y. Ludwig, U. Schadewald, and A. Pothérat
Department of Electrothermal Energy Conversion

The Junior Research Group "Electromagnetic Processing of Materials" (EPM) investigates the electromagnetic influence of strong magnetic fields on materials. The scientific goal of EPM is to install and develop the technical equipment, to produce materials in small quantities and to measure their properties.

In order to process glass melts in high magnetic fields special equipment is necessary. It consists of two basic components; a cryogen free magnet (CFM), manufactured by Cryogenic Ltd. London and a high temperature furnace, from Xerion - Advanced Heating Freiberg.

The most important component is the CFM, that provides a DC magnetic field with a flux density up to 5 Tesla. The CFM operates with a supra conducting coil of NbTi. In order to reach the supra conducting regime it is necessary to run the coil at a temperature of about 4 K. This is reached with the 4K-Cryocooler, a cryogen-free cooling system from Sumitomo. Gaseous helium is compressed in two steps so the heat is diverted from the supra conducting coil indirectly. The CFM and the cooling system are working separately, both are controlled independently from each other.

The magnetic flux density is operated by the power supply. This controls the current of the coil and thus the magnetic flux density. Once the chosen magnetic flux density is reached the coil can be disconnected from the power supply. The provided magnetic field is stable over several weeks (persistent mode). The CFM is tiltable, so that the work space (diameter 300 mm, height 400 mm) can be used in vertical and horizontal positions at room temperature.

For our high temperature investigations the CFM had been fitted with a specially designed high temperature furnace (HTO). This device allows temperatures up to 1500 °C for long periods of time. The diameter of the working room is 50 mm and the usable height is up to 100 mm. The positions of CFM and HTO were arranged in such a way, that the maximum temperature is on the same position as the maximum of the magnetic field.



Fig. 1: Cryogen free 5T-DC-magnet with high temperature furnace.

A gas supply providing Ar, CO/CO₂, O₂ and air atmosphere control with the furnace completes the equipment. It is possible to supplement the system with other elements for different applications. The whole system is quickly configurable and applicable for academic and industrial applications.

At the moment, ongoing EPM research focuses on the crystallisation of bariumhexaferrite (BHF, BaFe₁₂O₁₉) in the magnetic field. Basis for this work is the ternary system BaO-B₂O₃-Fe₂O₃. We are also dealing with the known glass crystallisation technique [2, 3] as well as with the direct crystallisation within the melt [4]. For all experiments a composition of 39.6 mol% BaO, 35.4 mol% B₂O₃ and 25 mol% Fe₂O₃ is used.

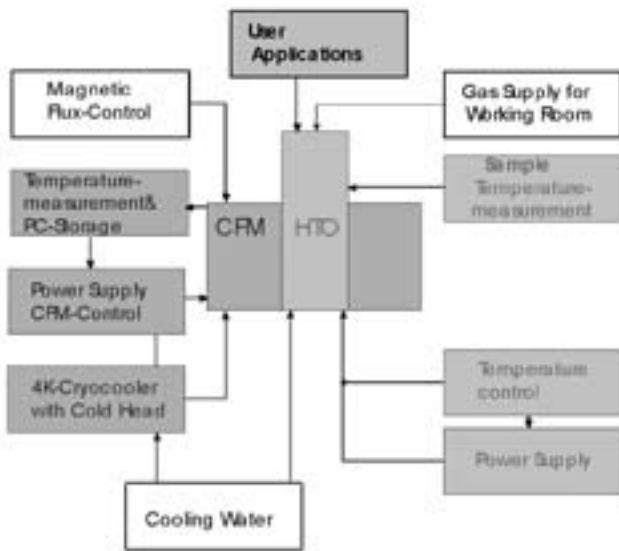


Fig. 2: Scheme of cooperation between the units. We are pleased to make the system available to potential academic and industrial users. You can find further information on the equipment in [1].

For the crystallisation in the melt we observed an orientation of the investigated BHF crystals on the surface of the solidified melt but not inside the melt itself. The reason is probably the low coercive field force and the low remanence at the crystallisation temperatures above the Curie point. At this time little can be said about the interaction between the used magnetic DC field and the BHF crystals in the melts. We assume, that there are significant interactions between the thermal induced streaming of the electrically conductive melt in the crucible and the magnetic field.

The magnetic properties of the final BHF crystals depend strongly on the tempering conditions. Figure 3 shows the dependence of magnetic properties from the temperature for material from the glass crystallisation technique (Ha-N, interrupted line) and of BHF made directly from the melt (HaFe5, continuous line). The magnetic properties are between already known soft magnetic materials and excellent hard magnetic ferrites.

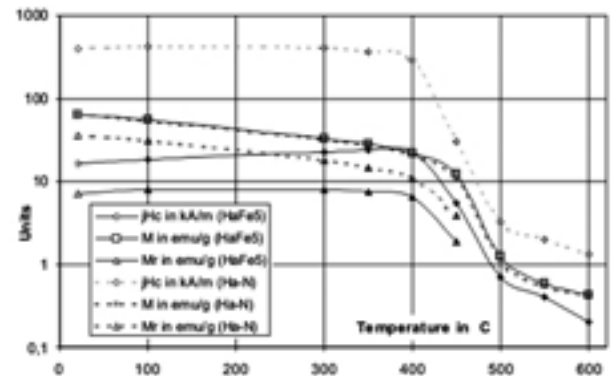


Fig. 3: Dependences on temperature of magnetic properties for different samples.

The BHF crystals grown in the melt as single crystals and have dimensions up to 5 mm in length. The thickness is a function of tempering duration. Such crystals have not been available yet. It is well imaginable, that they are applicable not only for manufacturing magnets. We propose to grow such crystals using crucibles with a wider surfaces. This particular geometry yields a higher quantity of well-shaped crystals [4].

[1] Hamann, B., Ludwig, Y., Lohse, U., Ertel-Ingrisch, W., Kraffert, C.: Experimentiereinrichtung für Kristallisation bei hohen Temperaturen im starken magnetischen Gleichfeld. - elektrowärme international, Heft 2, Jun 2006, p. 104 - 106.

[2] Knauf, O.: Nutzung großer Abkühlgeschwindigkeiten zum Amorphisieren spontan kristallisierender oxidischer Schmelzen, dargelegt am System BaO-Fe₂O₃-B₂O₃, Habilitation, Ilmenau, 1988.

[3] Ertel-Ingrisch, W., Hartmann, K., Ludwig, Y., Weih, P.: Crystallisation Inside High Magnetic DC Fields, 50. Intern. Wiss. Kolloq., Ilmenau, Sept. 2005.

[4] Hamann, Schawohl, J., Kraffert, C.: Large Hexaferrite single Crystals Grown in a DC magnet Field, 51th IWK, Reihe 7 (Electro-Process Technologies), Ilmenau, Sept. 2006.

Servo-hydraulic Brake Robot – Objectifying of the brake pedal feel of motorcars

K. Augsburg* and J. Sandler
Department of Automotive Engineering

Background

It is quite evident that the human-machine-interfaces of the braking system highly contribute to vehicle comfort and vehicle safety. Therefore the optimal design of those interfaces is an important development objective. There is a need for a system which allows the measurement of brake pedal characteristics under different driving and application conditions objectively. In addition, it is necessary to analyze car interfaces efficiently and to generate precise requirements. For that reason the brake robot was developed.



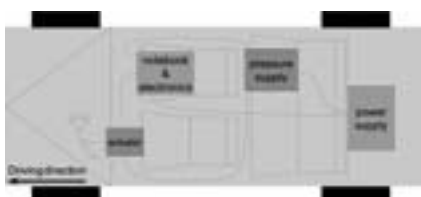
Objectives

The Brake Robot is capable for reproducing brake pedal actuation patterns with high dynamic and precision. With this measurement and actuation system the static and dynamic characteristics of the feel of applying the brake can precisely be determined. Standard pedal actuation patterns are pre-programmed. These patterns enable comparable and effective measurements which exceed the performance and effectivity of any test driver actuated measurement method.

Modular system design



Actuator (servo-hydraulic linear pedal actuation system).



Main modules.



Power supply.



Pressure supply.



Equipped test car.

Control and Data Acquisition Software

The system operates with any notebook equipped with an ethernet card. The software is programmed in LabVIEW RT.



Control and data acquisition software.

Pedal actuation patterns

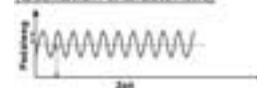
Moving car - force controlled:



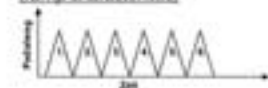
Not moving car - travel controlled: (ramp characteristic)



Not moving car - travel controlled: (Oscillation characteristic)



Not moving car - travel controlled: (ramp characteristic)



Specification

Actuation:

- Servo-hydraulic linear pedal actuation system

Operation range:

- Pedal force $F=0..1500$ N
- Pedal velocity $v=0..1000$ mm/s

Operation modes:

- Operation in moving and not moving cars
- Force and travel controlled mode
- Ramp and oscillation characteristic

Data acquisition:

- Pedal force, pedal distance, brake pressure, booster vacuum, vehicle speed, vehicle deceleration
- Scan rate up to 6 kHz

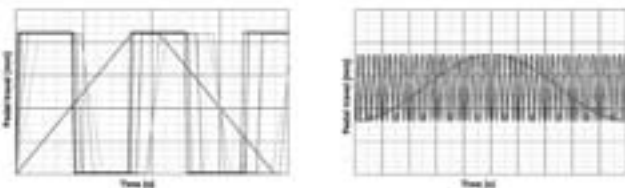
Safety:

- Fail safe mode (shut off and hydraulic unlock)
- Adjustable mechanical pedal force limitation

Measurement example

The following diagrams show some examples of measurements. The first diagrams show a not moving car controlled by a ramp or an oscillation pattern for the brake pedal actuation. The actuation speed was varied.

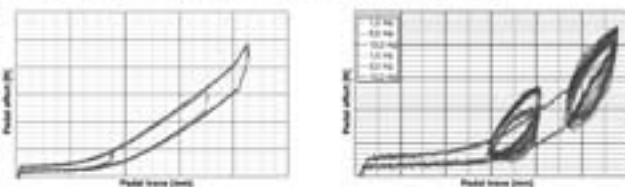
Not moving car - travel controlled (Ramp and oscillation characteristic):



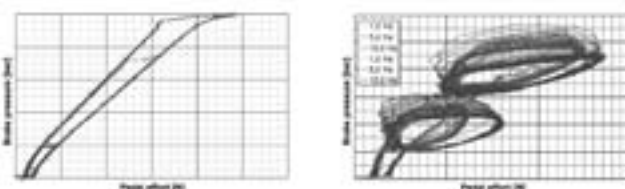
System output signals are shown on the next diagrams.

The top diagrams plot pedal force versus pedal distance (pedal characteristic) at different maximum distances and the bottom diagrams plot brake pressure versus pedal force (vehicle response).

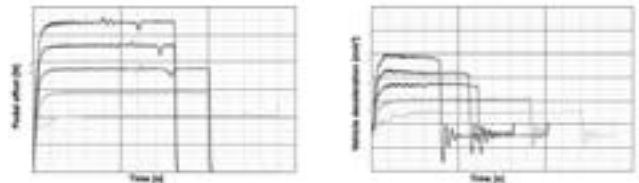
Pedal characteristic (Ramp and oscillation characteristic):



Vehicle response (Ramp and oscillation characteristic):

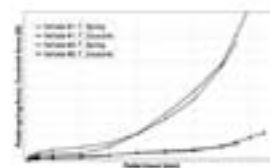


The next example shows brake characteristic measurements for a moving car. In contrast to the previous diagrams the brake pedal is controlled by a constant force pattern (left). The right diagram shows the resulting deceleration against time.

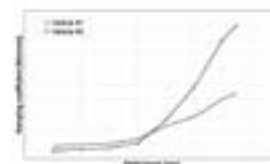


This precise actuation and measurement system is used to analyze different cars and to develop models which uniquely describe the brake characteristic. The model parameters for two different cars are shown in the following diagrams.

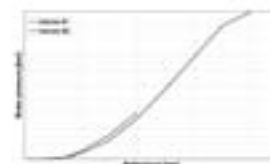
Pedal feel parameter: F_{max} , F_{min}



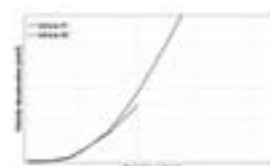
Pedal feel parameter: k



Pedal feel parameter: p_{max}



Pedal feel parameter: a_{br}



Representation of Controversial Scientific Topics in the Mass Media: An Analysis of Coverage of “Mobile Radio and Electronic Smog”

A. Kirpal*, M. Norbey, and S. Stierhof

Department of Technical and Economic History

Introduction

In recent years mobile radio has developed into one of the most significant technologies of our time. Meanwhile Germany has 70 million mobile phone users [1] – mobile radio has reached an important position in people’s everyday communication behaviour. Despite the tremendous market penetration of mobile radio, fear of electromagnetic pollution is heard in the population: The electromagnetic fields used in mobile radio technology are in suspicion to cause negative consequences on health.

For further success of mobile radio the public opinion is very important. Mass media such as newspapers, magazines, TV, or some online media play an important part in forming public opinion, especially in case of controversial and ambiguous themes. These can influence the public opinion decisively by their reporting [2],[3],[4]. This applies to the area of high technologies such as nanotechnology, too.

Many current analyses examine the broad variety of contributions. Besides, the results of technology application are examined. Analyses of relevant informatively popular-scientific and popular-technical articles – like explored in this study – were little proved until now. An exception is given in [5].

Research-leading Questions

The subsequently explained study deals with the main question how the national German newspapers “Frankfurter Allgemeine Zeitung” (FAZ) and “Süddeutsche Zeitung” (SZ) report about the topic “Mobile Radio and Electronic Smog”. This question is specified by the following partial questions: How has the coverage of “Mobile Radio and Electronic Smog” developed into a quantity basis during the analysed period from 1st January, 1993 till 31st December, 2004? On which topics is the coverage of “Mobile Radio and Electronic Smog” mainly focused and how has the topic structure developed during this period? How has the tendency of the coverage developed during the analysis period? Starting from these questions, hypotheses were developed and proved by means of content analysis.

Method

To analyse the coverage of “Mobile Radio and Electronic Smog”, the prior method is the quantitative content analysis which is defined as an

empiric method of the systematic, intersubjectively understandable description of content and the formal signs of communications [6]. It is its task to transfer the subjectively perceived extracts of reality into data structures so that these issues can be compared inter-subjectively. The main interest (of the content analysis) consists in reducing complexity in order to disclose structural information of text amounts. The concern of the content analysis is not only a pure description of communication but also gives reasonable statements about phenomena beyond the structure of the specific data material.

In this study the content analysis proves in which way the FAZ and SZ have reported about “Mobile Radio and Electronic Smog” from 1993 to 2004. All articles published in this period by FAZ and SZ about “Mobile Radio and Electronic Smog” are considered as analysis material.

To answer the main questions, eight principle categories are selected for the identification of the content: (1) legal aspects, (2) infrastructures, (3) technical aspects/functional principle/net organization, (4) limit values, (5) researches, (6) biophysical effects of the electromagnetic fields of the mobile radio, (7) benefits through the mobile radio and (8) tendency of the article concerning the evaluation of the mobile radio technology (positive, neutral, negative). Single articles are defined as encoding units.

Results

The evaluation of the analysed material shows the following central results. The number of articles titled “Mobile Radio and Electronic Smog” has strongly increased in the analysed newspapers during the analysis period and reached its maximum with 46 articles in 2001. Regarding the distribution of the articles, there is a strong imbalance between the two newspapers. 71% of the articles account for the SZ, 29% for the FAZ (see also Tab. 1). The majority of articles has been published under the columns regional, nature/science and technology, and economy, whereas the SZ focused a higher regional importance than the FAZ.

Besides the central topics “Mobile Radio and Electronic Smog” the biophysical effects are as well related to the electromagnetic fields of the mobile radio as to particular effects concerning cancer and non-thermal capacities.

	1993	1994	1995	1996	1997	1998	1999	2000	2001	2002	2003	2004
FAZ	14	2	1	2	1	6	6	3	14	11	3	4
SZ	4	12	7	10	14	9	13	22	32	21	8	13
Σ	18	14	8	12	15	15	19	25	46	32	11	17

Tab. 1: Absolute appearance of the articles on the subject "mobile radio and electronic smog" from 1993 to 2004.

Furthermore the location problem is seen as another important topic of the coverage, especially statements regarding the conservation resp. the further extension of the infrastructure and the demands to stop this extension resp. to reduce the infrastructure.

A similar statement can be made for the topic of research. There is a substantial interest in the description of current research activities, as well as statements that there are no unambiguous or even inconsistent results so far. The discussion about the legal valid limit belongs to the central topics, regarding values of height and of determination and the actually measured field strength.

Concerning the development of the topic structure during the analysed period, it can be stated that the proportion of articles referring to technology and benefit is very high in the first years, then decreases and increases before the implementation of the UMTS technology. Particularly the interest in effective radiated power of transmitting stations has clearly accumulated over the years. The proportions of the different categories of the topics biophysical effects, research and limit values are fluctuating - on a relatively high level. However, the discussion about limit values, an increase is registered in representation of demands for resp. against a reduction of the existing limit values (Fig. 1). The proportion concerning the location problem (especially the condition of the infrastructure in general, the demand for stop/reduction of the infrastructure as well as the conservation/extension of the infrastructure as a fact) grows.

The evaluation of the tendency of the coverage shows: 19% of 232 articles are classified as rather positive, 41% as neutral and 39% as rather negative. Clear differences appear between the two newspapers.

The representation of the topic "Mobile Radio and Electronic Smog" seems to be mainly neutral in the FAZ (64%), rather negative in the SZ (52%). A deviation of the tendency was observed during the analysed period and can be divided into three phases: The first phase from 1993 to 1996 has an overbalance of articles with neutral tenor. There is a deviation to rather negative articles in the second phase from 1997 to 2001.

	1993	1994	1995	1996	1997	1998	1999	2000	2001	2002	2003	2004
I	3	5	2	3	1	2	2	1	7	11	3	5
II	10	7	4	6	6	4	10	10	20	11	4	4
III	5	2	2	3	8	9	7	14	19	10	4	8
Σ	18	14	8	12	15	15	19	25	46	32	11	17

I = rather positive II = neutral III = rather negative

Tab. 2: Absolute appearance of the articles after tendency of the representation in the time course.

In the third phase from 2002 to 2004 the proportion of neutral articles decreases while the proportion of the articles with rather positive representation increases. In consequence of this development a polarized coverage can be stated in this phase (Tab. 2).

Conclusion

As a result, it can be held on that there is no uniform trend of coverage neither temporal nor related to content. It is to be supposed that in analysis of other media similarly different results would occur. If different topics from the field of science and technology would be analysed in this way, a similar inconsistent media reporting could be found. Continuing and deepening analyses on this topic are useful.

There is no statement possible, which proves knowledge transfer proceeded from newspaper to the audience. It is unknown, too, what people think about electronic smog and potential hazards. It is very difficult to examine because of the complex influences on human knowledge. Other researches are necessary.

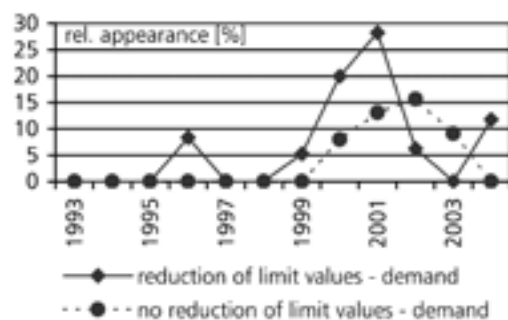


Fig. 1: Development of the subject "limit values" in the time course (relative appearance).

[1] Informationszentrum Mobilfunk, Online: <http://www.izmf.de/html/de/index.html> [01.02.2005].
 [2] W. Früh, Realitätsvermittlung durch Massenmedien, Opladen, 1994.
 [3] G. Bentele, Wie wirklich ist die Medienwirklichkeit?, in G. Bentele, and M. Rühl (eds.), Theorien öffentlicher Kommunikation, München, 1993, p. 152-171.
 [4] H. M. Kepplinger, Künstliche Horizonte, Frankfurt a. M./New York, 1989.
 [5] A. Kirpal, and M. Norbey, Technikkommunikation bei Hochtechnologien, Ilmenau, 2005.
 [6] W. Früh, Inhaltsanalyse, Konstanz, 2001.

Communication Research on Nanotechnologies

A. Ingerl* and N. Döring

Department of Media Design / Media Psychology

I. MEDIA COVERAGE OF NANOTECHNOLOGIES A CONTENT ANALYSIS OF GERMAN PRINT MEDIA

R. Petkova and L. Yordanova

As one of the most innovative and up-to-date technologies, nanotechnology is increasingly covered by the German mass media. The use of nanoproducts in our everyday life as well as the opportunities and challenges of this new key technology are featured more and more extensively in the German print and broadcast media. Reports about the advantages of nanotechnology, such as new approaches to cancer treatment or the usage of innovative chips for IT products, are often present in the German media. However, there are also news articles referring to possible risks of nanotechnologies, like unsafe nano-robots or toxic nanoparticles.

The goal of this project is to find out which aspects of nanotechnology are most frequently represented in German print and online media and how they are illustrated and evaluated.

The sample for the content analysis contains a) articles in the most widely spread German daily newspapers and news magazines (FAZ, Süddeutsche Zeitung, BILD, Die Welt, Die Zeit and Der Spiegel), b) the most popular science magazines (GEO, Spektrum der Wissenschaft, Bild der Wissenschaft and P.M.) as well as c) the frequently addressed online science portals and magazines (Morgenwelt, geoscience online, sciencegarden and bildungsforschung). All the articles published in the period from January 1, 2003 till December 31, 2005 will be analyzed using the SPSS statistics software package.

The results of the analysis should give an idea of the image of nanotechnology in German mainstream print and online media and indirectly about the forming of public opinion regarding this new technology. Future public-relations campaigns by the IMN - with the objective of making nanotechnology more understandable to different audiences as well as presenting the IMN as a center with great potential for further exploring and developing nanotechnology - can rely on the results of the study.

II. THE IMPACT OF NANOTECHNOLOGIES COVERAGE

AN EXPERIMENTAL STUDY ON KNOWLEDGE AND ATTITUDE EFFECTS

S. Riedel

How does a news article on nanotechnology (see study I) change the recipient's knowledge and attitude regarding the issue? To test knowledge and attitude shortterm effects an experimental study is conducted presenting different groups of subjects with different news articles. The articles are systematically altered in accordance with the communication studies theory of framing. Both visual and textual framing are involved. Results may help to further develop framing theory and to efficiently use framing as a communication method for public relations.

III. A NANOTECHNOLOGIES WEB SITE FOR THE PUBLIC WEB SITE DESIGN, PRODUCTION AND EVALUATION

I. Horlbeck, N. Weise and M. Kirsch

In the mass media nanotechnologies are most often presented as future technologies related with utopian or dystopian visions (see study I). Non-experts seem to be unaware of the current uses of nanoproducts in everyday life.

To increase the public interest and understanding of nanotechnologies, these everyday uses are to be emphasized and illustrated. The IMN can serve as an expert author of a respective nanotechnologies Web site for the public (information service) and may at the same time attract public attention and gain reputation via the Web site (public-relations function).

The aim of the project is to design, produce and evaluate an attractive and informative Web site. Its main purpose is to convey that micro- and nanotechnologies are already part of our daily life and not just a future vision (everyday frame, see study II). Examining specific examples the daily usage is shown and background information is provided (e.g.

automotive engineering, cosmetic products, solar installations, surface coating of eyeglasses or sanitary installations etc.).

Additionally the opportunities and challenges of micro- and nanotechnologies will be emphasized and discussed. News articles (see study I) are compared with expert statements from nanoscientists.

Furthermore, ongoing research projects at the IMN will be presented and explained to the public. Helpful links and book recommendations relating to the topic will also be provided.

During and after the Web site implementation and Web site diffusion (external links, search engine optimization etc.), an empirical evaluation study will be conducted testing the utility, usability and user experience of the Web site.

IV. PUBLIC RELATIONS FOR THE IMN DEVELOPING PR CONCEPTS AND MATERIALS

K. Fleischmann, M. Günther, N. Schmidt,
M. Seifert and K. Wand

The university seminar "Communication about Nanotechnologies" (lecturer: Andreas Ingerl) focuses on creating and realizing a public-relations concept together with and for the IMN/ZMN. It combines the expertise and ideas of media students with the expertise and opportunities of the IMN/ZMN. Target groups are scientists/students, companies and the general public. General PR concepts are discussed and developed and concrete PR materials are produced (see study III for a related and integrated project).



During the first semester the students offered useful ideas for all kinds of media and events. One priority is to support the IMN/ZMN presentation at the fair "Micronora", that takes place September 26 to 29, 2006 in Besançon, France, by creating video loops, slide shows, press portfolios and giveaways to make it a highlight.

The second semester will focus on the extension of the results, the conception of actions and the visualization of nanotechnologies.

Selected Publications and invited Conference Contributions

The Coulomb Instability of Charged Microdroplets: Dynamics and Scaling

T. Achtzehn, R. Müller, D. Duft, and T. Leisner, *European Physical Journal D* **34** (2005) 311-313.

Equation of state for C₆₀ fullerene aqueous solutions

I. Adamenko, K.O. Moroz, Y. I. Prylutsky, P. Eklund, P. Scharff, and T. Braun, *International Journal of Thermophysics* **26**(3) (2005) 795-805.

Microtribology of silicon, oxide, and carbide surfaces

S.I.-U. Ahmed, G. Bregliozzi, and H. Haefke, *Tribotest*, **12**(2) (2006), 175.

Pt/GaN Schottky diodes for hydrogen gas sensors

M. Ali, V. Cimalla, V. Lebedev, H. Romanus, V. Tilak, D. Merfeld, P. Sandvik, and O. Ambacher, *Sensors and Actuators B* **113** (2006) 797-804.

Phenylene-ethynylene/phenylene-vinylene hybrid polymers: optical and electrochemical characterization, comparison with poly[2-methoxy-5-(3,7-dimethyloctyloxy)-1,4-phenylene vinylene] and application in flexible polymer solar cells

M. Al-Ibrahim, A. Konkin, H.-K. Roth, D.A.M. Egbe, E. Klemm, U. Zhokhavets, G. Gobsch, and S. Sensfuss, *Thin Solid Films* **474**(1-2) (2005) 201-210.

The influence of the optoelectronic properties of poly(3-alkylthiophenes) on the device parameters in flexible polymer solar cells

M. Al-Ibrahim, H.-K. Roth, M. Schroedner, A. Konkin, U. Zhokhavets, G. Gobsch, P. Scharff, and S. Sensfuss, *Organic Electronics* **6**(2) (2005) 65-77.

Flexible large area polymersolar cells based on poly(3-hexylthiophene) / fullerene

M. Al-Ibrahim, H.-K. Roth, U. Zhokhavets, G. Gobsch, and S. Sensfuss, *Solar Energy Materials & Solar Cells* **85** (1) (2005) 13-20.

Effects of solvent and annealing on the improved performance of solar cells based on poly(3-hexylthiophene): Fullerene

M. Al-Ibrahim, S.Sensfuss, G. Gobsch, and O. Ambacher, *Appl. Phys. Lett.* **86** (2005) 201120. *Virtual Journal of Nanoscale Science & Technology* **11**(20) (2005).

Comparison of normal and inverse poly(3-hexylthiophene) / fullerene solar cell architectures

M. Al-Ibrahim, S. Sensfuss, J. Uziel, G. Ecke, and O. Ambacher, *Solar energy Materials and Solar Cells* **85**/2 (2005) 277.

Design Considerations for efficient planar optical systems

M. Amberg and S. Sinzinger, *Opt. Comm.* 2005 (accepted).

Strong dispersion of the surface optical phonon of silicon carbide in the near vicinity of the surface Brillouin zone center

T. Balster, F.S. Tautz, V.M. Polyakov, H. Ibach, S. Sloboshanin, R. Ötting, and J.A. Schaefer, *Surface Science* **600**(14) (2006) 2886.

Spectral broadening and diffusion by torsional motion in Biphenyl

W.J.D. Beenken and H. Lischka, *J. Chem. Phys.* **123** (2005) 144311.

Mechanical behaviour of overlap joints of titanium

J.P. Bergmann, *Science and Technology of welding and joining*, Vol. **10** No. 1 (2005) 50-60.

Strukturbiildung beim Mikro-Sandstrahlen mit Maskierung

R. Bergmann, C. Kremin, A. Albrecht, and T. Frank, *50. Internationales Wissenschaftliches Kolloquium*, TU Ilmenau (2005) 325-326.

Riporti superficiali laser: aumento di efficienza e flessibilità tramite processi ibridi

J.P. Bergmann, J. Wilden, and M. Dolles, *Rivista Italiana della Saldatura*, Numero **6** (2005) 809-816.

Metodi di giunzione laser per lamiere di acciaio zincato e per giunti ibridi di acciaio-alluminio

J.P. Bergmann, J. Wilden, M. Dolles, and M. Guyenot, *Rivista Italiana della saldatura*, Numero **1** (2005) 81-89.

Working zinc-coated steels and making steel-aluminiumalloys joints using high power lasers - brazing and braze welding

J.P. Bergmann, J. Wilden, M. Dolles, and M. Guyenot, *Welding International*, Vol. **20** 1 (2006) 37-44.

The Electrophoretic Deposition of Inorganic Nanoscaled Materials - A review-

A.R. Boccaccini, J. A. Roether, B.J. C. Thomas, M.S.P. Shaffer, E. Chavez, E. Stoll, and E.J. Minay, *Journal of the Ceramic Society of Japan* **114** (2006) 1 1-14.

LTCC-Technologie als Grundlage für mikro-mechanische Funktionselemente

J. Botiov, A. Albrecht, H. Wurmus, K.-H. Drüe, and M. Hintz, 50. Internationales Wissenschaftliches Kolloquium, TU Ilmenau (2005) 185-186.

Dielectric function and critical points of the band structure for AlGaIn alloys

C. Buchheim, R. Goldhahn, M. Rakel, C. Cobet, N. Esser, U. Rossow, D. Fuhrmann, and A. Hangleiter, *phys. stat. sol. (b)* **242**(13) (2005) 2610-2616.

Critical points of the bandstructure of AlN/GaN superlattices investigated by spectroscopic ellipsometry and modulation spectroscopy

C. Buchheim, R. Goldhahn, A.T. Winzer, C. Cobet, M. Rakel, N. Esser, U. Rossow, D. Fuhrmann, A. Hangleiter, and O. Ambacher, *phys. stat. sol. (c)* **3** (2006) 2009-2013.

Tuning of Surface Properties of AlGaIn/GaN Sensors for Nanodroplets and Picodroplets

C. Buchheim, G. Kittler, V. Cimalla, V. Lebedev, M. Fischer, S. Krischok, V. Yanev, M. Himmerlich, G. Ecke, J. A. Schaefer, and O. Ambacher, *IEEE Sensors Journal* (6) (2006) 881-886.

Evolution and experiences with different drop-on-demand systems

J. Burgold, F. Weise, M. Fischer, G. Schlingloff, Th. Henkel, J. Albert, G. Mayer, and A. Schober, *Macromol. Rapid Commun.* **26** (2005) 265-280.

Mobility edge in hydrogenated amorphous carbon

G. Cherkashinin and O. Ambacher, *Appl. Phys. Lett.* **88** (2006) 172114.

The performance of AlGaIn solar blind UV photo-detectors: responsivity and decay time

G. Cherkashinin, V. Lebedev, R. Wagner, I. Cimalla, and O. Ambacher, *phys. stat. sol. (b)* **7** (2006) 1713-1717.

Wet chemical etching of AlN in KOH solution

I. Cimalla, Ch. Förster, V. Cimalla, V. Lebedev, D. Cengher, and O. Ambacher, *phys. stat. sol. (c)* **3** (2006) 1767-1770.

Impact of device technology processes on the surface properties and biocompatibility of group III nitride based sensors

I. Cimalla, F. Will, K. Tonisch, M. Niebelschütz, V. Cimalla, V. Lebedev, G. Kittler, M. Himmerlich, S. Krischok, J. A. Schaefer, M. Gebinoga, A. Schober, T. Friedrich, and O. Ambacher, 51. Internationales Wissenschaftliches Kolloquium, TU Ilmenau (2006).

Surface conductivity of epitaxial InN

V. Cimalla, G. Ecke, M. Niebelschütz, O. Ambacher, R. Goldhahn, H. Lu, and W.J. Schaff, *phys. stat. sol. (c)* **7** (2005) 2254-2257.

Growth of AlN nanowires by metal organic chemical vapour deposition

V. Cimalla, Ch. Förster, D. Cengher, K. Tonisch, and O. Ambacher, *phys. stat. sol. (b)* **243** (2006) 1476-1480.

Pulsed mode operation of strained microelectro-mechanical resonators in air

V. Cimalla, Ch. Foerster, F. Will, K. Tonisch, K. Brueckner, R. Stephan, M. E. Hein, O. Ambacher, and E. Aperathitis, *Appl. Phys. Lett.* **88** (2006) 253501. *Virtual Journal of Nanoscale Science & Technology*, **14** (1) (2006).

The conductivity of Mg-doped InN

V. Cimalla, M. Niebelschütz, G. Ecke, O. Ambacher, R. Goldhahn, H. Lu, and W. J. Schaff, *phys. stat. sol. (c)* **3** (2006) 1721-1724.

Surface band bending at nominally undoped and Mg-doped InN by Auger Electron Spectroscopy

V. Cimalla, M. Niebelschütz, G. Ecke, V. Lebedev, O. Ambacher, M. Himmerlich, S. Krischok, J.A. Schaefer, H. Lu, and W.J. Schaff, *Physica Status Solidi (a)* **203** (2006) 59.

Polytype control and properties of AlN on silicon

V. Cimalla, V. Lebedev, U. Kaiser, R. Goldhahn, Ch. Förster, J. Pezoldt, and O. Ambacher, *phys. stat. sol. (c)* **2** (2005) 2199-2203.

The b subunit of the Na⁺/K⁺-ATPase follows the conformational state of the holoenzyme

R. Dempski, T. Friedrich, and E. Bamberg, *J. Gen. Physiol.* **125** (2005) 505-20.

Real-time position determination of light spot

T. Djamiykov, N. Nenov, S. Ovcharov, S. Hecht, and M. Milushev, 50. Internationales Wissenschaftliches Kolloquium, TU Ilmenau (2005) 283-284.

Localized donor state above the conduction band minimum in InN revealed by high pressure and temperature transport experiments

L.H. Dmowski, K. Dybko, J. Plesiewicz, T. Suski, H. Lu, W. Schaff, M. Kurouchi, Y. Nanishi, L. Konczewicz, V. Cimalla, and O. Ambacher, *phys. stat. sol. (b)* **243** (2006) 1537-1540.

Resonant localized donor state above the conduction band minimum in InN

L.H. Dmowski, J.A. Plesiewicz, T. Suski, Hai Lu, W. Schaff, M. Kurouchi, Y. Nanishi, L. Konczewicz, V. Cimalla, and O. Ambacher, *Appl. Phys. Lett.*, **86** (2005) 262105.

Dose Dependence of the optical properties of fullerene films subjected to the electron irradiation

O.P. Dmytrenko, M.P. Kulish, N.N. Belyi, Yu. I. Prylutsky, L.V. Poperenko, V.S. Stashchuk, V.G. Poroshin, E.L. Pavlenko, V.V. Shlapatskaya, H. Bernas, and P. Scharff, *Thin Solid Films* **495** (2006) 365-367.

Advanced electrical and stability characterization of untrimmed and variously trimmed thick-film and LTCC resistors

A. Dzedzic, A. Kolek, W. Ehrhardt, and H. Thust, *Microelectronics Reliability* **46** (2006) 352-359.

Defect related photoluminescence of epitaxial CuInS_2

J. Eberhardt, H. Metzner, R. Goldhahn, F. Hudert, U. Reislöhner, C. Hülsen, J. Cieslak, Th. Hahn, M. Gossla, A. Dietz, G. Gobsch, and W. Witthuhn, *Thin Solid Films* **480-481** (2005) 415-418.

Correlation Between Structural and Optical Properties of Composite Polymer/Fullerene Films for Organic Solar Cells

T. Erb, U. Zhokhavets, G. Gobsch, S. Raleva, B. Stühn, P. Schilinsky, C. Waldauf, and C.J. Brabec, *Adv. Funct. Mat.* **15**(7) (2005) 1193-1196.

Absorption and crystallinity of poly(3-hexylthiophene) / fullerene blends in dependence on annealing temperature

T. Erb, U. Zhokhavets, H. Hoppe, G. Gobsch, M. Al-Ibrahim, and O. Ambacher, *Thin Solid Films* **511-512** (2006) 483-485.

C_{60} single domain growth on indium phosphide and its reaction with atomic hydrogen

M. Eremtchenko, S. Döring, R. Temirov, and J.A. Schaefer, *Physical Review B* **71** (2005) 045410.

Surface reaction of C_{60} with atomic hydrogen: formation of a protecting hydrocarbon layer

M. Eremtchenko, R. Ötting, S. Krischok, S. Döring, R. Temirov, and J.A. Schaefer, *Fullerenes, Nanotubes, and Carbon Nanostructures* **13** Suppl. 1 (2005) 131-138.

Surface phonons of clean and hydrogen terminated Si(110) surfaces

M. Eremtchenko, F.S. Tautz, R. Ötting, V.M. Polyakov, F. Schwiertz, G. Cherkashinin, and J.A. Schaefer, *Surface Science* **582/1-3** (2005) 159-172.

Surface phonons of clean, hydrogen and deuterium terminated Si(001) surfaces

M. Eremtchenko, F.S. Tautz, R. Ötting, and J.A. Schaefer *Surface Science*, (accepted).

Formation of molecular order on a disordered interface layer: Pentacene/Ag(111)

M. Eremtchenko, R. Temirov, D. Bauer, J.A. Schaefer, and F.S. Tautz, *Physical Review B* **72** (2005) 115430.

Low temperature chemical vapor deposition of 3C-SiC on Si substrates

Ch. Förster, V. Cimalla, O. Ambacher, and J. Pezoldt, *Mater. Sci. Forum, Silicon Carbide and Related Materials 2004 (ECSCRM 2004)*, **483-485** (2005) 201-204.

Micro-electromechanical system based on 3C-SiC/Si heterostructures

Ch. Förster, V. Cimalla, K. Brückner, M. Hein, J. Pezoldt, and O. Ambacher, *Mater. Sci. Eng. C* **25** (2005) 804-808.

Processing of novel SiC and group III-nitride based micro-and nanomechanical devices

Ch. Förster, V. Cimalla, K. Brueckner, V. Lebedev, R. Stephan, M. Hein, and O. Ambacher, *phys. stat. sol.(a)* **202** (2005) 671-676.

Group III-nitride and SiC based micro- and nanoelectromechanical resonators for sensor applications

Ch. Förster, V. Cimalla, V. Lebedev, J. Pezoldt, K. Brückner, R. Stephan, M. Hein, E. Aperithitis, and O. Ambacher, *phys. stat. sol. (a)* **7** (2006) 1829-1833

A Model for Electromagnetic Control of Buoyancy Driven Convection in Glass Melts

C. Giessler, C. Sievert, U. Krieger, B. Halbedel, D. Hülsenberg, U. Lüdtkke, and A. Thess, *Fluid Dynamics and Material Processing*, Vol. 1 No. 3 (2005) 237-266.

Detailed analysis of the dielectric function for wurtzite InN and In-rich InAlN alloys

R. Goldhahn, P. Schley, A.T. Winzer, G. Gobsch, V. Cimalla, O. Ambacher, M. Rakel, C. Cobet, N. Esser, H. Lu, and W.J. Schaff, *phys. stat. sol. (a)* **203**(1) (2006) 42-49.

Critical points of the band structure and valence band ordering at the Γ point of wurtzite InN

R. Goldhahn, P. Schley, A.T. Winzer, M. Rakel, C. Cobet, N. Esser, H. Lu, and W.J. Schaff, *J. Cryst. Growth* **288**(2) (2006) 273-277.

Simulation of Nanoscale MOSFETs Using Modified Drift-Diffusion and Hydrodynamic Models and Comparison with Monte Carlo Results

R. Granzner, V. M. Polyakov, F. Schwierz, M. Kittler, R.J. Luyken, W. Rösner, and M. Städele, *Microelectron. Eng.* **83** (2006) 241-246.

Fast determination of evaporation enthalpies of solvents and binary mixtures using a micro silicon chip device with integrated thin film transducers

G.A. Groß and J.M. Köhler, *Thermochimica Acta* **432** (2005) 229-240.

Tribological characteristics of $WC_{1-x}W_2C$ and WC tungsten carbide films

M. Gubisch, Y. Liu, S. Krischok, G. Ecke, L. Spieß, J.A. Schaefer, and Ch. Knedlik, *Life cycle tribology, 31th Lyon-Leeds Symposium on tribology* **48** (2005) 409-417.

Entwicklung von nanoskaligen Wolframkarbid-Schichtsystemen für funktionelle Oberflächen einer NPM-Maschine

M. Gubisch, Y. Liu, T. Kups, H. Romanus, L. Spieß, J.A. Schäfer, and Ch. Knedlik, *50. Internationales Wissenschaftliches Kolloquium, TU Ilmenau* (2005) 35-36.

Nanoscale multilayer WC/C coatings developed for nanopositioning: Part I. Microstructures and mechanical properties

M. Gubisch, Y. Liu, L. Spiess, H. Romanus, S. Krischok, G. Ecke, J. A. Schaefer, and Ch. Knedlik, *Thin Solid Films* **488** (2005) 132-139.

Formation of Monomeric and Novolak Azo Dyes in Nanofluid Segments by Use of a Double Injector Chip Reactor

P.M. Günther, F. Möller, T. Henkel, J.M. Köhler, and G.A. Gross, *Chem. Eng. Technol.* **28**(4) (2005) 520-527.

Synthesis of diamond by electron irradiation of C_{60} intercalated graphite

V. Gupta, P. Scharff, and N. Miura, *Materials Letters* **59**(26) (2005) 3259-3261.

Synthese und Anwendungen von maßgeschneiderten $BaFe_{12-2x}A^{II}_x B^{IV}_x O_{19}$ -Pulvern

B. Halbedel, D. Hülsenberg, S. Belau, U. Schadewald, and M. Jakob, *cfi/Ber. DKG* **82** No. **13** (2005) 182-188.

Quantum mechanical magnetic-field-gradient drift velocity: An analytically solvable model

K. Handrich, *Phys. Rev. B* **72** (2005) 161308.

Room-temperature electroreflectance and reflectance of a GaAs/AlGaAs single quantum well structure

A. Herasimovich, S. Shokhovets, G. Gobsch, and D.S. Domanevskii, *Fiz. Tekh. Poluprovodn.* **39**(6) (2005) 729-734
Semiconductors **39**(6) (2005) 697-702.

Load Dependence and lifetime studies of self assembled monolayers

W. Hild, S.I.-U. Ahmed, G. Hungenbach, M. Scherge, and J.A. Schaefer, *Tribotest*, **12**(2) (2006) 161.

Microtribological properties of silicon and silicon coated with self-assembled monolayers: Effect of applied load and sliding velocity

W. Hild, S.I.-U. Ahmed, G. Hungenbach, M. Scherge, and J.A. Schaefer, *Tribology Letters*, (accepted).

Springende Wassertröpfchen

W. Hild, D. Duft, Th. Leisner, and J.A. Schaefer, *Physik in unserer Zeit* **2** (2006) 37.

Electronic Structure of the Surface of the Ionic Liquid [EMIM][Tf2N] Studied by Metastable Impact Electron Spectroscopy (MIES), UPS, and XPS

O. Höfft, S. Bahr, M. Himmerlich, S. Krischok, J.A. Schaefer, and V. Kempter, *Langmuir* **22** (2006) 7120.

Techniques in the Fabrication of Fibre-Optical MEMS Switches and their Application in Optical Communication Systems

M. Hoffmann, *MEMS/NEMS HANDBOOK: TECHNIQUES AND APPLICATIONS*, Editor: Cornelius T. Leondes, Springer-Verlag, 2006.

Morphology of polymer/fullerene bulk hetero-junction solar cells

H. Hoppe and N.S. Sariciftci, *Journal of Materials Chemistry* **16**(1) (2006) 45-61.

Nanometrology – Nanopositioning- and Nano-measuring Machine with integrated Nanoprobes

G. Jäger, T. Hausotte, E. Manske, H.-J. Büchner, R. Mastylo, N. Dorozhovets, R. Füßl, and R. Grünwald,
Proceedings of the International Conference on Advanced Manufacture (2005) in Taipei, 7-12 (Keynote speech).

Nanomesssysteme für Nanopositioniermaschinen

G. Jäger, T. Hausotte, E. Manske, H.-J. Büchner, R. Mastylo, and R. Grünwald,
50. Internationales Wissenschaftliches Kolloquium, TU Ilmenau (2005).

Surface passivation of GaAs using a Ge interface control layer

D. Jishiashvili, G. Gobsch, G. Ecke, V. Gobronidze, G. Mtskeradze, and Z. Shiolashvili,
phys. stat. sol. (a) **202**(9) (2005) 1778-1785.

Magnetische Aktoren in Mikrosystemen

M. Kallenbach,
50. Internationales Wissenschaftliches Kolloquium, TU Ilmenau (2005) 197-198.

Laser forming of LTCC ceramics for hot-plate gas sensors

J. Kita, F. Rettig, R. Moos, K.-H. Drüe, and H. Thust,
Journal of microelectronics and electronic packaging : a publication of the International Microelectronics and Packaging Society. – Washington, DC : IMAPS, ISSN 1551-4897, Bd. 2 (2005) 1, 14-18.

Chip devices for miniaturized biotechnology

J.M. Köhler and T. Henke,
Appl. Microbiotechnol. **69** (2005) 113-125.

Formation of isolated and clustered Au nanoparticles in the presence of polyelectrolyte molecules using a flow-through Si chip reactor

J.M. Köhler, J. Wagner, and J. Albert,
J. Mater. Chem. **15** (2005) 1924-1930.

Na,K-ATPase mutations in familial hemiplegic migraine lead to functional inactivation

J.B. Koenderink, G. Zifarelli, L.-Y. Qiu, W. Schwarz, J.J.H.H.M. De Pont, E. Bamberg, and T. Friedrich,
BBA-Biomembranes **1669** (2005) 61-68.

LESR study on PPV-PPE/PCBMcomposites for organic photovoltaics

A.L. Konkin, S. Sensfuss, H.-K. Roth, G. Nazmutdinova, M. Schroedner, and M. Al-Ibrahim,
Synth. Met. **148** (2005) 199-204.

Quantitative Auger electron spectroscopy of SiC

R. Kosiba, J. Liday, G. Ecke, O. Ambacher, J. Breza, and P. Vogrincic,
Vacuum **80** (2006) 990-995.

MIES and UPS(HeI) Studies on Reduced TiO₂(110)

S. Krischok, J. Günster, D.W. Goodman, O. Höfft, and V. Kempter,
Surface and Interface Analysis **37** (2005) 77-82.

A comparative study on the electronic structure of the 1-ethyl-3-methylimidazolium bis(trifluoromethylsulfonyl)amide RT-ionic liquid by electron spectroscopy and first principles calculations

S. Krischok, R. Öttking, W.J.D. Beenken, M. Himmerlich, P. Lorenz, O. Höfft, S. Bahr, V. Kempter, and J.A. Schaefer,
Zeitschrift für Physikalische Chemie, (accepted).

Lithium adsorption on TiO₂: Studies with Electron Spectroscopies (MIES and UPS)

S. Krischok, J. A. Schaefer, O. Höfft, and V. Kempter,
Surface and Interface Analysis **37** (2005) 83-89.

A Comparative Analysis of Electron Spectroscopy and First-Principles Studies on Cu(Pd) Adsorption on MgO

S. Krischok, P. Stracke, O. Höfft, V. Kempter, Yu. F. Zhukovskii, and E.A. Kotomin
Surface Science, (in press).

Metal(Cu; Pd)-Adsorption on MgO: Investigations with MIES and UPS

S. Krischok, P. Stracke, and V. Kempter,
Applied Physics A **82** (2006) 167.

Ausgewählte Methoden zur Charakterisierung der hydrodynamischen Bedingungen bei der elektrolytischen Metallabscheidung

P. Kutzschbach,
Zeitschrift Galvanotechnik, Eugen G. Leuze Verlag, Saalgau-Württb. Band **96** (2005) 560-570.

Schichtdicke und Benetzungsverhalten von Silikonelastomeren

M. Lang, N. Vasev, and P. Meier,
50. Internationales Wissenschaftliches Kolloquium, TU Ilmenau (2005) 329-330.

Defect related absorption and emission in AlGaIn solar-blind UV photodetectors

V. Lebedev, I. Cimalla, V. Cimalla, R. Wagner, U. Kaiser, and O. Ambacher,
phys. stat. sol (c) **2** (2005) 1360-1365.

Effect of nanoscale surface morphology on the phase stability of 3C-AlN films on Si(111)

V. Lebedev, V. Cimalla, U. Kaiser, Ch. Förster, J. Pezoldt, J. Biskupek, and O. Ambacher,
J. Appl. Phys. **97** (114306) (2005).

Correlation between structural and electrical properties of InN thin films prepared by molecular beam epitaxy

V. Lebedev, F.M. Morales, V. Cimalla, J.G. Lozano, D. González, M. Himmerlich, S. Krischok, J.A. Schaefer, and O. Ambacher, Superlattices and Microstructures, (accepted)

Nanocrystalline AlN: Si field emission arrays for vacuum electronics

V. Lebedev, F.M. Morales, M. Fischer, M. Himmerlich, S. Krischok, J.A. Schäfer, and O. Ambacher, phys. stat. sol. (a) **203** (2006) 1839-1844.

Doping efficiency and segregation of Si in AlN grown by molecular beam epitaxy

V. Lebedev, F.M. Morales, H. Romanus, G. Ecke, V. Cimalla, M. Himmerlich, S. Krischok, J.A. Schäfer, and O. Ambacher, phys. stat. sol. (c) **3** (2006) 1420-1424.

The role of Si as surfactant and donor in molecular beam epitaxy of AlN

V. Lebedev, F.M. Morales, H. Romanus, S. Krischok, G. Ecke, V. Cimalla, M. Himmerlich, T. Stauden, D. Cengher, and O. Ambacher, Journal of Applied Physics **98** (2005) 093508.

Stabilität und Zerfallsdynamik hochgeladener Flüssigkeitströpfchen

T. Leisner, Physik Journal **6** (2006) 41 (invited).

Hysteresis in organic field-effect devices: Simulated effects due to trap recharging

G. Lindner, G. Paasch, and S. Scheinert, J Appl. Phys. **98** (2005) 114505.

Simulated Operation and Properties of Source-Gated Thin-Film Transistors

T. Lindner, G. Paasch, and S. Scheinert, IEEE Transactions on Electron Devices **52** (2005) 47-55.

Tribological performance of selected bearings and bearing materials used for nanositioning

Y. Liu, W. Hild, M. Kitsche, S. Doering, S. Lasse, G. Hungenbach, M. Scherge, J.A. Schaefer, D. Dowson, M. Priest, G. Dalmaz, and A. Lubrecht, edited, Life cycle tribology: 31th Lyon-Leeds Symposium on tribology, Tribology and Interface Engineering Series No. 48 Elsevier (2005) 739-750.

Evaluation of the friction of WC/C solid lubricating films in vacuum

Y. Liu, M. Gubisch, T. Haensel, L. Spiess, and J.A. Schaefer, Tribology International, (accepted).

Nanoscale multilayer WC/C coatings developed for nanositioning: Part II. Friction and wear

Y. Liu, M. Gubisch, W. Hild, M. Scherge, L. Spiess, Ch. Knedlik, and J.A. Schaefer, Thin Solid Films **488** (2005) 140-148.

Nanoscale Multilayer WC/C Coatings Developed for Accurate Positioning Part II: Friction and wear

Y. Liu, M. Gubisch, W. Hild, L. Spieß, M. Scherge, and J.A. Schaefer, Thin Solid Films **488** (2005) 140-148.

Friction and adhesion of boundary lubrication measured by microtribometers

Y. Liu, S. Liu, W. Hild, J. Luo, and J.A. Schaefer, Tribology International, (accepted).

The sliding friction of thermoplastic polymer composites tested at low speeds

Y. Liu and J.A. Schaefer, Wear, (accepted).

Optical Information processing

A. Lohmann and S. Sinzinger, Universitätsverlag Ilmenau (2006) ISBN 3-939473-00-6.

Electronic structure of C₆₀, CuPc, and C₆₀/CuPc nanoparticles and their layers

I. Lysko, A. Gorchinskiy, E. Buzaneva, C. Tsamis, A.G. Nassiopoulou, P. Scharff, L. Carta-Abelmann, and K. Risch, Fullerenes Nanotubes And Carbon Nanostructures **13**(3) (2005) 259-272.

Advances in Traceble Nanometrology with the Nanositioning and Nanomeasuring Machine

E. Manske, R. Mastyllo, T. Hausotte, N. Hofmann, and G. Jäger, Nanoscale Calibration, Standards and Methods - Dimensional and Related Measurements in the Micro- and Nanometer Range; Wiley-Vch Verlag GmbH & Co. KGaA, Weinheim, Edition: Wilkening, Günter; Koenders, Ludger (2005) 47-59.

Intelligent Sensor Node for Building Monitoring and Control Applications

M. Marinov, I. Topalov, T. Djamiykov, and S. Hecht, 50. Internationales Wissenschaftliches Kolloquium, TU Ilmenau (2005) 289-290.

Transport properties of composites with carbon nanotube-based composites

L.Y. Matzui, I.V. Ovsienko, T.A. Len, Y.I. Prylutskyy, and P. Scharff, Fullerenes Nanotubes and Carbon Nanostructures **13** (2005) 259-265.

Reiterated tension testing of silicone elastomer
P. Meier, M. Lang, and S. Oberthür,
Plastics, Rubber and Composites, Vol. 34 NO 8
(2005) 372-377.

Modeling of Coupled Fluid-Structure Integration at a High Resolution Microstructured Cantilever Sensor for Fluid Flow Velocities Measuring
M. Milošević, Ž. Živković, J. Burgold, and H. Wurmus,
50. Internationales Wissenschaftliches Kolloquium,
TU Ilmenau (2005) 201-202.

High Precision Positioning and Measurement Systems for Microtribotesting
O. Mollenhauer, S.I.-U. Ahmed, F. Spiller, and
H. Haefke,
Tribotest 12(3) 189 (2006).

Luminescence properties of highly Si-doped AlN
E. Monroy, J. Zenneck, G. Cherkashinin,
O. Ambacher, M. Hermann, M. Stutzmann, and
M. Eickhoff,
Appl. Phys. Lett. 88 (2006) 071906.

α -SiC - β -SiC heteropolytype structures on Si(111)
F.M. Morales, Ch. Förster, O. Ambacher, and
J. Pezoldt,
Appl. Phys. Lett., 87 (2005) 201910-1 - 201910-3.

Analyse und Bewertung gehörrichtiger Schallemissions- und Schallimmissionsmessungen bei Diskothekenlärm
A. Müller, B. Albrecht, J. Grosch, M. Stubenrauch,
E. Emmerich, O. Mollenhauer, H.-P. Schade, and
H. Witte,
in: R. Grieshaber, M. Stadeler, H.-Ch. Scholle, (Hrsg.):
Prävention von arbeitsbedingten Gesundheitsge-
fahren und Erkrankungen - 11. Erfurter Tage. Jena :
Verlag Dr. Bussert & Stadeler,
2005. - ISBN 3-932906-64-0, 453-469.

Resistance Temperature Detector Calibration in LabVIEW Environment
G. Nikolov, B. Nikolova, M. Marinov, and S. Hecht,
50. Internationales Wissenschaftliches Kolloquium,
TU Ilmenau (2005) 291-292.

Untersuchung von chemisch abgeschiedenen nanoskaligen Nickeldispersionsschichten
M. Oberseider, C. Jakob, M. Petrova, Z. Noncheva,
and J. Schawohl,
Zeitschrift Galvanotechnik, Eugen G. Leuze Verlag,
Saulgau-Württb.
Band 96 (2005) 1214.

Regenwürmer als Vorbild für medizinische Instrumente – Ansteuerung für eine peristaltische Sonde aus Silikon
S. Oberthür and P. Meier,
Mechatronik F&M, Vol. 113, No: 11-12 (2005)
22-25.

Nanofriction mechanisms derived from the dependence of friction on load and sliding velocity from air to UHV on hydrophilic silicon
A. Opitz, S. I.-U. Ahmed, M. Scherge, and
J.A. Schaefer,
Tribology Letters 20 (2005) 229-234.

Operation and Properties of Ambipolar Organic Field-Effect Transistors
G. Paasch, T. Lindner, C. Rost, W. Riess, S. Karg, and
S. Scheinert,
J. Appl. Phys. 98 (2005) 084505-2 to 13.

Enhanced electron-phonon coupling of Ti-doped superconducting Nb₃Sn films investigated at microwave frequencies
M. Perpeet and M.A. Hein,
Phys. Rev. B 72, 094502 (July 2005), and
Virtual Journal of Applications of Superconductivity,
Vol. 9 (6), 15. Sept. 2005 (<http://www.vjsuper.org>).

Progress in the integration of planar and 3D coils on LTCC by using photoimageable inks
R. Perrone, H. Thust, and K.-H. Drüe,
Journal of microelectronics and electronic packaging :
a publication of the International Microelectronics
and Packaging Society. - Washington, DC : IMAPS,
ISSN 1551-4897, Bd. 2 (2005) 2, 155-161.

Electroless Deposition of Nanocomposite NiP-Coatings on Metal Substrates
M. Petrova and Z. Noncheva,
51. Internationales Wissenschaftliches Kolloquium,
TU Ilmenau (2006).

Magneto-hydrodynamic convection in microstructures with high aspect ratio
F. Petzoldt, U. Schmidt, and C. Jakob,
51. Internationales Wissenschaftliches Kolloquium,
TU Ilmenau (2006).

Nucleation control in FLASIC assisted short time liquid phase epitaxy by melt modification
J. Pezoldt, E. Polychroniadis, Th. Stauden, G. Ecke,
T. Chassagne, P. Vennegues, A. Leycuras, D. Panknin,
J. Stoemenos, and W. Skorupa,
Mater. Sci. Forum, Silicon Carbide and Related
Materials 2004 (ECSCRM 2004), 483-485 (2005)
213-216.

Classical correlations of defects in lattices with geometrical frustration in the motion of a particle
F. Pollmann, J.J. Betouras, and E. Runge,
Phys. Rev. B 73 (2006) 174417.

Spectral functions and optical conductivity of spinless fermions on a checkerboard lattice
F. Pollmann, P. Fulde, and E. Runge,
Phys. Rev. B 73 (2006) 125121.

Formation of Two-Dimensional Electron Gases in Polytypic SiC Heterostructures

V.M. Polyakov and F. Schwierz,
J. Appl. Phys. **98** (2005) 023709.

Low-Field Electron Mobility in Wurtzite InN

V. Polyakov and F. Schwierz,
Appl. Phys. Lett. **88** (2006) 032101.

Monte Carlo Study of Steady-State and Transient Transport in Wurtzite InN

V. Polyakov and F. Schwierz,
phys. stat. sol. (c) **3** (2006) 598-601.

Nonparabolicity effect on bulk transport properties in wurtzite InN

V.M. Polyakov and F. Schwierz,
J. Appl. Phys., paper (2006) 113705.

UWB Ranging - Chapter 6

D. Porcino, J. Sachs, R. Zetik, and A. Ward,
in "UWB Communication Systems a comprehensive Overview" edited by A. Molisch et al., Hindawi Publishing Corporation; ISBN 977-5945-10-0.

Fluid dynamics in subnanometer channels of carbon nanotubes

Y.I. Prylutsky, L.Y. Matzui, D.A. Gavryushenko,
V.M. Sysoev, and P. Scharff,
Fullerenes Nanotubes and Carbon Nanostructures **13** (2005) 287-291.

Mechanical properties of oxide-fiber reinforced glass matrix composites with BN or SnO₂ interfaces

D. Raab, K. Pfeifer, D. Hülsenberg, and A.R. Boccaccini,
Material Science and Engineering A **417** (2006) 341-347.

Mercury-plated thin film ITO microde array for analysis of heavy metals

V. Rehacek, K. Shtereva, I. Novotny, V. Tvarozek,
V. Breternitz, L. Spiess, and Ch. Knedlik,
Vacuum **80** (2005) 132-136.

Radiation damage to multi-walled carbon nanotubes and their RAMAN vibrational modes

U. Ritter, P. Scharff, C. Siegmund, O.P. Dmytrenko,
N.P. Kulish, Yu.I. Prylutsky, N.M. Belyi,
V.A. Gubanov, L.I. Komarova, S.V. Lizunova,
V.G. Poroshin, V.V. Shlapatskaya, and H. Bernas,
Carbon (2006) (accepted).

Infrared Gratings Based on SiC/Si-Heterostructures

C. Rockstuhl, H.P. Herzig, Ch. Förster, A. Leycuras,
O. Ambacher, and J. Pezoldt,
Mater. Sci. Forum, Silicon Carbide and Related Materials 2004 (ECSCRM 2004), **483-485** (2005) 433-436.

Reflectance difference spectroscopy RDS/RAS combined with spectroscopic ellipsometry for a quantitative analysis of optically anisotropic materials

U. Rossow, R. Goldhahn, D. Fuhrmann, and
A. Hangleiter,
phys. stat. sol. (b) **242**(13) (2005) 2617-2626.

Interpretation of near-field images of semiconductor nanostructures,

E. Runge and Ch. Lienau,
Appl. Phys. B. (accepted).

Near-field wave-function spectroscopy of excitons and biexcitons

E. Runge and C. Lienau,
Phys. Rev. B **71** (2005) 035347.

Principles of Ultra-Wideband Sensor Electronics - Chapter 17

J. Sachs,
In "Electromagnetic Aquametry – Electromagnetic Wave Interaction with Water and Moist Substances" edited by K. Kupfer, Springer Verlag; ISBN 3-540-22222-7.

Computer simulation of the early stages of nano scale SiC growth on Si

K.L. Safonov, Yu.V. Trushin, O. Ambacher, and
J. Pezoldt,
Mater. Sci. Forum, Silicon Carbide and Related Materials 2004 (ECSCRM 2004), **483-485** (2005) 169-172.

Rigorous shadowing effects for blazed transmission gratings on imaging optical elements

O. Sandfuchs, R. Brunner, D. Pätz, S. Sinzinger,
J. Ruoff,
Opt. Lett. 2006 (accepted).

Carbon nanotube peapods – insertion of C₆₀ into multi-wall carbon nanotubes

P. Scharff, T. Fröhlich, S. Osswald, and U. Ritter,
karbo **4** (2005) 224-227.

Fabrication and analysis of polymer field-effect transistor

S. Scheinert and G. Paasch,
in W. Brütting (ed.), Physics of organic semiconductors,
Wiley-VCH, 2005, ISBN 3-527-40550-X, pp. 343-391.

Influence of source/drain contacts on sub-micrometer organic field-effect transistors

S. Scheinert, G. Paasch, I. Hörselmann, and
A. Herasimovich,
phys. stat. sol. (a) **202** (2005) R82-R84.

Molecular determinants of KCNQ (Kv7) K⁺ channel sensitivity to the anticonvulsant retigabine

A. Schenzer, T. Friedrich, M. Pusch, P. Saftig, T.J. Jentsch, J. Grötzinger, and M. Schwake, *J. Neurosci.* **25** (2005) 5051-60.

Transition energies and Stokes shift analysis for In-rich InGaN alloys

P. Schley, R. Goldhahn, A.T. Winzer, G. Gobsch, V. Cimalla, O. Ambacher, M. Rakel, C. Cobet, N. Esser, H. Lu, and W.J. Schaff, *phys. stat. sol. (b)* **7** (2006) 1572-1576.

Growth of three-dimensional SiC clusters on Si modelled by KMC

A.A. Schmidt, V.S. Kharlamov, K.L. Safonov, Yu.V. Trushin, E.E. Zhurkin, V. Cimalla, O. Ambacher and J. Pezoldt, *Comput. Mater. Sci.* **33** (2005) 375-381.

Structural and Magnetic Properties of Ni/NiOxide and Co/CoOxide Core/Shell Nanoparticles and their possible Use for Ferrofluids

V. Schneider, A. Reinholdt, U. Kreibig, T. Weirich, G. Güntherodt, B. Beschoten, A. Tillmanns, H. Krenn, K. Rumpf, and P. Granitzer, *Z. Phys. Chem.* **220** (2006) 173-187.

The Influence of the Collector Dopant Profile on Breakdown Voltage and Cutoff

Frequency of Si-Based RF Bipolar Transistors
C. Schippel and F. Schwier, *phys. stat. sol. (c)* **3** (2006) 494-498.

An Electron Mobility Model for Wurtzite GaN

F. Schwier, *Solid-State Electron.* **49** (2005) 889-895.

Performance Trends of Si-Based RF Transistors

F. Schwier and C. Schippel, *Proc. IEEE EDSSC* (2005) 299-304 (Invited Paper).

RF Transistors: Performance Trends Versus ITRS Targets

F. Schwier, *Proc. 6th IEEE ICCDCS* (2006) (Invited Paper).

Electron Transport in InN

F. Schwier and V. Polyakov, To be presented at ICSICT 2006 (Invited Paper).

Optoelectronic Properties of Conjugated Polymer/ Fullerene Binary Pairs with variety LUMO level differences: Chapter 23

S. Sensfuss, M. Al-Ibrahim, in "Organic Photovoltaics: Mechanism, Materials and Devices", ed. by S.-S. Sun, and N.S. Sariciftci, CRC Press, Boca Raton, FL, USA, (2005) 529-557.

Linear and nonlinear microwave properties of calcium-substituted YBaCuO thin films

D. Seron, D.E. Oates, G. Hammerl, J. Mannhart, P.J. Hirst, R.G. Humphreys, A.C. Anderson, M.A. Hein, and J. Derov, *Phys. Rev. B* **72**, 104511 (2005), and *Virtual Journal of Applications of Superconductivity*, Vol. **9**(6) 15. Sept. 2005 (<http://www.vjsuper.org>).

Conduction band parameters of ZnO

S. Shokhovets, G. Gobsch, and O. Ambacher, *Superlattices and Microstructures* **39**(1-4) (2006) 299-305.

Momentum matrix element and conduction band nonparabolicity in wurtzite GaN

S. Shokhovets, G. Gobsch, and O. Ambacher, *Appl. Phys. Lett.* **86**(16) (2005) 161908.

Hydrogen microsensors based on NiO modified films

L. Spiess, M. Gubisch, J. Schawohl, I. Hotovy, and J. Huran, 50. Internationales Wissenschaftliches Kolloquium, TU Ilmenau (2005) 193-194.

Development of a reference field for a NPM-machine

L. Spiess, G. Machleidt, V. Cimalla, M. Gubisch, O. Ambacher, and K.H. Franke, 50. Internationales Wissenschaftliches Kolloquium, TU Ilmenau (2005) 45-46.

Moderne Röntgenbeugung - Röntgen-diffraktometrie für Materialwissenschaftler

L. Spieß, R. Schwarzer, H. Behnken, and G. Teichert, *Physiker und Chemiker*, 1. Aufl., B.G. Teubner, Wiesbaden 2005, S. 523. ISBN: 3-519-00522-0.

Rates of homogeneous ice nucleation in levitated H₂O and D₂O droplets

P. Stöckel, I. M. Weidinger, H. Baumgärtel, and T. Leisner, *Journal of Physical Chemistry A* **109** (2005) 2540-2546.

Anforderungen an die elektroforetische Infiltration zur Herstellung von**Oxid/Oxid-Faserverbundwerkstoffen,**

E. Stoll, P. Mahr, H.G. Krüger, H. Kern, and A.R. Boccaccini, 50. Internationales Wissenschaftliches Kolloquium, TU Ilmenau (2005).

Fabrication technologies for oxide-oxide ceramic matrix composites based on electrophoretic deposition,

E. Stoll, P. Mahr, H.G. Krüger, H. Kern, and A.R. Boccaccini, *Journal of the European Ceramic Society* **26** (2006) 1567-1576.

Progresses in the electrophoretic deposition technique to infiltrate oxide fibre mats for fabrication of ceramic matrix composites

E. Stoll, P. Mahr, H.G. Krüger, H. Kern, and A.R. Boccaccini,
Journal Key Engineering Materials **314** (2006) 195-200.

Progress in the characterisation of structural oxide/oxide ceramic matrix composites fabricated by electrophoretic deposition (EPD)

E. Stoll, P. Mahr, H.G. Krüger, H. Kern, I. Dlouhy, and A.R. Boccaccini,
Advanced Engineering Materials **8** (2006) 4 282-285.

Black silicon - new functionalities in microsystems

M. Stubenrauch, M. Fischer, C. Kremin, S. Stoebenau, A. Albrecht, and O. Nagel,
J. Micromech. Microeng. **16** (2006) 82-87.

A new method for handling and manipulation of valuable biological specimen in MEMS

M. Stubenrauch, J. Burgold, D. Voges, C. Schilling, M. Knoblauch, and W.S. Peters,
in U. Boenick, A. Bolz, Biomedizinische Technik; Volume **50** Suppl. vol. 1 Part 1, (2005) 191-192.

Control of emission by intermolecular fluorescence resonance energy transfer and intermolecular charge transfer

M. Sun, W.J.D. Beenken, P. Kjellberg, T. Pullerits, and K. Han,
J. Phys. Chem. A **110** (2006) 6324.

Comparison of the electronic structure of PPV and its derivative DIOXA-PPV

M. Sun, P. Kjellberg, W.J.D. Beenken, and T. Pullerits,
Chem. Phys. in print (2006).

Multidimensional High-Resolution Channel Sounding, in Smart Antennas in Europe – State-of-the-Art, EURASIP Book Series

R. Thoma, M. Landmann, A. Richter, and U. Trautwein,
Hindawi Publishing Corporation (2006) 27.

Piezoelectric properties of AlN films

K. Tonisch, V. Cimalla, and O. Ambacher,
Sensors and Actuators (2006) (accepted).

Piezoelectronic properties of thin AlN layers for MEMS application determined by piezoresponse force microscopy

K. Tonisch, V. Cimalla, Ch. Förster, D. Dontsov, and O. Ambacher,
phys. stat. sol. (c) **3** (2006) 2274-2277.

Continuous Synthesis of Gold Nanoparticles in a Microreactor

J. Wagner and J.M. Köhler,
Nano Letters (2005).

Phase selective growth and properties of rhombohedral and cubic indium oxide

Ch.Y. Wang, V. Cimalla, H. Romanus, Th. Kups, G. Ecke, Th. Stauden, M. Ali, V. Lebedev, J. Pezoldt, and O. Ambacher,
Appl. Phys. Lett. **89** (2006) 011904.

Forming of noncircular cross-section SiO₂ glass fibers

M. Wegmann, J. Heiber, F. Clemens, T. Graule, D. Hülsenberg, and K. Schuster,
Glass Sci. Technol. **78** No. 2 (2005) 69-75.

Growth of 3C-(Si_{1-x}C_{1-y})Ge_{x+y} Layers on 4H-SiC by Molecular Beam Epitaxy

P. Weih, H. Romanus, T. Stauden, L. Spieß, O. Ambacher, and J. Pezoldt,
Mater. Sci. Forum **483-485** (2005) 173-176.

Ion beam synthesis of 3C-(Si_{1-x}C_{1-y})Ge_{x+y} solid solutions

P. Weih, Th. Stauden, G. Ecke, S. Shokhovets, Ch. Zgheib, M. Voelskow, W. Skorupa, O. Ambacher, and J. Pezoldt,
phys. stat. sol. (a) **202** (2005), 545-549.

Manufacturing of titanium/aluminium and titanium/steel joints by means of diffusion welding

J. Wilden and J.P. Bergmann,
Welding Research Abroad Bd. **51** 6/7 (2005) 37-42.

Mechanised Plasma-Powder-Arc-Welding (PPAW) of aluminium sheets

J. Wilden and J.P. Bergmann,
Advanced Materials Research, Vol. **6-8** (2005) 225-232.

Untersuchung der metallurgischen Grundlagen zum Plasma-Pulver-Verbindungsschweißen dünner Aluminiumbleche

J. Wilden and J.P. Bergmann,
Schweißen und Schneiden **58**(5) (2006) 225-228.

Use of zinc-alloys for low temperature brazing of zinc coated steels

J. Wilden, J.P. Bergmann, M. Dolles, and S. Reich,
Advanced Materials Research, Vol. **6-8** (2005) 127-134.

Technologie zum Herstellen von Werkzeugen zum Mikrospritzgießen durch Diffusionsschweißen

J. Wilden, J.P. Bergmann, and S. Jahn,
Schweißen und Schneiden **58**(4) (2006) 189-195.

Mechanical properties and processing of low temperature diffusion welded hybrid joints

J. Wilden, J.P. Bergmann, S. Jahn, S. Herz, and S. Hägebarth,
In *Advanced Engineering Materials*, Volume 8(3) (2006) 212-218.

Electroreflectance spectroscopy of Pt/AlGaIn/GaN heterostructures exposed to gaseous hydrogen

A.T. Winzer, R. Goldhahn, G. Gobsch, A. Dadgar, A. Krost, O. Weidemann, M. Stutzmann, and M. Eickhoff,
Appl. Phys. Lett. **88** (2) (2006) 024101.

Determination of the polarization discontinuity at the AlGaIn/GaN interface by electroreflectance spectroscopy

A.T. Winzer, R. Goldhahn, G. Gobsch, A. Link, M. Eickhoff, U. Rossow, and A. Hangleiter,
Appl. Phys. Lett. **86** (18) (2005) 181912.

UWB: Ultra-Breitband-Kommunikation

M. Wolf, J. Sachs, and R. Zetik,
tecchannel compact – PC Welt Sonderheft Mai/Juni/ Juli 2005.

Design, fabrication, and application of a massively parallel single-bead microreactor system for high-throughput experimentation in heterogeneous catalysis

T. Zech, G. Bohner, O. Laus, J. Klein, and M. Fischer,
Review of Scientific Instruments, American Institute of Physics Volume **76**(6) (2005).

Raman studies of Ge-promoted stress modulation in 3C-SiC grown on Si(111)

Ch. Zgheib, L.E. McNeil, M. Kazan, P. Masri, F.M., Morales O. Ambacher, and J. Pezoldt,
Appl. Phys. Lett., **87** (2005) 041905.

Ge-modified Si(100) substrates for the growth of 3C-SiC(100)

Ch. Zgheib, L.E. Mc Neil, P. Masri, Ch. Förster, F.M. Morales, Th. Stauden, O. Ambacher, and J. Pezoldt,
Appl. Phys. Lett. **88** (2006) 211909.

Effect of Ge in corporation on stoichiometric composition of 3C-SiC thin films grown on Si(111) substrates

Ch. Zgheib, M. Kazan, P. Weih, O. Ambacher, P. Masri, and J. Pezoldt,
phys. stat. sol. (c) **2** (2005) 1284-1287.

Relation between absorption and crystallinity of poly(3hexylthiophene)/fullerene films for plastic solar cells

U. Zhokhavets, T. Erb, G. Gobsch, M. Al-Ibrahim, and O. Ambacher,
Chemical Physics Letters **418** (4-6) (2006) 347-350.

Effect of annealing of poly(3-hexylthiophene)/fullerene bulk heterojunction composites on structural and optical properties

U. Zhokhavets, T. Erb, H. Hoppe, G. Gobsch, and N.S. Sariciftci,
Thin Solid Films **496** (2) (2006) 679-682.

Theses

PhD-Theses

Rastislav Kosiba (01.02.05)

Department of Nanotechnology
„Augerelektronenspektroskopie und niederenergetischer Ionenbeschuss von Siliziumkarbid“

Ulrike Brokmann (15.06.2005)

Department of Glass and Ceramic Technology
„Mikrostrukturierung von fotostrukturierbarem Glas mittels UV-Laserstrahlung“

Susanne Mrotzek (17.06.2005)

Department of Glass and Ceramic Technology
„Kristallisation eines UV-strukturierbaren Glases im System $\text{Li}_2\text{O-Al}_2\text{O}_3\text{-SiO}_2$ “

Matthias Kallenbach (06.07.2005)

Department of Micromechanical Systems
„Entwurf von magnetischen Mini- und Mikroaktoren mit stark nichtlinearem Magnetkreis“

Christian Förster (14.10.2005)

Department of Nanotechnology
„Grenzflächenmodifizierung von Heterostrukturen aus Halbleitern großer Bandlücke“

Wolfram Hild (18.10.2005)

Department of Technical Physics I
„Tribologische Untersuchungen an Mikrosystemen: Einfluss der Benetzbarkeit“

Alexander Reinholdt (25.10.2005)

Department of Experimental Physics II
„Untersuchung zur Anwendbarkeit von Titanitrid- und Zirkonitrid-Nanopartikeln als Farbpigmente und zum magnetischen Verhalten von Nickel/Nickeloxid-Kern-Hülle-Nanopartikeln“

Frank Erler (28.10.2005)

Department of Materials for Electronics
„Herstellung und Eigenschaften von Nickel-dispersionswerkstoffen mit nanoskaligen Oxidkeramikpartikeln“

Uladimir Zhokhavets (November 2005)

Department of Experimental Physics I
„Composite Conjugated Polymer/Fullerene Films: Structure-Property Relation“

Heiko Frank (06.04.2006)
Department of Production Engineering
„Modellierung der Gefügeausbildung beim thermischen Spritzen“

Maher Al-Ibrahim (June 2006)
Department of Nanotechnology
„Technologieorientierte Forschung zur Herstellung und Optimierung von Polymersolarzellen auf flexiblen Kunststoffsubstraten“

Andreas Richter
Department of Electronic Measurement
„Estimation of Radio Channel Parameters: Models and Algorithms“

Diploma-Theses

Christoph Kluge (January 2005)
Department of Microperipherals
„Thermische Untersuchung und Bewertung von LTCC-Mikrowellengehäusen“

Marcel Himmerlich (31.01.2005)
Department of Technical Physics I
„Photoelectron Emission Microscopy and Photoelectron Spectroscopy of Ge on Si, InN and InP“

Michael Dietz (February 2005)
Department of Experimental Physics I
„Dotierstoffaktivierung zur Integration in Leistungstechnologien“

Thorsten Schiffer (February 2005)
Department of Experimental Physics I
„Investigation of Diamond Like Carbon (DLC) films for surface high voltage passivation in silicon power semiconductor devices“

Toni Fröhlich (February 2005)
Department of Chemistry
„Encapsulation of C₆₀ in Carbon nanotubes“

Christian Volmer (February 2005)
Department of Electronic Measurement
„HF- Takterzeugung für M-Sequenz Ultra-Wideband-Systeme“

Berhard Guddei (24.02.2005)
Department of Technical Physics I
„Entwurf, Aufbau und Test eines Kraftmesssystems für den Mikro- und Nanobereich“

Christian Köhler (March 2005)
Department of Production Engineering
„Entwurf und Auslegung einer Verdüsungsanlage zur Herstellung von pulverförmigen Werkstoffen“

Sebastian Reich (March 2005)
Department of Production Engineering
„Untersuchungen zum Laserstrahllöten von verzinkten Stahlblechen mittels Hochleistungsdiodenlasers und niedrigschmelzender Zusatzwerkstoffe“

Steffen Herrmann (04.03.2005)
Department of Micromechanical Systems
„FEM-Simulation einer strukturierten Membran für einen Niederdrucksensor“

Armin Spitznas (14.03.2005)
Department of Nanotechnology
„GaN-basierende Sensoren für biomedizinische Anwendungen“

Kerstin Reinhäckel (30.03.2005)
Department of Materials for Electronics
„Vergleichende Untersuchungen zum Schmelz- und Erstarrungsverhalten von Flüssigmetall-Legierungen auf Galliumbasis“

Jan Oberthür (19.04.2005)
Department of Micromechanical Systems
„Elektrochemische On-Chip Detektierung von Steroiden“

Frank Bußinger (21.04.2005)
Department of Micromechanical Systems
„Entwicklung eines stark miniaturisierten, polarisierten Magnetventils mit einem vorgegebenen Anreihmaß“

Christoph Kremin (10.05.2005)
Department of Micromechanical Systems
„Kombiniertes form- und kraftschlüssiges Fügeverfahren für Silizium“

Dorothea Förster (June 2005)
Department of Microperipherals
„Entwurf, Realisierung und Analyse von LTCC-Leitungsstrukturen und Filtern für das K-Band“

Sebastian Stobenau (10.06.2005)
Department of Micromechanical Systems
„Aufbau und Test von integrierten Katalysatoren in mikrofluidischen Systemen“

Stefan Cyriaci (13.07.2005)
Department of Materials for Electronics
„Mikrozugversuch an Dünnschichtstrukturen“

Katharina Lilienthal (25.07.2005)
Department of Micromechanical Systems
„Plasmaätzen von Gläsern“

Manuela Gutsch (August 2005)
Department of Experimental Physics I
„Anwendung der Scatterometrie zur Bestimmung des Lageversatzes bei der Chipherstellung“

Uwe Schadewald (24.08.2005)

Department of Glass and Ceramic Technology
„Untersuchungen zur bottom-up-Kristallisation von modifizierten Bariumhexaferritpulvern“

Andreas Pönicke (September 2005)

Department of Chemistry
„Development of carbon fiber enhanced aluminum oxide ceramic“

Andreas Weidemann (September 2005)

Department of Production Engineering
„Untersuchung zur Gefahr wasserstoffinduzierter Korrosion bei Verarbeitung und Einsatz hochfester Martensitphasenstähle“

Andreas Wetterhahn (September 2005)

Department of Production Engineering
„Untersuchung mechanischer Eigenschaften von geschäumten Dichtungen auf Türsystem-Trägerblechen“

Andreas Schicht (September 2005)

Department of Electronic Measurement
„Untersuchung von mm-Wellensignalen zur Überwachung von Gasturbinenschaufeln“

Janine Winkler (September 2005)

Department of Production Engineering
„Einsatz von hybriden Verfahren zum Beschichten von metallischen Werkstoffen“

Melanie Rieger (02.09.2005)

Department of Materials for Electronics
„Charakterisierung von Hartstoffschichten mit Hilfe der Glimmentladungs-spektroskopie“

Michael Kaiser (13.09.2005)

Department of Micromechanical Systems
„Präparation von Solarzellen in multikristallinen LLC-Si-Schichten“

Katja Tonisch (30.09.05)

Department of Nanotechnology
„AlGa_N-Mischkristalle für die Sensorik“

Andreas Benzler (October 2005)

Department of Electronic Measurement
„Coexistence techniques for an indoor position location system operating in the 2.4 GHz ISM band“

Daniel Gäbler (October 2005)

Department of Nanotechnology
„Entspiegelung von Silizium-Photodioden nach dem Vorbild der Nanooptik von Mottenaugen“

Merten Niebelschütz (October 2005)

Department of Nanotechnology
„Augerelektronenspektroskopische Untersuchungen an Gruppe III-Nitriden“

Florentina Will (October 2005)

Department of Nanotechnology
„Mikro- und nanoelektromechanische Resonatoren für die Sensorik“

Anita Neumann (27.10.2005)

Department of Technical Physics I
„Chemische Optimierung von Kohlenstoffnanoröhren für elektronische Bauelemente“

Richard Löw (November 2005)

Junior Research Group „PADeMiS“
„Finite Elemente Simulation von Silikongummi unter zyklischer Mehrfachbelastung am Beispiel einer sich peristaltisch fortbewegenden Sonde“

Sebastian Osswald (November 2005)

Department of Chemistry
„Raman spectroscopic investigation on carbon nanotubes and nanodiamonds“

Johannes Seyffarth (November 2005)

Department of Production Engineering
„Strategien zur Modifizierung des Oberflächenzustandes durch Niederdruckplasma“

Benedikt Lübbers (02.11.2005)

Department of Nanotechnology
„Optimierung von GaN-basierenden Sensoren für die nano- und pikofluidische Systeme“

Markus Wilke (10.11.2005)

Department of Materials for Electronics
„Untersuchungen zur Möglichkeit der rekalibrationsfreien Bestimmung der Schichtdicke (Verbindungsschicht, Diffusionsschicht) von nitrierten und nitrocarburierten Proben mit Hilfe der Glimmentladungspektroskopie (GD-OES)“

Jan Räthel (14.11.2005)

Department of Glass and Ceramic Technology
„Elektromagnetische Modifizierung von Entmischungen in Glasschmelzen“

Alexander Schulz (December 2005)

Department of Electronic Measurement
„Implementierung einer laufzeitoptimierten dynamisch-prozessoradaptiven Software-Bibliothek zur effizienten Lösung mehrerer Toeplitz-Gleichungssysteme auf Basis von x86-Plattformen“

Joana Rietz (01.12.2005)

Department of Materials for Electronics
„Tiefenaufgelöste röntgenografische Spannungsmessung“

Martina Mohr (January 2006)

Department of Experimental Physics I
„Zink-Phtalozyanin-Aufdampfschichten im Indium-Zinnoxid-Sputterprozeß“

Pascal Schley (January 2006)

Department of Experimental Physics I
„Optische Eigenschaften von InN und InGaN mit In- bzw. (InGa)- und N-Polarität“

Sören Selve (20.01.2006)

Department of Materials for Electronics
„Festkörperphysikalische Analyse an nanoskaligen funktionellen Keramikverbundschichten“

Michael Grosser (26.01.2006)

Department of Materials for Electronics
„Werkstoffe und Werkstoffkonzepte für elektrisch leitende Schichten im Hochtemperaturbereich“

Chunyu Wang (31.01.2006)

Department of Nanotechnology
„Herstellung und Charakterisierung von InOx-Nanoschichten für die Gassensorik“

Stefan Voigt (March 2006)

Department of Experimental Physics I
„Untersuchung von Polymer/Fulleren-Komposit-Solarzellen mittels Photoinduzierter Absorptionsspektroskopie“

Sören Neubeck (15.03.2006)

Department of Technical Physics I
„Aufbau eines Tieftemperatur-Rastertunnelmikroskops mit Spaltvorrichtung für den Betrieb in flüssigem Helium“

Jürgen Dienstmaier (31.05.2006)

Department of Glass and Ceramic Technology
„Einfluss paramagnetischer Kraftwirkungen auf die Kristallisation in Glasschmelzen“

Andreas Gißke (June 2006)

Department of Production Engineering
„Werkstoff- und prozesstechnische Aspekte beim Fügen von Mischverbindungen mittels kombinierter Laser- und Lichtbogentechnik“

Andreas Hautz (June 2006)

Department of Production Engineering
„Untersuchung des Einflusses verschiedener Fassungsstrategien auf die Oberflächendeformation eingeklebter, optischer Bauteile“

Tim Baumann (01.06.2006)

Department of Nanotechnology
„Quantifizierung von Gruppe III – Nitriden“

Nico Dix (16.06.2006)

Department of Technical Physics I
„Construction of a Low Temperature Magneto-Optical Kerr Effect Set-Up and Application on Ferromagnetic Oxide Thin Films“

Mario Hofmann (22.08.2006)

Department of Technical Physics I
„Optimization in Synthesis of Carbon Nanotubes and their Analysis“

Student research project reports

Andreas Pönicke (January 2005)

Department of Chemistry
„Production of single-walled carbon nanotubes by arc-discharge with various Ni-Y catalyst mixtures“

Katja Tonisch (07.02.2005)

Department of Nanotechnology
„Piezoelektronische Eigenschaften von AlN“

Claudia Blank (04.05.2005)

Department of Micromechanical Systems
„Voruntersuchungen zum Einsatz von Spin-on-Glas als Bondzwischen-schicht“

Dirk Philipp (17.05.2005)

Department of Micromechanical Systems
„Verfahren zur Equilibrierung mehrkanaliger miniaturisierter Fluidik-Systeme“

Chunyu Wang (31.05.2005)

Department of Nanotechnology
„Herstellung von InO-Schichten“

Tim Baumann (20.06.2005)

Department of Nanotechnology
„Elektrische Charakterisierung von GruppIII-Nitriden“

Michael Schuch (July 2005)

Department for Physical Chemistry and Microreaction Technology
„Analyse mizellarer Systeme in mikrofluidischen Anordnungen“

Sebastian Osswald (July 2005)

Department of Chemistry
„Structure and properties of nanometer carbon“

Ute Wenzel (01.07.2005)

Department of Glass and Ceramic Technology
„Untersuchungen zur thermischen Stabilität von Zerodur“

Michael Kaiser (15.09.2005)

Department of Micromechanical Systems
„Präparation von Emitterschichten für Si-Dünnschichtsolarzellen“

Michael Traut (28.09.2005)

Department of Micromechanical Systems
„Untersuchungen der Möglichkeit der beliebigen Einstellung verschiedener Wandwinkel beim trockenchemischen Ätzen“

Tobias Polster (30.9.2005)

Department of Micromechanical Systems
„Naßchemische Strukturierung anodisch bondbarer Gläser“

Katrin Ehnes (09.12.2005)

Department of Micromechanical Systems
„Anwendungsmöglichkeiten des Chemisch-Mechanischen Polierens zur Herstellung von vergrabenen Metallisierungen in Bondinterfaces“

Jens Wagner (12.12.2005)

Department of Micromechanical Systems
„Gestaltung internetbasierender Lernmodule zur Mikrosystemtechnik“

Dirk Schröpfer (21.12.2005)

Department of Glass and Ceramic Technology
„Untersuchungen zur Visualisierung von Strömungssituationen in elektromagnetisch gerührten Glasschmelzen“

Sven Klausnitzer (26.01.2006)

Department of Micromechanical Systems
„Spritzenpumpe I – Steuerung“

Christof Mauder (31.01.2006)

Department of Nanotechnology
„Epitaxie von Gruppe III – Nitrid-Schichten und –Heterostrukturen“

Stephan Maroldt (31.01.2006)

Department of Nanotechnology
„Charakterisierung elektronischer Eigenschaften niedrigdimensionaler Elektronengase“

Clemens Knippschild (15.02.2006)

Department of Micromechanical Systems
„Spritzenpumpe II – Konstruktion“

Stefan Weinberger (15.02.2006)

Department of Micromechanical Systems
„Piezoresistive Schichten als Sensor mit Polysilizium“

Xiaogung Wu (20.02.2006)

Department of Nanotechnology
„AlGaIn/GaN-Sensoren für pH-Messungen“

Peter Ort (28.02.2006)

Department of Nanotechnology
„Erstellung von nanostrukturierten Metallmasken für sensorische Bauelemente mit Applikationen in der Biomedizinischen Technik“

Christian Recknagel (March 2006)

Department for Physical Chemistry and Microreaction Technology
„Aufbau einer Messanordnung und Untersuchung des Einflusses von (DNA)Biomolekülen auf die Bildung von Au-Nanopartikeln in Mikroreaktoren“

Tobias Sprogies (March 2006)

Department for Physical Chemistry and Microreaction Technology
„Charakterisierung von Mikromischern“

Christian Rensch (15.03.2006)

Department of Micromechanical Systems
„Akustische Untersuchungen an Mikrofluidkomponenten“

Robert Henneberg (15.03.2006)

Department of Micromechanical Systems
„Bondeinrichtung zum anodischen Bonden“

Claus-Christian Röhlig (30.03.2006)

Department of Nanotechnology
„Sauerstoff- und Ozonsensoren für die biomedizinische Analytik“

Stefan Weinberger (08.04.2006)

Department of Micromechanical Systems
„Piezoresistive Schichten als Sensor mit Polysilizium“

Tom Creutzburg (19.04.2006)

Department of Micromechanical Systems
„Optimierung der Resistbeschichtung im Lithografieprozess“

Cesar Mayor Sanchez (23.05.2006)

Department of Glass and Ceramic Technology
„Investigation of the synthesis of mono crystalline La- and Co-substituted barium hexaferrite powders by glass crystallization technique“

Christian Haupt (09.06.2006)

Department of Nanotechnology
„Erstellung dreidimensionaler Nanostrukturen mit Hilfe der Elektronenstrahlolithographie“

Carsten Rackel (16.06.2006)

Department of Nanotechnology
„Nanomorphologie in Polymer und Polymer/Fulleren Kompositschichten“

Invited Talks and Colloquia

Prof. Martin Stutzmann

„Biofunktionalisierung von Halbleiter-Oberflächen“
Technische Universität München, 11.01.2005

Dr. Michael Gebinoga

„Mikrostrukturierte Ansätze der koineratorischen Chemie zur Wirkstoffentwicklung“
Georg-August-Universität Göttingen/TU Ilmenau, 09.02.2005

Prof. Gerhard von der Ende

„Aktive Elektroortung – Biosensoren nach dem Vorbild der Natur“
Rheinische Friedrich-Wilhelm-Universität Bonn, 14.02.2005

Prof. Günter Müller

„Feldemissionskathoden aus Kohlenstoff-Nanoröhren“
Bergische Universität Wuppertal, 23.02.2005

Dr. Gerd Teichert

„Glimmentladungsspektroskopie – eine moderne Methode der Schicht- und Materialanalytik“
Materialforschungs- und -prüfanstalt Weimar, 02.03.2005

Coworkers at the ZMN

„Projekt Pikofluidik“
Technische Universität Ilmenau, 14.04.2005

Dr. Peter Schreiber

„Design mikrooptischer Systeme“
Fraunhofer Institut für Angewandte Optik und Feinmechanik Jena, 20.04.2005

Dipl.-Ing. Roy Knechtel

„Waferbondverfahren zur Herstellung spezieller Substrate und zur Verkapselung von MEMS im industriellen Fertigungsprozess“
X-FAB Semiconductor Foundries AG, Erfurt, 04.05.2005

Dr. Toon Kuijpers

„A capacitive long-range displacement sensor for nano-positioning microactuator systems“
Universität Twente, NL, 24.05.2005

Dr. Thomas Friedrich

„Biomoleküle in Zellmembranen als elektrische und optische Signalgeber für Sensoranwendungen“
Max-Planck-Institut für Biophysik Frankfurt/
Technische Universität Ilmenau, 27.07.2005

Dr. Rainer Adelung

„Herstellung und Anwendung von Nanodraht-Kompositstrukturen“
Christian-Albrechts-Universität Kiel, 14.09.2005

Dr. Matthias Bickermann

„Herstellung und Eigenschaften von Volumen/kristalle und Substrate aus AlN“
Friedrich-Alexander-Universität Erlangen-Nürnberg, 02.11.2005

Prof. Ferdinand Scholz

„Selektive Epitaxie von GaN: bessere Wafer, hellere LED's?“
Universität Ulm, 14.02.2006

Prof. Andreas Neyer

„Lichtwellenleiter aus Polysiloxan für die optische Übertragungstechnik und Biosensorik“
Universität Dortmund, 01.03.2006

Several Departments of the IMN

„Summer term kick-off Kolloquium“
Institut für Mikro- und Nanotechnologien, 05.04.2006

Dr. Uwe Ritter

„Kohlenstoff-Nanotubes – Eine neue Dimension in der Kohlenstoffchemie“
FG Chemie, Technische Universität Ilmenau, 12.04.2006

Dipl.-Phys. Thomas Kups

„Transmissionselektronenmikroskopische Untersuchungen an Dotanden in SiC“
FG Werkstoffe der Elektrotechnik, Technische Universität Ilmenau, 26.04.2006

Dipl.-Biol. Caroline Augsburg

„Untersuchungen zum Differenzierungszustand dreidimensionaler Gewebekulturen im Cell-Chip basierten Bioreaktor“
Forschungszentrum Karlsruhe, 11.05.2006

Prof. Stefan Sinzinger

„Mikrooptik – Technologien und Anwendungen“
FG Technische Optik, Technische Universität Ilmenau, 24.05.2006

Dr. Volker Cimalla

„Nanoelektromechanische Bauelemente für die Sensorik“
FG Nanotechnologie, Technische Universität Ilmenau, 07.06.2006

Prof. Martin Hoffmann

„Mikro-(Elektro-)Mechanische System-Integration“
FG Mikromechanische Systeme, Technische Universität Ilmenau, 21.06.06

Dr. Vyacheslav Yunkin

„X-ray optics: design, fabrication and applications“
Russische Akademie der Wissenschaften, Moskau, 06.07.2006

Dr. Vadim Lebedev

„Mechanisms of heterogeneous crystal growth in highly mismatched systems: Insights from III-nitrides“
 FG Nanotechnologie, Technische Universität Ilmenau,
 19.07.2006

Dipl.-Biochem. Daniel Kloß

„3D Biosensoren für sphäroidbasierte Impedanz Spektrometrie“
 Universität Leipzig, 26.07.2006

Dr. Bernd Hamann

„5 Tesla - Gleichfeld-Equipment für die Werkstoffentwicklung“
 FG Elektrothermische Energiewandlung, Technische Universität Ilmenau, 02.08.2006

Dr. Mike Günther

„Optisches online Monitoring in Mikrofluidsystemen mit MORES-Sensoren“
 Institut für Physik, Technische Universität Ilmenau,
 09.08.2006

Prof. Alfred Kirpal

„Technikkommunikation bei Hochtechnologien“
 FG Technik- und Wirtschaftsgeschichte,
 Technische Universität Ilmenau, 16.08.2006

Prof. Eberhard Schultheiss

„PVD-Beschichtungstechnik für Optik und Elektronik: das FEP Dresden als Systemlieferant“
 Fraunhofer-Institut für Elektronenstrahl- und Plasmatechnik Dresden, 30.08.2006

Fr. Elvira Remdt / Dr. Henry Romanus

„Probenpräparation für die Elektronenmikroskopie – herkömmliche Verfahren sowie Einsatzmöglichkeiten der Focused Ion Beam“
 Zentrum für Mikro- und Nanotechnologien,
 Technische Universität Ilmenau, 27.09.2006

Prof. Hideaki Matsueda

„Optoelectronic Couplings of Semiconductor Quantum Dots“
 Department of Information Science Kochi University,
 Japan, 10.10.2006

Several Departments of the IMN

„Winter Term Kolloquium“
 Institut für Mikro- und Nanotechnologien,
 18.10.2006

Dr. Norbert Klein

„Dielektrische Nanostrukturen für die Terahertz-Sensorik“
 Institut für Bio- und Nanosysteme
 Forschungszentrum Jülich, 25.10.2006

Hr. Andreas Stamm

„Trockenätzen und Deposition mit Plasmaverfahren (ICP-)RIE, (ICP-)PECVD, ALD“
 OXFORD Instruments GmbH,
 Plasma Technology, Wiesbaden, 08.11.2006

Scientific Projects 2005/2006

Federal Ministry of Education and Research (Bundesministerium für Bildung und Forschung, BMBF)

Aufbau eines Aus- und Weiterbildungsnetzwerks innerhalb der Mikrosystemtechnik in Thüringen (FASIMIT) Project manager: Prof. Wurmus
 Mike Stubenrauch, Verein MicroComp e.V.

Aufbau eines Aus- und Weiterbildungsnetzwerks innerhalb der Mikrosystemtechnik in Thüringen (FASIMIT), Förderphase 2, Project manager: Prof. Hoffmann
 Ilona Hirt, Verein MicroComp e.V.

Nanobiotechnologie-Verbundprojekt: Kristalloides P-Protein, -Prototyp bioanaloger Nanoaktuatoren; Teilprojekt 3: Prototypische Anwendungen (P-Protein) Project manager: Prof. Wurmus
 Karin Friedel, Mike Stubenrauch, Danja Voges, Jörg Burgold

Verbundprojekt: Serientaugliche Fertigungsverfahren für mikrostrukturierte Induktivitäten mit erweitertem Funktions- und Parameterbereich (MIKROFUN) Project manager: Prof. Hoffmann
 Heike Bartsch de Torres, Matthias Kallenbach, Michael Hintz, Mike Stubenrauch, Clemens Wystup, Elvira Remdt, Christine Lohmann, Karin Friedel, Dagmar Raab

InnoRegio Inprosys - Verbundprojekt: „Hochpräzise optoelektronische Messsysteme für die Präzisionsfertigung“ (HOMS) Project manager: Prof. Jäger
 Victor Mandryka, Nataliya Dorozhovets, Dr. Uwe Gerhardt

Material- und Verfahrensanalyse zur Erzeugung von Kohlenstoffstrukturen in naturfasergefüllten Polymeren für den Einsatz in der Brennstoffzellentechnik: Materialcharakterisierung, polymerphysikalische Grundlagenuntersuchungen chemische Oberflächenreaktionen (Arbopyrnet) Project manager: Prof. Schäfer
 Stefan Krischok, Marcel Himmerlich, Rolf Ötting, Rosina Staneva, Anita Neumann, Anette Löffert

Zell- und proteinbasierte Biosensorsysteme für die Wirkstoffsuche an Membranproteinen (Bio-MeP-Sens) Project manager: Dr. Schober
 Andreas Schober, Frank Weise, Irina Cimalla, Christoph Kremin, Michael Fischer, Thomas Friedrich, Michael Gebinoga, Caroline Augspurger, Katharina Lilienthal, Maren-Jödis Klett

Multifunktionale System-in-Package (SiP) Technologien für Mikrowellenanwendungen bis 80 GHz. (MultiSysTeM) Project manager: Dr. Müller Jens Müller, Sven Rentsch, Michael Fischer, Torsten Thelemann, Rubén Perrone, Matthias Mach, Christoph Kremin, Christine Lohmann, Ina Koch

Funktionale Mikrostrukturen für innovative Sensorkonzepte (InnoSens) Project manager: Prof. Ambacher Arne Albrecht, Katharina Lilienthal, Martin Amberg, Katja Tonisch, Mario Kittler, Andreas Winzer, Florentina Will, Ali Majdeddin

German Science Foundation (Deutsche Forschungsgemeinschaft, DFG)

Heteroepitaxie von Gruppe III-Nitriden auf Diamantsubstraten für optoelektronische und elektronische Anwendungen (Diamant I/II) Project manager: Prof. Ambacher Dorin Cornel Cengher, Rastislav Kosiba, Markus Mehnert

Entwicklung piezoelektrischer, mit Halbleiterbauelementen integrierbarer AlGaN/Si-Nanoresonatoren für elektrokeramische Hochfrequenzsensoren (Pi-NEMS I/II) Project manager: Prof. Ambacher Prof. Matthias Hein, Ralf Stephan, Klemens Brückner, Christian Förster, Katja Tonisch, Florentina Will

Nanomechanics with Nanowires (Mech(n)ano) Project manager: Prof. Ambacher Volker Cimalla, Katja Tonisch, Florentina Will, Chunyu Wang

Bauelementeverhalten und Transporteigenschaften organischer Feldeffekt-Transistoren: Experiment-Simulation-Theorie Project manager: Dr. Scheinert Andrej Herasimovich, Ingo Hörselmann, Silvia Klaube

Aufklärung des Funktionsprinzips und Optimierung eines organischen lichtemittierenden Feldeffekttransistors Project manager: Dr. Scheinert Jörg Geßner, Andrej Herasimovich, Ingo Hörselmann, Silvia Klaube

Development of lateral polarity AlN/GaN heterostructures for nonlinear optical applications (LPH-GaN) Project manager: Prof. Schäfer Stefan Krischok, Oliver Ambacher, Rüdiger Goldhahn, Vadim Lebedev, Pierre Lorenz, Sindy Hauguth

Thuringian Ministry of Culture (Thüringer Kultusministerium)

Zell- und Biomolekül-Sensoren in Piko- und Nanofluidischen Systemen

(Pikofluidik) Project manager: Prof. Ambacher Majdeddin Ali, Arne Albrecht, Falko Baier, Volkmar Breternitz, Carsten Buchheim, Jörg Burgold, Volker Cimalla, Lothar Dressler, Karl-Heinz Drüe, Michael Fischer, Karin Friedel, Uwe Genatis, Jörg Geßner, Maik Gubisch, Gabriele Harnisch, Birgitt Hartmann, Michael Hintz, Rene Hoffmann, Matthias Kallenbach, Gabriel Kittler, Mario Kittler, Ina Koch, Stefan Krischok, Regina Lenk, Rostyslav Mastylo, Christian Müller, Andreas Opitz, Elvira Remdt, Henry Romanus, Jens Schawohl, Frank Schwierz, Martina Sieler, Lothar Spieß, Mike Stubenrauch, Frank Weise, Jaroslav Kita, Annette Löffert, Rolf Ötting, Andreas Schober, Björn Schwenke, Aneta Sutor

Anisotrope Nanostrukturen aus Funktionspolymerkompositen für optische und elektronische Bauelemente

(NANORG 1) Project manager: Prof. Gobsch Thomas Kups, Uladzimir Zhokhavets, Elke Langhammer, Maher Al-Ibrahim, Andrej Herasimovich

Zentrum für Innovationskompetenz am Zentrum für Mikro- und Nanotechnologien: Peripherik und Komplexe Systeme für Elektronik und Biosensorik (MacroNano) Project manager: Prof. Ambacher Jens Müller, Thomas Friedrich

Zentrum für Innovationskompetenz MacroNano®, Nachwuchsforscherguppen 'Mikrofluidik und Biosensorik' und 'Funktionalisierte Peripherik' (MacroNano) Project manager: Dr. Müller, Dr. Schober

Integrierte optisch-fluidische Mikrosysteme für die Mikromanipulation und Sensorik in der Biotechnologie (Integrierte mikrooptische Pinzette) Projekt manager: Prof. Sinzinger Arne Albrecht, Stefan Krischok, Lothar Spieß, Christoph Kremin, Rolf Ötting, Thomas Kups, Torsten Gramsch, Martin Amberg

Thüringer Ministerium für Wirtschaft, Technologie und Arbeit

Realisierung eines zweidimensionalen Positionier-/systems mit nm-Genauigkeit mit integrierten Präzisionsführungen (PräFü) Project manager: Prof. Ambacher Mike Stubenrauch, Wolfram Hild, Matthias Kallenbach

Kostengünstige Indium- und Zinkoxid basierende, integrierbare Detektoren zum Nachweis von Ozon (InOzon) Project manager: Prof. Ambacher
Volker Cimalla, Rüdiger Goldhahn, Armin Spitznas, Vasil Yanev, Marcel Himmerlich, Thomas Kups, Katja Tonisch, Florentina Will, Dorin Chengler, Merten Niebelschütz, Benedikt Lübers, Carsten Buchheim, Pascal Schley, Chunyu Wang, Andreas Winzer, Ulrich Liebold, Ilona Hirt, Annette Löffert

Keramische Fluidkomponenten mit elektromagnetischem Aktor (Kerafema) Project manager: Prof. Thust/Dr. Drüe
Michael Hintz, Silvana Rotzoll, Heike Bartsch de Torres, Christian Koch, Annette Funfak, Jörg Wagner, Mike Günther, Lahbib Abahmane, Clemens Wystup, Alexander Sprowitz, Steffen Schneider

Komplexe holographisch-optische Bauelemente (Komphor) Project manager: Prof. Sinzinger
Sebastian Stoebenau, Marcel Teschke, Hans-Peter Helm, Dagmar Raab, Olga Kreis

Nanometertestgerät zur statischen und dynamischen Kalibrierung von Nanotastern der Mikro- und Nano-Technik (NanoTest) Project manager: Prof. Jäger
Andreas Müller, Uwe Gerhardt

European Union (Europäische Union)

Herstellung und Optimierung von 3C-SiC-Schichten auf Siliziumsubstraten durch eine Kombination der Molekularstrahlepitaxie und des lichtinduzierten Ausheilens von Defekten (FLASIC) Project manager: Dr. Pezoldt
Volker Cimalla, Gernot Ecke, Christian Förster, Rastislav Kosiba, Ilona Marquardt, Thomas Stauden, Petia Weih, Charbel Zgheib, Guennadi Tcherkachinine, Markus Mehnert

New Generation of GaN-based sensor arrays for nano- and pico-fluidic systems for fast and reliable biomedical testing" (GANANO) Project manager: Prof. Ambacher (Koordinator)
Ulrich Liebold, Gabriel Kittler, Dorin Cornel Cengher, Simone Gutsche

New Process for Realisation of Electrical Connections between Layers of printed Circuit Boards and a Method to implant Micro Components using the Embedded Micro Connector (EMCI) Project manager: Prof. Winkler
Aneta Sutor, Gernot Bischoff, Ashraf Mokayyes

Gemeinschaftliches Aktionsprogramm in der Berufsbildung, Verfahren B (Microteaching) Project manager: Prof. Hoffmann
Ilona Hirt

Office of Naval Research (ONR)

Pyroelectric AlGaIn/GaN HEMTs for ion, gas & Polar liquid sensors (NICOP) Project manager: Prof. Ambacher
Volker Cimalla, Gernot Ecke, Christian Förster, Rastislav Kosiba, Vadim Lebedev, Ilona Marquardt, Jörg Pezoldt, Thomas Stauden, Petia Weih

Arbeitsgemeinschaft industrieller Forschungsvereinigungen „Otto von Guericke“ e. V. (AiF)

Untersuchung und Entwicklung der hard- und softwaretechnischen Grundlagen für eine automatisch gesteuerte Vorrichtung mit Inline Messung zum strukturbewahrenden Präzisionsabgleich (Präzisionsabgleich) Project manager: Prof. Thust
Dr. Waleed Y. Ehrhardt, Dr. Torsten Thelemann

Fluidiksimulation für Zellkultursysteme – FLUZ; Entwicklung eines mikrofluidischen Messplatzes für Zellkultursysteme (FLUZ Auf) Project manager: Dr. Schober
Andreas Schober, Frank Weise

Entwicklung eines transparenten Quantumwell-Fotosensors für ein Stehende-Wellen-Interferometer (Stehende Welle) Project manager: Prof. Jäger
Oliver Ambacher, Sindy Hauguth, Katja Tonisch, Florentina Will

Deutsche Bundesstiftung Umwelt (DBU)

„Syn and Sort‘ ressourcensparendes kombinatorisches Synthesesystem" (Syn and Sort) Project manager: Prof. Ambacher
Dr. Michael Gebinoga, Dr. Siegmund Hecht, Lothar Dressler, Gabriele Harnisch

German Aerospace Society (Deutsches Zentrum für Luft- und Raumfahrt, DLR)

Keramische Mikrowellenschaltkreise für die Satellitentechnik (KERAMIS) Project manager: Prof. Thust
Karl-Heinz Drüe, Uwe Genatis, Matthias Hein, Ralph Münnich, Ruben Perrone, Martina Sieler, Ralf Stephan, Johannes Trabert

Volkswagen Stiftung

Cluster-jet addressing of nanoparticles to provide functional structures (Cluster-Nano-Jet) Project manager: Prof. Rangelow
Stefan Klett, Elshad Guliyev

General Electric Company (GE)

Pyroelectric AlGa_N/Ga_N and SiC sensor studies for ion, gas and polar-liquid detection

Project manager: Prof. Ambacher

Gabriel Kittler, Ali Majdeddin

Industry

Thüringer Institut für Textil- und Kunststoff-Forschung e.V. (TITK)

„Polymere Feldeffekttransistoren“

Project manager: Dr. Scheinert

Andrej Herasimovich

Degussa AG

„Fertigung von Prototypensystemen mit miniaturisierter verfahrenstechnischer Komponente“

Project manager: Prof. Wurmus

Mike Stubenrauch, Heike Bartsch de Torres

Kennametal Technologies GmbH

„Schichtuntersuchungen an Hartmetallwerkzeugen“

Project manager: Dr. Spieß

Björn Hoschke

Institut für Bioprozess- und Analysenmesstechnik e.V.

„Oberflächenanalytik“

Project manager: Dr. Spieß

Sören Selve, Michael Grosser

XTREME technologies GmbH

„Aktive Düsen zur Tropfenerzeugung in EUV-Injektionssystemen“

Project manager: Prof. Hoffmann

Christoph Kremin, Arne Albrecht



Adresses

IMN
Institute of Micro- and Nanotechnologies
Gustav-Kirchhoff-Str. 7
98693 Ilmenau
Germany

phone: +49-(0)3677-69-3402
fax: +49-(0)3677-69-3499

e-mail: oliver.ambacher@tu-ilmenau.de
URL: <http://www.tu-ilmenau.de/imn>

Prof. Oliver Ambacher:
oliver.ambacher@tu-ilmenau.de
phone: +49-(0)3677-69-3402

Prof. Klaus Augsburg:
klaus.augsburg@tu-ilmenau.de
phone: +49-(0)3677-69-3842

Prof. Nicola Döring:
nicola.doering@tu-ilmenau.de
phone: +49-(0)3677-69-4704

Dr. Thomas Friedrich:
thomas.friedrich@tu-ilmenau.de
phone: +49-(0)3677-69-3380

Prof. Gerhard Gobsch:
gerhard.gobsch@tu-ilmenau.de
phone: +49-(0)3677-69-3701

Prof. Matthias Hein:
matthias.hein@tu-ilmenau.de
phone: +49-(0)3677-69-2832

Prof. Martin Hoffmann:
martin.hoffmann@tu-ilmenau.de
phone: +49-(0)3677-69-2487

Prof. Dagmar Hülsenberg:
dagmar.huelsenberg@tu-ilmenau.de
phone: +49-(0)3677-69-2802

Prof. Gerd Jäger:
jaeger@mb.tu-ilmenau.de
phone: +49-(0)3677-69-2822

Prof. Christine Jakob:
christine.jakob@tu-ilmenau.de
phone: +49-(0)3677-69-3106

Prof. Heinrich Kern:
kern@tu-ilmenau.de
phone: +49-(0)3677-69-2533

Prof. Alfred Kirpal:
alfred.kirpal@tu-ilmenau.de
phone: +49-(0)3677-69-4694

Prof. Christian Knedlik:
christian.knedlik@tu-ilmenau.de
phone: +49-(0)3677-69-3611

Prof. Michael Köhler:
michael.koehler@tu-ilmenau.de
phone: +49-(0)3677-69-3629

Prof. Thomas Leisner:
thomas.leisner@tu-ilmenau.de
phone: +49-(0)3677-69-3672

Dr. Petra Meier:
petra.meier@tu-ilmenau.de
phone: +49-(0)3677-69-1804

ZMN
Center for Micro- and Nanotechnologies
Gustav-Kirchhoff-Str. 7
98693 Ilmenau
Germany

phone: +49-(0)3677-69-3400
fax: +49-(0)3677-69-3499

e-mail: herwig.doellefeld@tu-ilmenau.de
URL: <http://www.tu-ilmenau.de/zmn>

Dr. Jens Müller:
jens.mueller@tu-ilmenau.de
phone: +49-(0)3677-69-3381

Prof. Jürgen Petzoldt:
juergen.petzoldt@tu-ilmenau.de
phone: +49-(0)3677-69-3717

Prof. Ivo Rangelow:
ivo.rangelow@tu-ilmenau.de
phone: +49-(0)3677-69-3717

Prof. Erich Runge:
erich.runge@tu-ilmenau.de
phone: +49-(0)3677-69-3707

Prof. Jürgen A. Schäfer:
juergen.schaefer@tu-ilmenau.de
phone: +49-(0)3677-69-3609

Prof. Peter Scharff:
peter.scharff@tu-ilmenau.de
phone: +49-(0)3677-69-3602

Dr. Susanne Scheinert:
susanne.scheinert@tu-ilmenau.de
phone: +49-(0)3677-69-3222

Dr. Andreas Schober:
andreas.schober@tu-ilmenau.de
phone: +49-(0)3677-69-3387

Prof. Dietmar Schulze:
dietmar.schulze@tu-ilmenau.de
phone: +49-(0)3677-69-2852

Prof. Stefan Sinzinger:
stefan.sinzinger@tu-ilmenau.de
phone: +49-(0)3677-69-2490

Prof. Reiner Thomä:
reiner.thomae@tu-ilmenau.de
phone: +49-(0)3677-69-2622

Prof. Heiko Thust:
heiko.thust@tu-ilmenau.de
phone: +49-(0)3677-69-2605

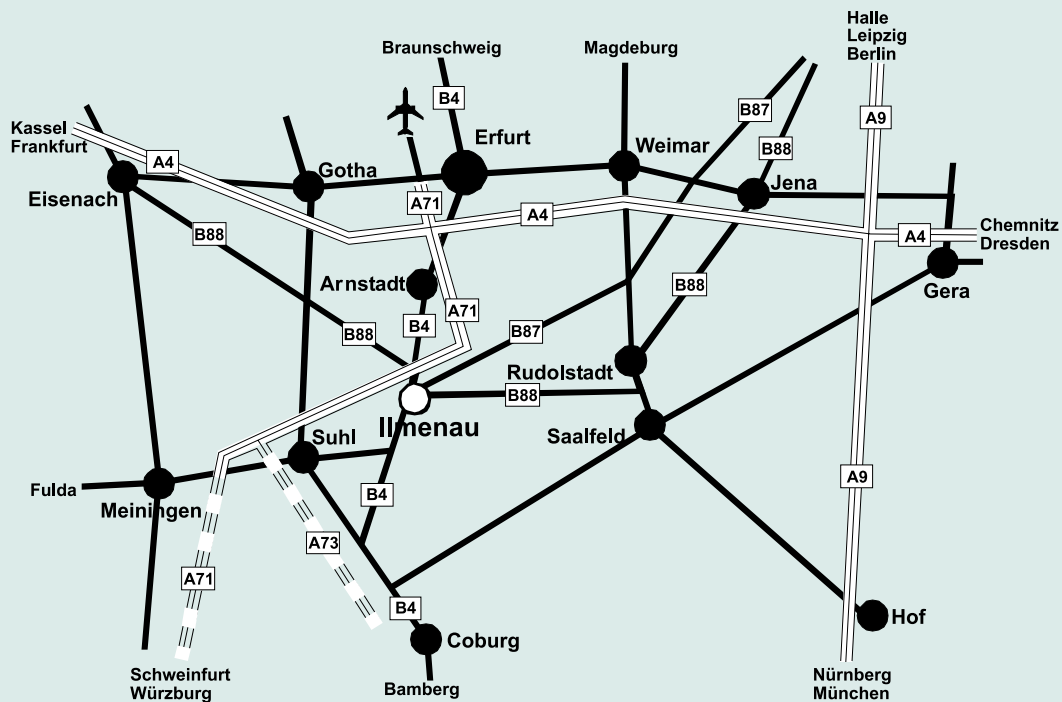
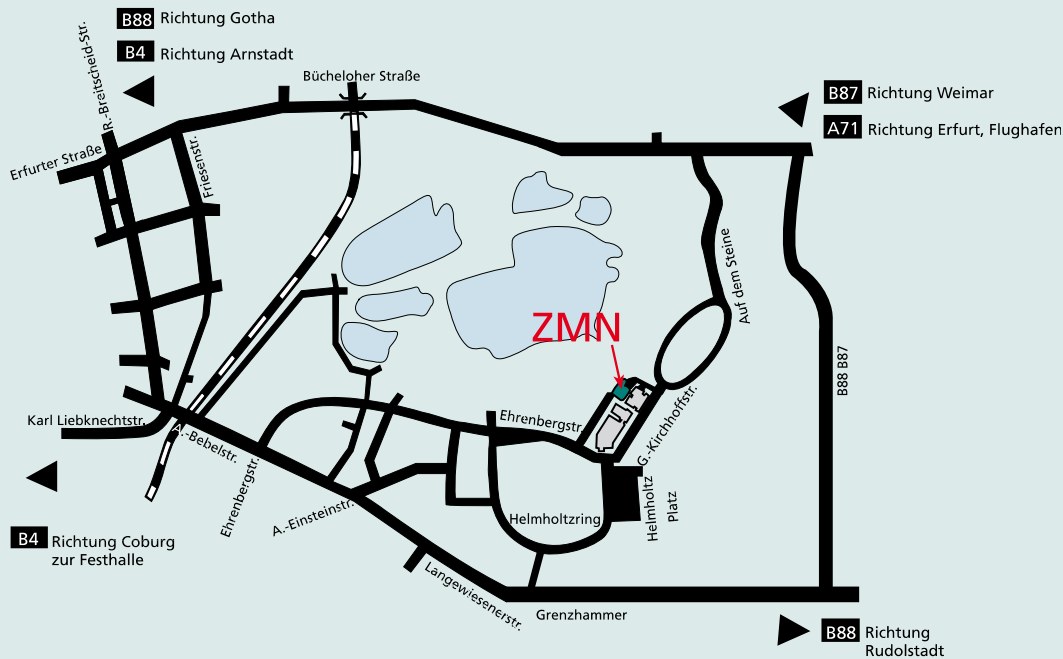
Prof. Johannes Wilden:
johannes.wilden@tu-ilmenau.de
phone: +49-(0)3677-69-2981

Prof. Gert Winkler:
gert.winkler@tu-ilmenau.de
phone: +49-(0)3677-69-2606

Prof. Hartmut Witte:
hartmut.witte@tu-ilmenau.de
phone: +49-(0)3677-69-2456

Prof. Helmut Wurmus:
helmut.wurmus@tu-ilmenau.de
phone: +49-(0)3677-69-2487

IMN, Institute of Micro- and Nanotechnologies
 ZMN, Center for Micro- and Nanotechnologies



IMN, Institute of Micro- and Nanotechnologies
 Gustav-Kirchhoff-Str. 7
 98693 Ilmenau, Germany
 phone: +49-(0)3677-69-3402
 fax: +49-(0)3677-69-3499
 email: oliver.ambacher@tu-ilmenau.de
 URL : <http://www.tu-ilmenau.de/imn>

Director: Prof. Dr. Oliver Ambacher
 Deputy Director: Prof. Dr. Michael Köhler

ZMN, Center for Micro- and Nanotechnologies
 Gustav-Kirchhoff-Str. 7
 98693 Ilmenau, Germany
 phone: +49-(0)3677-69-3400
 fax: +49-(0)3677-69-3499
 email: herwig.doellefeld@tu-ilmenau.de
 URL : <http://www.tu-ilmenau.de/zmn>

Director: Prof. Dr. Oliver Ambacher
 Contact: Dr. Herwig Döllefeld